भौतिक अनुसंधान प्रयोगशाला, अहमदाबाद
Physical Research Laboratory, Ahmedabad

वार्षिक प्रतिवेदन
Annual Report
2015-2016

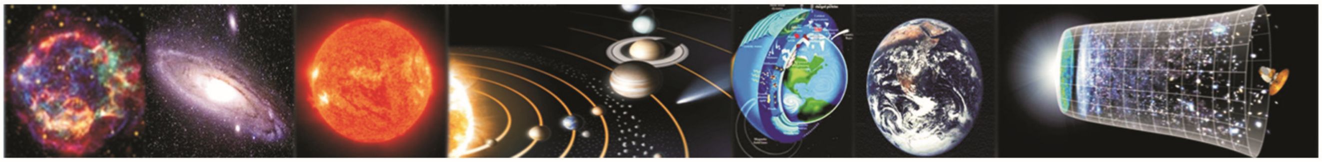

Front cover page:	PRL main campus, Ahmedabad.
Inside back cover pages:	Events at PRL
Back cover page:	Top Panel: IR Observatory, Mt. Abu. Bottom Panel: Multi Application Solar Telescope, Udaipur Solar Observatory.
	(photo courtesy of panoramic view of USO: Dainik Bhaskar, Udaipur)

Compilation and Layout by:
Office of the Dean, PRL.

Published by:
Physical Research Laboratory, Ahmedabad.

Printed by:
Chandrika Corporation, Ahmedabad.

Annual Report

2015 – 2016

Physical Research Laboratory,
Ahmedabad.

PRL Council of Management

Chairman

Professor U.R. Rao Antariksh Bhavan, New BEL Road Bengaluru-560231	Former Chairman, ISRO

Members

Shri A. S. Kiran Kumar Secretary, Department of Space, Govt. of India Antariksh Bhavan, Bengaluru-560231	Chairman, ISRO
Shri A. Vijay Anand, IRS Department of Space, Govt. of India Antariksh Bhavan, Bengaluru-560231	Additional Secretary & FA, DOS
Shri Sanjay S. Lalbhai Ahmedabad Education Society Ahmedabad-380009	Nominee, Ahmedabad Education Society
Shri Kartikeya V. Sarabhai Director Centre for Environment Education Ahmedabad-380054	Nominee, Karmakshetra Educational Foundation
Shri Pankaj Joshi, IAS and Nominee, Government of Gujarat Principal Secretary Higher and Technical Education Government of Gujarat, Gandhinagar-382010	
Professor Utpal Sarkar Director Physical Research Laboratory, Ahmedabad-380009	Ex-Officio (Up to 31.05.2016)
Shri Tapan Misra Director Physical Research Laboratory, Ahmedabad-380009 and Space Applications Centre, Ahmedabad-380015	Ex-Officio (From 01.06.2016)

Member - Secretary

Wg. Cdr. (Retd.) Vibhas Gupta Registrar Physical Research Laboratory, Ahmedabad-380009	Ex-Officio

Contents

Director's Foreword

I have the proud privilege of being the director PRL since 01 June 2016, in addition to my regular role as Director, Space Applications Centre, Ahmedabad. I thus find myself at the helm of a team of PRL scientists, both young and at the senior levels, working at the frontier areas of various fields of science pursued here, ranging from Theoretical Physics to Astronomy and Astrophysics, Solar Physics, Space and Atmospheric Sciences, Atomic, Molecular and Optical Physics and Geo and Planetary Sciences. It is an experience to lead PRL, which unlike other ISRO units is more cerebral in nature with freedom and gentle disregard for hierarchy to support its basic cerebral nature. The primary mandate of the PRL faculty, is to carry out research, publish scientific papers on their respective fields of expertise and to develop appropriate instrumentation to enable their specific science goals. That this mandate is being upheld is apparent from the nearly two hundred research publications, mostly in high impact peer reviewed journals this year. Nineteen Ph.D. theses were submitted during the year and PRL faculty members received invitations to give more than a hundred and fifty lectures at Conferences, Symposia, Workshops, Universities and other Academic Institutions. PRL also invited close to twenty faculty members from both within the country and abroad for scientific interactions.

PRL faculty members have been recognized at both national and international academic fora. The recognitions include the Shanti Swarup Bhatnagar Award 2015, the National Geosciences Award for excellence 2014, the Fellowship of Indian Geophysical union, Lunar and Planetary Institute (Houston, USA) Career development Award, INSA-Senior Scientist Position, Fellowships of National Academy of Sciences, Indian Academy of Sciences and Elsevier Reviewer Recognition Certificates. PRL faculty members serve as Council Members of National and International Science Academies as well as in Council and Advisory Committees of several academic institutions, government departments such as SERB, CSIR and MOES. Several PRL research scholars have also received awards for their presentation in scientific meets.

Significant progress has been made in the initiatives taken last year. The Multi-Application Solar Telescope at Udaipur Solar Observatory is now operational and has started regular observations. The PARAS spectrograph set up as part of the 12^{th} plan has now produced significant science that includes one PhD thesis. Establishment of a new 2.5m telescope facility at Mt. Abu is well underway with AMOS, Belgium as the prime contractor. A focal plane instrument for Hard X-ray polarization measurement has been developed and developmental work on several payloads for the upcoming Chandrayaan-2 and proposed Aditya missions are progressing well.

PRL also contributes to the society by way of providing highly skilled scientists and researchers and in this endeavour the laboratory has a strong Human Resource Development (HRD) component with Doctoral and Post-Doctoral programmes. In addition, PRL conducts a Visiting Scientist programme for university teachers and project training for graduate and post graduate students in both engineering and computer applications. PRL organizes intensive summer programmes for students as well as college teachers every year. The purpose is to provide them an insight into current research activities being pursued at PRL which they can continue even after returning back to their colleges. It is also aimed at motivating them to take up research in basic sciences. In the last one year, PRL had put in a collective effort to increase its outreach activities. A three day open house science exhibition was organized during February-March 2016 which received overwhelming response. Around 3000 people including kids and young school/college/university students visited PRL during this event.

PRL endeavours to promote the use of Hindi in scientific and other official communications. As part of the initiatives to promote usage of Hindi, various activities were carried out such as: Scientific and Technical Seminars in Hindi, Hindi Pakhwada Celebration with word quiz, essay and elocution in Hindi, Bilingual publication of scientific literature meant for public consumption and invited lectures by eminent scientists in Hindi.

As a constant endeavour to serve and strengthen the ongoing scientific, technical and administrative activities, PRL recruited 11 new academic faculty members and 14 new scientific assistants. Efforts to add more manpower at various levels and for various PRL sections are ongoing.

I am indebted to all the members of the PRL Council for their encouragement, invaluable advice and support for all the scientific activities pursued at PRL. I am also grateful to Dr. A. S. Kiran Kumar, Chairman, ISRO for his whole hearted support and encouragement.

Tapan Misra

Director

Science Highlights

Astronomy and Astrophysics

- Broad-band spectral studies of binary X-ray pulsars provide important information regarding the geometry, magnetic field and emission mechanism of the neutron star in the binary systems. Broad-band spectral properties of the X-ray pulsar Cep X-4 was investigated by using a Suzaku observation in 2014 July. In the pulsar spectrum, components such as a cyclotron line at $\sim$28 keV and two Gaussian components for iron lines at 6.4 and 6.9 keV were detected. Apart from these, an additional absorption feature at $\sim$45 keV was clearly detected in residuals obtained from the spectral fitting. This additional feature at $\sim$45 keV was seen in phase-resolved spectra of the pulsar. This feature was identified as the first harmonic of the fundamental cyclotron line at $\sim$28 keV. The ratio between the first harmonic and fundamental line energies (1.7) was found to be in disagreement with the conventional factor of 2, indicating that the heights of line-forming regions are different or viewed at larger angles.

- Timing and spectral properties of the transient Be/X-ray binary pulsar KS 1947+300 were investigated during a giant outburst in 2013. Using observations at the peak and declining phase of the outburst, barycentric corrected spin period of the pulsar was estimated to be 18.81 s. Comparing the spin period with earlier reported values, it was found that the pulsar was spinning-up. Using the spin-up rate, the magnetic field of the pulsar was estimated to be 1.2×10^{12} G. The pulse profiles were found to be single-peaked up to $\sim$10 keV beyond which a sharp peak followed by a dip-like feature appeared at hard X-rays. Iron lines at 6.4 keV and 6.7 keV, identified as emission from neutral and He-like iron atoms, were detected in the pulsar spectrum. A pulsating soft X-ray excess component was detected in the pulsar. This suggests that the accretion column and/or accretion stream as the most probable regions of the soft X-ray excess emission in KS 1947+300.

- Be/X-ray binaries with neutron star as the compact objects show regular X-ray outbursts during which the luminosity of the pulsar increases by an order of magnitude or more. Therefore, these sources offer an excellent opportunity to understand the timing and spectral properties of the X-ray pulsar. One such transient Be/X-ray binary pulsar GX 304-1 was observed with space based X-ray observatory Suzaku in 0.5-70 keV energy range in 2010 August and 2012 January. Pulsations at 275 s were detected in the pulsar and the pulse profiles were found to be strongly energy dependent. A phase-shift of 0.3 was detected while comparing the phase of main dip in the pulse profiles below and above 35 keV. A cyclotron absorption line was detected at 53 and 50 keV, indicating a marginal positive dependence on source luminosity. This positive dependence and significant pulse-phase variation of cyclotron parameters are interpreted in the perspective of theoretical models on cyclotron absorption line in X-ray pulsars.

- The Wolf-Rayet (W-R) stars represent a late phase in the evolution of O stars and can significantly influence the local neighbourhood through the kinetic energy contained in their very powerful winds. A multi-wavelength analysis of a mid-infrared bubble N46, which hosts a WN7 W-R star, was conducted to explore the star formation process in extreme environments. The ^{13}CO line data are used to trace an expanding shell surrounding the W-R star. At least five compact radio sources are physically linked with the edges of the bubble and each of them is consistent with the radio spectral class of a B0V–B0.5V type star. Furthermore, the photometric analysis has revealed that star formation continues into the molecular cloud associated with the bubble N46. In the bubble there exists an apparent age gradient between the W-R star and young sources. Taken together, the star formation activities around the bubble are influenced by the feedback of the W-R star.

- Nova V5668 Sgr was studied in near-infrared (NIR). NIR spectral features are used to classify it as a Fe II class of nova with a bipolar flow. The presence of carbon monoxide first overtone bands were found in emission which are modelled to make estimates of the mass, temperature and column density. The ^{12}C/^{13}C ratio is also estimated to be ~ 1.5. V5668 Sgr was a strong dust producing Nova. Analysis of the dust Spectral Energy Distribution yields a dust mass of 2.7×10^{-7} $M_\odot$, a blackbody angular diameter of the dust shell of 42 mas and a distance estimate to the nova of 1.54 kpc.
- NIR studies of Nova Scorpii 2014 suggested a symbiotic system with secondary star spectral type of M5III ± (two sub-classes). The emission line profiles are very broad and flat topped with full width at zero intensities approaching 9000-10000 km s^{-1}. Although X-ray emission was observed no γ-ray emission was reported. It is also puzzling that no signature of a decelerating shock is seen in the NIR, as seen in similar systems like RS Oph, V745 Sco and V407 Cyg, due to rapid narrowing of the line profiles. The small outburst amplitude and the giant secondary strongly suggest that NSco14 could be a recurrent nova.
- Photospheric magnetic fields in the latitude range 45^o-78^o for the period of 1975.14-2014.42 showed a steady decline starting from about 1995. In addition, interplanetary scintillation (IPS) observations of the inner heliosphere for the period 1983–2013 and in the distance range 0.2–0.8 AU, have also shown steady decline in solar wind micro-turbulence levels, in sync with the declining photospheric fields. Our analysis suggests that the estimated peak (yearly) sunspot number for solar Cycle 25 is likely to be ~62 ± 12. Our observations suggest that we may be headed towards a Maunder like solar minimum beyond solar cycle 25 when the Sun can be almost completely devoid of sunspots for long periods of time corresponding to 5 or more successive cycles. Our studies also indicate that the night time ionospheric cut-off frequency may go well below 10 MHz. If this lasted for 5 or more solar cycles, it could be a boon for ground based low frequency radio astronomy.
- We have studied a radio galaxy J1216+0709 that displays three pairs of lobes in the 610 MHz image obtained with Giant Meterwave Radio Telescope (GMRT). We classify this source as a 'Triple-Double Radio Galaxy (TDRG)' in which three pairs of lobes are result of three different episodes of AGN jet activity. This is only the third such source reported after B0925+420, and Speca. The host galaxy resides in a small group of three galaxies ($m_r \leq 17.77$) and is possibly going through the interaction with faint, dwarf galaxies in the neighbourhood, which may have triggered the recent episodes of AGN activity.
- CZTI offers a unique capability for polarization measurement of incident X-rays.Polarimetric sensitivity of CZTI was investigated using detailed Monte-Carlo simulation and had shown that it will have significant sensitivity to measure polarization in the energy range of 100 - 300 keV few bright X-ray sources. Crab, being a standard calibration source for hard X-ray instruments, has been observed for more then a dozen times by CZTI during the six months of performance verification phase of Astrosat operation. A set of specific criteria was derived to identify proper background and based on this further analysis of all Crab observation was carried out. With this the hard X-ray polarization in Crab nebula was detected significantly in almost all observations with exposure greater then 20 ks. The fitted modulation amplitude and polarization angle in the CZTI plane are 14% and ~390 respectively. The measured polarization is found to be ~25% in 100-300 keV. This agrees with very few polarimetric observations of Crab available in the history of X-ray astronomy.
- Sub meter accuracy in Radial Velocity was obtained on nightly average bin data for Tau Ceti. These observations were taken by PRL Advance Radial Velocity Abu sky Search (PARAS) in November 2015. This was to prove that there is no short period planet around Tau Ceti which was speculated in 2012-2013. These observations of Tau Ceti are in tune with the capabilities of PARAS that was recently improved upon by adding combination of octagonal shape of optical fibres with circular fibres.
- PRL was involved in a multi-observatory, multi-institute attempt to capture the onset of a new quasi-periodic outburst in OJ287. It is the only confirmed binary black hole AGN and shows quasi-periodic outbursts with 12 yr cycle. A successful monitoring of the source in outburst resulted in determination of orbit parameters, leading to accurate calculation of the spin of the primary black hole as 0.313. The study also made it possible to predict the on-start of the next outburst on 28 July 2019.

Solar Physics

- Multi-Application Solar Telescope (MAST) which was operationalised in June 2015 is now recording regular images in G-band (photosphere) and in H_α (chromosphere) for studies of solar active regions and filaments.
- Adaptive optics system for achieving high resolution observations has been integrated with the MAST.
- A spectro-polarimeter developed at USO for measuring magnetic fields has been integrated with the MAST and is currently being operationalised.
- Statistical analysis of umbral dots observed by Hinode was carried out to understand the fine structure of sunspots. The results show that their speed is 0.62 km/s and their lifetime varies from 8 to 40 minutes.
- Analysis of GOLF onboard SOHO observations show that the velocity amplitudes of global p-mode oscillations in the Sun vary with the phase of solar cycle.
- Study using HMI/SDO and GONG data provided the evidence that the magnetic-jerks in the active regions during flares can induce oscillations in the solar atmosphere.
- A multi-wavelength analysis of a solar eruption from a sigmoid in an active region shows evidence of unusual motions of flare sources before the impulsive phase of the flare which do not comply with the standard flare model.
- Study of interacting CMEs observed by STEREO / SECCHI observations under an oblique-collision scenario reveal that their physical and propagation characteristics decide the nature of their collision.

- Numerical simulation studies comparing the intensity of current sheets which are formed close and away from the null points reveal their potential application to understanding of reconnection mechanism in solar flares.

Planetary Sciences and PLANEX Program

- The Cr isotopic compositions of $\sim$15 AGB grains (according to their C, N isotopes) imaged using nanoSIMS indicates higher anomaly ($\sim$10 %) in ^{54}Cr as predicted by theoretical calculations.
- Combined Mg and O isotope analyses of the core, mantle and rim of a coarse-grained Type B CAI having heterogeneous O isotopic compositions suggest formation/alteration of the core CAI via evaporation under conditions suitable for Mg isotope fractionation and interaction with a planetary-like O isotope reservoir.
- Oxygen isotopes measurements in hibonite-spinel-perovskite mineral assemblages from a unique hibonite-bearing Allende CAI (EK5-2A) were observed in the range from ^{16}O-rich compositions (Δ^{17}O $\sim$ -20 ‰) in the WL rim to Δ^{17}O values between $\sim$ -5 ‰ in the interior, and leads to the inference that the inclusion may contain relict phases and/or exposure with distinct nebular gases.
- Extreme variations in δ^{30}Si have been observed in microanalysis of silicates and metal enriched phases of unequilibrated enstatite chondrite, suggesting that very light Si observed in enstatite chondrites (compared to carbonaceous and ordinary chondrites) are primarily due to presence of metal. Comparisons of Si isotope composition of BSE (Bulk Silicate Earth) to that of enstatite chondrites (which are quite heterogeneous) is made to draw inferences about the light elements inside Earth's core.
- Simultaneous Silicon and Magnesium isotopic compositions have been measured in bulk samples of various meteorites. All the samples show very uniform composition of δ^{25}Mg despite having significantly different Si isotope composition among different meteorites. Similar δ^{30}Si of HED meteorite (a differentiated achondrite) to the carbonaceous and ordinary chondrites, questions the role of core formation in producing heavier Si in bulk silicate Earth.
- Komar Gaon meteorite fell (26°56'98"N, 93°46'11"E) during the daylight (12:00 pm IST) on November 13, 2015 in Komar Gaon of Golaghat district of Assam, India. Simultaneous measurements of noble gases and nitrogen by step heating were performed to estimate the cosmic ray exposure age (CREA), and also to decipher the trapped gas components. The CREA as obtained from ^{3}He$_c$, ^{21}Ne$_c$, ^{38}Ar$_c$, ^{83}Kr$_c$, and ^{126}Xe$_c$ are 4.8, 7.1, 6.8, 7.1 and 7.1 Ma respectively. The average CREA for Komar Gaon is estimated as 7.0 Ma, suggesting that this chondrite belongs to one of the peaks in CRE age distribution of L chondrites.
- Using the morphological and topographic evidences, a new volcanic province (Tanaica Montes; 39.55N, 269.17E) spanning over $\sim$150 $\times$ 200 km^2 has been found on Mars, wherein glacial deposits resulting from an extensive glacial phase ($\sim$0.1-1 Ga) are preserved.
- Thermophysical characterization of Gale Crater floor, Mars was performed using the in situ rover measured temperatures and a one-dimensional subsurface heat conduction model. The thermal inertia estimates reveal the diverse processes that had undergone over the Gale crater floor.
- Using Gauss's Law, the maximum radius of levitating particles is estimated to be in the picometre range near the lunar terminator, in contrast to existing calculations which determined a nanometer to micrometer range for such levitating grains.

Space and Atmospheric Sciences

- First three dimensional wave characteristics in the daytime upper atmosphere have been obtained using ground-based multiwavelength oxygen dayglow emission measurements. Large field of view measurements at three oxygen dayglow emissions enabled this inference. This technique forms a new capability for the investigations of vertical coupling of atmospheres in the daytime upper atmosphere.
- Effect of marathon events and estimates of anthropogenic and biogenic emissions of VOCs at urban site of India in winter season.
- Apportionment of the measured aerosol absorption coefficients revealed that annual mean contributions by fossil fuel and biomass burning to black carbon over an urban region are 80% and 20% respectively, and that during monsoon fossil fuel emissions dominate as emissions from biomass burning are minimal.
- Single scattering albedo of aerosols reduces when aerosol scattering coefficient is corrected for relative humidity, highlighting the need to incorporate relative humidity correction on aerosol optical characteristics over urban regions.

Geosciences

- The relationship between monsoon rainfall and its δ^{18}O values was further refined based on data analysis as well as modelling so that speleothem δ^{18}O values can be interpreted precisely in terms of the past monsoons. New study of cave drip water was also completed.
- Based on 21 years of phytoplankton and environmental monitoring data from the surface water of coastal southeast Arabian Sea, we demonstrated a shift in phytoplankton community towards higher sample genus richness and diatom abundance during the two decades of observations.
- Studies in estuaries of the Eastern India indicate release of enormous quantity of REEs, Mn and other trace elements from the suspended particulates in the middle salinity range. The release is associated with decrease in oxygen content of the water indicating release of REEs from Fe-Mn hydroxide coating of the particulates in the reducing condition. Such gigantic supply of dissolved trace elements from the particulates of these estuaries provide one order of magnitude higher REEs compared to their riverine dissolved phase and could contribute significantly to their global oceanic budget.

Theoretical Physics

- Memory function formalism or projection operator technique is an extremely useful method to study the transport and optical properties of various condensed matter systems. A recent revival of its uses in various correlated electronic systems is being observed. It is being used and discussed in various contexts, ranging from non-equilibrium dynamics to the optical properties of various strongly correlated systems such as high temperature superconductors. However, a detailed discussion on this method, starting from its origin to its present day applications at one place is lacking. The memory function approach focusing on its uses in studying the dynamics and the transport properties of correlated electronic systems is studied.

- An explicit perturbative computation of the Mori's memory function was performed by Goetze and Woelfle (GW) to calculate Generalized Drude scattering (GDS) rate for the case of electron-impurity and electron-phonon scattering in metals by assuming constant electronic density of states at the Fermi energy. In the present investigation, we have gone beyond this assumption and extend the GW formalism to the case in which there is a gap around the Fermi surface in electron density of states. The resulting GDS has been compared with a recent one by Sharapov and Carbotte (SC) obtained through a different route. We have found good agreement between the two at finite frequencies. However, we have found discrepancies in the dc scattering rate. These are due to a crucial assumption made in SC. No such high frequency assumption made in the memory function based technique.
- The octant of the 2-3 leptonic mixing angle and the CP phase are two of the major unknown neutrino oscillation parameters and the precise determination of these is interlinked through the octant-CP degeneracy. We studied the proficiency of the DUNE experiment at Fermilab, which is the first beam based experiment to use a baseline longer than 1000 km, to determine these parameters and studied the optimal combination of neutrino and antienutrino runs that can give maximum sensitivity.

  The scalar triplet contribution to the low-energy lepton flavour violating (LFV) and lepton number violating (LNV) processes within a TeV-scaleleft-right symmetric framework was explored. It was found that a triplet of mass comparable to or smaller than the largest right-handed neutrino mass scale can give sizeable contribution to the LFV processes, except in the quasi-degenerate limit of light neutrino masses. In particular, a moderate value of the heaviest neutrino to scalar triplet mass ratio was found to be still experimentally allowed and can be explored in the future LFV experiments. Similarly, the contribution of a relatively light triplet to the LNV process of neutrinoless double beta decay could be significant, disfavouring a part of the model parameter space otherwise allowed by LFV constraints. Regions of parameter space consistent with both LFV and LNV searches, for which the values of the total effective neutrino mass can be accessible to the next generation ton-scale experiments were obtained. Such light triplets can also be directly searched for at the LHC, thus providing a complementary probe of this scenario.
- The discovery of 125 GeV Standard Model (of particle physics) like Higgs boson with no substantial hints of new physics yet at Large hadron Collider (LHC) dictates the primary course of current research in high energy physics. On the other hand, neutrino oscillation data profoundly established the fact that at least some of the neutrinos are massive but having a extremely tiny mass. So any theory for neutrino mass needs to accommodate this minuscule mass parameter naturally. Noting that the neutrinos are the only SM particle for which we can also write Majorana mass terms, the most general mass term is a combination of both Dirac and Majorana terms. Different seesaw mechanisms naturally explain these scenarios with neutrino mass. Here we are investigating LHC phenomenology for TeV scale seesaw mechanisms and whether Large Hadron Collider (LHC) data can be used to indirectly extract information of the seesaw parameters.
- With no existing hints for new physics, stability of electro-weak vacuum, based on the present inputs from Higgs mass, Top mass together with strong coupling constant, can shed light on scale of new physics and that in turn also can constrain parameters. We also include constraints from unitarity as well as charge breaking minima on new physics models and possibly of detecting new resonances at the LHC.
- Another strong indication of the existence of dark matters from wide range of experiments indirectly favours a possibility of a new fundamental stable dark matter particle. We study and propose new constraint variables for mass measurements and reconstruction of these semi-invisible events produced at the LHC.
- Scenario with compressed particle spectrum in popular supersymmetric model is problematic since the signals can easily escape the detection at the traditional searches at the Large Hadron Collider (LHC). In fact, that can be one possibility for our failure to detect supersymmetry (if it is there) so far at the LHC. Early studies with compressed spectrum was searched with the mono-jet signals. We investigated with details calculations to show that both mono-jet and the multi-jet signals can provide a complimentary such strategy to detect in this direction.
- By employing a relativistic coupled-cluster method, electric dipole moment (EDM) of ^{225}Ra due to parity and time-reversalviolating tensor-pseudotensor (T-PT) and nuclear Schiff moment (NSM) interactions are obtained as $d_a = -10.01 \times 10^{-20} \mathrm{C_T} \langle \sigma_n \rangle$ e-cm and $d_a = -6.79 \times 10^{-17} \mathrm{S}/(|e| fm^3)$, respectively, with the T-PT coupling constant $\mathrm{C_T}$ and NSM S. Suitable hyperfine transitions in ^{211}Fr have been identified for the first time to unambiguously measure its nuclear octupole moment. Many magic wavelengths in the singly charged alkaline earth-metal ions have been determined for future ion based optical clocks. Previously reported inconsistencies in the measured and theoretical studies of lifetimes of the $5D$ states in the Cs atom have been removed by carrying out sophisticated relativistic many-body calculations including QED corrections. A plausible experimental scheme to measure parity non-conservation effect, predominantly due to the nuclear anapole moment, in ^{210}Fr using the Cyclotron and Radioisotope Center (CYRIC) facility at Tohoku University, Japan has been reported.
- We consider the generation and evolution of magnetic field in a primordial plasma at temperature T $\leq$ 1 MeV in presence of asymmetric neutrino background i.e. the number densities of right- handed and left-handed neutrinos are not same. Semi-classical equations of motion of a charged fermion are derived using the effective low-energy Lagrangian. It is shown that the spin degree of freedom of the charged fermion couples with the neutrino background. Using this kinetic equation we study the collective modes of the plasma. We find that there exists an unstable mode. This instability is closely related with the instability induced by chiral-anomaly in high temperature T

$\geq$ 80 TeV plasma where right and left-handed electrons are out of equilibrium. We find that at the temperatures below the neutrino decoupling the instability can produce magnetic field of 10 Gauss in the Universe. We discuss cosmological implications of the results.

Atomic, Molecular and Optical Physics

- Polarization properties of Airy beam, a special class of beam with properties of non−diffraction, self acceleration and self healing, were analyzed experimentally as well as theoretically.
- A new method for direct dating past earth quake via the dating of sediment intrusions using luminescence was developed. Its application to sequences in Assam gave a recurrence interval of 300 years for earthquakes of Mw $\geq$ 7 in Assam.
- Optical vortices are finding applications in variety of fields such as optical tweezing and spanning, optical communication and quantum information and computation, however, their divergence was not defined properly. We defined as well as experimentally verified divergence of optical vortex beams independent of their mode of generation.
- Generated non−diffracting speckles with a “perfect” vortex beam which may find applications in metrology as well as cryptography.
- Collaborative work in Central Indian shield zone indicated multiple neotectonic events in Gavilgarh Fault Zone at ca. 6580 ka, 50 ka, 3040 ka, and 14 ka. This evidence of neotectonic activity, presence of active geothermal springs, and recent earthquakes suggest the need for proper seismic monitoring of this region.
- We provided chronology of the coastal bio- clastic sediments of Saurashtra and helped resolve decades old debates on their origin and regional tectonics and stratigraphic interrelationships.
- Generated “perfect” vortex of variable size and observed its effect in angular spectrum of the down-converted photons.
- Produced high-power, high-repetition-rate, Yb-fiber laser based femtosecond source at 355 nm
- Experimentally studied frequency-doubling characteristics of high- power, ultrafast phase singular optical beams
- The first VUV photo-absorption spectra of nitrile bearing molecules such as aceto, propio, butyro and iso-butyronitrile molecules are reported for ices prepared at 10 K and at higher temperatures suggest that the detection of continuous absorption in the 150 nm to 175 nm region may be a good indicator of the detection of nitrile molecules in the surface ice of Pluto.
- Electron irradiation of carbon dioxide (CO_2) and carbon disulphide (CS_2) molecular ice mixture at 85 K coupled to ChACE data revealed presence of CS_2 on lunar South Pole.
- Damages observed in the Bharathidasan Engineering College, Natrampalli, were found to be aftermath of a rare impact event by an object of space origin, travelling at high velocities.
- It has been pointed out by various astronomers that in accordance to the spectroscopic behaviours and chemical abundances, very interesting relationship exist between interstellar alcohols and their corresponding thiols (sulfur analogue of alcohols). Based on our quantum chemical calculation and chemical modelling, we find that ‘Tg’ conformer of 1-propanethiol is a good candidate of astronomical interest.
- Vacuum ultraviolet photoabsorption of prime ice analogs of Pluto and Charon are recorded which will help decipher the data returned from the P-Alice payload onboard New Horizons spacecraft.
- To-date Hartley band (220 nm 310 nm) of ozone is widely used to detect the presence of ozone. Upon irradiation of O_2, CO, CO_2, CO_2+H_2O, SO_2, NO, N_2O and NO_2 ices, and subsequent recording of spectra, strong absorption in the Hartley band was observed. Implication of this experimental data could lead to the identification of ozone precursor molecules on icy satellites by observing the Hartley band, where many of the icy satellites are known to harbour a variety of ozone precursors, simple oxygen bearing molecules.
- Study and report of numerous run-outs / mass wasting on Rhea, an icy satellite of Saturn. Global mapping of these run outs/ mass wasting are carried out and the major cause for these run outs are examined by delineating the impact triggered and non impact origin.
- Electron irradiation of nitrous oxide (N_2O) and carbon disulphide (CS_2) were carried out in order to understand the molecular synthesis on cometary nucleus. Sulphur dioxide (SO_2) and carbon subsulphide (C_3S_2) were found to be the major products.

Awards and Honours

Faculty

A. K. Singhvi

1. Chaired the INSA-National Comm. for IUGS, SCL and INQUA
2. Leaded Indian Delegation to INQUA.
3. Awarded the National Geosciences Award for Excellence −2014, by the Ministry of Mines, Government of India.
4. Elected as Vice President, International Quaternary Union.

R. Ramesh

5. Elected to the council of the Indian Academy of Sciences, Bengaluru.

M. M. Sarin

6. Vice-Chairman, United Nations Group of Experts on Scientific Aspects of Marine Environmental Protection (GESAMP) An interagency advisory body of the United Nations.
7. Co-Chair, MoES-DBT (India)-NERC (UK) Workshop on “Atmospheric Pollution and Human Health”, 12-13 May, 2015, New Delhi.
8. Chairman, National Scientific Committee on Oceanic Research (SCOR-INSA).
9. Chairman, Programme Advisory & Monitoring Committee National Programme on “Atmospheric Chemistry”, MoES (New Delhi).
10. Co-Chair, GESAMP Session hosted by UNESCO-IOC (Paris), 31 August-03 September, 2015.
11. Member, Scientific Advisory Committee Space Physics Laboratory, Trivandrum.
12. Associate-Editor “Biogeosciences” Journal of the European Geosciences Union.
13. Co-Guest-Editor Special Issue of “Atmospheric Environment” on “South Asian Aerosols in Perspective”.
14. Certificate of Outstanding Contribution in Reviewing for “Atmospheric Environment” and “Atmospheric Research” (Elsevier Journals).

H. Chandra

15. Member of Editorial Advisory Board, The Open Atmospheric Science Journal.
16. Editor, Asian J. Physics.
17. Guest editor, Special volume of Asian J. Physics, June 2015.

S. Ramachandran

18. Certificate in recognition of his outstanding contributions to reviewing for the Journal of Atmospheric Solar-Terrestrial Physics-Elsevier Publishers, The Netherlands.
19. Session Chair in 1A on “Aerosol Chemistry”, 19th National Space Science Symposium, SPL, VSSC, Trivandrum, 09-12 February 2016.

D. Pallamraju

20. Chairman, Aeronomy Satellite Study Team, constituted by ADCOS, DOS.

21. Main Scientific Organizer of Session S6: Future opportunities using upcoming new missions and planned ground-based instrumentation in the 14^{th} International Symposium on Equatorial Aeronomy held during 19-23 October, 2015 in Bahir Dar, Ethiopia.
22. Guest Editor, Annales Geophysics, Special Issue on “14^{th} International Symposium on Equatorial Aeronomy”.

Nandita Srivastava

23. Elected, Member Steering Committee for the IAU Division E on The Sun and the Heliosphere.
24. Member, SOC, 3rd Asia-Pacific Solar Physics Meeting, Seoul, Korea, November 3-6, 2015.
25. Session Chair in W4 session on “Results from New Solar Telescope (NST) at BBSO”, 3rd Asia-Pacific Solar Physics Meeting, Seoul, Korea, November 4, 2015.
26. Member, SOC, ISEST/SCOSTEP meeting, Mexico City, Mexico, October 26-30, 2015
27. Member, LOC, Science for Space Weather, Goa, January 24-29, 2016.

S. Goswami

28. Selected as the Fellow of National Academy of Sciences, Allahabad, India.

J. S. Ray

29. Shanti Swarup Bhatnagar Award 2015.

S. K. Singh

30. Elected Fellow of Indian Academy of Sciences, Bengaluru.
31. Member of RAC, Wadia Institute of Himalayan Geology.
32. Chairman, Patterson Award committee, Geochemical Society.

D. Banerjee

33. Chaired the session “Science Results from Chandrayaan-1 and Mars Orbiter Mission”, 19^{th} National Space Science Symposium, SPL, VSSC, Trivandrum, 09-12 February, 2016.

B. K. Sahoo

34. Selected by INSA as one of the founding members of INYSA to serve till year 2019.
35. Member of Editorial Board, Asian Journal of Physics.

V. Sheel

36. Elected as President, Planetary Science section, Asia Oceania Geosciences Society (AOGS) at the AOGS general elections held in Singapore, 02-07 August, 2015 for the term 2016-2018.
37. Vice President, Planetary Science section, Asia Oceania Geosciences Society (AOGS) for 2015-2016.
38. Main Convener, “Science and exploration of Mars and Venus”, 12^{th} annual Asia Oceania Geosciences Society (AOGS) meeting, Singapore, 02-07 August, 2015.
39. Selected as Academic Member of the Athens Institute for Education and Research in 2016.

N. Rastogi

40. Best paper award in Plenary Session 1A “Space based Meteorology, Oceanography, Geosphere-Biosphere Interactions - Aerosols, Trace Gases and Radiative Forcing” 19^{th} National Space Science Symposium, SPL, VSSC, Trivandrum, 09-12 February, 2016.

D. Chakrabarty

41. Elected co-convener in the S5 (Equatorial aeronomy related to atmosphere-ionosphere coupling) session of 14^{th} International Symposium on Equatorial Aeronomy (ISEA14) during 19-23 October, 2015 at Bahir Dar University, Bahir Dar city, Ethiopia.

B. Kumar

42. Session chair in the session on “Helioseismology and Dynamo”, International Conference on “Advances in Seismology A Dialogue across Disciplines”, TIFR, Mumbai, India, December 7-11, 2015.

L. K. Sahu

43. Certificate of Outstanding Contribution in Reviewing for the Atmospheric Environment, Elsevier, The Netherlands, November, 2015.

S. K. Sharma

44. Main Convener, “Science and Explorations of the Atmosphere of the Earth and other Planets”, 12^{th} Annual Asia Oceania Geosciences Society (AOGS) meeting, Singapore, 02-07 August, 2015.

B. Sivaraman

45. Visiting Lecturer, International Space University, Strasbourg, France.
46. Best paper award in National Space Science Symposium held in VSSC Trivadrum, February 2016. Title: Vacuum Ultraviolet Photoabsorption Spectra of Nitrile Ices for their Identification on Pluto.
47. Guest Editor for the Special Issue on ”Low energy interactions related to atmospheric and extreme conditions” in European Physical Journal-D.

S. Kumar

48. Associate Editor, Frontiers in Marine Science.

A. D. Shukla

49. Elected Fellow, Indian Geophysical Union (IGU), 2015.
50. Elected Fellow, The Society of Earth Scientists, 2015.

Neeraj Srivastava

51. Co-convener, PS-5 The solar system bodies including planetary system, 19^{th} National Space Science Symposium, SPL, VSSC, Trivandrum, 09-12 February, 2016.

K. D. Prasad

52. Awarded 2016 LPI Career Development Award from Lunar and Planetary Institute (LPI), Houston, Texas, USA.

S. K. Goyal

53. Best oral presentation for the paper ”Supra Thermal & Energetic Particle Spectrometer (STEPS), subsystem of ASPEX payload (onboard Aditya - L1 mission)”, 19^{th} National Space Science Symposium, SPL, VSSC, Trivandrum, 09-12 February, 2016.

M. S. Shah

54. Best paper award in session: Meteorology Oceanography and Remote Sensing for paper “Low cost automated Flow Injection Analyzer for determination of dissolved iron in sea water”, 19^{th} National Space Science Symposium, SPL, VSSC, Trivandrum, 09-12 February, 2016.

Research Scholars/Post-Doctoral Fellows/Project Associates

A. Aadhi

55. Second place in the poster presentation sponsored by SPIE for the work on “Generation of 2.5 GHz repetition rate femto−second Airy beam radiation”, Winter College on Optics: Optical Frequency Combs, ICTP, Trieste, Italy, 15-26 February, 2016.
56. Incubic / Milton Chang travel grant and the OSA Foundation travel grant from the Optical Society of America (OSA) for the work, “Airy Beam Optical Parametric Oscillator”, presented at the Frontiers in Optics Conference in San Jose, USA, 18-22 October, 2015.
57. Best Ph.D. Thesis award in the Physical Sciences category, Gujarat Science Academy, 2016.

M. V. Jabir

58. Best poster award for paper, “Study of angular spectrum of spontaneous parametric down converted photons using variable size perfect vortex beam”, 24^{th} DAE BRNS National Laser Symposium (NLS-24), RRCAT, Indore, 2-5 December, 2015.

K. Pandey

59. Best Poster Award for paper, “Estimation of Nighttime Equatorial E-region Current Densities using Electrojet Model”, 19^{th} National Space Science Symposium, SPL, VSSC, Trivandrum, 09-12 February, 2016.
60. Best Poster Award for paper, “Estimations of Nighttime Equatorial E-region Currents”, 2^{nd} URSI-Regional Conference on Radio Science, JNU, New Delhi, 16-19 November, 2015.

S. Bose

61. Best poster award for paper, “Thermal inertia estimation at Gale crater, Mars using Curiosity REMS data, 19^{th} National Space Science Symposium, SPL, VSSC, Trivandrum, 09-12 February, 2016.

Human Resource Development

Research and Internship Programmes

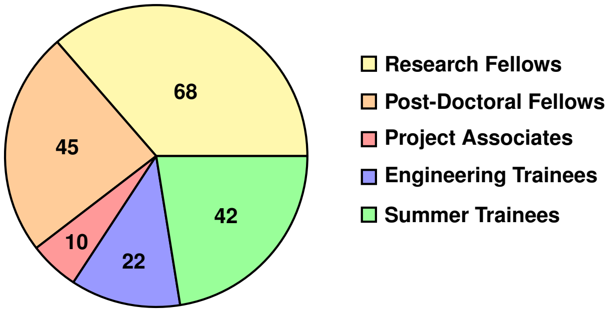

Scientific Contributions

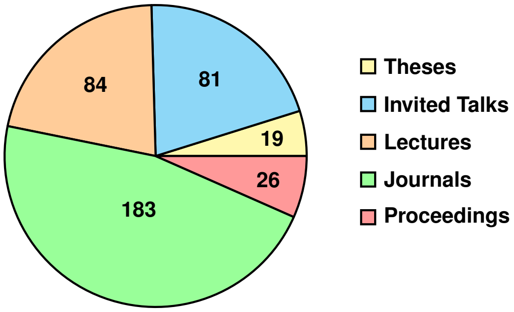

Administrative and Auxiliary staff structure

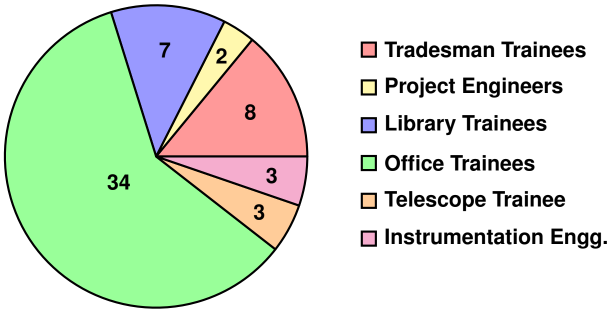

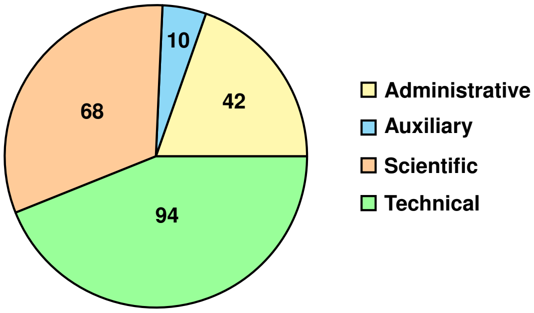

The laboratory has a strong Human Resource Development (HRD) component with Doctoral, Post–Doctoral, visiting Scientist programs. In addition we have an Associate program for university teachers and project training for graduate and post graduate students in both engineering and computer applications. PRL organizes intensive summer programmes for students as well as college teachers every year. The purpose is to provide them an insight into current research activities being pursued at PRL which they can continue even after returning back to their colleges. It is also aimed at motivating them to take up research in basic sciences. The scientific output and staff details in numbers during the reporting year are presented in the above pie charts.

As a part of HRD activity under the PLANEX, following programmes were organized by PRL:

1. The 3^{rd} Mars Orbiter Mission Data Analysis Workshop, 4-5 September, 2015.
2. The 16^{th} PLANEX Workshop on “Exploration of inner solar system objects”, 7-10 March, 2016.

Theses Submitted

P. S. Bhavya

1. “Nitrogen and Carbon cycling in estuarine and marine environments”, Mohanlal Sukhadia University, Udaipur, June, 2015.

P. R. Lekshmy

2. “Stable isotopic studies on monsoon vapour/clouds and precipitation over Kerala”, Mohanlal Sukhadia University, Udaipur, June, 2015.

Y. Singh

3. “Permanent Electric Dipole Moments of Closed Shell Atoms”, Mohanlal Sukhadia University, Udaipur, June, 2015.

A. Aadhi

4. “Generation and characterization of coherent beams of tunable spectral and spatial properties using optical parametric oscillators”, Indian Institute of Technology, Gandhinagar, July, 2015.

D. K. Nandy

5. “Studies Towards the Possible Temporal Variation of the Fine Structure Constant”, Indian Institute of Technology, Gandhinagar, July, 2015.

S. G. Reddy

6. “Optical vortices scattering through random media”, Mohanlal Sukhadia University, Udaipur, July, 2015.

A. Rao

7. “Study of Spectral and Timing Properties of Accretion Disk in Black Hole Binaries”, Indian Institute of Technology, Gandhinagar, September, 2015.

A. Roy

8. “Finite Temperature effects in the Condensates of Dilute Atomic Gases”, Indian Institute of Technology, Gandhinagar, September, 2015.

M. Ghosh

9. “Present aspects and future prospects of neutrino mass and oscillation”, Mohanlal Sukhadia University, Udaipur, September, 2015.

G. K. Chakravarty

10. “Constraint on Particle Physics and Modified Gravity Models from observations”, Mohanlal Sukhadia University, Udaipur, October 2015.

G. Tomar

11. ”Study of particle physics models with implications for dark matter and cosmic ray phenomenology” Indian Institute of Technology, Gandhinagar, November 2015.

G. Bambhaniya

12. “Signature of Neutrino mass models in current and future experiments”, Mohanlal Sukhadia University, Udaipur, November, 2015.

M. Midhun

13. “Stable water Isotopologues in the Indian Summer Monsoon Rainfall”, Indian Institute of Technology, Gandhinagar, November, 2015.

T. Chattopadhyay

14. “Observational aspects of hard X-ray polarimetry”, Indian Institute of Technology, Gandhinagar, November 2015.

M. Shanmugam

15. “Development and Characterization of Silicon Drift Detector based X-ray spectrometer for the Space-borne experiments”, Dharmsinh Desai University, Nadiad, January, 2016.

N. Chandra

16. “Tropospheric greenhouse gases: Emission characteristics and dynamical effects”, Indian Institute of Technology, Gandhinagar, January, 2016.

P. Chaturvedi

17. “Radial Velocity Studies of Eclipsing Binary Systems”, Mohanlal Sukhadia University, Udaipur, January, 2016.

U. Kushwaha

18. “Multi-wavelength investigations of solar eruptive phenomena”, Indian Institute of Technology, Gandhinagar, February, 2016.

G. P. Kadam

19. “Phenomenological studies of strongly interacting matter under extreme conditions”, Mohanlal Sukhadia University, Udaipur, March, 2016.

back to contents

Colloquia/Public Lectures by Visitors

Prof. Prasanta K. Panigrahi
Indian Institute of Science Education and Research (IISER), Kolkata
Human Brain & Market Behaviour: Are they Identical?

Prof. B. P. Das
Indian institute of Astrophysics, Bangaluru
Electric Dipole Moment of the Electron: Present Status and Future Prospects

Dr. Chaitanya Giri
Max Planck Institute for Solar System Research, Germany
Detection of organics with MOMA onboard 2018 ExoMars Rover: Future Prospects of GC MS in Solar System Exploration

Prof. Girish S. Agarwal
Department of Physics Oklahoma State University, USA
Amazing Photons

Mr. Kaustubh Thirumalai
Institute for Geophysics, The University of Texas at Austin,TX,USA
Centennial-scale links between Atlantic Ocean dynamics and hydroclimate: a spotlight on the Little Ice Age

Prof. Avinash Deshpande
Astronomy and Astrophysics Group, Raman Research Institute, Bangalore
Fascinating Life-stories of Pulsars

Dr. Ipsita Mandal
Perimeter Institute for Theoretical Physics, Canada
UV/IR mixing in non-Fermi liquids

Prof. Biswarup Mukhopadhyaya
Harish-Chandra Research Institute, Allahabad, India.
The Messiah of Mass and Message about More

Dr. Atreyee Bhattacharya
University of Colorado Boulder, United States
Understanding environmental response to decadal and longer droughts in the Sahara-Sahel region of North Africa: Insights from two new 4He based dust records.

Dr. Durgesh Tripathi
Inter-University Centre for Astronomy and Astrophysics (IUCAA), Pune
The Solar Ultraviolet Imaging Telescope on board Aditya-L1

Prof. Pankaj S. Joshi
Dept. of Astronomy and Astrophysics, TIFR, Mumbai
Can I see a Black Hole? –Life and Death of Massive Collapsing Stars in the Universe

Dr. Meenakshi Wadhwa
School of Earth and Space Exploration at Arizona State University,USA.
From Dust to Planets: The Cosmochemical Perspective

Dr. Ravikumar Hosamani
University of New Mexico/NASA Ames Research Center, Space Biosciences Division Moffett Field, USA
How tiny fruit flies are helping us better understand the astronauts health in space?

Prof. Frank Deppisch
Department of Physics & Astronomy University College London Gower Street, London WC1E 6BT, UK
Neutrinos and New Physics

Prof. C. V. Vishveshwara
Institute of Astrophysics and Emeritus Director, Jawaharlal Nehru Planetarium, Bangaluru
Black hole and gravitational waves What LIGO saw

Dr. Anand Sen Gupta
Physics Department, IIT Gandhinagar, Gandhinagar
The Discovery of GW 150914 from imarging binary black holes

Prof. K. Sridhar
Theoretical Physics, TIFR, Mumbai
Gauge Symmetries: Hiding and Seeking

Dr. Divya Oberoi
The National Centre for Radio Astrophysics, Pune
Solar observations with MWA

Dr. K. Sankarasubramanian
ISAC, Bangalore
Solar Polarimetry

Dr. Mateja Dumbovic
Hvar Observatory, Croatia
Space weather research in Hvar Observatory

Conferences/Symposia/Workshops by PRL

Solar Physics

1. “Solar Ultraviolet Imaging Telescope meeting”, Udaipur Solar Observatory, Udaipur, 16-17 December, 2015.

Planetary Sciences and PLANEX Program

2. “16^{th} PLANEX Workshop”, PRL Ahmedabad, 7-10 March, 2016.
3. “Mars Orbiter Mission Data Analysis Workshop”, PRL Ahmedabad, 4-5 September, 2015.

Theoretical Physics

4. “Fundamental Physics using Atomic Systems (EFPAS 2015)”, Physical Research Laboratory (PRL), Ahmedabad, 6-8 May, 2015.

Atomic, Molecular and Optical Physics

5. New Horizons@PRL, In PRL on 14th July 2015 celebrating the day of Pluto exploration.

Invited Talks at Conference / Symposia / Workshops

Astronomy and Astrophysics

P. Janardhan

1. "Solar and Heliospheric Signatures from Observations of Solar Magnetic Fields and Heliospheric Microturbulence Levels during the past three solar cycles?", 2^{nd} URSI Regional conference on Radio Science, Jawaharlal Nehru University, New Delhi, 16-19 November 2015.
2. "Cause and consequences of a prolonged IMF-Bz and solar wind density pulses observed at 1 AU.", Science for Space Weather, Goa, India, 23-29 January 2016.

A. Chakraborty

3. "Radial Velocity Precisions and Future Developments to detect Earth like Planets", Workshop on State of the Art Radial Velocity Instrumentation and limitations, Yale University, Connecticut, USA, 6 July, 2015.

V. Singh

4. "AGN Jets in distant dusty galaxies", international conference on Extragalactic Relativistic Jets: Cause and Effect, International Centre for Theoritical Science (ICTS), TIFR, Bangaluru, 12-20 October, 2015.

S. V. Vadawale

5. "Initial results with Astrosat-CZTI", 34^{th} Meeting of Astronomical Society of India, 10-13 May, 2016, Kashmir University, Srinagar.

T. Chattopadhyay

6. "X-ray polarimetry with Astrosat CZT-I", In CZTI workshop at IUCAA, Pune, 5-10 November, 2015.

N. P. S. Mithun

7. "Preflight calibration and generation of response matrix for CZTI", CZTI workshop at IUCAA, Pune, 5-10 November, 2015.
8. "Astrosat CZTI: Preflight calibration and preliminary results from PV observations", In National Space Science Symposium, VSSC, Trivandrum, 9-12 February, 2016.

K. S. Baliyan

9. "The study of AGNs using Blazar variability as a tool", Recent Trends in Compact Object-2015, ARIES, Nainital, 6-9 May, 2015.
10. "Multiwavelength study of blazar variability in Fermi era", Fermi Asian Network Workshop-6, Muju, Leollabuk-do, South Korea, 18-22 January, 2016.

Solar Physics

B. Joshi

11. "Multi-wavelength overview of solar flares", International Conference on Space and Plasma Science, Department of Physics, Govt. Vivekanand P. G. College, Maihar, Satna, M.P., 22-24 September, 2015.

12. “Observational aspects of magnetic reconnection and energy release in solar flares: The RHESSI perspective”, Asia-Pacific Solar Physics Meeting (APSPM), Seoul National University, Seoul, South Korea, 3-6 November, 2015.
13. “Solar activity and its effect in the interplanetary medium: Current research and future prospects”, Research Orientation Workshop sponsored by Directorate of Higher Education, Uttarakhand State Government, M.B. Govt. P. G. College, Haldwani, Nainital, Uttarakhand, 22 January, 2016.

B. Kumar

14. “Seismology of the solar interior and solar surface activity”, International Conference on Space and Plasma Science, Department of Physics, Govt. Vivekanand P. G. College, Madhya Pradesh, 22-24 September, 2015.

Nandita Srivastava

15. “Study of interacting CMEs using STEREO/SECCHI observations”, Science for Space Weather, Goa, 24-29 January, 2016.

R. Bhattacharyya

16. “Magnetic field and current in the solar corona”, 30^{th} National Symposium on Plasma Science & Technology (PLASMA-2015), Saha Institute of Nuclear Physics, Kolkata, 1-4 December, 2015.

Planetary Sciences and PLANEX Program

N. Srivastava

17. “Hyperspectral remote sensing of Moon and Mars”, IEEE GRSS workshop on Hyper spectral Remote Sensing, CEPT University, Ahmedabad 1 March, 2016.

M. Shanmugam

18. “Space instrumentation” Michael Faraday IET International Summit-2015 , Kolkata, $12-13$, September, 2015.
19. “Indian Moon and Mars mission payloads”, Workshop at DDU, Nadiad, 2 May, 2015.

K. K. Marhas

20. “Poor man’s Space probe in laboratory - Organics in Meteorites!” Sixth Indo-American Kavli Frontiers of Science Symposium, Indo$-U.S.$ Science and Technology Forum - U.S. National Academy of Sciences at Irvine, California, 10-12 August, 2015.

K. D. Prasad

21. “Testing of Prototype of Wireless Sensor Nodes (WSN) for Lunar and Planetary Exploration”, AOGS-2015, Singapore, $2-7$ August, 2015.

J. P. Pabari

22. “Role of Electronics and Communication in Space Research”, Electronics and Communication Organization Day, Nirma Institute of Technology, Nirma University, Ahmedabad, 19 August, 2015.
23. “Research in Wireless Sensor Network”, Latest Research in Wireless Communication, Shantilal Shah Engineering College, Bhavnagar, 21 July, 2015.
24. “Space Research Instrumentation for Planetary Mission”, Research Week-2015, GTU, Ahmedabad, 24 April, 2015.

S. K. Goyal

25. “Supra Thermal and Energetic Particle Spectrometer (STEPS), subsystem of ASPEX payload (onboard Aditya - L1 mission)”, National Space Science Symposium, SPL, Thiruvananthapuram, 9-12 February, 2016.

Space and Atmospheric Sciences

D. Chakrabarty

26. “Prompt penetration electric fields and their impact on low latitude ionosphere-thermosphere system” in session A43 (Characterization of Ionospheric and Magnetospheric Processes from Ground and Satellite Observations and Their Connection to Space Weather), 26^{th} IUGG/IAGA General Assembly, Prague, Czech Republic, 22 June-2 July, 2015.

D. Pallamraju

27. Upper atmospheric dynamics: Influence of solar radiation versus forcing from below, in Science for Space Weather-2016 International Living With a Star workshop, Goa, 23-29 January, 2016.

L. K. Sahu

28. “Measurements of volatile organic compounds (VOCs) using PTR-TOF-MS system: Impact of anthropogenic and natural sources in ambient air”, National Space Science Symposium (NSSS), Thiruvananthapuram, 9-12 February, 2016.

R. Sekar

29. “Results on equatorial electrojet irregularities over Indian sector” AOGS 12^{th} annual meeting, Singapore, 2-7 August, 2015.

R. Sridharan

30. “L-band scintillations, Challenges and Accomplishments (Unknotting a naughty problem)”, CODEC meeting, Kolkata, 16-18 December, 2015.

S. Lal

31. “Ozone and trace gases in India: Effects of transport and emissions”, 2^{nd} Workshop on Atmospheric Composition and the Asian Monsoon (ACAM), Bangkok, Thailand, 8-10 June, 2015.

S. Ramachandran

32. “Aerosol Radiative Forcing and Climate”, NEMO-AM Science Workshop, Space Applications Centre, Ahmedabad, 28 April, 2015.
33. “Changing Climate: Role of Aerosols”, International Ozone Day, IMS Ahmedabad Chapter, Physical Research Laboratory, Ahmedabad, 16 September, 2015.
34. “Aerosols and Climate Change: Challenges and Insights”, National Space Science Symposium, Space Physics Laboratory, Trivandrum, 9-12 February, 2016.
35. “Aerosols, and Climate Change: What we know”, Keynote Address, Interdisciplinary Research Scholars Meet, Sardar Patel University, Vallabh Vidyanagar, 3-4 March, 2016.

Geosciences

R. Ramesh

36. “Paleoclimate observations in India”, National Climate Science Conference, Divecha Center for Climate Change, IISc, Bengaluru, 2-3 July, 2015.
37. “Isotopes as useful tools for testing food authenticity”, 3^{rd} Annual Conference of India Section of AOAC INTERNATIONAL, Pune, 19-20 November, 2015.
38. Prof. Kartic Khilar Memorial Lecture at the Pandit Deendayal Upadhyaya Petroleum University, Gandhinagar, 23 November, 2015.
39. “^{15}N as a tracer of aquatic geochemical processes”, National Seminar on lakes, rivers and wetlands-Climate Change Perspective (LakeClimate-2016), Annamalai University, Chidambaram, 28 March, 2016.

S. K. Singh

40. “Trace Element Biogeochemistry in the Northern Indian Ocean”, Goldschmidt Conference-2015, Prague, Czech Republic, 16-21 August, 2015.
41. “Erosion and Weathering in the Western Ghats and geochemical and sedimentary fluxes to adjacent Seas”, National Centre for Earth Science Studies, Trivandrum, 2 January, 2016.

J. S. Ray

42. “Third Rock from the Sun: The Story of the Earth”, National Institute of Science and Technology, Berhampur, 27 January, 2016.
43. “Learning from Volcanoes: the story of Indias only active volcano”, Indian Institute of Science Education and Research Kolkata, 7 March, 2016.
44. “Understanding the planet Earth”, KIIT University, Bhubaneswar, 11 March, 2016.

R. D. Deshpande

45. “Hydro-meteorological processes in India: revelations from stable isotopes in precipitation”, International Atomic Energy Agency (IAEA), Vinenna, Austria, 14 May, 2015.
46. “Stable Isotopes in Precipitation: Insight into hydro-meteorological processes in India”, University of Heidelberg, Heidelberg, Germany, 21 May, 2015.
47. “Water on earth -Challenges and solutions”, DST-INSPIRE Camp K.L. University, Vaddeswaram, Guntur, 30 June, 2015.
48. “Water on earth -Challenges and solutions”, DST-INSPIRE Camp, Sri Mata Vaishno Devi University, Katra, 22 July, 2015.
49. “Isotope Characterization of groundwater from Gujarat and its importance in Management of Groundwater Resources”, Central Ground Water Board (CGWB), Ahmedabad, 30 March, 2016.

N. Rastogi

50. “Atmospheric Aerosols & Cloud Formation”, in Integrated Isotope Hydrology Research Programme in India - a leap forward from IWIN meeting held at PRL, Ahmedabad, 30-31 July, 2015.
51. “Secondary Organic Aerosol in Ambient Atmosphere”, in Symposium on Recent advancements in Atmospheric Chemistry Research, Uka Tarsadia University, Bardoli, Surat, as a part of 34^{th} annual conference of Indian Council of Chemist, 26-28 December, 2015.

S. Kumar

52. “Rates of nitrogen transformation in terrestrial ecosystems”, iLEAPS International Workshop on Biosphere-Atmosphere Interactions and Impacts on Climate and Air quality, IISER Mohali, India, 21 March, 2016.

M. M. Sarin

53. “Atmospheric organic aerosols from biomass burning emissions over Northern India: Implications and Impact on air-quality”, International ILEAPS (Integrated Land Ecosystem-Atmosphere Processes Study) Workshop, IISER-Mohali (Chandigarh), 21 March, 2016.

R. Bhushan

54. “Bomb Radiocarbon sink in the northern Indian Ocean: Air-Sea CO_2 exchange fluxes and some GEOTRACES Results”, CNA, University of Sevilla, Sevilla, 6 July, 2015.

Theoretical Physics

B. K. Sahoo

55. “Parity and Time Reversal Symmetry Violations in Atomic Systems”, Highly Charged Ion (HCI) workshop, WIPM, Wuhan, China, 22-23 March, 2016.
56. “An Overview of Parity and Time Reversal Symmetry Violations in Atoms”, Frontiers in Atomic, Molecular and Optical Sciences (FAMOS 2016) workshop, IACS, Kolkata, 19 - 20 February, 2016.
57. “Modern Atomic Clocks: From time keeping devices to probe fundamental physics”, International Year of Light and 100 Years of Theory of Relativity meeting, Kadi Sarva Vishwavidyalaya, Gandhinagar, 19-20 January, 2016.
58. “Electric dipole moments of the closed-shell atoms”, Fundamental Physics using Atoms (FPUA 2015) meeting, RIKEN, Japan, 30 November-1 December, 2015.
59. “An Atom: a natural laboratory for studying fundamental physics”, A skill based workshop on Computational Methods and Applications in Physics, Department of Physics, Utkal University, 5-6 November, 2015.
60. “Rigorous estimate of nuclear Schiff moments and the present improved limit on $\Theta_{\rm QCD}$”, The interplay between atomic and nuclear physics to study exotic nuclei, ECT, Trento, Italy, 14 - 27 August, 2015.

D. Angom

61. “Suppression of phase separation in warm condensate mixtures”, Frontiers in Atomic, Molecular and Optical Sciences (FAMOS-2016), IACS, Kolkata, 19-20 February, 2016.

H. Mishra

62. “Transport coefficients in Hadron Resonance Gas Model”, Conference on Advances in Nuclear Physics, Institute of Physics, Bhubaneswar, 26-30 June, 2015.
63. “Transport coefficients in hot and dense matter”, Workshop on High Energy Physics Phenomenology, (WHEPP), IIT Kanpur, 4-13 December 2015.

S. Goswami

64. “Global Picture of Neutrino Oscillations”, Unification day 2 workshop, University of StonyBrook, USA, October, 2015.
65. “Neutrino Oscillations: Current Status”, NuHoRIzon, VI, Harish Chandra Research Institute, Allahabad, March, 2016.
66. “Neutrino Oscillations: Past, Present and Future”, AAPCOS 2015, Saha Institute of Nuclear Physics, Kolkata, October, 2015.

R. Rangarajan

67. “Constraints on Just Enough Inflation Preceded by a Thermal Era” International Conference on Gravitation and Cosmology (ICGC) - 2015, Indian Institute of Science Education and Research (IISER), Mohali, 14-18 December, 2015.

P. Konar

68. “’T’ cup and beyond: some recent developments”, Frontiers in High Energy Physics (FHEP), Institute of Mathematical Sciences, Chennai, 22-25 March, 2016.
69. “New kinematic variables” Top Quark Physics meeting, PRL, Ahmedabad, 17-18 March, 2016.

Atomic, Molecular and Optical Physics

R. P. Singh

70. “Pre−detection characteristics for effective fibre coupling of entangled photon sources”, Quantum Optics and Optics of Quantum Systems, JNU, New Delhi, 18-19 March 2016.
71. “Phase singular beams and violation of Bell’s inequality: Experiment”, International Conference on Quantum Foundations 2015 (ICQF15), 30 November 4 December, 2015, NIT Patna.
72. “Non−separable states of light Application to vortex scattering”, Frontiers in Light−Matter Interaction (FiLMI 2016), Indian Institute of Technology, Ropar, 4-5 March, 2016.
73. “Experimenting with entangled photons produced in spontaneous parametric down conversion process”, Quantum Information Processing and Applications (QIPA−2015), Harish−Chandra Research Institute (HRI), Allahabad, 7-13 December, 2015.
74. “Recovering the vorticity of light after scattering using classical entanglement”, International Conference on Light Quanta Modern Perspectives and Applications (ICLQMPA−2015), Physics Dept., University of Allahabad, 14-16 December, 2015,

P. Kumar

75. “Low Energy Ion Spectrometer for Aditya−L1 Mission Solar Wind Ion Spectrometer (SWIS)”, 19th National Space Science Symposium, VSSC, Thiruvananthapuram, 9-12 February. 2016.

B. Sivaraman.

76. “”Synthesizing the basic PAH unit”, PS- 4, National Space Science Symposium, VSSC, Trivandrum, 9-12 February, 2016.
77. “Vacuum ultraviolet photoabsorption spectra of nitrile ices for their identification on Pluto”, PS-5, National Space Science Symposium, VSSC, Trivandrum, 9-12 February, 2016.

N. Chauhan

78. “Investigation of Luminescence Sensitivity Changes in Natural Quartz”, National Conference on Luminescence and its application”, Nagpur, February 18-20, 2016.

V. Kumar

79. “Component Fitting of Optically Stimulated Luminescence Decay Curves Applications, Implication and Cautions for the determination of Paleodose”, National Conference on Luminescence and its application, Nagpur , 18−20 February, 2016.

H. M. Rajapara

80. “SAR−OSL,TT−OSL, and pIRIRSL analysis from Quartz and Feldspars samples of high antiquity implications”, National Conference on Luminescence and its application, Nagpur, 18−20 February, 2016.

A. K. Singhvi

81. “Luminescence Dating of Lacustrine Deposits Applications, Implications and some Caveats”, 13th International Palelimnology Congress, Lanzhou, 4-7 August, 2015.

Lectures at Universities / Institutions

Astronomy and Astrophysics

P. Janardhan

1. “Are we headed towards a Maunder like ‘Grand’ Solar Minimum?”, Institut fr Theoretische Physik IV; Lehrstuhl fr Weltraum und Astrophysik, Arbeitsgruppe Heliophysik, 24 June 2015.
2. “A 20 year decline in solar magnetic fields - heliospheric response and possible consequences? New Paradigms for the Heliosphere”, Physikzentrum Bad Honnef, Germany, 29 June - 03 July 2015.
3. “Declining Solar Activity - What to expect Beyond Solar Cycle 25”, Colloquium, MPIFR - Bonn, 26 June 2015.
4. “Is a Maunder like ‘Grand’ Solar Minimum Around the Corner?”, Colloquium - Kipenheuer Institt Fr Sonnenphysik - Freiburg, 17 June 2015.
5. “Prolonged period Low solar activity - are we headed to a Grand Solar Minimum Ground Based Solar Observations in the Space Instrumentation Era”, Coimbra, 5-9 October 2015.
6. “Grand Solar Minimum: Past Occurrences and Future Possibilities.”, Special Colloquium TIFR, Bombay, 18 January, 2016.

V. Singh

7. “Radio-loud AGN science with Square Kilometre Array, Continuum survey science with SKA: The Indian perspective”, National Centre for Radio Astrophysics, Pune, India, 25 January 2016.

S. Naik

8. “X-ray Binaries : Accretion Powered X-ray Pulsars”, Pacific University, Udaipur, Rajasthan, 12 December 2015.

Solar Physics

B. Joshi

9. “Destabilisation and eruption of active region prominences”, School of Space Research, Kyung Hee University, Yongin, South Korea, 10 November 2015.

B. Kumar

10. “Helioseismology and the GONG Program”, Department of Applied Physics, Pacific University, Udaipur, 9 February, 2015.

A. Ambastha

11. “Cosmic scales and structures”, DST-Inspire Camp, Sir Padampat Singhania University, Bhatewar, Udaipur, 8 April, 2015.
12. “How and what do we understand about the Sun and stars?”, DST-Inspire Camp, Shrinathji Institute of Pharmacy, Rajasthan University of Health Sciences (Jaipur), Nathdwara, Rajsamand, 10 September, 2015.
13. “The life cycle of Sun and stars”, DST-Inspire camp, Shrinathji Institute of Technology and Engineering, Nathdwara, Rajsamand, 6 October, 2015.

14. “Why do we observe our daytime star, the Sun?”, DST-Inspire Camp, Sir Padampat Singhania University, Bhatewar, Udaipur, 22 December, 2015.

Nandita Srivastava

15. “Space Exploration: ISRO’s efforts”, Sunrise Group of Institutions, Udaipur, 15 September, 2015.

R. Bhattacharyya

16. “A Tale of Two Scales: The Solar Corona”, The National Centre for Radio Astrophysics, Pune, 5 February, 2016.

Planetary Sciences and PLANEX Program

J. P. Pabari

17. “Wireless Sensor Network-Research Opportunities”, SVIT, GTU, Valsad, 10 October 2015.
18. “Wireless Sensor Network-Research Avenues”, Nirma Institute of Technology, Nirma University Ahmedabad, 7 October 2015.

K. K. Marhas

19. “Late irradiation scenario”, Johnson Space Science Center (NASA), Houston, 16 September, 2015.

K. D. Prasad

20. “Exploration of the Moon by Indigenous Technology”, RGUKT (IIIT), Basar, Telangana, 26 February, 2015.

Space and Atmospheric Sciences

D. Chakrabarty

21. “Charged and neutral particles in the ionosphere of Mars”, 16th PLANEX Workshop on Exploration of inner solar system objects, 8 March, 2016.
22. “Exploration of plasma and neutral dynamics on Mars”, the 3rd MOM (Mars Orbiter Mission) workshop in PRL, 4-5 September, 2015.

D. Pallamraju

23. Space Weather: Science and Applications, Department of Physics, Bangalore University, 16 July, 2015.

H. Chandra

24. 15 lectures on planetary atmospheres and ionospheres to M. Sc. Physics students (Space & Atmospheric Sciences), and 5 lectures on ionosphere and techniques to Ph. D. students as part of course work, Dibrugarh University: 19-30 April, 2015.

S. K. Sharma

25. “Explorations of the Earth Middle Atmosphere Using Ground and Satellite based Instruments”, NE-SAC, Shillong, 6 May, 2015.
26. “Oceanic Impact on the Atmosphere: Scientific and Societal Perspectives”, INCOIS, Hyderabad, 28 September, 2015.
27. “Atmospheric Explorations using Unique Source of Light”, Kadi Sarva Vishwavidyalaya, Gandhinagar, Gujarat, 20 January, 2016.
28. “Societal Perspectives of Space and Atmospheric Research In India”, DST INSPIRE Program, Government Science College, Idar, Gujarat, 24 January, 2016.
29. “Study of Cloud Base Height measurements and Cloud dynamics from Ceilometer and MODIS satellite over Western India” ISRO-TCG (AT-CTM) review meeting, ARIES, Nainital, 16 March, 2016.

S. Ramachandran

30. “Global Warming, Ozone and Air Pollution”, School of Energy Sciences, Madurai-Kamaraj University, Madurai, 24 August, 2015.
31. “Global Warming, Ozone and Air Pollution”, The American College, Madurai, 25 August, 2015.
32. “Global Warming, Ozone and Air Pollution”, Institute of Infrastructure Development and Management, 30 September, 2015.

S. Lal

33. Atmospheric trace gases: Effects of changes in their abundances, IISER, Mohali, 6 August, 2015.
34. Importance of trace gases in the atmosphere, Dayalbagh Educational Institute, Agra, 23 November, 2015.

Geosciences

M. M. Sarin

35. “Atmospheric organic aerosols over Indo-Gangetic Plain”, Dept. Civil Engineering, Indian Institute of Technology, Kanpur, 7 March, 2016.

R. Ramesh

36. “Oceanography”, IESO Training Camp, Anna University, Chennai organized by the Geological Society of India, 27-30 May and 8-9 September, 2015. (14 lectures).
37. “Stable Isotope Geochemistry”, IISER, Pune, 9-13 November, 2015. (5 lectures).
38. “Nitrogen isotopes in the Oceans”, Special meeting of the Current Science Editorial Board, IISc., Bengaluru, 30 November, 2015.
39. “DST-INSPIRE lectures”, K.R. Rangasamy College, Thiruchengodu, 27 July, 5 September and 12 December, 2015.(4 lectures).

40. “Climate Change”, Gujarat University, Ahmedabad, August-September 2015 and January-February, 2016. (20 lectures).
41. “Nitrogen isotope study of processes in the Arabain Sea”, Department Day, Department of Earth Sciences, IIT Kanpur, 5 February, 2016.
42. “Principles of geochemistry”, Centre for Earth and Space Sciences, University of Hyderabad, 15-19 February, 2016. (15 lectures).
43. “Using isotopes to detect extra terrestrial life”, National Centre For Cell Science, Pune, 2 March, 2016.
44. “Research Methodology”, Centre for Earth and Space Sciences, University of Hyderabad,14-18 March, 2016.(11 lectures).
45. “Introduction to Oceanography”, Dept. of Earth Sciences, Pondicherry University, 30 March, 2016.

A. Singh

46. “Study of Harmful Algal Blooms and other Aspects of Sardine Habitats around the Indian sub-continent (SHABASHI) NANO Indian Subcontinent regional project”, Japan Agency for Marine-Earth Science and Technology (JAMSTEC), Yokohama, 27 January, 2016.
47. “Dinophysis in the Arabian Sea”, Central Marine Fisheries Research Institute (CMFRI), Cochin, 13 February, 2016.
48. “Nitrogen Biogeochemistry in the Northern Indian Ocean”, Central Marine Fisheries Research Institute (CMFRI), Cochin, 16 February, 2016.

Theoretical Physics

S.D. Rindani

49. “Looking for new physics with the top quark at the LHC”, IIT Bombay, 1 October, 2015.
50. “Looking for new physics with the top quark at the LHC ”, IIT Guwahati, 22 December, 2015.

N. Singh

51. “Hot electron relaxation in metals within the Goetze-Woelfle memory function formalism”, IISc, Bengaluru, 11 January, 2016.
52. “Hot electron relaxation in metals within the Goetze-Woelfle memory function formalism”, RRI, Bengaluru, 14 January, 2016.

S. Goswami

53. “Probing leptonic CP violation in current and future experiments”, Northwestern University. IL, USA, October 2015.
54. “Neutrinos: The invisible messengers, Colloquium at Indian Institute of Technology”, Kanpur, October 2015.
55. “Neutrinos: The invisible messengers”, Colloquium, Jawharlal Nehru University, August 2015.
56. “Exploring CP violation in future neutrino oscillation experiments” , Talk at University of Calcutta, Kolkata, May 2015.

R. Rangarajan

57. “Gravitinos, Reheating and the Matter-Antimatter Asymmetry of the Universe”, IIT Madras, 23 April, 2015.
58. “General Relativity and Gravitation”, IAPT Seminar on 100 Years of General Relativity, Gujarat Science City, 28 June, 2015.
59. “Gravitinos, Reheating and the Matter-Antimatter Asymmetry of the Universe”, Dept. of Theoretical Physics Colloquium, TIFR, Mumbai, 1 September, 2015.
60. “Elementary Particles in the Universe and the Search for the Higgs Boson”, Bhavnagar University, 19 September, 2015.
61. “General Relativity and Gravitation”, Keynote address, Symposium on International Year of Light & 100 Years of the Theory of Relativity, Kadi Sarva Vishwavidyalaya, Gandhinagar, 19 January, 2016.
62. “Gravitation, Reheating and the Matter-Antimatter Asymmetry of the Universe”, Colloquium, IISER Bhopal, 26 February, 2016.
63. “Cosmology: The Story of Our Universe”, AU-NASI Science Lecture, Ahmedabad University, 8 March, 2016.

P. Konar

64. “Some developments on mass reconstruction at hadron collider”, IISER-Kolkat, 20 May, 2015.
65. “An alternative description on mass constraining at the LHC”, Indian Association for the Cultivation of Science, Kolkata, 12 May, 2015.
66. “Statistical Methods in Physics”, SERC Preparatory School in THEP, IISER, Bhopal, 6-11 July, 2015.

B. K. Sahoo

67. “Relativistic atomic many-body methods for probing new and fundamental particle physics”, Institute of Applied Physics and Computational Mathematics, Beijing, China, 28 March, 2016.
68. “Electron correlation trends in Ca^{+} ion”, Wuhan Institute of Physics and Mathematics (WIPM), Wuhan, China, 1 April, 2016.
69. “Optical atomic clocks: prospective and applications”, Institute of Physics, Chinese Academy of Sciences, Beijing, China, 29 March, 2016.
70. “New theoretical motivation towards studying hyperfine structures and parity nonconservation effects in Fr” at the Radiation Nuclear Physics Group, Department of Physics, Tohoku University, Sendai, Japan, 3 December, 2015.
71. “Atomic clocks for fundamental physics”, Physics Dept., Revenshaw University, Cuttack, 6 November, 2015.
72. “Extracting precise limit on $\Theta_{\rm QCD}$ parameter”, Seminar at Annual Theory Discussion Days, PRL, Ahmedabad, 8-10 September, 2015.

73. “Parity nonconservation effects in Fr isotopes”, Fr PNC group, Istituto Nazionale di Fisica Nucleare, Laboratori Nazionali di Legnaro, Italy, 3 September, 2015.

Computer Centre

T. N. Sarvaiya

74. ”Cyber Security”, Government Engineering College (GEC), Rajkot, 17 June, 2015.

Atomic, Molecular and Optical Physics

R. P. Singh

75. “Dislocations in light a controlled generation and their applications”, Sambalpur University, Sambalpur, 6 November, 2015.

B. Sivaraman

76. ”Laboratory Astrochemistry”, Department of Applied Chemistry, National Chaio Tung University, Taiwan, 30 December 2015,
77. ”Experimental Astrochemistry”, Space Science Division, Space Astronomy Group, ISRO Satellite Centre, Bengaluru, India.8 October 2015,
78. ”Laboratory Astrochemistry”, Department of Chemistry, Indian Institute of Technology-Madras, 4 February 2016, .
79. ”Recent results from VUV and IR experiments”, Astrochemistry group, The Open University, UK. 28 April 2015,
80. ”VUV spectroscopy of astrochemical ices” Molecular Physics group, National Synchrotron Radiation Research Center, Taiwan.

N. Chauhan

81. Three day course on “Luminescence Dating Principles and Applications”, ISR Gandhinagar, 4-6 April, 2016.

A. K. Singhvi

82. Two day course on “Luminescence Dating Principles, Applications and Implications, China University of Geosciences, Wuhan, China, 8-9 August, 2015.
83. “Luminescence Dating Principles, Application and implications”, Beijing University, 11 August, 2015.
84. “Societal Relevance of and Scientific Challenges for−Geosciences as Services”, Chinese Academy of Sciences, Beijing, 12 August, 2015.

back to contents

Science

Astronomy and Astrophysics

Near-infrared studies of the carbon monoxide and dust-forming Nova V5668 Sgr

Near-infrared (NIR) observational studies of Nova V5668 Sgr using the Mt Abu telescope are presented here between 2 and 107 days after outburst. NIR spectral features are used to classify it as a Fe II class of nova. The spectra follow the evolution of the spectral lines from a P-Cygni stage to a pure emission phase where the shape of the profiles suggests the presence of a bipolar flow. A notable feature is the presence of carbon monoxide first overtone bands which are seen in emission. The CO emission is modelled to make estimates of the mass, temperature and column density to be $(0.5-2.0)\times 10^{-8}$ $M_\odot$, 4000 $\pm$ 300 K and $(0.36-1.94\times 10^{19}$ cm^{-2} respectively. The ^{12}C/^{13}C ratio is estimated to be ~ 1.5. V5668 Sgr was a strong dust producer exhibiting the classical deep dip in its optical light curve during dust formation. Analysis of the dust SED yields a dust mass of 2.7×10^{-7} $M_\odot$, a blackbody angular diameter of the dust shell of 42 mas and a distance estimate to the nova of 1.54 kpc which agrees with estimates made from maximum magnitude versus rate of decline relations.

(D. P. K. Banerjee, M. K. Srivastava, N. M. Ashok, V. Venkataraman)

Near Infrared studies of Nova Ophiuchi 2015

Multi-epoch near-infrared observations of Nova Ophiuchi 2015 using the Mount Abu telescope are presented here. Nova Oph 2015 was discovered during outburst in 2015 March. This nova showed a few special properties viz. (i) it displayed a prolonged flat-top light curve, (ii) it showed evidence for possessing a evolved secondary in the outbursting binary system, and (iii) it made a rare reverse hybrid transition from the He/N class to Fe II class early during its outburst. The present studies focus on the spectroscopic evolution of the object around maximum light and early decline. We show that there was a unique and rapid strengthening and decline in the He 1.0831, 2.0581 μm line strengths during this stage, wherein the nova combined the traits of both the He/N and Fe II classes. Possible causes for this behavior are discussed. The relative strengths of the Ly-β fluoresced OI 0.8446, 1.1287 μm lines are used to estimate the reddening to the nova. A recombination Case B analysis of the early spectra is used to set constraints on the electron density and emission measure, and a later time spectrum, when the ejecta were optically thin to the H lines, is used to estimate the ejecta mass to be (0.95 - 1.9) $\times$ 10^{-4} $M_\odot$. Power law fits made to study the evolution of the continuum over the course of observations, show a fairly constant slope which differs from that expected for either a blackbody or free-free emission.

(M. K. Srivastava, D. P. K. Banerjee, N. M. Ashok, V. Venkataraman)

Nova Sco 2014 - Studying a puzzling outburst in a rare symbiotic nova system.

We followed Nova Scorpii 2014 in NIR immediately after its outburst and shown that this outburst was occurred in a symbiotic system where the secondary star of the system is an evolved giant star. Nova outburst in a symbiotic binary system is extremely rare for a classical Nova but appropriate for T CrB type recurrent novae. NIR spectra were obtained at various phases of the outburst and used along with the pre-outburst JHKs magnitudes to show the symbiotic nature of the secondary star. This nova was also found bright in Hα images in pre-outburst quiescence phase. The spectral class of secondary was estimated to be M5III ± (two sub-classes). The maximum magnitude versus rate of decline relations give an unacceptably large value of 37.5 kpc for the distance. The spectra are typical of the He/N class of novae with strong He I and H lines. The emission line profiles are very broad and flat topped with full width at zero intensities approaching 9000-10000 km s^{-1}. These lines are also having a sharp narrow component which is attributable to emission from the giant's wind. Hot shocked gas, accompanied by X-rays and γ-rays, is expected to form when the high-velocity ejecta from the nova ploughs into the surrounding wind from giant secondary star.

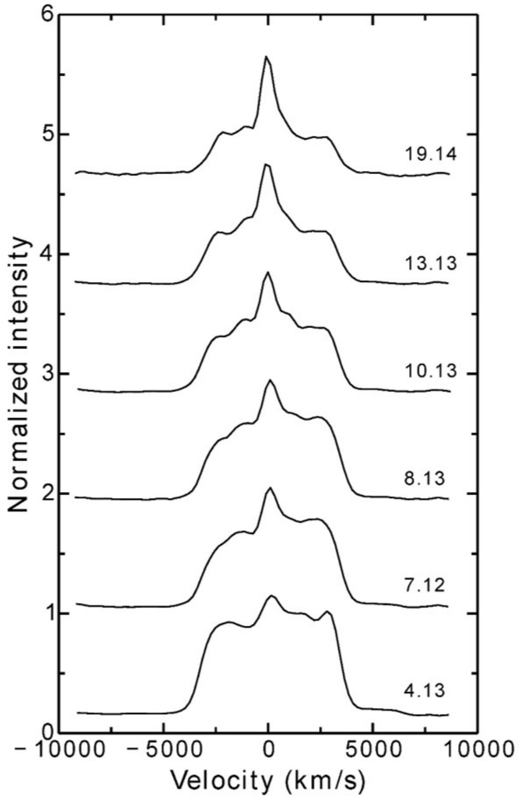

Figure 1: Evolution of the He I 1.0831 μm line profile with time. Days after outburst is shown at the right end of each spectrum. No evidence of narrowing of emission line with time is seen.

Although X-ray emission was observed no γ-ray emission was reported. It is also puzzling that no signature of a decelerating shock is seen in the NIR, seen in similar systems like RS Oph, V745 Sco and V407 Cyg, as rapid narrowing of the line profiles. Figure 1 shows the evolution of HeI 1.0831 μm in which no indication of narrowing of emission lines are seen. The small outburst amplitude and the giant secondary strongly suggest that Nova Sco 2014 could be a recurrent nova.

(V. Joshi, D. P. K. Banerjee, N. M. Ashok, V. Venkatraman)

Annealing and oxidation of dust in nova events

An eruptive nova-like event took place in 1994 in the stellar-merger candidate V4332 Sgr. Following the eruption, dust consisting of refractory silicate-rich dust grains containing a significant component of AlO bonding was formed sometime between 1998 and 2003. Observations using Spitzer between 2005 and 2009 show significant changes in the 10 μm silicate stretch feature. There is a deepening of the 10 μm silicate stretch as well as the development of a feature between about 13 and 20 μm consistent with a blend of the MgO and FeO stretching features and the O-Si-O bending mode of increasingly ordered silicate dust.

Near-infrared observations show the presence of AlO and water vapour in the outflow in 2003, 2004, and 2005: the AlO has significantly decreased in spectra obtained in 2014 while the water vapor remains largely unchanged. An attempt is made to correlate these observations and understand the significance of these changes using DUSTY modeling. The observations appear consistent with the kinetically controlled condensation of highly underoxidized SiO/AlO/Fe/Mg dust grains in the outflow followed by the continuous evolution of the initial condensate due to thermal annealing and oxidation of the dust via reaction with ambient O, OH, and H_2O in the expanding, cooling shell. Periodic monitoring of this dust shell over the mid-infrared spectral range could yield useful information on the evolution of underoxidized silicate condensates exposed to hot water vapor in more conventional circumstellar environments.

(D. P. K. Banerjee, N. M. Ashok)

Post-maximum Near-infrared Spectra of SN 2014J: A Search for Interaction Signatures

Near-infrared (NIR) spectroscopic and photometric observations of the nearby Type Ia SN 2014J are presented. The 17 NIR spectra span epochs from +15.3 to +92.5 days after B-band maximum light, while the JHK photometry include epochs from -10 to +71 days. The observations were made with the Mt Abu telescope and the 8.2m telescope of the Gemini Observatory. These data are used to constrain the progenitor system of SN 2014J utilizing the Paschen beta line, following recent suggestions that this phase period and the NIR in particular are excellent for constraining the amount of swept-up hydrogen-rich material associated with a non-degenerate companion star. We find no evidence for Paschen beta emission lines in our post-maximum spectra, with a rough hydrogen mass limit of less than or equal to 0.1 solar mass, which is consistent with previous limits in SN 2014J from late-time optical spectra of the H-alpha line. Nonetheless, the growing data set of high-quality NIR spectra holds the promise of very useful hydrogen constraints.

This work was done in collaboration with Dr. David Sand of the Texas Technical University, US.

(D. P. K. Banerjee, V. Joshi, V. Venkataraman)

The Early Infrared Temporal Development of Nova Delphini 2013 (V339 Delphini)

The early temporal development of Nova Delphini 2013 (V339 Del) was studied using ground-based infrared photometry, JHK spectroscopy, and 5-28 μm SOFIA FORCAST (Stratospheric Observatory for Infrared Astronomy) spectroscopy. Mount Abu contributed NIR photometric and spectroscopic observations. From the observations, estimates were made of the distance, outburst luminosity, ejected gas mass and the dust yield in this fast CO nova.

This work was done in collaboration with Prof R.D. Gehrz of the University of Minnesota, USA and other collaborators.

(D. P. K. Banerjee, N. M. Ashok, V. Joshi)

A Twenty Year Decline in Solar Photospheric Magnetic Fields and Heliospheric Microturbulence

We have observed a steady 20 year decline of solar photospheric fields at latitudes $\geq 45^o$ starting from $\sim$1995. This prolonged and continuing decline, combined with the fact that Cycle 24 is already past its peak, implies that magnetic fields are likely to continue to decline until $\sim$2020, the expected minimum of the ongoing solar Cycle 24.

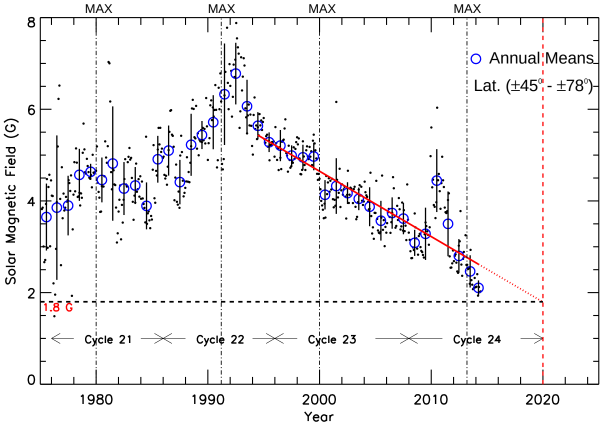

Figure 2: Photospheric magnetic fields in the latitude range 45^o-78^o, computed from the NSO/KP magnetograms, for the period of 1975.14-2014.42. While the solid filled dots are actual measurements of magnetic fields, the open blue circles are annual means with one sigma error bars. The solid red line is a best fit to the declining trend of the annual means, while the dotted red line is an extrapolation of the best fit line until 2020, indicated by a dashed red vertical line. The horizontal dashed line is marked at 1.8 G, the expected field strength in 2020. The vertical dotted lines are marked at the respective solar maximum of Cycles 21, 22, 23, and 24.

Figure 2 shows photospheric magnetic fields in the latitude range 45^o-78^o, computed from the NSO/KP magnetograms, for the period of 1975.14-2014.42. While the solid filled dots are actual measurements of magnetic fields, the open blue circles are annual means with one sigma error bars. The solid red line is a best fit to the declining trend of the annual means, while the dotted red line is an extrapolation of the best fit line until 2020, indicated by a dashed red vertical line. In addition, interplanetary scintillation (IPS) observations of the inner heliosphere for the period 1983–2013 and in the distance range 0.2–0.8 AU, have also shown a similar and steady decline in solar wind micro-turbulence levels, in sync with the declining photospheric fields. Figure 3 shows the normalized scintillation index (m) as function of years for observations of 27 radio sources after making them both source size and distance independent. While the fine dots show the actual measurements of m, the large open circles are annual means of m. The solid line is a best fit to the declining trend while the dotted line is an extrapolation to the declining trend until 2020, the expected minimum of Cycle 24, indicated by a red dashed vertical line. The black dot-dashed vertical lines demarcate solar cycles 21, 22, 23, and 24, respectively. Using the correlation between the polar field and heliospheric magnetic field (HMF) at solar minimum, we have estimated the value of the HMF in 2020 to be 3.9 ($\pm$0.6) nT and a floor value of the HMF of $\sim$3.2 ($\pm$0.4) nT. Given this floor value for the HMF, our analysis suggests that the estimated peak (yearly) sunspot number for solar Cycle 25 is likely to be $\sim$62 $\pm$ 12. Our observations suggest that we may be headed towards a Maunder like solar minimum beyond solar cycle 25 when the Sun can be almost completely devoid of sunspots for long periods of time corresponding to 5 or more successive cycles.

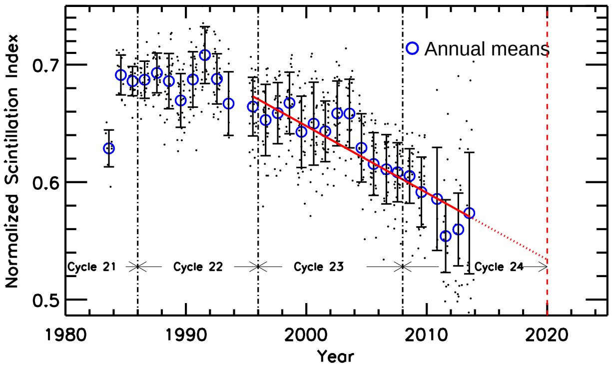

Figure 3: Shows the normalized scintillation index (m) as function of years for observations of 27 sources after making them both source size and distance independent. While the fine dots show the actual measurements of m, the large open circles are annual means of m. The solid line is a best fit to the declining trend while the dotted line is an extrapolation to the declining trend until 2020, the expected minimum of Cycle 24, indicated by a red dashed vertical line. The black dot-dashed vertical lines demarcate solar cycles 21, 22, 23, and 24, respectively.

(P. Janardhan, S. K. Bisoi, R. Sridharan)

Geomagnetic Signatures Corresponding to Episodic Solar Wind Density Enhancements during an Unusually prolonged Weakly Southward IMF-Bz Condition

W investigated multiple enhancements observed in the geomagnetic field which showed a distinct one-to-one correspondence with the density pulses observed at 1 AU, during 0700–1700 UT on May 03, 1998. The spectral analysis of both the variations showed the same discrete frequencies of 0.48, 0.65 and 0.75 mHz, demonstrating that solar wind density enhancements can cause detectable global geomagnetic disturbances. The observations, thus, provide a deeper insight into the possible causes and geomagnetic consequences of a prolonged ($\sim$44 hours) weakly southward IMF-B$_z$ condition during May 02–04, 1998. In-$situ$ observations, during the period, showed the passage of an expanding magnetic cloud embedded in an interplanetary coronal mass ejection (ICME), followed up by a shock and an interplanetary discontinuity driven by another ICME. The magnetic configuration of the source regions of the IMF associated with the ICME interval were also examined, which showed open magnetic field structures, emanating from a small active region on the north of the heliospheric current sheet (HCS). The structures remained constantly to the north of the HCS, both on April 29 and May 01, 1998 suggesting no change in their polarity. The draping of these outward directed radial field lines around the propagating CMEs in the shocked plasma explains the observed polarity changes of the IMF-B$_z$ at 1 AU.

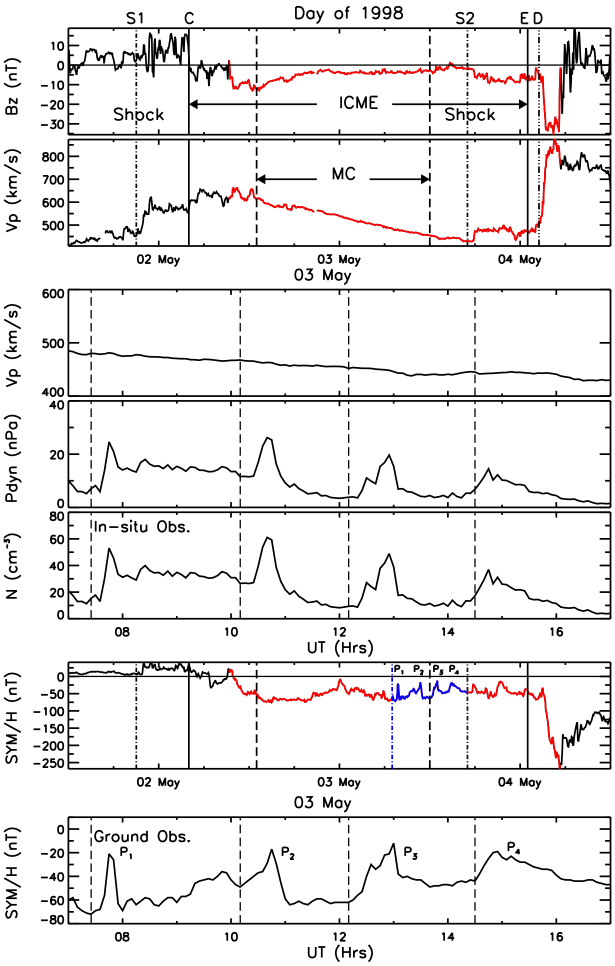

Figure 4: The uppermost group of two panels show.in-situ measurements of magnitude of the z component of the magnetic field (Bz) and the proton velocity (v$_p$. The two vertical dash-dotted lines (S1 and S2) and the vertical long dash-dotted line (D), mark the arrival of shocks and discontinuity. The two solid lines (C and E) mark the arrival and end of the CME, respectively, while the vertical dashed lines indicate the start and end of magnetic cloud (MC). The next group of three panels show the variations of the solar wind velocity, the solar wind dynamic pressure, and the density as a function of time in UT on May 03, 1998. The multiple enhancements observed in SYM-H index, during 0700 UT 1700 UT on May 03, have been shown by the blue solid line, indicated between the blue vertical dash-dotted lines in the sixth panel and the bottom most panel is a blow up of the region between the blue vertical dash-dotted lines.

Figure 4 in-situ measurements of magnitude of the z component of the magnetic field (Bz) and the proton velocity (v$_p$, the solar wind the solar wind dynamic pressure, and the density as a function of time in UT on May 03, 1998. The multiple enhancements observed in SYM-H index, during 0700 UT 1700 UT on May 03, have been shown by the blue solid line, indicated between the blue vertical dash-dotted lines in the sixth panel and the bottom most panel is a blow up of the region between the blue vertical dash-dotted lines.

(P. Janardhan, D. Chakrabartry, S. K. Bisoi)

A Maunder-like Grand Solar Minimum around the Corner - Implications to Near-Earth Space

F-region densities show diurnal, day-day, monthly (solar rotation), seasonal, semi-annual, and annual variations. In addition, it is well known that F-region densities also exhibit solar cycle variations showing good correlation with the sunspot numbers, the latter being used as a proxy to the solar EUV radiation that is primarily responsible for the formation of the ionosphere. Over any location, the F-region densities are controlled by production, loss and transport. The role of transport is crucial and differs from location to location. To establish the dependence of solar activity represented by sunspot number alone, one should concentrate on the background representative ionization devoid of transport effects. Additionally, while using foF2 to study any long term trends, the known sources of variations should be carefully accounted for. In the present study, we have specifically used the foF2 values at 0300 LT and the choice has been arrived at from these considerations. Over the magnetic equator, only electro-dynamical processes dominate in changing the number density distribution and since these processes dominate only during the daytime and all the direct and indirect forcing reach a steady state well past midnight, over any location, and since sunrise effects are yet to be registered, it is perceived that the densities at ∼0300 LT would be a good representation of the quiescent ionosphere that is directly controlled by solar activity. Using our estimated value of the heliospheric magnetic field (HMF) in 2020, the peak sunspot number for solar Cycle 25 was found to be 69 (±12).

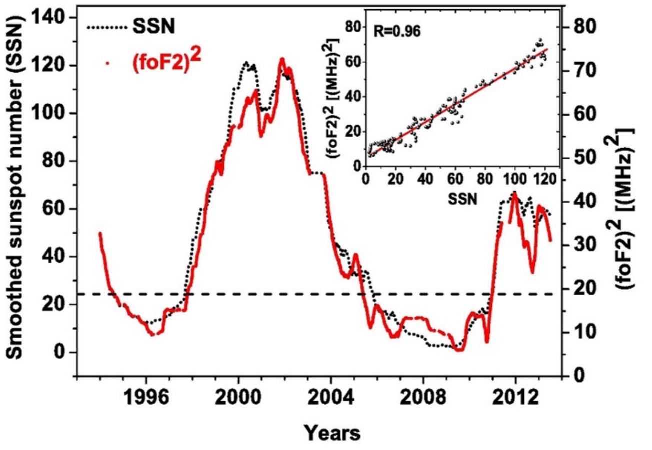

Figure 5: The correlation between the measured (foF2)2 with that of the sunspot number. A linear correlation plot between these two parameters, with a correlation coefficient of R=0.96 is shown in the inset. The horizontal dashed line is drawn at a sunspot number of 25 corresponding to a very low level of sunspot activity.

These results and the fact that solar magnetic fields continue to decline at present, begs the question as to whether we are headed towards a long period of very low sunspot activity similar to the well known Maunder minimum between 1645 and 1715. An assessment of possible impact of such a likely grand minimum on terrestrial ionospheric current systems, based on the one-to-one correlation of sunspot number and night time F-region maximum electron density, reveals that the period post 2020 will be useful for undertaking systematic ground based low-frequency radio astronomy observations, as the night time ionospheric cut-off frequency could be well below 10 MHz. Figure 5 shows the correlation between the measured $(\text{foF2})^2$ with that of the sunspot number. A thirteen month running mean, to smooth out both semi-annual and annual variations, has been applied for both parameters. A linear correlation plot between these two parameters, with a correlation coefficient of R=0.96 is shown in the inset. It is apparent from the y-intercept of the inset in Figure 5 that foF2^2 drops well below 10 MHz, implying that the night time ionospheric cut-off frequency drops significantly below 10 MHz and hence the period post 2020 can be used for undertaking systematic ground based low-frequency radio astronomy observations.

(P. Janardhan, S. K. Bisoi)

Optical variability study of Blazar S5 0716+714 during 2013-2015

Aiming at investigating optical variability in BL Lac source S5 0716+714, we observed it for 46 nights during 2013 January 14 to 2015 June 1 using 1.2-m Mt. Abu InfraRed Observatory (MIRO) telescope mounted with CCD camera. During 29 nights source was monitored for more than two hours with high temporal resolution, resulting in 6256 data points in R-band, to study intra-night variability, which puts upper limit on the size of the emission region.

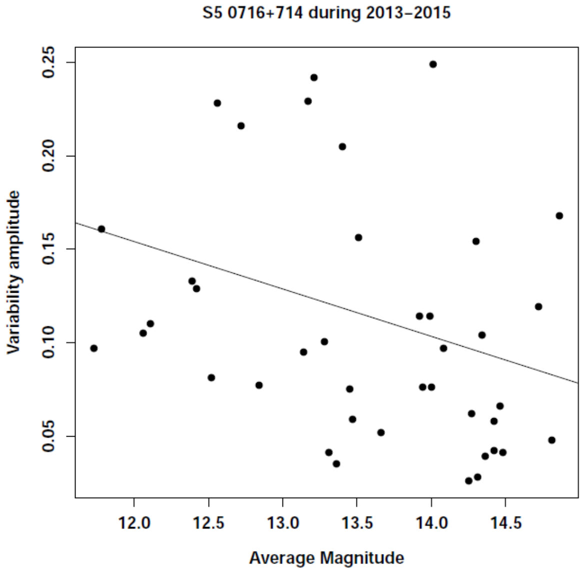

Figure 6: Amplitude of variation (mag) as a function of R-band brightness, for the source S5 0716+71 during 2013-15.

Observations were also made in B, V and I bands with 159, 214, and 177 data points, respectively, to address inter-night variability and the color behavior of S5 0716+71 during the observed period. The light-curves generated and statistical studies performed suggest the source showing intra-night variability during 9 nights (variability duty cycle more than 31%) and a significant night-to-night variation. The average brightness magnitudes obtained during the period in B, V, R, I Johnson-Cousins filters were found to be 14.42, 14.02, 13.22, 13.02, respectively, indicating that source was in relatively bright state. A mild bluer when brighter (BWB) behavior is shown by S5 0716+71 during the period of present observations supporting shock-in-jet model. S5 0716+71 also became bluer in colour with time during this duration, perhaps indicating to its very active phase. We notice larger amplitudes of variation when source was brighter/flaring as shown in the Figure 6. On pne of the night (December 28, 2013), the source shows signs of quasi-periodic behaviour with a period of 1.1 Hr. Based on shortest time scale of variability and causality argument, we estimated upper bound on the size of the emission region as 0.9×10^{15} cms and the mass of the black hole as 10^9 M$\odot$.

(N. Kaur, K. S. Baliyan, Sameer, S. Ganesh)

OJ287: binary black hole blazar system, in new flaring phase

OJ287, the only confirmed binary black hole blazar system, undergoes large optical flares twice in 12 years. Due to good coverage over past more than 100 years, the times of the flares onset have been predicted successfully for last 5-periods using a black hole binary model. In this model a secondary black hole goes around a primary black hole, impacting the accretion disk of the latter twice per orbital period, creating a thermal flare. It helps determine several parameters of the system- black hole masses, orbit, spin rate of primary etc. The 2015 November/December flare started, as predicted, on November 18, went into the phase of rapid flux rise on November 25, on the centenary of Einstein's General theory of Relativity, and peaked on December 5 with R = 13.04 mag, the brightest in over 30 years in R-band. The peak and the decay of the flare were nicely captured by the observations at MIRO in R-band. Apart from this short term flare, we also detected intra-night variability on one day with high significance. To trace the complete flare, multi-site observations from different locations on the earth were carried out. Since the orbit solution is strongly over-determined, the next flare is predicted to peak on July 28, 2019.

A detailed monitoring of this event should allow us to test, for the first time, the celebrated black hole no-hair theorem for a massive black hole at the 10% level. The main difficulty of observing OJ287 from Earth during July 2019 is its closeness to the Sun. Therefore, it is desirable to monitor OJ287 from a space-based telescope not in the vicinity of Earth. Such a unique opportunity for testing the above theorem of General Relativity using OJ287 will not be available again until several orbital cycles later.

This work was the result of co-ordinated effort among University of Turku, TIFR, MIRO, Mt Suhora Obs. INFN-Perugia, North carolina University and ESAC-Madrid.

(K. S. Baliyan, N. Kaur, S. Ganesh, Sameer, Rathnakumar)

Long-term variability behaviour of blazar 3C66A

Under the ongoing long-term program for the study of blazars, a subclass of AGN, we are monitoring a sample of sources. Here we present results based on the observations of blazar 3C66A, an intermediate BL Lac, from 2005 November 06 to 2015 October 30 in the BVRI broadbands using 1.2m telescope of Mt. Abu InfraRed Observatory (MIRO). The source was observed on 142 nights out of which on 61 nights it was monitored for more than 1 hr to check for intra-day variability (IDV). Blazar 3C66A exhibited significant variations in optical flux on short and long term time scales. However, unlike highly variable S5 0716+71, it showed IDV duty cycle of about 13% only. Our statistical studies suggest IDV time scales ranging from $\sim$ 20 min to about 3.5 hours, and, at least in one case, possibility of quasi-periodic oscillations with $\sim$ 35 min periodicity. Such rapid variations are most probably the result of emitting plasma encountering local inhomogeneities or over-densities in the jet. The IDV amplitudes in R$-$band were found to vary from 0.02 mag to as high as 1.1 mag, with larger amplitude of variation when source was relatively fainter. Normally one would expect larger variability amplitude while source is more active- flaring. The typical rate of flux variation was estimated to be $\sim$0.06 mag hr^{-1} in both, the rising and falling phases. The shortest timescale of variation, 16 min, sets an upper limit of 3.0×10^{14} cm on the size of the emission region and about 1.6×10^{8} $\mathrm{M}_{\odot}$ as an estimate of the mass of black hole. The long-term study suggests a mild bluer-when-brighter behavior, typical for blazars, supporting shock-in-jet model of emission.

(Sameer, N. Kaur, K. S. Baliyan, S. Ganesh)

Optical Spectroscopy of Comet C/2014 Q2 (Lovejoy)

Comet C/2014 Q2(Lovejoy) is an Oort cloud comet which had brightened to a peak visual magnitude of 4.9 during its close approach to Earth in the month of January 2015. Spectra of this comet were taken with low resolution spectrograph, LISA, mounted on the 50 cm telescope at the Mount Abu Infrared observatory, Mount Abu. LISA is a grating spectrograph designed to study the spectra of faint and extended objects. Observations were carried out during the months of January-May 2015 covering perihelion and post perihelion periods.

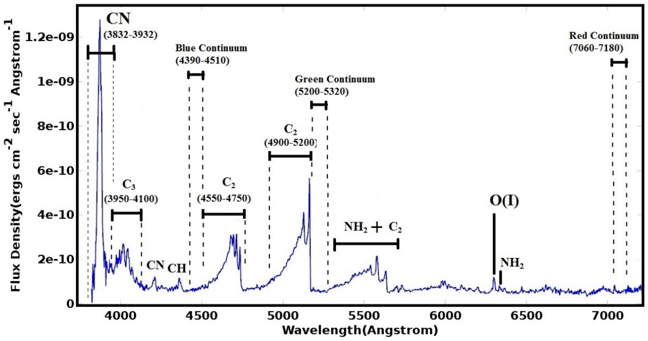

Figure 7: Low resolution spectra of Comet C/2014 Q2(Lovejoy) taken from LISA mounted on ATVS telescope at MIRO. Prominent molecular lines are seen.

Various molecular emission bands (e.g. CN, C_2, C_3, etc - c.f. Figure 7) were seen in the optical spectra of this comet. The gas distribution was studied by modeling it for various emission bands. Production rates were estimated for those species. This was done at various epochs in order to study the variation with heliocentric distance. Comet C/2014 Q2 (Lovejoy) was found to be more active in the post-perihelion phase, thus showing an assymetric behaviour about perihelion.

(K. Venkataramani, S. Ganesh, K. S. Baliyan, U. C. Joshi, S. Ghetiya, V. K. Agnihotri)

Spectroscopic follow up of Asteroid 2015 TB145

2015 TB145 is a near Earth asteroid (NEA) discovered on 10th October 2015, only a couple of weeks before close flyby (2015 October 31) of Earth at 1.2 lunar distance. This asteroid was first discovered by the PanSTARRS telescope. During its close approach on 31st October, optical spectra were obtained with LISA, a low resolution spectrograph, mounted on the 50 cm telescope at the Mount Abu Infra-red Observatory. This asteroid had a large orbital inclination of 39 deg to the ecliptic and hence comet like spectral emission features were expected. However, our spectra show that this object had features common to other asteroids and was quite unlike any cometary spectrum. The spectra also revealed a key absorption feature at 4300 Ångström, which might indicate presence of Fe^{+} ions.

(K. Venkataramani, S. Ganesh, K. S. Baliyan)

Three episodes of AGN jet activity detected in a radio galaxy J1216+0709

Radio galaxies are powerful radio emitters with total size of hundreds of kiloparsec to even a few megaparsec. Typically, radio morphology consists of a core producing a pair of bipolar collimated jets terminating in the form of lobes. Therefore, the detection of ‘core-jet-lobe’ radio morphology is a clear indication of AGN activity. Furthermore, radio morphological structure and spectral properties can be used to probe the history of AGN activity. We have studied a rare class of radio galaxy named as J1216+0709 that displays three pairs of lobes in the 610 MHz image obtained with Giant Meterwave Radio Telescope (GMRT). We classify this source as a ‘Triple-Double Radio Galaxy (TDRG)’ in which three pairs of lobes are result of three different episodes of AGN jet activity. This is only the third such source reported after B0925+420, and Speca. The host galaxy resides is a small group of three galaxies ($\mathrm{m_r} \leq$ 17.77) and is possibly going through the interaction with faint, dwarf galaxies in the neighbourhood, which may have triggered the recent episodes of AGN activity.
This work has been done in collaboration with Ishwara-Chandra (NCRA-TIFR) and Preeti Kharb (IIA).

(V. Singh, S. Srivastava, P. Janardhan)

Optical IR Variability study of Narrow-Line Seyfert galaxies (NLS1s) using Mt. Abu telescope

Narrow line Seyfert 1 galaxies (NLS1s) are a subclass of Active Galactic Nuclei (AGN) that show broad permitted Balmer emission lines of widths relatively narrower (FWHM of Hβ ¡ 2000 km s^{-1}) than that are found in normal AGN.

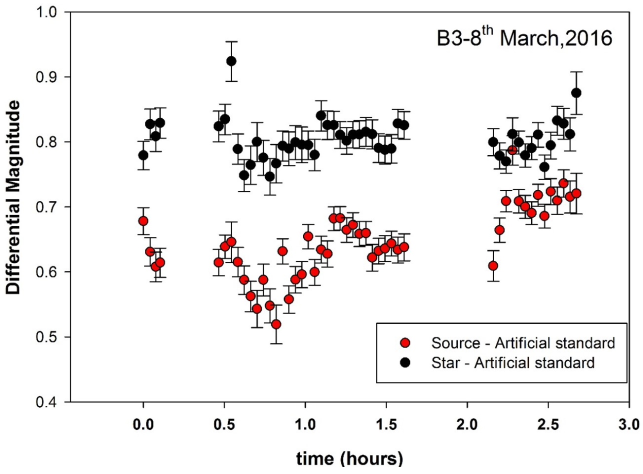

Figure 8: Differential light curves of a NLS1 named ‘B3 1702+457’ obtained from Mt. Abu 1.2m telescope on March 08, 2016.

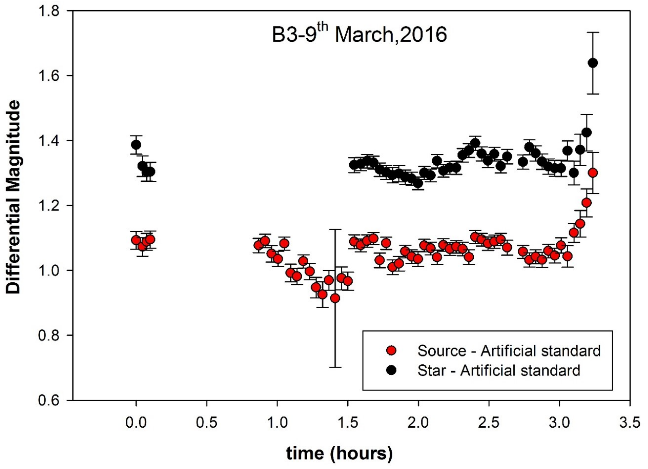

Figure 9: Differential light curves of a NLS1 named ‘B3 1702+457’ obtained from Mt. Abu 1.2m telescope on March 09, 2016.

Also, unlike Broad-Line AGN (BL-AGN), NLS1s exhibit relatively weaker forbidden emission lines (e.g., [O III]/H$\beta < 3$), strong permitted Fe II emission lines, steep soft X-ray spectra, rapid X-ray variability (Panessa et al. 2011). NLS1s are believed to possess smaller SuperMassive Black Holes (SMBHs; 10^5 - 10^8 M$_{sun}$) with relatively higher accretion rates (Foschini et al. 2015). Several NLS1s are detected in gamma-ray inferring the presence of powerful relativistic jets viewed close to the line-of-sight. The presence of the relativistic jets motivates us to search for optical variability in RL-NLS1s, because of the well-known beaming effect (e.g., Wagner & Witzel 1995). Radio-loudness can be used as a proxy for the jet production efficiency. We are carrying out optical, IR observations of a sample of NLS1s using Mt. Abu 1.2m telescope. The sample consists of very radio-loud ($R > 100$) NLS1s as these are expected to posses strong relativistic jets with small viewing angle. Such sources are more likely to show short time-scale optical, IR variability. The search on optical variability in RL-NLS1s will allow us to probe whether all RL-NLS1s posses relativistic jets with small viewing angle. Our sample also include RL-NLS1s that are not detected in Fermi gamma-ray observations as it is unclear if such sources lack gamma-ray emission or merely fall below the Fermi detection limit.

(V. Singh, K. S. Baliyan, S. Ganesh, Sameer)

Co-evolution of Active Galactic Nuclei and their host galaxy

It is believed that almost all galaxies host Super-Massive Black Hole (SMBH) in their centres and accretion on to SMBH is manifested as Active Galactic Nuclei (AGN). It has been shown that mass of SMBH is correlated with galaxy properties such as bulge mass, galaxy luminosity. The correlations between SMBH and galaxy properties suggest that both SMBH and their host galaxies evolve together, probably mutually regulating each other (Alexander and Hickox 2012, for a review). Therefore, it is important to understand the properties of host galaxies during the periods of AGN activity (when SMBH grows via accretion) for building up a cogent theoretical framework for galaxy evolution. Extragalactic radio sources are amongst the best studied distant AGN, due to the ease with which large samples of such objects can be observed up to larger redshifts. In order to understand the co-evolution of AGN and host galaxies we have carried out 325 MHz deep GMRT radio surveys of extragalactic fields named as the XMM-LSS, ELAIS-N1 and Lockmann hole. The radio surveys have yielded a large sample of radio galaxies spanning over a large range of redshifts and luminosities. These fields have also been surveyed at optical (SDSS, CFHT-LS), near-IR (UKIDDS, VIDEO), mid-IR (Spitzer) and far-IR (Herschel). Using deep multiwavelength data we attempt to understand the evolution of AGN population across cosmic epochs and the nature of their host galaxies and surrounding environments.
This work is being done in collaboration with Yogesh Wadadekar, Ishwara-Chandra (NCRA-TIFR), Sandeep Sirothia (SKA, South Africa), Alexander Beelen (IAS, France) and Alain Omont (IAP, France).

(V. Singh)

PARAS sub meter accuracy of Radial Velocities in Tau Ceti

High accuracy precision radial-velocity planet searcher spectrographs have turned out to be the most efficient and only possible ground based technology to determine masses of Exoplanets. Technological advances for precision radial velocity (RV) measurements have focused on building extremely stable instruments in the recent past and will be the trend in the future as well. This includes achieving higher precision with higher resolution to detect analogs of the Earth or massive Earths (up to 5 Earth Mass) with 0.5 m/s velocity amplitudes or better (down to 0.1m/s) around G and K dwarfs. Thus the future spectrometers need to improve upon the state of the art, higher sampling, greater stability in the illumination of the spectrometer optics and better detectors, more precise wavelength calibration, and broader bandwidth spectra. Main data analysis challenges for the precision RV measurements include distinguishing centre of mass, Keplerian motion from photospheric velocities (time correlated noise) and the proper treatment of telluric contamination. Success here is coupled to the instrument design, but also requires the implementation of robust statistical and modelling techniques. We report the the sub meter accuracy in RV on nightly average bin data for Tau Ceti (Figure 10). These observations were taken by PARAS in Nov. 2015. This was to prove that there is no short period planet around Tau Ceti which was speculated in 2012-2013 by Tuomi, M et. al.

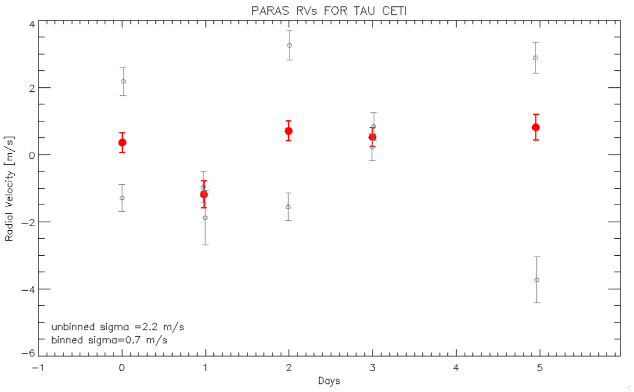

Figure 10: Tau Ceti radial velocities observed by PARAS showing nightly average scatter of 70 cm/sec.

These observations of Tau Ceti are in tune with the capabilities of PARAS that was recently improved upon by adding combination of octagonal shape of optical fibres with circular fibres. Table 1 lists the key parameters for principal Doppler surveys around the world, which includes PRL Advance Radial velocity Abu sky Search (PARAS). This work was done incollaboration with Fischer et al. and other experts across the world in this field.The programs are sorted by the demonstrated single measurement precision (SMP). Exoplanets are an important subfield of astronomy but higher precision RV measurements are required to serve as a discovery technique for potentially habitable worlds, to confirm and characterise detections from transit missions, and to provide mass measurements for future space-based missions. PARAS on the PRL 2.5m Telescope, which is expected to see first light in late 2019, will play pivotal role in determining massive Earth's masses of candidates that will come up from TESS (NASA) and PLATO (ESA) missions.

Current Doppler Planet Search Programs

Spectrograph	slit or fiber	Temp Control	Spectral Resolution	Wavelength range [nm]	Wavelength calibrator	SMP [m s^{-1}] SNR = 200	Number of stars	Duration of program
HARPS	f	Y	115,000	380 – 690	ThAr	0.8	2000	2003 –
HARPS-N	f	Y	115,000	380 – 690	ThAr	0.8	500	2012 –
PARAS	f	Y	67,000	380 – 690	ThAr	1.0	27	2012 –
CHIRON	f	Y	90,000	440 – 650	Iodine	1.0	35	2011 –
SOPHIE	f	Y	75,000	387 – 694	ThAr	1.1	190	2011 –
PFS	s	Y	76,000	390 – 670	Iodine	1.2	530	2010 –
HIRES	s	Y	55,000	364 – 800	Iodine	1.5	4000	1996 –
Levy (LCPS)	s	Y	110,000	376 – 970	Iodine	1.5	100	2013 –
Levy (CPS)	s	Y	100,000	376 – 940	Iodine	2.0	300	2013 –
SONG	s	N	90,000	440 – 690	Iodine	2.0	12	2014 –
HRS	s	Y	60,000	408 – 784	Iodine	3.0	100	2001 – 2013
Hamilton	s	N	50,000	390 – 800	Iodine	3.0	350	1987 - 2011
UCLES	s	N	45,000	478 – 871	Iodine	3.0	240	1998 –
Tull	s	N	60,000	345 – 980	Iodine	5.0	200	1998 –

(A. Chakraborty, A. S. Rajpurohit, P. Chaturvedi, J. S. S. Neelam, V. Prasad, V. Shah, B. G. Anandarao)

EPIC211089792 b: an aligned and inflated hot jupiter in a young visual binary

We report the discovery of a new hot Jupiter co-discovered in the K2 and archival Super-WASP data. The host star is the primary of a visual binary system. The star EPIC211089792 was observed during K2 campaign 4 which also targeted both the Pleiades and the Hyades cluster. It is unlikely that this system belongs to Pleiades. Interestingly, we note that the system has Lithium (for this stellar temperature) and Iron abundances that are compatible with the Hyades. Moreover, the systemic radial velocity of the star also agree with the Hyades. The EPIC211089792 b planet having a period of 3.25d, a mass of 0.73 ± 0.04 Mjup, and a radius of 1.19 ± 0.02 Rjup. In Fig. 11, we plot the phase-folded radial velocity data together with the best-fit model and the residuals. The host star of this system is a relatively bright (V=12.5) G7 dwarf with a nearby K5V companion. Based on stellar rotation and the abundance of Lithium, we find that the system might be as young as about 450 Myr. The observation of the Rossiter-McLaughlin effect shows the planet is aligned with respect to the stellar spin. Given the deep transit (20mmag), the magnitude of the star and the presence of a nearby stellar companion, the planet is a good target for both space- and ground-based transmission spectroscopy, in particular in the near-infrared where the both stars are relatively bright.

This work has been done in collaboration with Dr. Santerne, A. of the Instituto de Astrofsica e Ciencias do Espaco, Universidad do Porto, Portugal along with other collaborators.

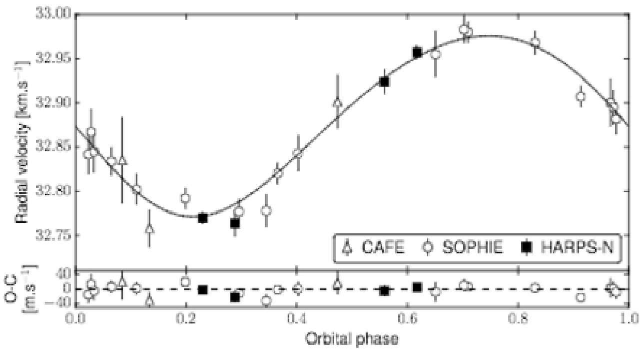

Figure 11: Phase-folded radial velocities of the exoplanet EPIC211089792 b. The black line is the best model found and the bottom panel is the corresponding residuals.

(A. S. Rajpurohit)

Spectral energy distribution of M-subdwarfs: A study of their atmospheric properties

M-type subdwarfs are metal-poor low-mass stars and probe for the old populations in our Galaxy. Accurate knowledge of their atmospheric parameters and composition is essential for understanding the chemical history of our Galaxy. The purpose of this work is to perform a detailed study of M-subdwarf spectra covering the full wavelength range from the optical to the near-infrared. It allows to do a more detailed analysis of the atmospheric composition in order to determine the stellar parameters, and to constrain the atmospheric models. The study will allow us to further understand physical and chemical processes such as increasing condensation of gas into dust, to point out the missing continuum opacities and see how the main band features are reproduced by the models. The spectral resolution and the large wavelength coverage used is a unique combination to constrain the process that occur in cool atmosphere. We obtained medium-resolution (R = 5000-7000) spectra over the wavelength range 0.3-2.5 μm of ten M-type subdwarfs with X-SHOOTER at VLT. These data constitute an unique atlas of M-subdwarfs from optical to near-infrared. We performed spectral synthesis analysis using a full grid of synthetic spectra computed from BT-Settl models and obtained consistent stellar parameters such as effective temperature, surface gravity and metallicity. We show that self-consistent atmospheric models correctly represent the overall shape of their spectral energy distribution, as well as atomic and molecular line profiles both in the optical and near-infrared.

This work has been done in collaboration with Dr. France Allard, of ENS Lyon, France along with other collaborators.

(A. S. Rajpurohit)

Detection of a very low mass star in an Eclipsing Binary system

We report the detection of a very low mass star (VLMS) companion to the primary star 1SWASPJ234318.41+295556.5A (J2343+29A), using radial velocity (RV) measurements from the PARAS (PRL Advanced Radial-velocity Abu-sky Search) high resolution echelle spectrograph. The periodicity of the single-lined eclipsing binary (SB1) system, as determined from 20 sets of RV observations from PARAS and 6 supporting sets of observations from SOPHIE data, is found to be 16.953 d – much higher than the 4.24 d period reported from SuperWasp photometry. It is likely that inadequate phase coverage of the transit with SuperWasp photometry led to the incorrect determination of the period for this system. We derive the spectral properties of the primary star from the observed stellar spectra: Teff = 5125 ± 50 K, [Fe/H] = 0.1 ± 0.05 and log g = 4.6 ± 0.1, indicating a K1V primary. Applying the Torres relation to the derived stellar parameters, we estimate a primary mass 0.875 ± 0.042 $\mathrm{M}_{\odot}$ and a radius of 0.848 ± 0.032 $\mathrm{R}_{\odot}$ (formal errors only).

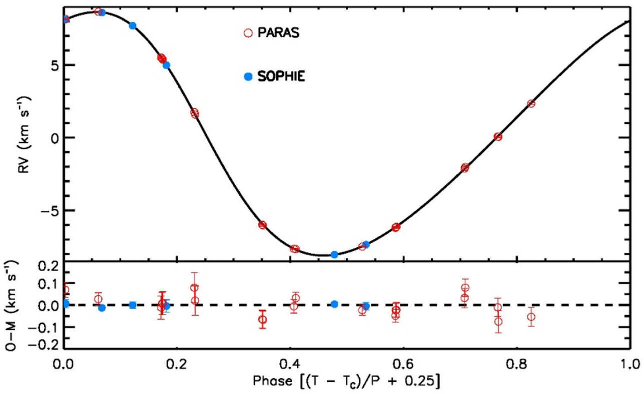

Figure 12: Top panel: PARAS, Mount Abu (open red circles) and SOPHIE (filled blue circles) observed data points along with the estimated errors are plotted. RV model curve for star 1SWASP J2334318+295556 obtained from EXOFAST is overplotted against orbital phase on the observed data points in black solid line. Bottom panel: the residuals from the best fit are plotted below the RV plot.

We combine RV data with SuperWASP photometry to estimate the mass of the secondary, $\mathrm{M_B}$ = 0.098±0.003$\mathrm{M}_{\odot}$, and its radius, $\mathrm{R_B}$ = 0.128±0.005 $\mathrm{R}_{\odot}$, with an accuracy of $\sim$ 4 %. Although the observed radius is found to be consistent with the Baraffe's theoretical models, the uncertainties on the mass and radius of the secondary reported here are model dependent and should be used with discretion. Figure 12 illustrates a plot of RV versus orbital phase for J2343+29A. Red open circles (top panel) show RV measurements of the primary taken with PARAS, and filled blue circles denote the same for SOPHIE. The solid black curve indicates the best-fitting model from fitting routine EXOFAST based on the best derived parameters. The bottom panel in Figure 12 shows the model fit and the residuals (Observed & 8722;Model). The best-fitting model spectra determined for J2343+29 are shown in Figure 13. The black solid line indicates the observed normalized spectra from PARAS, and the overlaid red dashed line is the best-fitting model determined from this work.

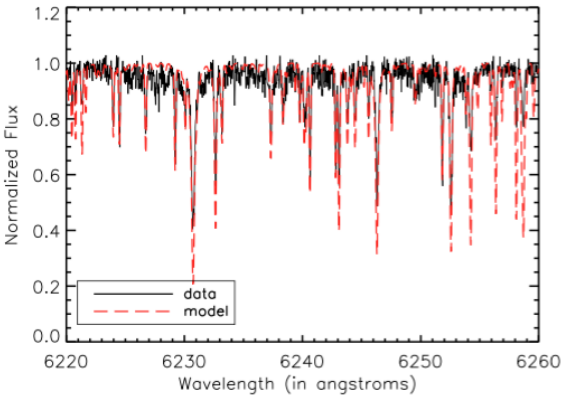

Figure 13: Observed normalized spectra for J2343+29 (solid black line) plotted across the wavelength region of 6220-6260 angstrom. Over plotted is the modelled spectra (red dash line) obtained from PARAS SPEC analysis, with temperature value of T_{eff} of 5125 K, [Fe/H] of +0.1 and log g of 4.6.

(P. Chaturvedi, A. Chakraborty, B. G. Anandarao)

Indian multi-wavelength astronomy mission *AstroSat*

AstroSat, Indias first dedicated astronomical satellite was launched on 28th September, 2015. Since then it has been successfully operating in space and is carrying out observations of the variety of astrophysical sources in the ultra-violet to hard X-ray wavebands. After initial spacecraft health checkout, all five payloads namely, Cadmium-Zinc-Telluride Imager (CZTI), Scanning Sky Monitor (SSM), Large Area Xenon Proportional Counter (LAXPC), Soft X-ray Telescope (SXT) and Ultra-Violet Imaging Telescope (UVIT), were successfully made operational over next two months. The period of first six months after the launch was designated as performance verification phase for all payloads, which was completed in March 2016. From April 2016, *AstroSat* is carrying out astrophysical observations under the guaranteed time operations for all instrument teams, which will continue till September 2016. From October 2016 onwards, *AstroSat* will be operated as observatory open to all Indian astronomers.

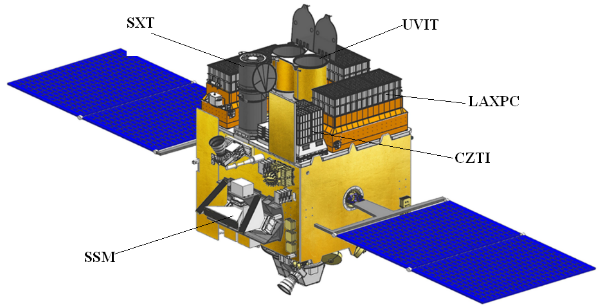

Figure 14: *AstroSat* - Indias first multi-wavelength astronomy satellite - launched on 28th September 2015. It has total five instruments out of which four instruments (UVIT, SXT, LAXPC and CZTI) carry out pointed observations of celestial source in wavelengths ranging from visible light to hard X-rays; and one instrument (SSM) monitor the whole sky every orbit for new transient sources.

(N. P. S. Mithun, T. Chattopadhyay, S. V. Vadawale)

In-flight operations and initial results with *AstroSat*-CZTI

CZTI was the first scientific instrument to be switched on within about week after the launch of *AstroSat*. It was made fully operational on 6th October 2015 with the first scientific observation of the supernova remnant, Crab nebula.

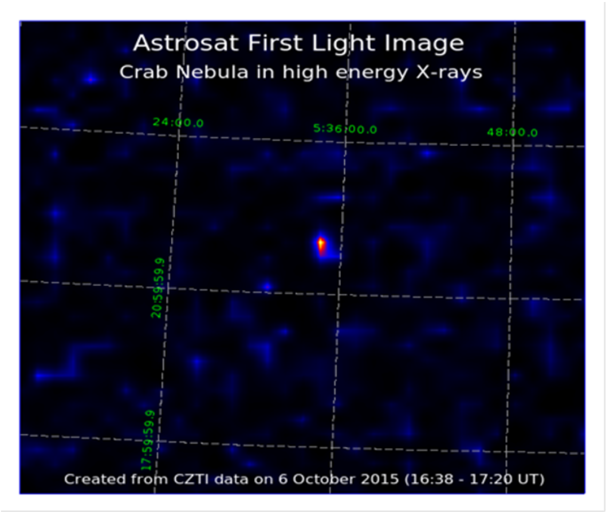

Figure 15: First light image of the Crab nebula with *AstroSat*-CZTI. Some artifacts due to the noise are visible in the image.

Figure 15 shows the first light image of the Crab nebula in hard X-rays (energy range 30 - 100 keV). We were closely involved in the operationalization of the CZTI instrument with our team being present at the ISTRAC (ISRO Telemetry, Tracking and Command centre) during all early observations. The performance verification phase observations of CZTI were completely planned by us and the analysis of all these observations was carried out our team. Though the data analysis software as well as calibration database was prepared based on extensive ground calibration, the onboard observations did pose many challenges and surprises. The ground software, calibration database, data analysis algorithm were extensively modified to accommodate all new challenges. As an example of improvement in the noise performance of the instrument, a later image of the Crab nebula can be seen in Figure 16, where all other artefacts in the image are significantly reduced.

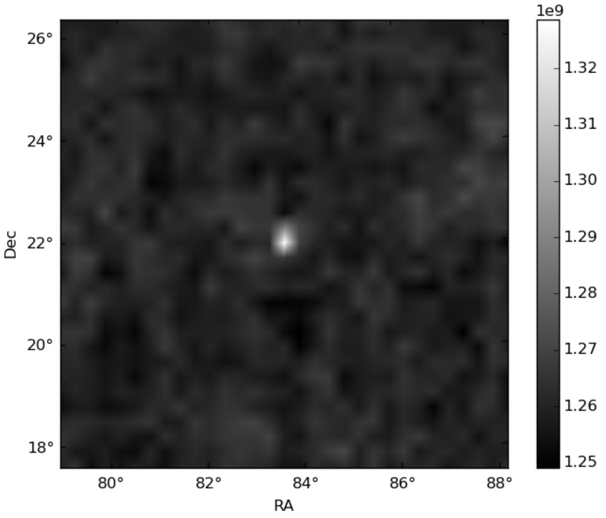

Figure 16: Image of the Crab nebula from the later observations. It can be seen that with the improved pipeline software, data cleaning algorithms and calibration database, the image artefacts are negligible.

Crab nebula is a standard candle source in X-ray astronomy and all new instruments are calibrated against this source. Figure 17 show the hard X-ray spectrum of the Crab nebula as measured by CZTI and modelled using the canonical power-law model. The fitted spectral index, 2.09, is very close to the expected value of 2.1. Absolute flux calibration requires more extensive observations and is under progress. The Crab pulsar is also used a timing calibrator with its pulse period of 33 milli-seconds. The pulse profile of the Crab pulsar observed by CZTI is shown in Figure 18. The peak positions agree with the radio pulse profile within 200 micro-seconds establishing the absolute timing accuracy of CZTI.

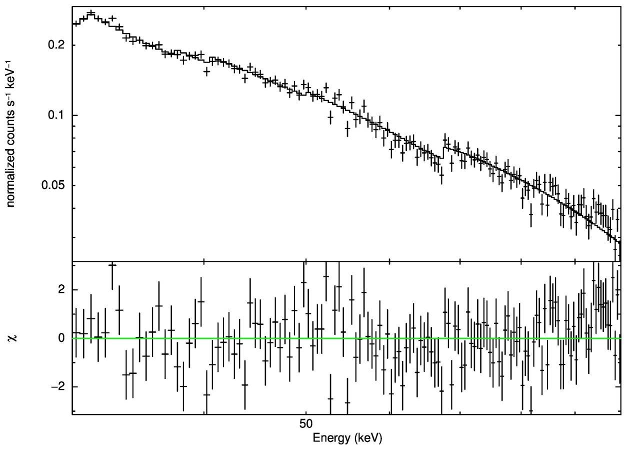

Figure 17: Hard X-ray spectrum of the Crab nebula in 30 - 100 energy range as measured by CZTI.

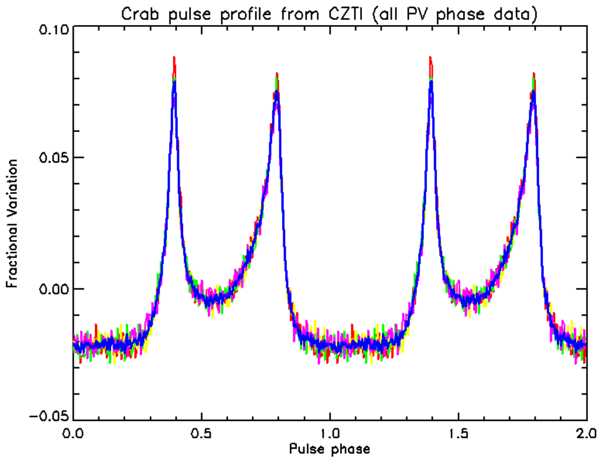

Figure 18: Pulse profile of the Crab pulsar determined from the CZTI observations.

(N. P. S. Mithun, T. Chattopadhyay, S. V. Vadawale)

Hard X-ray Monitoring with CZTI

Primary scientific objective of *AstroSat*-CZTI is hard X-ray imaging and spectroscopy in the energy range of 20 - 100 keV. However, the CZT detectors with thickness of 5 mm have significant efficiency beyond 100 keV, where the CZTI coded mask and other support structure starts becoming transparent. CZTI also has a 1 cm thick veto detector which together with the CZT detector plane results in the largest effective area among all other open detector operational at present. Thus CZTI can also act as wide field monitor in the energy range of 100 - 300 keV and detect the bright hard X-ray transient sources such as gamma-ray bursts (GRB). So far CZTI has detected GRBs almost at the rate of one GRB per month as expected.

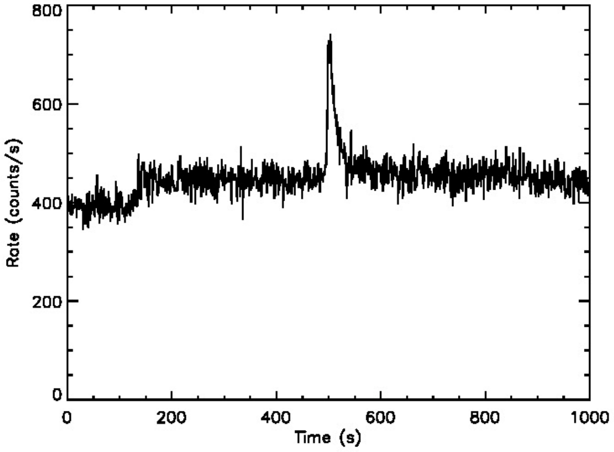

Figure 19: Representative GRBs detected by *AstroSat* CZTI - GRB151006A.

Representative GRBs detected by CZTI are shown in Figure 19. CZTI also has rudimentary localization capability for GRBs. One very significant utility of hard X-ray monitoring capability over a large portion of the sky is in the detection of electro-magnetic counter parts of the exotic events such as the first gravitational wave detection due to two black hole merger. To utilize this capability, the CZTI team has an MOU with the LIGO collaboration to quickly obtain triggers for possible gravitational wave detection events.

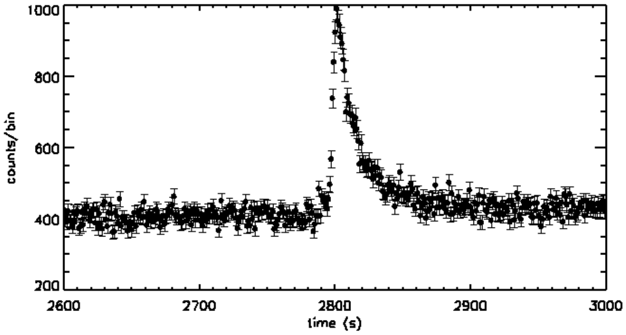

Figure 20: Representative GRBs detected by *AstroSat* CZTI - GRB160131A.

(N. P. S. Mithun, T. Chattopadhyay, S. V. Vadawale)

Hard X-ray polarimetry with *AstroSat*-CZTI

CZTI consists of a large pixilated detector plane with total active area of 976 cm^2 and individual pixel size of 2.46 mm × 2.46 mm. Due to this pixelated nature of the detector plane and significant detection efficiency at energy beyond 100 keV where the Compton scattering dominates, CZTI offers a unique capability for polarization measurement of incident X-rays. Earlier we had investigated polarimetric sensitivity of CZTI using detailed Monte-Carlo simulation and had shown that it will have significant sensitivity to measure polarization in the energy range of 100 - 300 keV few bright X-ray sources.

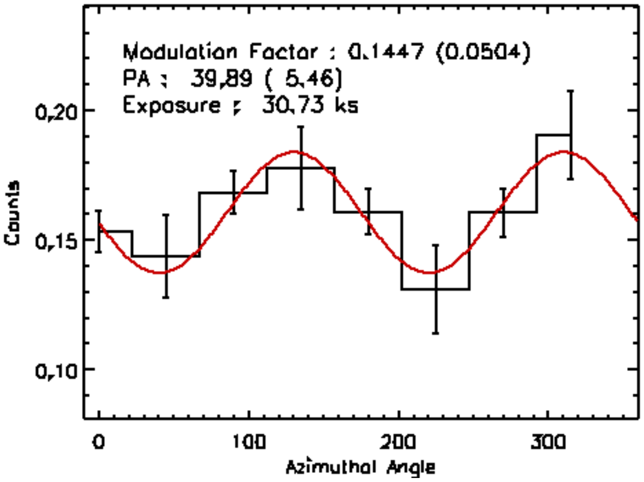

Figure 21: Modulation curve for a representative 30 ks observation of the Crab nebula in October, 2015.

The supernova remnant, Crab Nebula and high mass black hole X-ray binary, Cygnus X-1 are the two persistent X-ray sources, which provide sufficient photon flux in hard X-rays to attempt polarization measurement with CZTI. Crab, being a standard calibration source for hard X-ray instruments, has been observed for more then a dozen times by CZTI during the six months of performance verification phase of *AstroSat* operation. We have carefully analyzed these observations as per the polarimetry algorithms identified earlier with ground experiments. One new but critical element in the polarimetric analysis of the flight data was to carry out appropriate background subtraction. After number of iterative steps, a set of specific criteria were derived to identify proper background and based on this further analysis of all Crab observation was carried out. With this we could significantly detect the hard X-ray polarization in Crab nebula in almost all observations with exposure greater then 20 ks. Figure 21 show the modulation curve (which provides measure of polarization degree) for a representative Crab observation having exposure of 30 ks. The red solid line is the cos2ϕ fit to the azimuthal angle distribution. The fitted modulation amplitude and polarization angle in the CZTI plane are 14% and ∼390 respectively. The absolute degree of polarization is obtained by normalizing the obtained modulation amplitude with respect to the modulation amplitude for 100% polarized radiation estimated from simulation the same fitted polarization angle. We have analysed all Crab observations in the similar manner and Figure 22 shows the obtained polarization degree as a function of different observation ids. Two different colours represent two different blank sky observations for estimation of background azimuthal angle distributions. Overplotted dashed lines and the dashed regions refer to the average over the polarization fractions and the standard deviation respectively. We find the measured polarization to be ∼25% in 100-300 keV. This is agreement with very few polarimetric observations of Crab available in the history of X-ray astronomy. This not only proves the hard X-ray polarimetric capability of CZTI but also provide the most sensitive measurement of Crab X-ray polarization in this energy range. With this new capability, CZTI is likely to provide many interesting results in future.

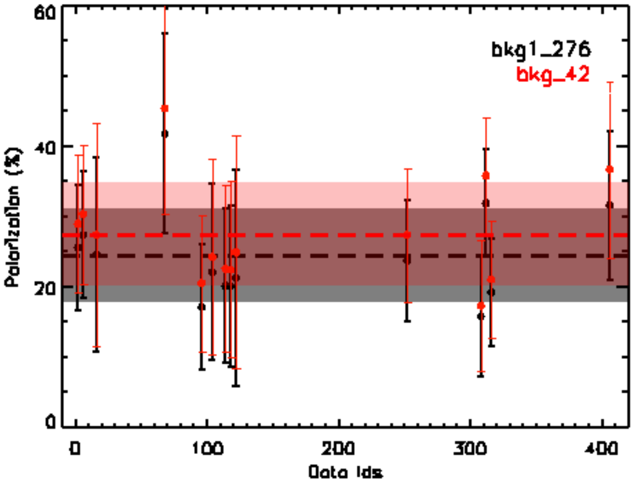

Figure 22: Measured polarization degree for all observations of Crab by CZTI. Refer to text for more details.

(N. P. S. Mithun, T. Chattopadhyay, S. V. Vadawale)

Detection of fundamental and first harmonic cyclotron line in binary X-ray pulsar Cep X-4

Cyclotron resonance scattering features (CRSF) are generally seen in the hard X-ray spectrum of the accretion powered X-ray pulsars with surface magnetic field of ∼10^{12} G. These are absorption like features which appear due to the resonant scattering of photons with electrons in quantized Landau levels. The energy difference between these levels depends on the strength of magnetic field and expressed through the relation $E_{cyc} = 11.6\ B_{12} \times (1 + z)^{-1}$ keV (without relativistic correction), where B_{12} is the magnetic field in the unit of 10^{12} G and z is the gravitational redshift. Detection of fundamental CRSF in the spectra of accretion powered X-ray pulsars provides the direct estimation of local magnetic field of the neutron stars in line-forming region. At the same time, the study of the harmonics (multiples of fundamental cyclotron line) gives crucial information about the optical depth of the line-forming region. As of now, CRSF has been seen in about 20 accretion powered X-ray pulsars. However, the harmonics of the fundamental cyclotron line are detected only in a few cases. We investigated the broad-band spectral properties of the X-ray pulsar Cep X-4 by using a Suzaku observation in 2014 July. The 0.8-70 keV spectrum was found to be well described by three continuum models - Negative and Positive power-law with Exponential cut-off (NPEX), high-energy cut-off power-law and CompTT models. Additional components such as a cyclotron line at ∼28 keV and two Gaussian components for iron lines at 6.4 and 6.9 keV were required in the spectral fitting. Apart from these components, an additional absorption feature at ∼45 keV was clearly detected in residuals obtained from the spectral fitting (Figure 23).

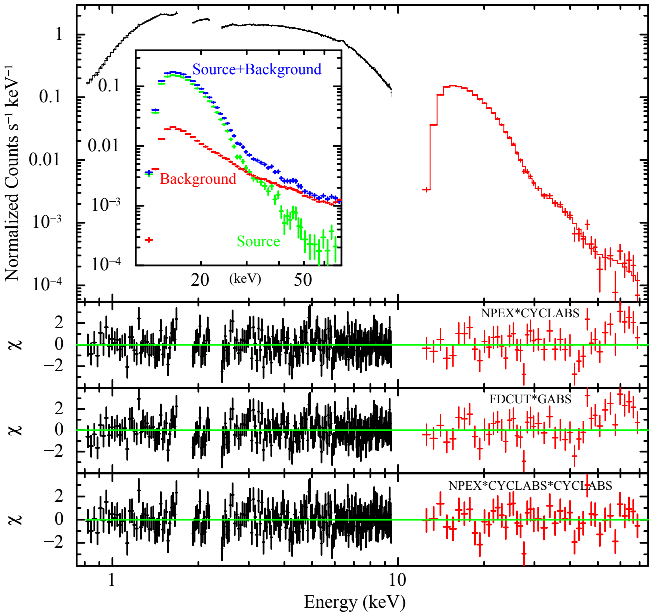

Figure 23: Energy spectrum of Cep X-4 in 0.8-70 keV range obtained from XIS-3 and HXD/PIN data, along with the best-fit model comprising a partial covering NPEX model, two Gaussian functions for iron emission lines and two cyclotron absorption components. The second and fourth panels show the contributions of the residuals to χ^2 for each energy bin for the partial covering NPEX continuum model with one and two cyclotron absorption components, respectively. The third panel shows the residuals for Fermi-Dirac cutoff power-law model with one GABS component. The inset shows the HXD/PIN spectrum of the pulsar with background, without background and the simulated HXD/PIN background spectrum.

This additional feature at ∼45 keV was clearly seen in phase-resolved spectra of the pulsar. We identified this feature as the first harmonic of the fundamental cyclotron line at ∼28 keV. The ratio between the first harmonic and fundamental line energies (1.7) was found to be in disagreement with the conventional factor of 2, indicating that the heights of line-forming regions are different or viewed at larger angles. The phase-resolved spectroscopy of the fundamental and first harmonic cyclotron lines shows significant pulse-phase variation of the line parameters. This is interpreted as the effect of viewing angle or the role of complicated magnetic field of the pulsar. This is the first time that an an-harmonic spacing between fundamental and harmonic lines has been detected in the transient binary X-ray pulsar Cep X-4.

(S. Naik, G. K. Jaisawal)

Suzaku view of the Be/X-ray binary pulsar GX 304-1 during Type I X-ray outbursts

Be/X-ray binaries represent about two-third of High-Mass X-ray Binary (HMXB) systems. The compact object in these systems is generally a neutron star (pulsar) whereas the companion is a B-type star that shows emission lines in its optical/infrared spectrum. The objects in these binary systems are typically in a wide eccentric orbit. The neutron star in these Be/X-ray binary systems accretes matter while passing through the circumstellar disk of the companion Be star. The abrupt accretion of huge amount of matter onto the neutron star while passing through the circumstellar disk of the Be companion or during the periastron passage results in strong X-ray outbursts. During such outbursts, the X-ray emission from the pulsar can be transiently enhanced by a factor of more than 10. Be/X-ray binary systems generally show periodic normal (type I) X-ray outbursts that coincide with the periastron passage of the neutron star and giant (type II) X-ray outbursts that do not show any clear orbital dependence apart from the persistent low-luminosity X-ray emission during quiescent. The neutron stars in the Be/X-ray binary systems are found to be accretion powered X-ray pulsars, except for a very few cases. We investigated the timing and spectral properties of the Be/X-ray binary pulsar GX 304-1 using two Suzaku observations during its 2010 August and 2012 January X-ray outbursts. Pulsations at ∼275 s were clearly detected in the light curves obtained from both observations. Pulse profiles were found to be strongly energy-dependent. During the 2010 observation, the prominent dips seen in soft X-ray ($\leq$10 keV) pulse profiles were found to be absent at higher energies. However, during the 2012 observation, the pulse profiles were complex as a result of the presence of several dips. Significant changes in the shape of the pulse profiles were detected at high energies (¿35 keV). A phase shift of ∼0.3 was detected while comparing the phase of the main dip in the pulse profiles below and above ∼35 keV. The broad-band energy spectrum of the pulsar was well described by a partially absorbed negative and positive power law with exponential cut-off (NPEX) model with 6.4 keV iron line and a cyclotron absorption feature. The energy of the cyclotron absorption line was found to be ∼53 and 50 keV for the 2010 and 2012 observations, respectively, indicating a marginal positive dependence on source luminosity. Based on the results obtained from phase-resolved spectroscopy, the absorption dips in the pulse profiles were interpreted as due to the presence of additional matter at same phases. Observed positive correlation between the cyclotron line energy and luminosity, and the significant pulse-phase variation of cyclotron parameters are discussed from the perspective of theoretical models on the cyclotron absorption line in X-ray pulsars.

(S. Naik, G. K. Jaisawal, P. Epili)

Broad-band Spectroscopy of the transient X-ray binary pulsar KS 1947+300 during 2013 giant outburst: Detection of pulsating soft X-ray excess component

The transient Be/X-ray binary pulsar KS 1947+300 was discovered on 1989 June 8 with the Kvant/TTM coded-mask X-ray spectrometer on the Mir space station. The pulsar was first detected at a flux level of 70 mCrab that later decreased to ∼10 mCrab within 2 months of detection. The spectra obtained from these observations were described by an absorbed power-law with a photon index of 1.72. Pulsation from the BATSE/CGRO observations in April 1994 was first estimated to be 18.7 s. A Be star with a visible magnitude of 14.2 at a distance of ∼10 kpc was discovered as the optical counterpart of the pulsar. We present the results obtained from detailed timing and spectral studies of the Be/X-ray binary pulsar KS 1947+300 during its 2013 giant outburst. We used data from Suzaku observations of the pulsar at two epochs, i.e. on 2013 October 22 (close to the peak of the outburst) and 2013 November 22. X-ray pulsations at ∼18.81 s were clearly detected in the light curves obtained from both observations. Pulse periods estimated during the outburst showed that the pulsar was spinning up. The pulse profile was found to be single-peaked up to ∼10 keV beyond which a sharp peak followed by a dip-like feature appeared at hard X-rays. The dip-like feature has been observed up to ∼70 keV. The 1-110 keV broad-band spectroscopy of both observations revealed that the best-fit model was comprised of a partially absorbed Negative and Positive power law with EXponential cutoff (NPEX) continuum model along with a blackbody component for the soft X-ray excess and two Gaussian functions at 6.4 and 6.7 keV for emission lines. Both the lines were identified as emission from neutral and He-like iron atoms. To fit the spectra, we included a cyclotron absorption line at 12.2 keV. From the spin-up rate, the magnetic field of the pulsar was estimated to be 1.2×10^{12} G and found to be comparable to that obtained from the detection of the cyclotron absorption feature. Pulse-phase resolved spectroscopy revealed the pulsating nature of the soft X-ray excess component in phase with the continuum flux. This confirms that the accretion column and/or accretion stream are the most probable regions of the soft X-ray excess emission in KS1947+300. The presence of the pulsating soft X-ray excess in phase with continuum emission may be the possible reason for not observing the dip at soft X-rays.

(S. Naik, P. Epili, G. K. Jaisawal)

Star formation activity in the neighbourhood of W-R 1503-160L star in the mid-infrared bubble N46.

The energetics of massive stars can strongly influence the surroundings. However, the feedback processes of massive stars are still poorly understood. The Wolf-Rayet (W-R) stars represent a late phase in the evolution of O star. We carried out a multi-wavelength analysis of a mid-infrared (MIR) bubble N46 (l = $27^o.31$; $b = -0^o.11$), which hosts a spectroscopically characterized source WN7 W-R star and is referred to as a broken or incomplete ring (see Figure 24a). The main purpose of this work is to explore the physical processes governing the interaction and feedback effect of a W-R star on its surroundings. The distribution of ionized emission observed in the MAGPIS 20 cm continuum map is mostly seen toward the edges of the bubble (see the inset on the bottom right in Figure 24a).

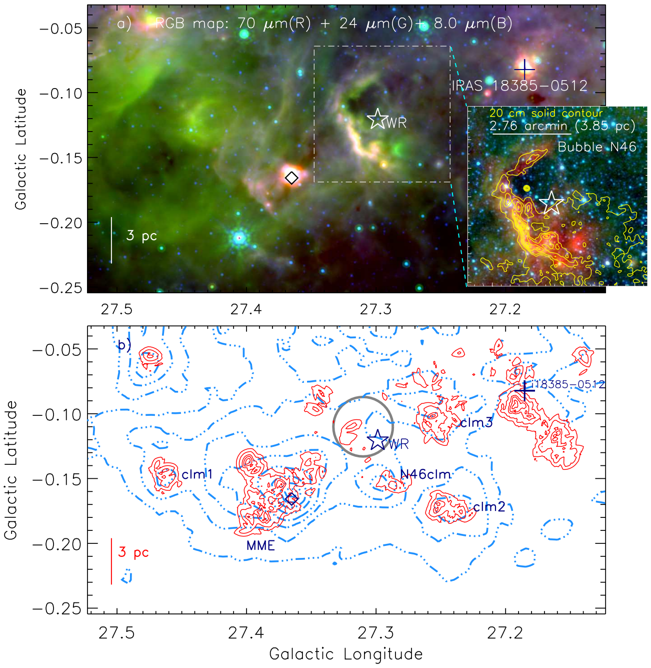

Figure 24: a) RGB color image (in log scale) of the region around the bubble N46. The inset on the bottom right represents the bubble N46 in zoomed-in view, using a three-color-composite image (24 μm (red), 8 μm (green), and 3.6 μm (blue); in log scale) (see the dotted-dashed box in figure). The MAGPIS 20 cm mission is also overlaid by yellow solid contours with levels of 0.0023, 0.0035, 0.0046, 0.0064, 0.0081, 0.0099, and 0.011 Jy/beam. b) Molecular ^{13}CO gas in the direction of the bubble N46. The CO integrated velocity range is from 87 km s^{-1} to 100 km s^{-1}. The CO contours are 45.27 K km s^{-1} × (0.1, 0.2, 0.3, 0.4, 0.55, .7, 0.85, 0.95). A big circle indicates the location of the bubble N46. In both panels, the positions of IRAS 18385−0512 (+), 6.7 - GHz methanol maser emission (◊), and W-R 1503-160L star (⋆) are marked. The scale bar corresponding to 3 pc at a kinematical distance of 4.8 kpc is shown in both panels.

The molecular cloud associated with the bubble N46 (i.e. N46 molecular cloud) is well traced in a velocity range of 87–100 km s^{-1} (see Figure 24b). The ^{13}CO line data are used to trace an expanding shell (with a velocity of 3 km s^{-1}) surrounding the W-R star containing about five condensations (clm1, clm2, clm3, N46clm, and MME) within the N46 molecular cloud (see Figure 24b). Interestingly, the early phase of massive star formation ($<$ 0.1 Myr) is occurring in the MME condensation, as traced by the presence of the 6.7 GHz MME. The photometric analysis of point-sources reveals a total of 370 young stellar objects (YSOs). In the clustering analysis, we found that the clusters of YSOs are spatially seen toward the molecular condensations (see Figure 24b), which are associated with a range of temperature and density of about 18–24 K and 0.6–9.2 × 10^{22} cm^{-2} ($A_V \sim$7–98 mag). Some YSOs are also seen on the edges of the bubble without any clustering (not shown here). Several compact radio sources (crss) are identified on the edges of the bubble and are consistent with radio spectral types B0V–B0.5V (see the inset on the bottom right in Figure 24a). Infrared images revealed the individual infrared-counterparts (IRcs) of three crss that have masses (13–20 $M_\odot$) and ages (1–2 Myr). It is evident that star formation continues into the N46 molecular cloud (see Figure 24b). The pressure calculations (P_{rad} and P_{wind}) indicate that the stellar wind associated with WN7 W-R star (with a mechanical luminosity of $\sim$4 × 10^{37} ergs s^{-1}) can be considered as the major contributor for the feedback mechanism. In the N46 cloud, there exists an apparent age gradient between the W-R star and young sources (YSOs, IRcs of crss, and 6.7 GHz MME).

Taking into account all the observational results obtained with our multi-wavelength analysis, we conclude that there is a possibility of triggered star formation toward the edges of the bubble. Furthermore, the star formation activities in the N46clm, clm2, clm3, and MME condensations appear to be influenced by the energetics of WN7 W-R star.

This work was done in collaboration with T. Baug (TIFR, Mumbai), D.K. Ojha (TIFR, Mumbai), J.P. Ninan (TIFR, Mumbai), A. Luna (INAOE, Mexico), and I. Zinchenko (IAPRAS, Russia).

(L. K. Dewangan, P. Janardhan)

Design and Development of MFOSC-P: An Optical Imager-Spectrograph for Mt. Abu 1.2m Telescope.

A Faint Object Imager-Spectrograph, Named - Mt. Abu Faint Object Spectrograph and Camera-Pathfinder (MFOSC-P) is being developed for the existing PRL 1.2m telescope at Mt. Abu Infra-Red Observatory. The instrument would provide imaging and spectroscopic capabilities in optical wavelength regime. Faint Object Camera and Spectrograph (FOSC) series of instruments have been proven to be workhorse of several optical telescopes around the world e.g. EFOSC for ESO 3.6m telescope, FOCAS for 8.2m Subaru telescope, FORS for 8m ESO VLT, IFOSC on IUCAA 2m telescope, HFOSC on Himalayan Chandra Telescope Hanle etc. Due to their relatively simpler design and ability to quickly switch into imaging, spectroscopy and polarimetry modes, they are preferred to have as a general purpose instrument on any small or moderate aperture telescope. As PRL is gearing up to have a 2.5m optical telescope, to exploit its full potential in visible regime a FOSC type versatile general user first generation instrument is extremely desirable. However towards the development of FOSC, we proposed to develop a scale down version of FOSC for existing PRL 1.2m telescope at Mount Abu as a pathfinder instrument: MFOSC-P. MFOSC-P is envisioned to work in the same operational modes as a FOSC, but with shorter development period and with relatively smaller financial budget. Though MFOSC-P would be having fewer imaging and spectroscopic modes (with lesser number of filters and grisms), it could very well be adaptable to the specific need of the users. The option to couple FOSC-P with the existing IR instruments (NICS and NICMOS) on PRL 1.2m telescope would also be explored for simultaneous optical/IR observations. The optical design for MFOSC-P has been done in house and is discussed below.

MFOSC-P is envisioned as a general purpose user's instrument providing both the imaging as well spectroscopy options within the same optical chain. The baseline optical design of MFOSC-P has been deduced from a common imaging and spectroscopic requirements required for variety of science programs of the division. Considering the seeing condition at Mt. Abu, spatial sampling of 3 pixels per arc-second is considered for the imaging mode, while in spectroscopy mode the resolution of $\sim$ 2000 and $\sim$1000 at optical wavelengths corresponding to 1 arc-sec slit width are being considered. Table-1 gives the optical design parameters of MFOSC-P.

MFOSC-P has been designed as a focal reducer instrument, based on collimator-camera design concept. In such a design focal plane of the telescope is re-imaged with suitable magnification/demagnification to achieve proper sampling of seeing limited image on the detector plane. Considering the median seeing of 1 arc-sec and telescope

MFOSC-P Preliminary Optical Design Parameters

Parameters	Values
Wavelength Range	4500-8500 Å
Imaging Field of View	5 × 5 arc-minute square
Imaging Pixel Scale	$\sim$3 pixels per arc-sec
Imaging Mode Quality Requirement	$\sim$80% Encircled Energy Diameter would be within 1 pixel (0.33 arc-seconds)
Magnification of the FOSC-P optical Chain	~ 0.55, corresponding to 1.2m telescope plate scale of 76 μm per arc-sec
Camera F/Number	$\sim$6.5
CCD Detector	$\sim$1K X 1K CCD with 13.5 μm pixel size
Broad Band Filters	Bessell's UBVRI
Spectral Coverage	4500-7000 Å using two different Gratings/Grisms
Spectral Resolutions	$\sim$2000 and 1000 around 6500 Å and 5500 Å respectively for 1 arc-sec slit width
Pupil Diameter	$\sim$35mm
Grating's Specifications	Two Plane reflection gratings with 500 and 350 line pair per mm blazed at $\sim$6500 and $\sim$5500 Å respectively
Grism's Specifications	To Be decided
Optical Track Length	$\sim$1300 mm
Operating Temperatures	-2 to 35 degree Celsius

plate scale (76 microns per arc-sec), a sampling scheme of 3 pixels per resolution element would require magnification of $\sim$0.55 in the imaging mode. Similarly for a slit limited spectroscopy (1 arc-sec slit width), to achieve the resolution of $\sim$2000 and 1000 around $\sim$6500 and $\sim$5500 Angstroms, corresponding specification of the gratings as well as grisms have been derived and optimized. Various parameters of the preliminary optical design are given in Table-1. Optical design of MFOSC-P is shown in Figure 25, for one of the spectroscopy modes using reflection grating.

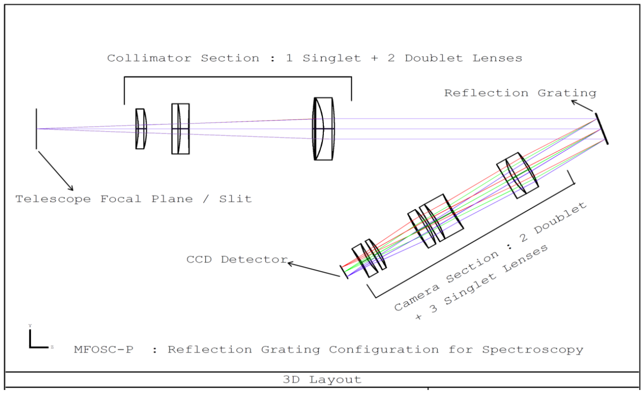

Figure 25: Optical Design of MFOSC-P.

(M. K. Srivastava, V. Dixit, M. Jangra)

Design and Development of a general purpose Electronic Instrument Control System (ECS)

Considering the current and future instrumentation requirements of PRL existing 1.2m and upcoming 2.5m telesopes at Mt. Abu an micro-controller based electronic control system is being developed. In general, most of the telescope backend instruments contain an optical chain with both movable and fixed optical components. While these instruments are mounted on the telescope, they are to be operated from a control PC in the telescope control room. Such instruments could also have several motion components (e.g. filter wheel, Grism wheel/motion stage, slit wheel/motion stage, fold mirrors for calibration/guiding etc.) equipped with feedback components (e.g. rotatory optical encoders) and limit switches. Further there are multiple requirements for several switching operations e.g. calibration lamps, shutter control etc. Several analog and digital feedbacks would also be present for the operation/calibration of the system. Thus as a common solution to all these, a micro-controller based electronic instrument control system (ECS) is envisioned to route all these operations for any such instrument. ECS is a micro-controller based system built on the master-slave architecture. ECS would be consisting of 4 or 5 identical controller cards. The individual cards would work in slave mode while the control PC would act in master mode. The communication between PC to the controller card is based on RS-485 based serial link. At the core of each card is an Arduino mega 2560 controller board consisting of AVR Atmel 2560 microcontroller. Each ECS card is having control and driver circuits for three stepper motors capable of driving upto 16 microstepping mode of the motors. This also includes the optical quadrature encoder readout electronics and readout for limit position sensors. Thus enabling the closed loop motion control of the stepper motors. Three relays are provided on each card for various switching oprations. Three additional switching circuits are provided to control external relays. Each card is having provisions for USB as well as serial communication (in addition to PC-card serial communication link) links to be able to comminicated with any other third party control system. Industry standard PCB sizes and enclosure designs have been chosen. ECS is currently under development including card electronics as well as the PC software and micro-controller's embedded firmware.

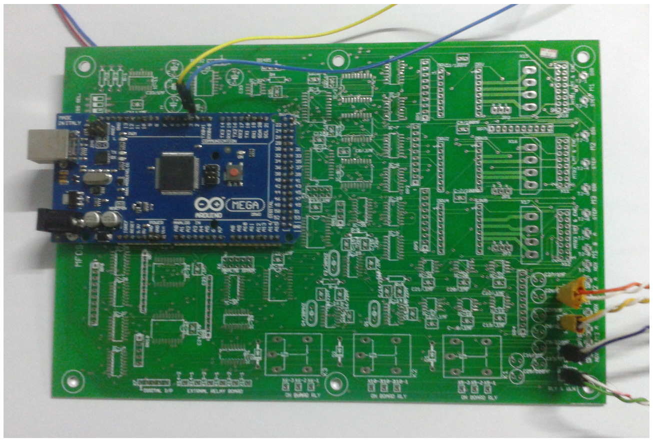

Figure 26: Printed Circuit Board of a ECS card based on Arduino mega 2560 micro-controller board.

(M. K. Srivastava, N. Ahmed, A. B. Shah, S. Ganesh)

Design and Development of Quadcopter: Unmanned Aerial Vehicle (UAV) for scientific research program

A lightweight ground controlled Unmanned Aerial Vehicle (UAV) has become very productive instrument in the last decade for scientific community to conduct various scientific experiments within the Earth atmosphere. PRL has initiated design and development of Micro UAV class - Quadcopter (four rotors) - flying robot. Quadcopter is electro-mechanical flying robot having on board intelligence for stable hovering, execution of manoeuvring commands, self calibration of on board sensors, payload data uploading etc. Quadcopter flight controller is realized using dual ATMEL MEGA 2560 Microcontrollers (MCU) in master-slave configuration. Inertial Measurement Unit (IMU) 6050 MPU has been interfaced to master MCU for orientation estimation . Master MCU receives throttle, Pitch, Roll and Yaw commands, reads angular velocity and acceleration data from IMU, calculates thrust values using real-time Proportional Integration Derivative (PID) algorithm, generate Pulse Width Modulated (PWM) signals for Electronics Speed Controller (ESC) to control speed of all four rotors and communicates with slave MCU. Slave MCU acts as a sensors controller. Ultrasonic, Global Position System (GPS), Optical flow, Temperature, Wind Speed and Barometer sensors will be interfaced with this controller. It will help in estimating UAV position, velocity, orientation and navigation. Ground Station (PC/Laptop) wirelessly connected with UAV through radio frequency (2.4 Ghz) transceiver. It sends maneuvering commands and receives UAV house keeping and payload data. Labview based GUI software is being developed which will simulate virtual pilot panel and graphical representation of received data. To measure atmospheric vertical profile of temperature, pressure, humidity and solar radiation scientific payload development is in progress. Calibration of the sensor used is also being carried out.

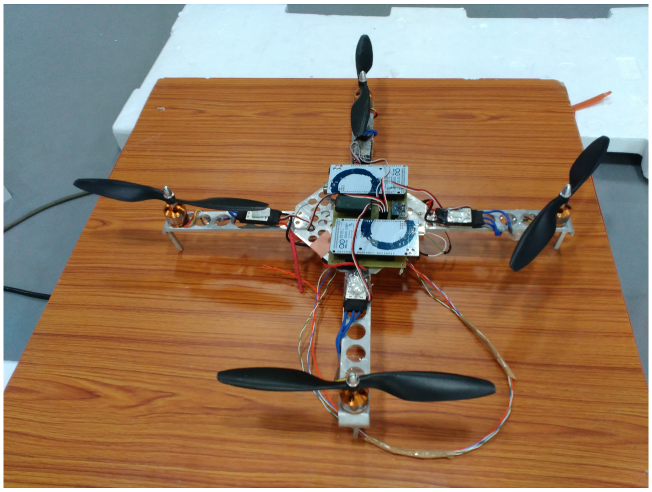

Figure 27: Lab-model of Quadcopter being tested at PRL Thaltej .

(A. B. Shah, H. S. Mazumdar, N. Tiwari, C. Kumar, M. Devan, K. Kumar, A. Sarda, J. Krishna, P. Neelum, M. Shanmugam, K. D. Prasad)

Science

Solar Physics

Solar cycle changes seen in the velocity amplitudes of global p-mode oscillations in the Sun

Sound waves are believed to be stochastically excited inside the Sun due to high turbulence in the convection zone, just beneath the solar surface. These sound waves produce standing waves (known as p-modes), which are trapped in the resonant cavities globally inside the Sun. These global p-mode oscillations of the Sun have shown changes in their frequencies over the solar activity cycle. We have studied the amplitude modulation of these p-modes between the maximum and minimum phases of the Solar Cycle 23, using the disk-integrated Sun-as-a-star velocity observations obtained by the GOLF instrument onboard SOHO space mission.

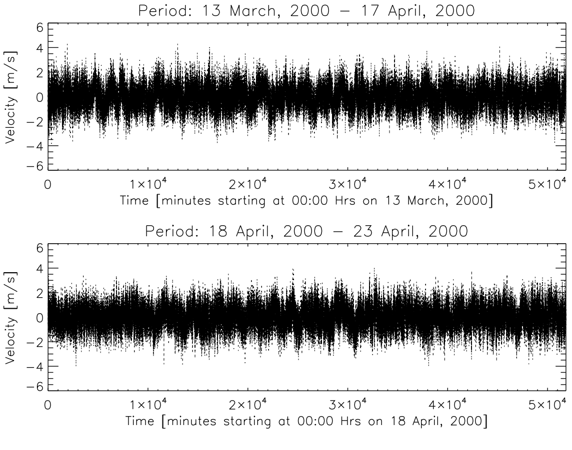

Figure 1: Plots showing the disk-integrated Sun-as-a-star velocity observations (two 36-days time series) obtained by the GOLF instrument onboard SOHO space mission with a cadence of one minute during the maximum phase of the Solar Cycle 23.

In the Figure 1 and Figure 2, we show two 36-days velocity time series obtained from the GOLF with a cadence of one minute during the maximum phase and the minimum phase of the Solar Cycle 23, respectively.

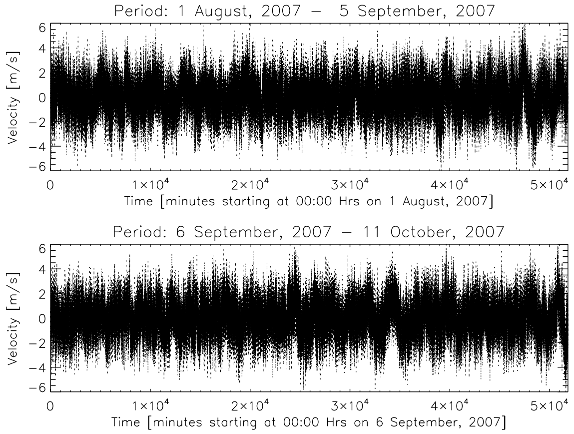

Figure 2: Plots showing the disk-integrated Sun-as-a-star velocity observations (two 36-days time series) obtained by the GOLF instrument onboard SOHO space mission with a cadence of one minute during the minimum phase of the Solar Cycle 23.

A 36-days time series is considered in order to cover one full solar rotation. It is seen that the amplitudes of these velocity oscillations are having higher values during the minimum phase as compared to the maximum phase of the Cycle 23. We have further estimated average Fourier power spectra from these 36-days time series, separately, for the maximum phase and the minimum phase of the Cycle 23 (c.f., Figure 3). We find that the power of the global velocity oscillations is significantly suppressed during the maximum phase as compared to the minimum phase of the Cycle 23.

This indicates that the structural and magnetic changes in the sub-surface layers of the Sun during the period of high solar activity have an impact on the amplitudes of the global modes of oscillations in the Sun. These results can give important clue to the understanding of magnetic activity cycles in the Sun-like-stars using the high quality observations from the space missions dedicated to asteroseismology, such as Kepler and CoRot.

This work has been done in collaboration with Savita Mathur of Space Science Institute, Boulder (USA), Rafael A. Garćia of IRFU/DSM/CEA, Saclay (France), Antonio Jimenez of IAC, Tenerife (Spain).

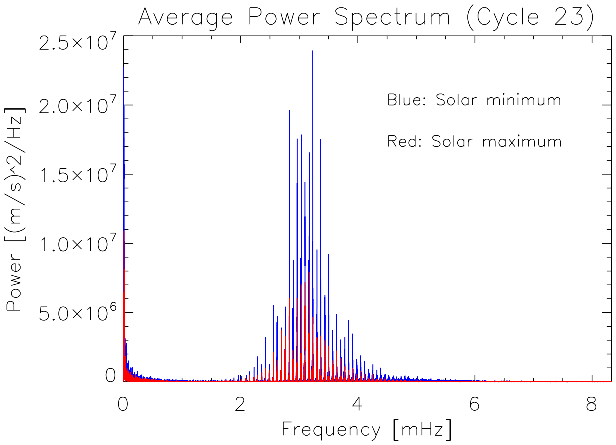

Figure 3: Comparison of the average Fourier power spectra as estimated for solar minimum (blue solid lines) and the solar maximum (red solid lines) from the two 36-days time series of the disk-integrated Sun-as-a-star velocity observations obtained by GOLF during the minimum and maximum phases of the Solar Cycle 23. It is clearly seen that the power of the global velocity oscillations is significantly suppressed during the period of high solar activity during the Cycle 23.

(B. Kumar)

Evidence that magnetic-jerk in the active regions during flares can induce oscillations in the solar atmosphere

The magnetic field configuration in the solar corona rapidly changes during flares and the signatures of these appear in the form of the evolution of the photospheric magnetic fields. The changes in the photospheric magnetic fields during flares take place, both on short time-scales of few minutes during the impulsive phase of the flare and longer time-scales of hours covering the phases before and after the flare. The abrupt changes in the photospheric magnetic fields during the flare produce Lorentz-force-transients in the solar atmosphere and are termed as "magnetic-jerk". In the recent years, solar researchers have found good spatial and temporal correlation between the sites of magnetic jerks in the active regions during flares and the localized enhancement of photospheric velocity oscillations. These results indicate that "magnetic-jerk" can drive the localized photospheric acoustic oscillations in the Sun. Now, since the magnetic field lines tied to the solar photosphere extends above in the corona, hence it would be important to study the effect of magnetic jerks simultaneously at the solar surface as well as in the higher layers of the solar atmosphere. Using the velocity and magnetic field observations obtained by HMI instrument onboard SDO space mission, we have earlier shown that magnetic jerks at various locations in the active region NOAA 11719 during a large flare on 11 April 2013 could power localized photospheric velocity oscillations. Motivated by those findings, we have now also analyzed the chromospheric observations of this flare event obtained in the spectral line H$_\alpha$ 6562.8 Å by the GONG instrument located at the Udaipur Solar Observatory, in order to search for any enhancements in the chromospheric oscillations corresponding to the sites of magnetic jerks in the active region during the flare.

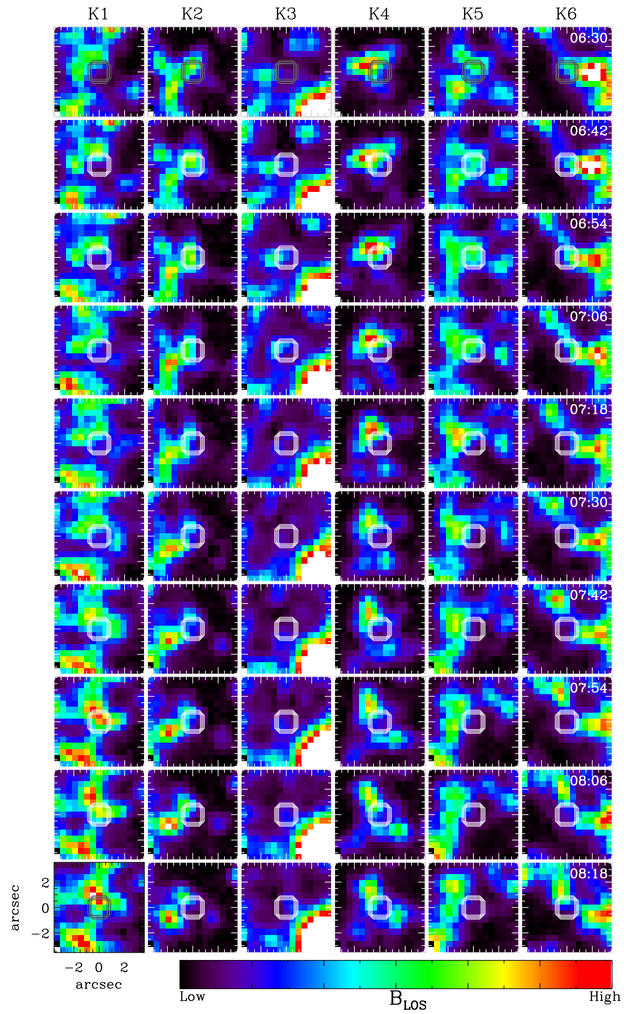

Figure 4.: Mosaic of images showing the time evolution of line-of-sight magnetic fields (Blos) over a grid of 15×15 pixels containing the raster of 3×3 pixels at its center (enclosed by white box) corresponding to the locations 'K1', 'K2', 'K3', 'K4', 'K5', and 'K6' in the active region NOAA 11719 for the period from 06:30 UT to 08:18 UT on 11 April 2013, at the time interval of twelve minutes spanning the flare obtained by SDO/HMI. The aforementioned identified locations have shown rapid changes in B_{los} during the flare. Each column is representing the temporal evolution of B_{los} for a given kernel from top to bottom. The dynamic range of B_{los} is different for the columns (kernels), however within a column the range is same. For the locations 'K3', and 'K6', the pixels with high values of B_{los} are made saturated in order to enhance the visibility of the morphological evolution of magnetic features within the white boxes. The FOV is about 7.5×7.5 arcsec^2

In the Figure 4, we show the mosaic of the raster of line-of-sight magnetic fields at various locations of the active region NOAA 11719 during the aforementioned flare as obtained by SDO/HMI. This mosaic of images illustrates rapid changes in the morphology of line-of-sight magnetic fields at the various locations of the active region during the flare. It is to be noted that these locations are found to be away from the H_α flare ribbons as well as in the vicinity of these flare ribbons. In the Figure 5, we show the comparison of the H_α oscillatory power before and spanning the flare at the sites affected by the "magnetic-jerk" corresponding to the locations shown in the Figure 4. It is observed that these power spectra show a general enhancement in the oscillatory power during the flare as compared to the pre-flare condition for all the identified locations. These magnetically induced oscillations observed in the different layers of the solar atmosphere are important for understanding the transport of acoustic energy from the photospheric levels to the higher atmospheric layers in the Sun.

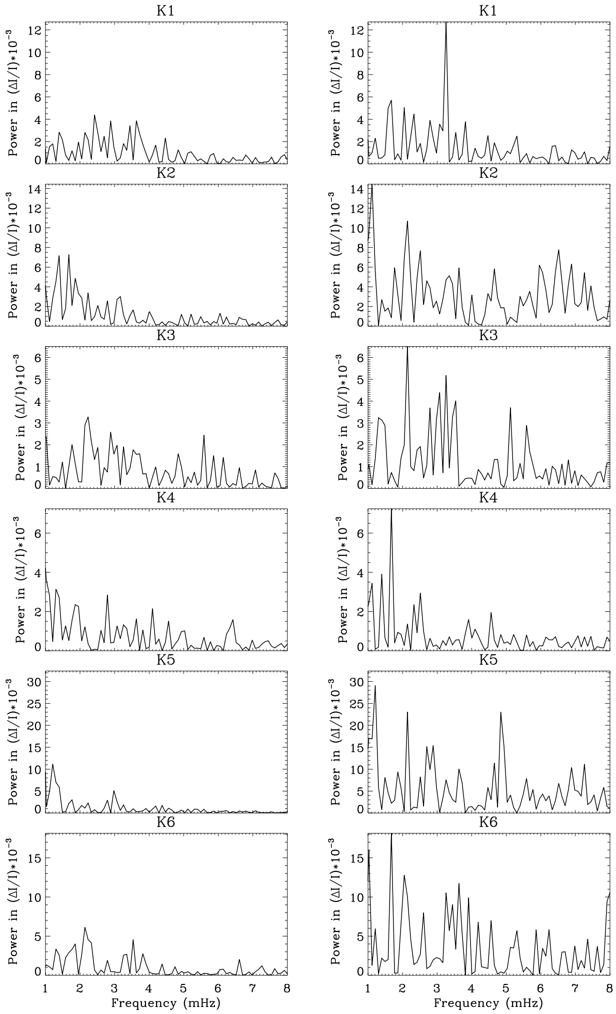

Figure 5.: Plots shown in the left panels are the average Fourier power spectrum of ΔI/I (extracted from H_α light curves from GONG observations) estimated over a raster of nine pixels within the locations of magnetic jerks in the active region ('K1', 'K2', 'K3', 'K4', 'K5', and 'K6') during the period from 03:01 UT to 06:01 UT on 11 April 2013 (pre-flare condition). Similarly, the plots shown in the right panels are the average Fourier power spectrum of ΔI/I (extracted from H_α light curves from GONG observations) estimated over the same rasters of nine pixels within the aforementioned locations of the active region for the period from 06:31 UT to 09:31 UT on 11 April 2013 (spanning the flare). It is evident that the power of ΔI/I oscillations (proxy for chromospheric velocity oscillations) is enhanced in the aforementioned locations during the flare.

(B. Kumar, A. R. Bayanna, P. Venkatakrishnan, S. K. Mathew)

Statistical properties of umbral dots

The analysis of sunspot fine-structures is crucial to understand the subsurface energy transport in sunspots. The strong and vertical magnetic field in umbra suppresses the convection in umbrae, which causes these structures to be cooler relative to the quite regions of the Sun. However, the suppression due to convection cannot explain the observed brightness of umbrae. It is believed that some form of magnetoconvection is responsible for the observed umbral brightness. Umbral Dots (UDs) are dot-like bright features observed in almost all sunspot umbrae and pores, are thought to be manifestation of magnetoconvection. Generally, UDs are divided into central umbral dots (CUDs) and peripheral umbral dots (PUDs) based on their positions inside an umbra.

We present the physical properties of UDs observed in different regular isolated sunspots using G-band observations obtained by the Broadband Filter Imager (BFI) of the Solar Optical Telescope aboard *Hinode* satellite.

We have developed an automatic UD identification and tracking method in order to derive their physical properties. The position information of an UD in each frame is used to track the UD in the image sequences. The statistical properties of UD such as effective diameter, maximum and mean intensity of UD, local background intensity, lifetime, birth-death distance, trajectory length, and velocity were determined after the implementation of an automated algorithm for identification and tracking.

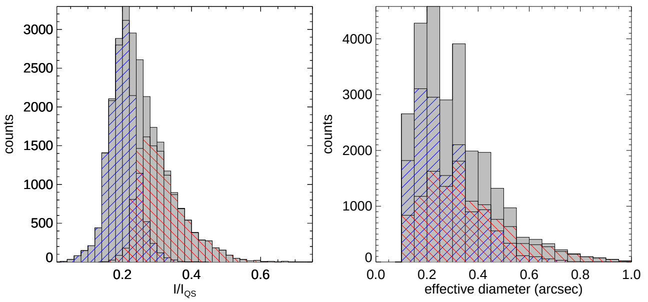

Figure 6: The histograms of the CUDs and PUDs identified in seven different active region sunspots. The bin size for mean normalised intensity (left) and effective diameter (right) are $0.02\mathrm{I}_{\mathrm{QS}}$ and 0.04 arcsec (36 Km), respectively. The blue and red color hashed histogram represents CUDs and PUDs, respectively, whereas the filled grey histogram is for all UDs.

The physical properties for all identified UDs located in different active regions are listed in table 1. The obtained results are summarized as follows. The spatial location of UDs in general do not show specific patterns. We observed that an UD can be found in any part of the umbrae and their brightness depend on the background intensity which confirms the previous results. The umbral background intensity near the penumbra is brighter as compared to central dark part of umbra. As a consequence PUD appears brighter as compared to the CUD (Figure 6). We found that their size (effective radius, d_{eff}) can vary from 0.22 – 1.0 $arcsec$ the bigger size might be the resultant size of two or more than two UDs. The histogram of mean diameter exhibits a maximum at 0.29 arcsec (210 Km). UDs do not exhibit a typical lifetime, they can attain a lifetime between 8 – 40 minutes. The obtained mean lifetime of all UDs is $\approx$7.5 min. Most of the UDs live for a short time ≈68% (less or equal to mean value) and ≈ 8% of identified UD have lifetime greater than 20 minutes (Figure 7). The mean speed of UD obtained is 0.62 Km/sec. These finding are in good agreement with the recent results.

Obtained physical properties of CUDs and PUDs

AR NOAA	10933	10940	10944	10953	10960	10961	10963
Tracked UDs	775	342	138	838	136	199	219
I_{CUD}	0.26 (0.04)	0.22(0.05)	0.26 (0.03)	0.26 (0.04)	0.23 (0.031)	0.23(0.04)	0.21 (0.06)
I_{PUD}	0.39 (0.08)	0.33 (0.04)	0.37 (0.06)	0.39 (0.08)	0.3 (0.04)	0.3 (0.04)	0.33 (0.04)
D_{eff} CUD ($''$)	0.17 (0.041)	0.29(0.09)	0.14(0.06)	0.15(0.06)	0.3(0.03)	0.31 (0.05)	0.31 (0.08)
D_{eff} PUD ($''$)	0.24(0.07)	0.43 (0.15)	0.20(0.06)	0.22 (0.06)	0.37 (0.09)	0.40 (0.10)	0.43(0.12)
Lifetime (min)	7.048	8.5951	6.154	8.18	8.88	11.19	10.47
Displacement (Km)	179.68	250.412	160.8	190.5	130.1	153.45	241.9
Trajectory (Km)	380.1	315.09	262.1	309.94	237.5	278.98	318.44
Velocity (Km/sec)	0.90	0.63	0.728	0.63	0.47	0.44	0.52

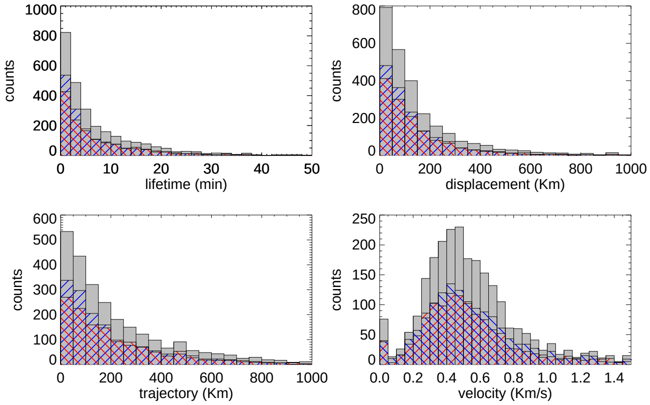

Figure 7: The histograms of the CUDs and PUDs identified in seven different active region sunspots. The binsize for lifetime, displacement, trajectory length and velocity are 2 minutes, 50 Km, 50 Km and 0.05 Km/sec, respectively. The blue and red color hashed histogram represents CUDs and PUDs, respectively, whereas the filled grey histogram is for all UDs.

(R. Yadav, S. K. Mathew)

Eruption from a sigmoid active region NOAA 11719: A multi-wavelength study

We have carried out a comprehensive multi-wavelength analysis of solar eruption from sigmoid active region NOAA 11719 on 2013 April 11. The active region displayed a relatively simple bipolar magnetic structure with $\beta\gamma$ magnetic configuration and the flaring activity was associated with the following part of it. We have studied the evolution of this active region over a period of ten hours (00:00-10:00 UT) during which EUV sigmoid structure was formed by the interaction of coronal loops system. The evolution of sigmoid was observed at AIA 94 Å images which imply that this structure comprised of very high temperature plasma (∼6MK). With the expansion of twisted flux ropes, the sigmoid underwent an activation phase and subsequently erupted (see Figure 8). During its eruption, we observed a large M6.5 flare.

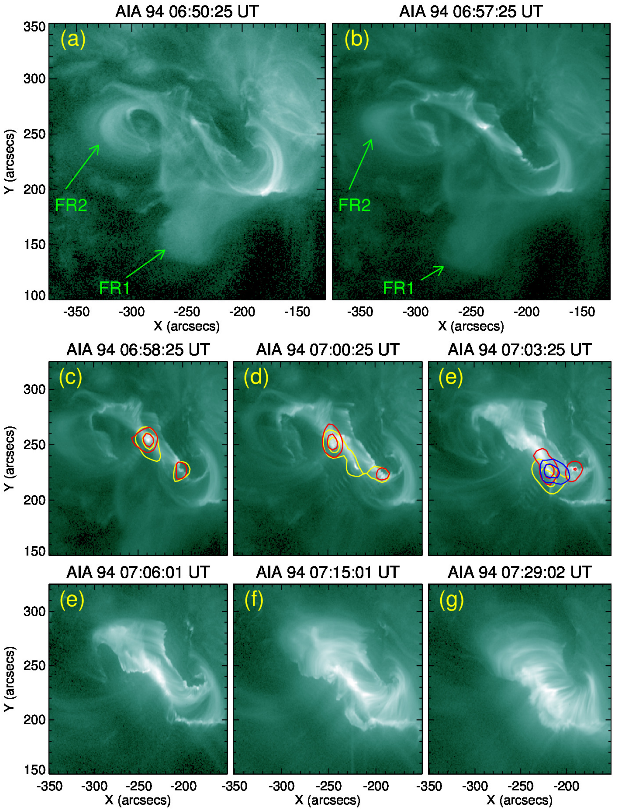

Figure 8: Sequence of AIA 94 Å images showing expansion and eruption of the flux rope (FR) during various stages of an M6.5 flare. We have marked the expanding fronts as FR1 and FR2 at the top panel. A few co-temporal HXR contours in 12-25 keV (yellow), 25-50 keV (red), and 50-100 keV (blue) are also over plotted on the representative AIA 94 Å images (middle panels). A bright post-flare loop arcade is developed after the eruption of the flux ropes (bottom panels).

The flare exhibited characteristics of a typical long duration event (LDE) with gradual variation in soft X–ray emissions between 06:55 and 07:45 UT (Figure 9). The soft X-ray time profile indicates a prolonged rise phase lasting for ∼21 minutes during which multiple hard X-ray bursts were observed above 25 keV energies (Figure 8). Moreover, the early rise phase of the flare (Figure 9) is characterized by converging motions of H_α and UV flare ribbons and decrease in the separation of HXR footpoints. These observations provide concrete evidence of unusual motions of flare sources before the main energy release phase (i.e., impulsive phase) which do not comply with the standard flare model.

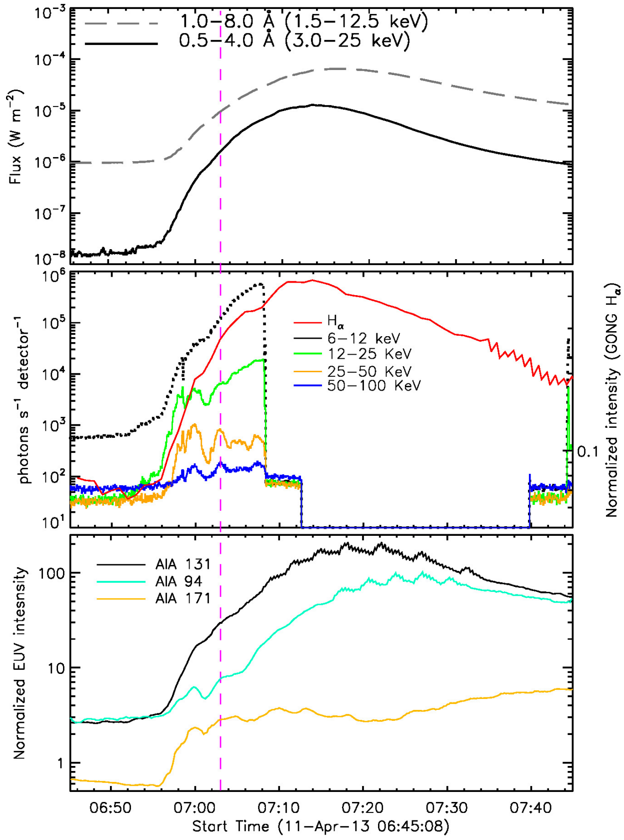

Figure 9: X-ray and EUV lightcurves of M6.5 flare on 2013 April 11. Top panel: The GOES SXR profiles at 0.5-4 and 1-8 Å energy channels. Middle panel: HXR lightcurves in 4 different energy bands along with H$_\alpha$ intensity profile of flaring region. Bottom panel: EUV lightcurves in 131, 94, and 171 Å channels are presented. The flare is characterized by prolonged rise phase of 21 minutes. We have drawn a vertical dashed line to differentiate between early rise phase and late rise phase of the flare.

(B. Joshi, U. Kushwaha)

Nature of collision of Coronal Mass Ejections observed in the heliosphere

Coronal mass ejections (CMEs) are the most energetic events on the Sun and are expanding magnetized plasma blobs in the heliosphere. Understanding their collision is of interest because of its impact on many areas of heliospheric physics research. Colliding CMEs can display changes in their kinematics and morphology after the collision, and hence the prediction of their arrival time to the Earth becomes challenging. However, the knowledge about nature of collision of CMEs can be utilized to predict their post-collision kinematics. In earlier studies, the nature of collision, i.e. coefficient of restitution is found to vary from super-elastic to inelastic range. This poses a question as to what determines the exact nature of collision. We have addressed the limitations of previous studies, and attempted to examine the role of characteristics of CMEs, e.g. direction, mass, propagation speed, expansion speed and angular size, on the collision nature. For this purpose, we selected two CMEs which occurred almost 7 hr apart on 2013 October 25 and collided with each other at around 37 solar radii from the Sun. We have exploited the NASA's STEREO spacecraft observations of the CMEs for our study. By adopting head-on as well as oblique collision scenarios, we have quantified the range of uncertainties involved in the calculation of the coefficient of restitution for expanding magnetized plasmoids. The observed kinematics of the CMEs and their angular half-width ranging between 5 to 350 results in a probability of approximately 75.6% for inelastic and 24.4% for super-elastic collision. Figure 10 shows that a relatively large expansion speed of the following CME than that of the preceding CME, results in a higher probability of super-elastic collision. We also infer that a relative lower approaching speed of the CMEs as compared to the sum of their expansion speeds increases the chance of a super-elastic collision. Considering reasonable errors in the observed parameters of the selected CMEs reveals a larger probability of an inelastic collision between them. As the larger expansion speed and internal pressure imply to harden the CME, we ideate that collision tends to be super-elastic if the following CME is harder than the preceding CME. This implies that different physical characteristics of the interacting CMEs plasma may change the nature of collision.

This work has been carried out in collaboration with Wageesh Mishra and Yuming Wang of University of Science and Technology, China.

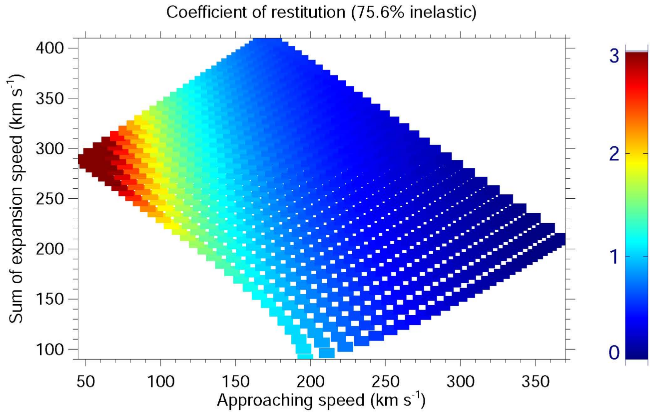

Figure 10: The panels in the left and right show the coefficient of restitution (e) values. In the left:The conventional X and Y-axis represents the half angle of the CME1 and CME2, respectively. The X and Y-axis at top and right side, respectively show the expansion speed of CME1 and CME2. The dashed white line marks the boundary of super-elastic and inelastic regime. In the right:X-axis represents the relative approaching speed of the CMEs and the sum of expansion speed of CME1 and CME2 is shown along the Y-axis. The color bar is stacked below the X-axis (for left panel) and right (for right panel) of the figure.

(Nandita Srivastava)

Validation of CME arrival time and geomagnetic forecast alerts under COMESEP

An automated space weather alert system has been developed for the estimated occurrence of SEP radiation and CME geomagnetic storms under the EU FP7 project COMESEP (COronal Mass Ejections and Solar Energetic Particles). It provides an estimation of the CME arrival probability and its likely geo-effectiveness, based on CME parameters, as well as an estimate of the geomagnetic-storm duration. Here, we present an evaluation of the COMESEP Alert System based on a study of several geo-effective CMEs observed during 2014-2015. Based on the alerts released by the COMESEP tool, the validation of the forecast tool is done for a set of recent CME events in two ways. First the performance of the forecast tools is evaluated by comparing the actual arrival time of the CMEs estimated from measurements by in-situ spacecraft with that predicted by the COMESEP Alert System. Second, a comparison of the geomagnetic activity forecast with the actual geomagnetic storm occurrence has also been made in an attempt to test the tools for predicting geomagnetic activity. In addition, the COMESEP alerts have also been compared with the alerts of other existing space weather forecasting tools operated by NOAA's Space Weather Prediction Center (SWPC) and Community Coordinated Modeling Center (CCMC) of the GSFC.

From a total of 33 COMESEP forecasts issued over the period of 2 years (2014-2015), we have found the following:11 true alarms for events which resulted in moderate to intense geomagnetic activity in near-Earth space. (Dst range -70 nT to -223 nT). The difference between the actual arrival speeds of these CMEs at the Earth and that predicted by the COMESEP using Drag based model ranges from 3–247 km/s and the time difference ranges from 5 to 29 hours. COMESEP also missed 7 events which were observed in near-Earth space. There were 12 false alarms which were predicted by COMESEP but were not detected at the Earth. The results are important and will be used to improve and fine tune the algorithms and tools implemented for automatically predicting the arrival time of CMEs and their geomagnetic impact.

This work was done in collaboration with Mateja Dumbovic, Hvar Observatory, Croatia and Andy Devos, Royal Observatory of Belgium, Belgium

(Nandita Srivastava)

Continuous development of current sheets near and away from magnetic nulls

Numerical computations presented in this work aim to compare intensity of current sheets (CSs) near the magnetic nulls against those which develop throughout the volume and their governing dynamics. For the purpose, we simulate the viscous relaxation of an incompressible, thermally homogeneous magnetofluid with infinite electrical conductivity. A suitable initial magnetic field is constructed from a force-free field with complex field line topology, as it successfully manifests the distributed CSs in presence of two dimensional (2D) and three dimensional (3D) magnetic nulls. Importantly, the simulations reported rely on the proven implicit large eddy simulation (ILES) property of non-oscillatory numerics in regularizing the under-resolved scales through onset of magnetic reconnections (MRs), concurrent and collocated with developing CSs.

The results show the development of first generation of CSs away from the nulls which are distributed throughout the volume (Figure 11). The decay of these CSs through MRs generates flow which is dissipated by viscous drag. The subsequent dynamics illustrates the squashing of X-type null, leading to formation of an extended CS along with two Y-type nulls (Figure 12). Also, notable is a complete collapse of fan and spine structures of the 3D nulls which enables pressing of non-parallel MFLs to generate CSs (Figure 13). The collective decay of CSs, near X-type and 3D nulls, further develops the dynamics. With all 2D and 3D nulls destroyed, the subsequent relaxation forms the next generation of distributed CSs (not shown), having geometry similar to the ones which is shown in Figure 11 but with different spatial distribution.

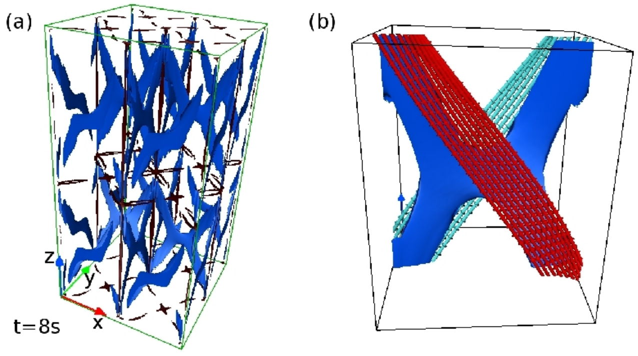

Figure 11: Panel (a) depicts CSs (color blue) with magnetic nulls (color maroon), highlighting formation of CSs away from nulls and distributed throughout the computational volume. The MFLs across the CS are misaligned by an angle around 90° (Panel (b)).

Based on the above analysis, the CSs can broadly be classified into three categories. The first one corresponds to the distributed CSs that develop away from the nulls or in absence of the nulls (Figure 11). The second consists of the CSs originating around 2D nulls (Figgure 12).

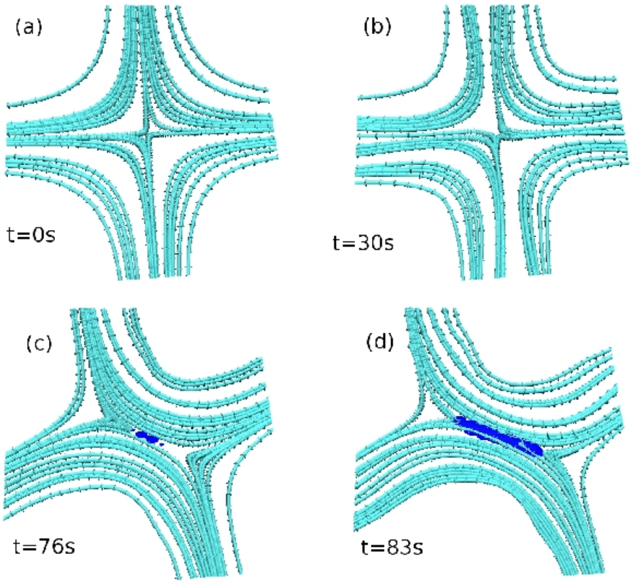

Figure 12: Evolution of field lines in the vicinity of an X-type null overlaid with CSs (blue color). Noteworthy is the generation of a localized extended CS along with two Y-type nulls.

The CSs created by the collapse of 3D nulls fall into the third category (Figure 13).

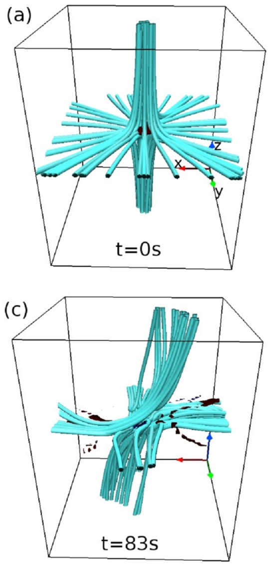

Figure 13: Time sequence of MFLs in the immediate neighborhood of a representative 3D magnetic null overlaid with CSs (blue color). Noteworthy is the development of CSs by the collapse of fan and spine structures of the 3D null.

To explore the features associated with these CSs, additional computations are carried-out on different sized grids. Figure 14 documents scaling of peak current density ($|\mathbf{J}|_{\max}$) with resolution. The figure confirms that the CSs near 2D nulls have strongest scaling compared to the CSs near 3D nulls or the distributed ones. In addition, the figure also reveals the intensity to be larger for the CSs around 2D nulls than the other types of CSs. This difference in intensity can be attributed to the angle by which the MFLs are misaligned across a CS. For instance, the MFLs are misaligned by the angle 180° for a CS around 2D null (panel d, Figure 12). While the angle is much less than 180° for a CS which generates away from the nulls (panel b, Figure 11).

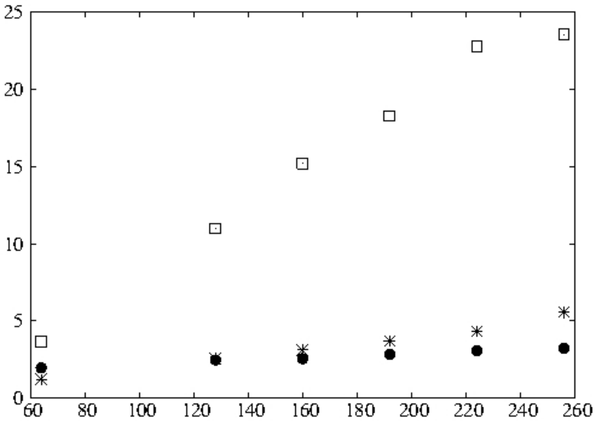

Figure 14: Scaling of $|\mathbf{J}|_{\max}$ with resolution, for the CSs near 2D nulls (squares), 3D nulls (stars), and away from these nulls (dots). The abscissa is grid resolution along z whereas the ordinate is $|\mathbf{J}|_{\max}$.

Notably, the strongest scaling physically signifies the reconnections near 2D nulls to be faster and energetically more explosive than the ones near volume-distributed CSs; a scenario congruent with the energetics of eruptive events and possible nano-flares, occurring at the solar corona.

(S. Kumar, R. Bhattacharyya)

Imaging spectro-polarimeter for Multi-Application Solar Telescope (MAST): Preliminary results in 6173 Å

An imaging spectro-polarimeter has been developed at USO as a back-end instrument of Multi-Application Solar Telescope (MAST) for measuring the magnetic field in the photosphere and chromosphere at two different wavelengths. The system consists of a narrow-band imager and a polarimeter. Narrow-band imager uses two lithium-niobate Fabry-Perot etalons in tandem with a blocking filter for spectral analysis and the polarimeter consist of two Liquid Crystal Variable Retarder (LCVR) and a Glan-Thompson polarizer for polarization analysis. Calibration of the instrument is carried out for the solar spectral lines at Fe I 6173 Å and Ca II 8542 Å. The polarimeter is operated in two modes:

- Vector mode, in which Stokes vector [I Q U V] are measured for deriving vector magnetic fields.
- line-of-sight (LOS) mode, in which only Stokes parameter I and V are measured for deriving the LOS magnetic field.

We have observed several active regions by operating the imaging spectropolarimeter in longitudinal mode using the optical setup shown in Figure 15.

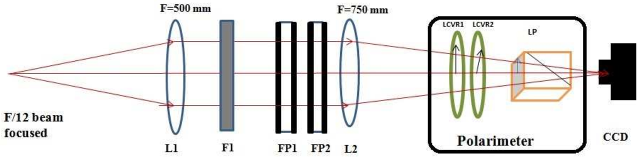

Figure 15: Schematic diagram of the imaging polarimeter for MAST: In this setup a F/12 beam coming from the telescope is collimated using the lens L1. Then the collimating beam passes through narrow-band imager consists of two Fabry-Perot etalons (FP1 and FP2) and prefilter F1. Polarimeter consisting of two LCVRs and a Glan-Thompson polarizer is kept in between the CCD and imaging lens (L2) in the converging beam made by imaging lens (L2).

Here we report the observation of an active region (AR 12436, N09 W20) which was carried out on 24th October 2015. The observations were obtained from 04:00 UT to 05:30 UT when the seeing was moderate. The imager sampled magnetically sensitive Fe I 6173 Å line at 27 wavelength positions with a wavelength spacing of 15 mÅ. By changing the retardance of the LCVRs, 20 images were alternately captured each for I+V and I-V measurements with an exposure time of 65 milliseconds. The images were acquired with a plate scale of $0.145''$ per pixel. Stokes I and V image along with their mean intensity profile is shown in Figure 16. The top row left and right panel show the intensity and Stokes V images, respectively. The bottom panel show corresponding Stokes profiles averaged for magnetic (solid line) and quiet regions (dotted line). The broadening of the line profile and the strong Stokes V signal is clearly seen in the figure for the profiles averaged over the magnetic region.

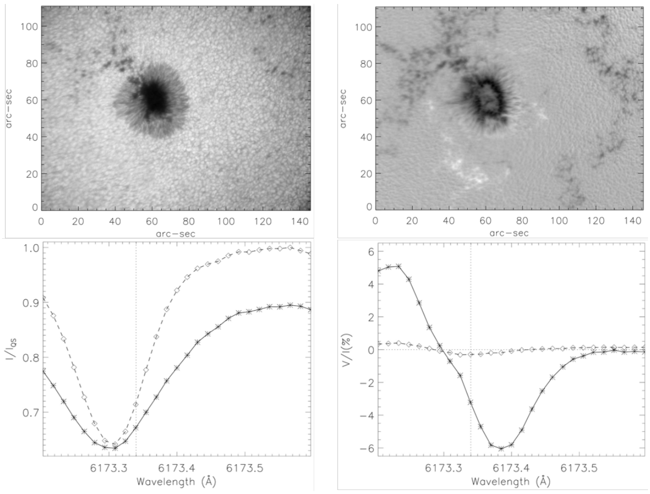

Figure 16: Top row: Mean Stokes I image (left) and Stokes V image at wavelength position 6173.26 Å. Bottom Row: Profiles of Stokes I (left) for quiet sun and sunspot region along with the profile of Stokes V for the same regions.

For a comparison of our Stokes V measurements, we obtained the data for the active region NOAA AR 12436 observed by Helioseismic Magnetic Imager (HMI) on board Solar Dynamics Observatory (SDO) on 24th October 2015 around 04:30 UT. Both the instruments are operated at the same spectral line 6173 Å, though the HMI provides full disk images with a pixel resolution of $0.5''$ and the field-of-view (FOV) of MAST is around $200''$. Since SDO is a space-borne instrument, the full disk HMI magnetograms are free from atmospheric seeing whereas the image quality of MAST is degraded due to seeing.

The active region observed from HMI/SDO was cropped and rescaled to the same size as of the MAST image. The Stokes V signal is normalized with the quiet sun intensity in both the cases. The images from the continuum intensity and Stokes V observed at one wavelength point on the line profile from HMI/SDO and MAST are shown in top and middle row of Figure 17. In the bottom row of Figure 17, scatter plots in the left and right panels illustrates the relationship between Stokes V signal from SDO and from MAST with LOS magnetic field strength of HMI/SDO, respectively. It is evident from the Figure 17 that both the measurements follow a similar trend, even though we observed a factor of two difference in the absolute Stokes V values, the origin of this difference is being analyzed. The above comparison proves the validity of our measurements, further comparison will be carried out for all the Stokes parameters with similar SDO/HMI measurements.

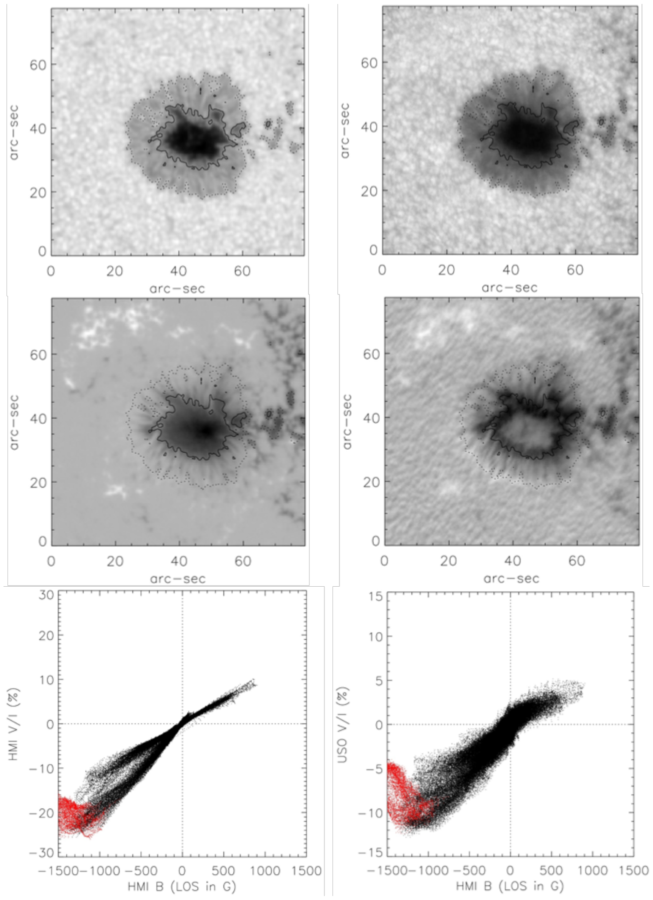

Figure 17: Top row: Stokes I image taken by HMI (left) and MAST (right); Middle row: Stokes V image at wavelength position 6173.26 Å taken by HMI (left) and MAST (right); bottom row: scatter plot made between Stokes V of HMI and longitudinal magnetic field of HMI (left) and scatter plot made between Stokes V of MAST and longitudinal magnetic field of HMI (right).

(A. R. Tiwary, S. K. Mathew, A. R. Bayanna, P. Venkatakrishnan)

Science

Planetary Sciences and PLANEX Program

Meteorite Studies

Cr isotopic composition in Murchison presolar grains

^{54}Cr isotopic anomalies have been reported in various acid leached samples in different meteorites. It has been interpreted in terms of Supernovae (SNe) presolar grains carrying high anomaly in neutron rich isotopes of various elements close to Fe (transition elements). Chromium is one of these elements, which is primarily a product of inner shell nucleosynthesis within supernovae. Thus Cr- anomalies found in supernovae presolar grains (X-grains) can provide information regarding amount of mixing taking place within the various shell of supernovae during explosion and formation of presolar SiC. In general, the inherited chromium isotopes can be further s- processed in various Red Giant stars (RGB) or Asymptotic Giant Branch (AGB) stars. The s-process nucleosynthetic calculations suggest significant overproduction of ^{54}Cr isotope (δ^{54}Cr values $\sim$ +200 ‰) with limited variations in rest of the isotopes of Cr. Here, we report Cr isotopic data along with C & N isotopic data abundances for 15 individual mainstream presolar grains (KJF series) along with two A/B grains and one X-grain from Murchison meteorite using JSC-NanoSIMS 50L (nano Secondary Ion Mass spectrometer). Identification and classification of presolar grains were based on C, N isotopic composition using a Cs+ source of $\sim$1pA. Followed by rastered O- primary beam of $\sim$ 50 pA to analyze ^{28}Si, ^{52}Cr, ^{53}Cr, ^{54}Cr, ^{55}Mn and ^{56}Fe in multicollection mode. All grains measured belonging to mainstream grains, have their carbon isotope ranging from 29 $<$ ^{12}C/^{13}C $<$ 108 and N isotopes ranging from 259$<$ ^{14}N/^{15}N $<$ 7800. In case of the two A/B grains ^{12}C/^{13}C are $\sim$4.7, $\sim$4.8 and ^{14}N/^{15}N are $\sim$1353, $\sim$340. Whereas, X-grain has^{12}C/^{13}C, ^{14}N/^{15}N $\sim$ 71.7, 30.4 respectively. The NanoSIMS imaging technique, helped in distinguishing Cr contamination from the presolar SiC grains. An expected mainstream Cr- pattern is observed with negligible enrichment/depletion in ^{53}Cr with average δ ^{53}Cr $\sim$ 4 ‰. Though the statistical errors for ^{54}Cr are quite large, the average value for δ^{54}Cr centers $\sim$ 107 ‰indicating enrichment as per nucleosynthetic calculations. Whereas in case of X grain, we used Rauscher et al. data (nucleosynthesis.org) to test the amount of Cr isotopes being produced and the variation has been observed between various shells of SNe.

This work is done in collaboration with Dr. S. Messenger, Johnson Space Center.

(K. K. Marhas)

Oxygen and Magnesium isotope imaging of Wark Lovering rims

The outer portion/margin of some Calcium Aluminium Inclusions (CAI) are surrounded by 10-50 thin sequence of a few layer of variable thickness but mono-minerallic composition that are collectively called Wark-Lovering (WL) rim. The layer sequence going from inner to outer usually consists of spinel (hibonite and pervoskites), melilite and pyroxene and sometimes forsterite. The timing, location, and mode of formation of WL rim which represent the final high temperature stage of formation of Ca-Al-rich inclusions (CAIs) of the Wark-Lovering rims has interesting information regarding early history of the solar system. O isotopic heterogeneity within some WL rims provides evidence that CAIs migrated between near-solar and planetary nebular regions. It is of great interest to obtain coordinated O isotopic compositions and Al-Mg systematic of WL rims and their host CAIs to constrain the dynamics and nebular lifetimes of early solar system condensates. Al-Mg isotopic imaging study of the fine grained minerals within the core, mantle and rim of a coarse-grained Type B CAI with heterogeneous O isotopic compositions has been obtained. The CAI named “Big Guy” is a fragment of a large Type B1 inclusion from the reduced CV3 Vigarano of 1200 µm x 750 µm. Mineralogically, it is composed of a grossmanite core and thick, zoned melilite mantle that is partially surrounded by a WL rim. The WL rim sequence has a basal layer of hibonite+spinel+perovskite, followed by layers of gehlenite, anorthite, zoned pyroxene, and outermost, forsterite. A partial accretionary rim contains fine-grained forsterite, minor metal and several micro-CAIs. Mg isotopic images of major mineral phases in the CAI interior and of the WL rim were obtained with the JSC NanoSIMS 50L. Isotopic images were obtained in multi-detection mode using seven electron multipliers for ^{24,25,26}Mg, ^{27}Al, ^{28}Si, ^{40}Ca and ^{56}Fe. The resolvable ^{26}Mg excesses in hibonite and melilite in WL rim are consistent with canonical initial ^{26}Al/^{27}Al, within error. Anorthite reveals lack of excess ^{26}Mg at ^{27}Al/^{24}Mg ratios $>$300, consistent with late formation of anorthite, after rim hibonite and melilite. Resolvable ^{26}Mg excesses in melilite in the mantle of the CAI is consistent with canonical initial ^{26}Al/^{27}Al. Stable Mg isotope show no mass dependent fractionation of Mg in the WL rim relative to terrestrial standards, contrary to isotopically heavy ^{25,26}Mg was found in the grosmanite core and melilite mantle of the CAI. The isotopic analyses suggest a complex heating history of the CAI involving formation/alteration of the core CAI via evaporation under conditions suitable for Mg isotope fractionation and subsequently interaction with a planetary-like O isotope reservoir. WL rim formation occurred at a later time in an environment with solar-like O isotopes and conditions, which precluded significant Mg isotope fractionation.

This work is done in collaboration with Dr. A. Needham, Johnson Space Center.

(K. K. Marhas)

Oxygen in hibonites

Oxygen isotopes in hibonite-spinel-perovskite mineral assemblages were acquired from a unique hibonite-bearing CAI (EK5-2A) from Allende. EK5-2A is a unique Hibonite bearing Allende CAIs that has distinct mineral assemblages of similar mineral association within the core and in the mantle/rim regions. These unique setting of similar mineral associations make the study of oxygen isotopes in these mineral phases present within the core and the rim region very interesting to document the petrogenetic evolution of CAIs either of evolving composition or alternatively of transport passage through regions of diverse composition. Oxygen isotopic composition of these mineral phases obtained using JSC NanoSIMS suggests a variation in oxygen going from ^{16}O rich oxygen compositions in the core to the ^{16}O poor planetary like composition in the intermediate regions followed finally by interaction with ^{16}O rich oxygen composition during the formation of WL-rim. Perovskites in different mineral assemblages range from ^{16}O-rich compositions (Δ^{17}O $\sim$ -20 ‰) in the WL rim to Δ^{17}O values between $\sim$ -5 ‰ in the interior, presenting isotopic evidence that the inclusion may contain relict phases and/or exposure with distinct nebular gases.

This work is done in collaboration with Dr. R. K. Mishra, Johnson Space Center.

(K. K. Marhas)

Ion Implantation on presolar grains in Supernovae environment

Presolar grains are nanometer to micrometer sized grains condensed in the outer envelope of stars during their mass ejection phase, which survived molecular cloud collapse and other energetic processes in the interstellar medium. These grains are found in the matrix of least metamorphosed chondrites and in interplanetary dust particles, and are identified from their isotopic anomalies of up to four orders of magnitude which cannot be explained by any of the processes occurring within our solar system. Existing presolar grains in the envelope of dying stars are exposed to nuclei with high velocity, ejected from the core of the star which results in implantation within these grains. Volatile elements like Zinc (Zn) may have condensed in grains; or they may have been implanted in the grains by grain-gas collision. We have investigated ion implantation of Zn and Cr atoms in SiC grains. It should be noted that projectile energies vary significantly, depending on the velocity of the ejecta and the time after explosion. This gives an energy range between 1 KeV to 10000 KeV as per the velocities of different shock waves at different times in a few supernovae that have been studied so far. Studying sputtering and recoil effects simultaneously will give us a complete model of ion implantation in presolar grains from the supernova ejecta.

TRIM simulations with several of these energies for angles covering -90 to +90 (degrees) have been worked out, the results assigning appropriate weights as required for a spherical surface (TRIM assumes planar surfaces). We have also analyzed the effects of sputtering and sputtering yields for Zn and Cr and found that sputtering yield increases significantly with increased oblique incidence of the ion. Sputtering yields were found to be maximum for ion energies around 100 KeV. At low angles of incidence, we have found implantation to dominate over sputtering effects, thus adding a net mass to the grain whereas at high angles of incidence, sputtering dominates. In both the cases, ppm of mass added or lost is very less ($\sim$0.1 ppm). A maximum concentration of around 0.13 ppm for Zn and 0.11 ppm for Cr has been seen to be implanted in a SiC grain of size 1 micron. Maximum depths vary as square roots of the ion energy, in the energy range 1 kev to 100 kev. At higher energies ($\sim$10 MeV, very few ($\sim$5 in 4000) ions were implanted in the grains. These model observations will provide insights for future experimental studies for Zn and Cr isotopes in presolar SiC grains.

(L. Shukla, P. Sharda, K. K. Marhas)

Silicon isotopic variation within Enstatite Chondrite

Enstatite chondrites are unique amongst the primitive meteorites since they have formed under extremely reducing conditions with C/O ratio $>$1. In such a reducing environment, Si becomes siderophilic and a set of new minerals are formed which are typically not stable on Earth, such as Fe–Ni metal with $\sim$3% Si, a suite of Mg, Ca and Mn bearing sulphides, TiN and Si_2N_2O etc. Striking similarity of Enstatite chondrites with Bulk Silicate Earth (BSE) for a number of isotope systems such as O, Cr, N, Mo, Ni, Ti, and Os has led to its consideration as a major building block of Earth. However, there appears to be resolvable isotopic differences between E-chondrites and BSE with respect to Silicon isotope. This difference is postulated to be due to preferential enrichment of light Si in metallic phase with implications towards presence of Si in Earth's core. Moreover, E-chondrites appear to have undergone significant refractory lithophile element fractionation, as evinced by their low Mg/Si and Al/Si ratios, compared to other meteorites. Such a substantial fractionation must invoke kinetic fractionation during its early nebular evolution either due to preferential loss of more volatile Si relative to Mg, equilibrium isotopic fractionation between gaseous SiO and solid forsterite or due to any giant impact. Hence it is crucial to re-asses the exact cause of Si isotope fractionation in Enstatite chondrites before concluding its origin due to any parent body process. In this study, various phases of two EH3 chondrites such as silicate bearing clasts, matrices, metals and chondrules were micromilled after their characterization using EPMA. Si was purified from these phases using cation exchange resin. Si isotopic analyses were carried out by Thermo Neptune Plus MC-ICPMS at PRL. Terrestrial rocks that represent BSE display negligible variation in Silicon isotopic values (δ^{30}Si=-0.29 to -0.26 ‰) (Figure 1). In contrast, various phases of Enstatite chondrite define a broad range of isotopic values (δ^{30}Si=-0.28 to -6.8 ‰). Whereas Si in the metal phases of E-chondrites are significantly lighter than that of silicates. The intrinsic heterogeneity among its different phases calls off the use of Si isotope value of bulk Enstatite chondrite to constrain the amount of Si in the core of Earth. Rather it indicates complex mixing of different components of Enstatite meteorites in different space and time over a wide range of nebular composition.

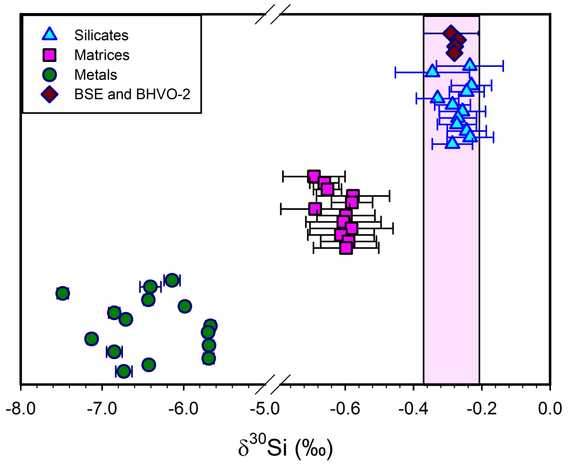

Figure 1: Silicon isotope composition of microdrilled phases of Enstatite chondrites

(J. Sikdar, V. K. Rai)

Simultaneous determination of Si and Mg isotopic composition in meteorites

The variation of Mg/Si ratio among chondrites and Bulk Silicate Earth (BSE) is an enigmatic aspect of cosmochemistry. The superchondritic Mg/Si ratio of BSE is thought to reflect the presence of Si in the Earth's core. It has been suggested that Si isotope fractionation between silicate mantle and metallic core has caused BSE to get enriched in heavier Si isotopes compared to chondrites. However, high temperature melting, recrystallization and subsequent differentiation are very fundamental process and it is difficult to visualize that a significant isotopic fractionation can be induced at temperature-pressure conditions prevalent in core-mantle boundary, which could account for heavier Si in BSE. The decreasing equilibrium isotopic fractionation factor with increasing temperature also makes this scenario less likely. So, a comprehensive investigation of both Mg and Si isotope fractionation pattern among different primitive and differentiated planetary objects can help us in elucidating the origin of Mg/Si variation and Si isotopic offsets among them.

A new chromatographic procedure has been developed for simultaneous purification of Si and Mg from a single aliquot of rock sample using cation exchange resin. Isotopic analyses of both Si and Mg in a number of terrestrial rock samples, ten ordinary, three carbonaceous, four enstatite chondrites, one aubrite and eight HED meteorites have been carried out. Terrestrial samples show a limited range in Si isotopic compositions (Mean δ^{30}Si= -0.27±0.02 ‰, 2SE). The similarity of δ^{30}Si in Ordinary chondrites, Carbonaceous chondrites and HED meteorites (Mean δ^{30}Si= -0.42±0.03 ‰, 2SE) suggests that core formation in 4-Vesta did not induce any Si isotopic fractionation (Figure 2). Mg and Si have comparable volatilities and hence should fractionate more or less to similar extent in any planetary or impact induced processes. Simultaneous analyses of Si and Mg in same aliquot of E-Chondrites and Aubrite show fairly uniform Mg isotopic composition (Mean δ^{26}Mg= -0.30±0.03 ‰, 2SE) which is indistinguishable from BSE and ordinary-carbonaceous chondrites, despite of having significantly lighter Si isotopic composition (Mean δ^{30}Si = -0.67±0.04 ‰, 2SE). This suggests that the Si isotopic fractionation pattern of E-chondrite has been more likely inherited from solar nebula chemistry and is not related to any later stage planetary process such as core formation, giant impact or loss of Si from magma-ocean.

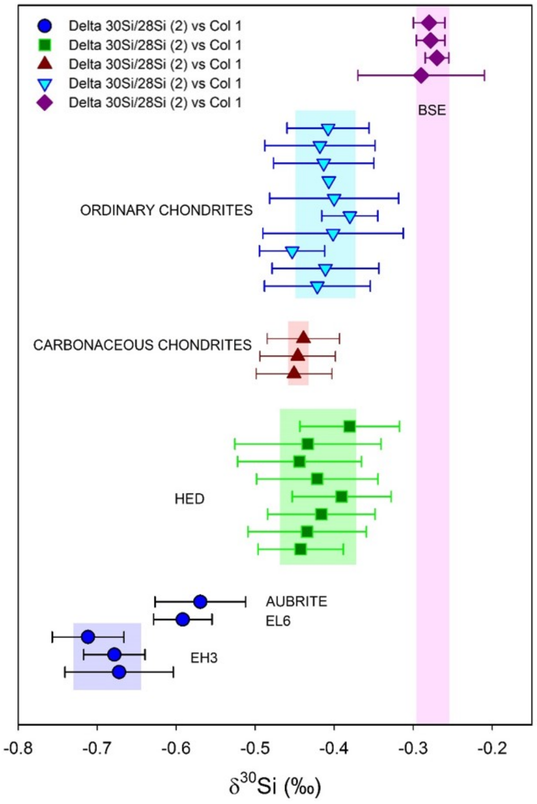

Figure 2: Si isotopic composition of bulk samples of Carbonaceous Chondrites, Ordinary Chondrites, HEDs, Aubrites and Enstatite Chondrites

(J. Sikdar, V. K. Rai)

Nitrogen in HED meteorites

Results from the recent DAWN mission have further affirmed the Vesta-HED meteorites connection. Laboratory studies of HED meteorites are thus most valuable in learning about the evolution of Vesta, the only intact surviving planetesimal in the solar system. Oxygen isotopic composition of HEDs suggests that Vesta precursors are most likely made of 78 % H chondritic and 22 % CV chondritic matter. From a mass balance using average N contents of H and CV it is apriori expected that Vesta should have about $\sim$19 ppm N with a δ^{15}N of -27 ‰, assuming a homogenized object. Partial N loss due to magma ocean degassing and loss due to low gravity of Vesta, and partitioning of N between silicate (mantle) and metal (core) will modify both the N content and its isotopic signature in the silicate part of Vesta.

In addition, later impacts would certainly leave material on the surface that will admix with the ‘Vesta’ material, modifying the N contents and the δ^{15}N. We have analysed a set of HEDs to infer the N systematic of Vesta. The measured N in HEDs is a mixture of indigenous N, cosmogenic N and the components contributed by the impactors. Using the simultaneously measured cosmogenic Ne or Ar we have corrected for the cosmogenic N contribution and obtain the δ^{15}N, that is a mixture of indigenous N with contribution from impactor(s). Ni abundance in a HED meteorite serves as a good proxy for impactor contribution. From our N data and Ni/Al from literature, using the plot of δ^{15}N vs. Ni/Al (Figure 3) we infer at least three N components. An indigenous N of HEDs (and hence that of Vesta) with a δ^{15}N $=\sim$ 30±10 ‰, is admixed with 2 lighter N components from impactors.

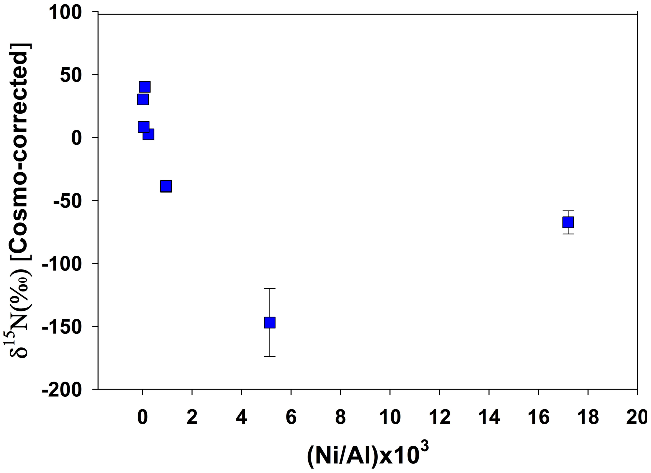

Figure 3: The cosmogenic corrected δ^{15}N for each meteorite is plotted against the corresponding elemental ratio (Ni/Al) (taken from literature) to resolve the N components

(S.V.S. Murty, S. Managave)

Noble gas study in Santa Lucia (2008) (L6) chondrite, a recent fall from Argentina.

Santa Lucia (2008), one the most recent falls from San Juan province of Argentina, on 23 Jan. 2008. We studied noble gases and nitrogen isotopes with the objectives to get cosmic ray exposure age, as well as to look for trapped gas components. Isotopic measurement was done in 78 mg specimen using Multi-Collector Noble Gas mass spectrometer (Noblesse) facility at Thaltej campus with gases extracted in stepwise heating method in resistance furnace. Noble gas isotopes indicate that neon (Ne) is purely cosmogenic while all other noble gasses are a mixture of cosmogenic, radiogenic and trapped components. Solar wind gases are absent. Excesses over spallation production are clearly seen at ^{82}Kr due to (n, γ) reactions on ^{80}Br, implying large pre-atmospheric meteoroid (Fig 4). The cosmic ray exposure (CRE) ages obtained using ^{3}He$_{c}$, ^{21}Ne$_{c}$ and ^{38}Ar$_{c}$ are T_3 = 18, T_{21} = 24 and T_{38} = 17 Ma respectively. The average CRE age obtained from ^{3}He$_{c}$, ^{21}Ne$_{c}$ and ^{38}Ar$_{c}$ is 20 Ma for Santa Lucia (2008). This CRE age, 20 Ma is consistent with the central peak of CRE age distribution of L chondrites. The radiogenic K-Ar age of 2.96 Ga, while the young U, Th-He are of 1.2 Ga indicates that Santa Lucia (2008) lost radiogenic ^{4}He more recently. Low cosmogenic (^{22}Ne/^{21}Ne)$_{c}$ and absence of solar wind noble gases are consistent with irradiation in a large body. Heavy noble gases (Ar/Kr/Xe) indicated trapped gases similar to ordinary chondrites. The elemental ratios ^{36}Ar/^{132}Xe = 67 and ^{84}Kr/^{132}Xe = 0.73 also indicates the presence of Q type trapped component. The nitrogen content in Santa Lucia (2008) is 0.9 ppm is within the range of ordinary chondrites with δ^{15}N = 17 ‰. We obtain the trapped nitrogen signature is δ^{15}N = 8.1 ‰similar to other ordinary chondrites.

This work is done in collaboration with Dr. M. E. Varela of ICATE-CONICET, Argentina and J. L. Joron of IPG Paris France.

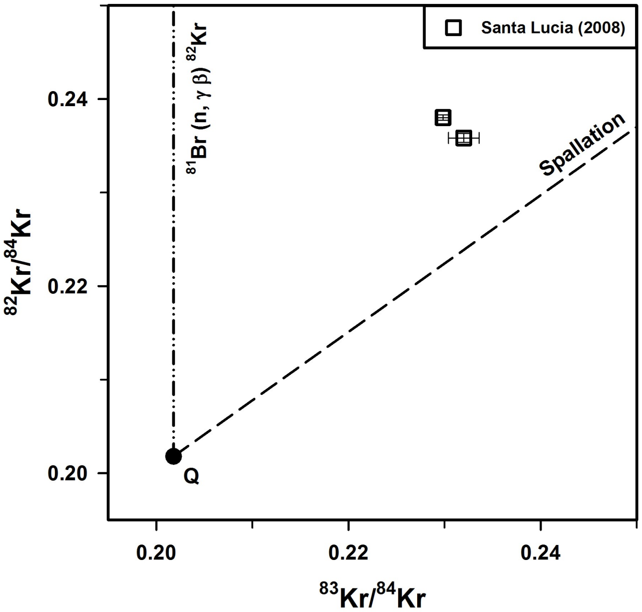

Figure 4: Plot of ^{82}Kr/^{84}Kr vs ^{83}Kr/^{84}Kr in Santa Lucia chondrite

(R. R. Mahajan)

Olivine-hosted melt-inclusions in Martian meteorite Tissint

One of the key geochemical findings about the bulk interior of Mars was the polybaric two-stage mantle melting and subsequent differentiation to generate the parent magma of the incompatible trace-element depleted Martian basalts. Using REE data of melt-inclusions in Tissint, a depleted Martian meteorite of type shergottite, the generation of parent magma of the shergottites from the depleted Martian mantle (DMM) and the subsequent fractionation and enrichment were quantitatively modelled.

Megacrystic olivines contain sparsely occurred melt-inclusions. Two types of melt-inclusions in Tissint are distinguished. Type-I melt-inclusions are sub-rounded with 40-80 m in largest diameter and occur in the olivine core (Fo$_{76-70}$). Type-II melt-inclusions are mostly rounded with $\leq$30 m in largest diameter and occur at Fo$_{62-55}$ of the host olivine. A trend of decreasing Mg# and increasing Si-, Al- and alkali-contents were observed from the Type-I to Type-II melt-inclusions. The calculated bulk compositions of the melt-inclusions are more magnesian than the melts in-equilibrium with host olivines, which indicates significant post-entrapment re-equilibration of Fe (and Mg) with the host olivine. It has been estimated that the true parent magma of Tissint required an extra 22 wt % olivine-addition to the bulk composition. Trace-element analyses were done on exposed surface of the melt-inclusions. REE-plot indicates Type-I melt-inclusions are most depleted in comparison to the Type-II melt-inclusions (Figure 5). The absolute REE content in Type-II melt-inclusions displays parallel trend but somewhat lower value in comparison to the Tissint whole rock. The light REEs (e.g., La to Nd) in Type-I melt-inclusions are an order of magnitude depleted compared to that in Type-II and the whole-rock.

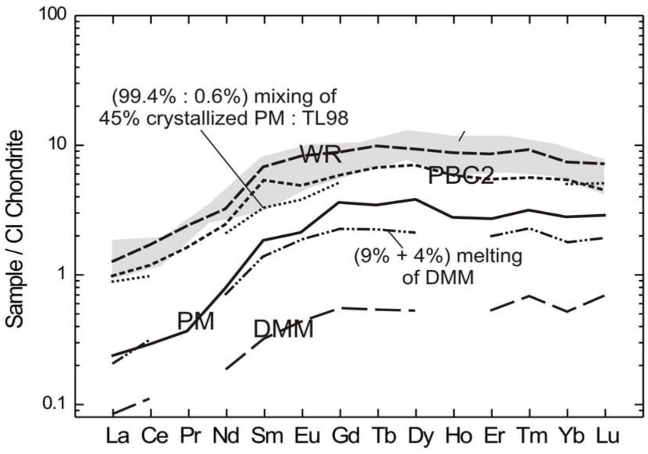

Figure 5: CI-normalized REE patterns of average Type-I (PM), Type-II (PBC2), whole rock (WR), and depleted Martian mantle (DMM). Calculated 2-stage melting of DMM, and mixing melt of PM with residual trapped melt (TL98)

The enrichment of Al, Ca, Na, P and REE contents in the whole-rock of Tissint may indicate the effect of crustal assimilation or magma mixing processes during the late-stages of crystallization of primary Mg-rich phases. The REE-enrichment was 3-5 times for LREE (La-Sm), 2-3 times for MREE (Eu-Er) and 1-2 times for HREE (Tm-Lu) from Type-I to Type-II melt-inclusions. The difference in REE content between the Type-I and Type-II melt-inclusions demonstrates a large range (20-80 %) of crystallization.

Model calculation indicates 0.1-2 % mixing of the enriched crustal and trapped melt components was required to reproduce the Type-2 melt-inclusions, and whole rocks of Tissint and LREE of QUE 94201 compositions (Figure 5). This calculation suggests that the enrichment during the Type-II to the later stages did reset the whole-rock trace-element budget in Tissint, since the incompatible trace-elements can enhance their content in the bulk sample via carrier phases of very low modal abundances, which is insensitive to the mass balance. This study indicates the presence of Al, Ca, Na, P and REE- rich layer at the shallower upper mantle above the depleted mantle source region during the geologic evolution of Mars.

This work was carried out in collaborations with E.V.S.S.K. Babu and T. Vijaya Kumar of National Geophysical Research Institute, Hyderabad.

(A. B. Sarbadhikari)

Lohawat howardite: Carbonaceous chondrite impactors and re-equilibrated components

The Lohawat achondrite, fell at Rajasthan, India on October 30, 1994, was recognized as a polymict breccia howardite, a mixture of eucrite and diogenites clasts and loosely bound regolith materials. Small chondrules were reported to be present in the regolith. We present here detailed mineral and bulk chemistry, nitrogen and noble gas composition of its separated minerals, fine matrix and different clasts. Mounted grains and separates were chemically characterized using EPMA. Trace element analyses were performed using ICP-MS. Noble gas and nitrogen isotope analysis was done using 'Noblesse' (Nu Instruments) multi-collector noble gas mass spectrometer.

Pyroxene shows a wide range of compositions in all the different type of clasts. The diogenitic pyroxenes are predominantly high-Mg orthopyroxenes. In the eucritic clasts pyroxenes are finer grained and show exsolution lamellae. Both exsolution of clinopyroxene in orthopyroxene host and the vice versa are observed. In Ca-Mg-Fe compositional space eucritic pyroxenes are plotted as main-group and Mg-rich cumulate eucrite (Figure 6).

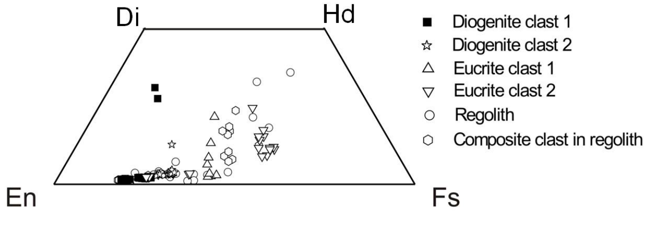

Figure 6: Pyroxene quadrilateral diagram displays pyroxene compositional range of different clasts and regolithic components of Lohawat

In regolith, pyroxene composition has the widest range, which implies that matrix regolith materials are pulverized mixture of different components. Equilibration temperatures are 940$\pm$30 ^{o}C for main-group type eucrite clasts and 830 $\pm$ 30 ^{o}C for cumulate eucrite clasts. Partially or fully melted impact spherules are present in the matrix. REE abundance in separated diogenitic and regolith clasts, melt spherules and bulk sample indicates highly depleted nature of the diogenitic clasts. REE trend in the regolith is almost parallel and similar with the diogenitic clasts except the LREEs, indicating regolithic clasts have mostly been contributed from the diogenites. The glassy spherules are the most enriched in REEs and show a relatively large negative Eu-anomaly. High REE abundance of the melt spherules is similar to that of the eucrites, indicating low-T eucrite clasts were transformed to the melt spherules. Various degree of thermal metamorphism of the eucrite clasts indicates re-equilibration prior to their emplacement on the surface and before becoming part of the Lohawat howardite. Presence of diogenitic, cumulate and basaltic eucrite materials in the Lohawat mass indicates a large degree of reworking took place on the Vestan surface.

Study of the noble gases and nitrogen isotopes indicates that planetary type (Ne-HL) and solar wind (Ne-SW) trapped gases are present in several separated grains of Lohawat (Figure 7).

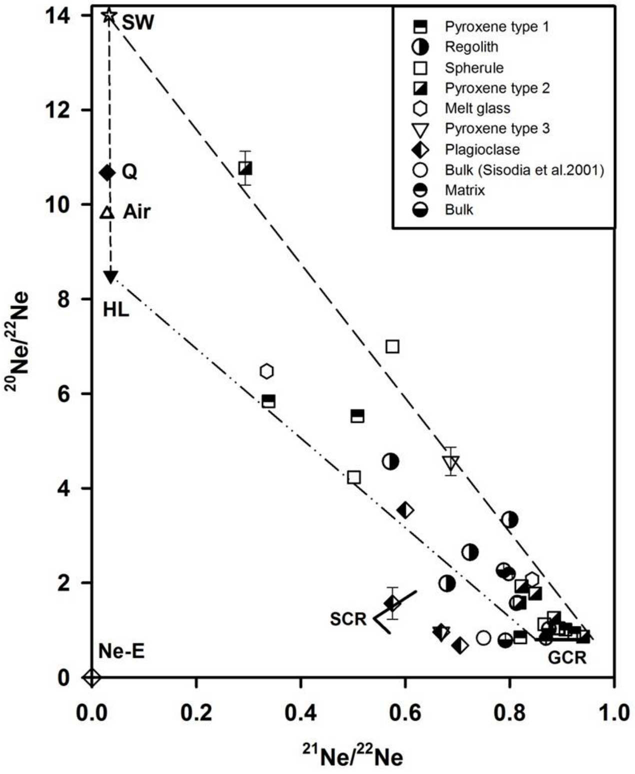

Figure 7: Three isotope plot of ^{20}Ne/^{22}Ne versus ^{21}Ne/^{22}Ne for Lohawat

Presence of solar wind in separated grains indicates their residence on surface of Vesta top layer in the regolith. Few grains have Ne-HL component signifying retention of primordial noble gases in them. The SCR effect in some of the grains also supports their residence within the uppermost layers of regolith. Argon is a mixture of radiogenic, cosmogenic and trapped components. The ^{40}K-^{40}Ar age, calculated in few grains, is unrealistically higher than the solar system age. This calculated higher age is because of excess ^{40}Ar present in these grains. ^{40}Ar present in much larger quantities is attributed to in-situ decay of ^{40}K. The excess ^{40}Ar is construed as radiogenic but is called 'parent-less' as it is removed from its parent. It is inferred that this parent-less argon has probably been derived during the melting of chondritic impactor and gets implanted in the grains. The average cosmic ray exposure age of grains using ^{21}Ne$_c$ and ^{38}Ar$_c$ ranges from 25 to 224 Ma. The variability in exposure ages of grains is because of the fact that different clastic and regolithic components of Lohawat suffered different duration of exposure to cosmic rays depending on their residence time as well as depth in the regolith. The nitrogen in bulk measurement of Lohawat is 0.74 ppm and δ^{15}N is 38.8 ‰, while after correcting the nitrogen for cosmogenic effects we obtain the trapped nitrogen as δ^{15}N$_{tr}$ = -97 ‰which is lighter than indigenous nitrogen. This nitrogen signature is due to mixing of indigenous nitrogen of Vesta, solar wind and impactor. It is important to note that few grains show heavy nitrogen composition that must have been derived from the impactor. Carbonaceous chondrite type of impactor is inferred from simultaneous nitrogen and noble gas study. Perhaps the chondrite components were mixed in the pulverized matrix regoliths or in the melt spherules.

This work was carried out in collaborations with J. Misquita and M. Shyam Prasad of National Institute of Oceanography, CSIR, Dona Paula, Goa.

(A. B. Sarbadhikari, R. R. Mahajan, M. S. Sisodia, N. Bhandari)

Fall, Petrology, Noble gas isotopes and Cosmogenic records of Komar Gaon meteorite - the latest fall in India

Komar Gaon meteorite fell (26°56' 98"N, 93°46' 11"E) during the daylight (12:00 pm IST) on November 13, 2015 in Komar Gaon of Golaghat district of Assam, India. The single piece of stone has a mass of ~12 kg and the local villagers witnessed the trail and subsequently observed its impact on a well ploughed field forming a 45 cm diameter by 90 cm deep hole.

Morphological signatures of atmospheric flight are well documented in view of development of at least three generation of fusion crusts identifiable with various colour and morphology (Figure 8). Well developed regmaglypts and distinct flow lines are also present and enable to identify the front and rear side of the meteorite during its fall through Earths atmosphere. The light grey matrix is highly recrystallised and studded with disseminated sulphide-metal specs make hard to recognize any distinct chondrule outline. Under BSE, a very few chondrules (both PO chondrule and BO chondrule, Figure 9) were identified in transparent coarsely recrystallised aggregate of mainly olivine (Fa: 24.9±0.68), low-Ca pyroxene (Fs: 21.14±0.4), Fe-Ni metal (Taenite and Kamacite) and troilite. Other minor and accessory mineral phases include high-Ca pyroxene (Wo:44±0.7, En:48±0.58, Fs:8±0.85), chromite (Cr_2O_3:53-56 wt %; FeO$_t$:29-31 wt %) and merrilite (CaO:50-52 wt %; P_2O_5:40-42 wt %). Locally, the shock veins (sometimes interconnected) are also present. Large secondary plagioclase ($>$60 μm), along with homogeneous silicate mineral composition suggest extreme thermal metamorphism (temp ~710°C based on olivine-chromite geothermometry) that corresponds to type 6. Planar fracture and significant presence of irregular fracturing of olivine and pyroxene grains are the most diagnostic shock features (Shock stage attained at least S3).

Simultaneous measurements of noble gases and nitrogen were carried out from the same aliquot of sample (~331 mg) by step heating using "Noblesse" multicollector Noble gas Mass Spectrometer with an aim to calculate the cosmic ray exposure age (CREA), and also look for the trapped gas components. Ne is purely cosmogenic while all other noble gasses are a mixture of cosmogenic, radiogenic and trapped components. The CREA as obtained from ^{3}He$_c$, ^{21}Ne$_c$, ^{38}Ar$_c$, ^{83}Kr$_c$, and ^{126}Xe$_c$ are T_3 = 4.8, T_{21} = 7.1, T_{38} = 6.8, T_{84} = 7.1 and T_{126} = 7.1 Ma. The average CREA for Komar Gaon is estimated as 7.0 Ma, excluding T_3 and also suggests this chondrite belongs to one of the peak in CRE age distribution of L chondrites. Lower T_3 is understood due to loss of gas.

The radiogenic K-Ar age of 684 Ma, while the young U,Th-He are of 160 Ma further confirms the gas loss. Heavy noble gases (Ar/Kr/Xe) indicate Q type trapped gases. The elemental ratios for ^{36}Ar/^{132}Xe and ^{84}Kr/^{132}Xe yielded the values 91 and 1.52 respectively. Isotopic composition of Kr with the presence of Q-type trapped gases is shown in Figure 10. The nitrogen concentration is 0.9 ppm and δ^{15}N = 18 ‰are well within the range for ordinary chondrites. We measured cosmogenic radionuclides (^{7}Be, ^{26}Al, ^{22}Na, ^{54}Mn and ^{57}Co) in a 200 g fragment of Komar Gaon meteorite using a 148 cm^3 volume ultra low background, high purity germanium gamma ray spectrometer housed in a 10 cm thick lead shield.

The estimated activities for shorter half life radionuclides are a bit lower, but appear consistent with the expected behavior of galactic cosmic ray modulation due to solar activity as this meteorite fell just after the maxima of current solar cycle. Interestingly the activities are comparable to the Bhawad LL6 chondrite, which fell near the maxima of solar cycle 23. The absence of ^{60}Co radionuclide indicate that the preatmospheric size of the Komar Gaon may not be large and further suggest that pre-atmospheric size of Komar Gaon is small and consistent with low thermal neutron flux and low shielding depth and also causes the low ^{26}Al activity.

Komar Gaon is a highly equilibrated chondrite and is classified as L6, S3 (based on petrography, olivine composition and microstructure). Temperature of thermal metamorphism is calibrated nearly 700°C. Melt veins are absent, however evidence of incipient shock veins suggest local scale disequilibrium melting.

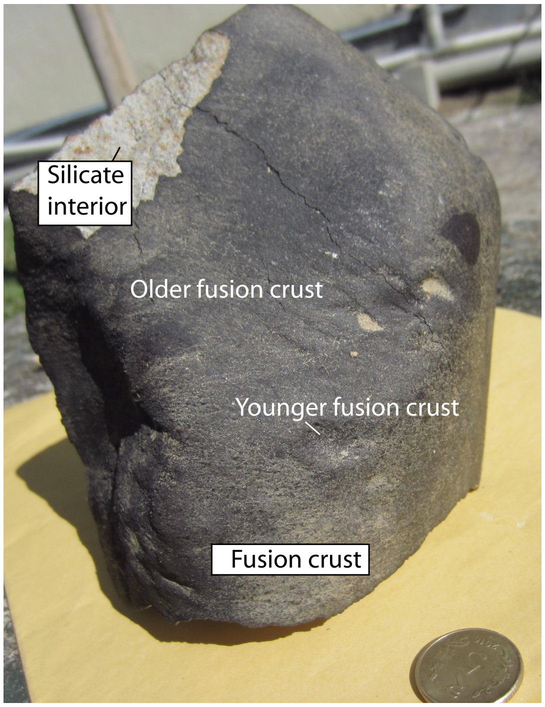

Figure 8:Hand Specimen of Komar Gaon meteorite with outer fusion crust and silicate interior

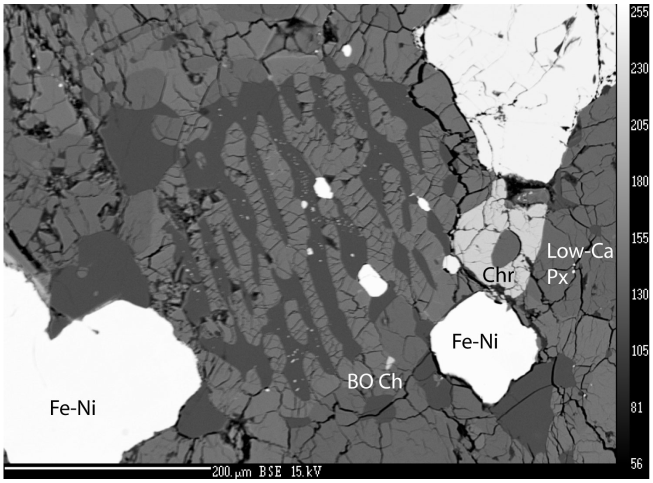

Figure 9: BSE image of Barred Olivine (BO) chondrule

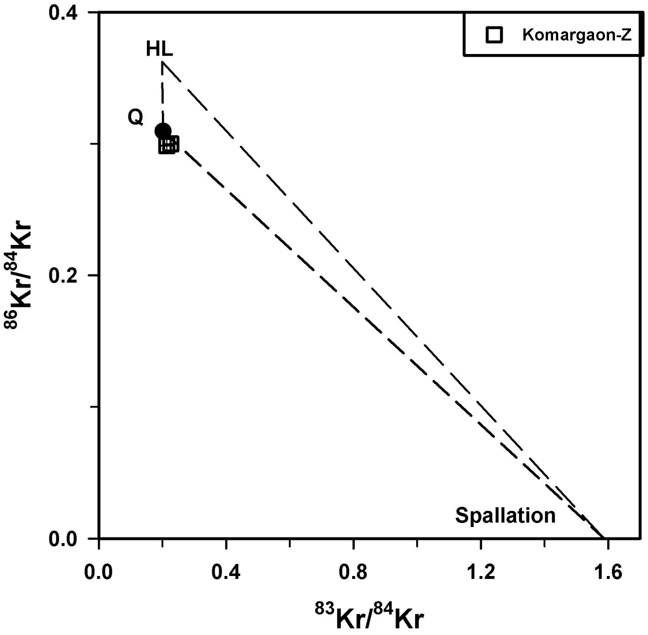

Figure 10: Krypton three isotope plot for Komar Gaon chondrite

(D. Ray, R. R. Mahajan, A. D. Shukla)

Remote Sensing Data Analysis

Mineralogy of Lowell crater region on the Moon

Lowell crater region has been established as one of the most promising site on the Moon for future lunar exploration on the basis of detailed geomorphological investigations (Srivastava et al., 2013; Gupta et al., 2014; Srivastava & Varatharajan, 2015). In this study, spectral diversity of the Lowell crater region has been worked out in detail using M^3 data from Chandrayaan-1. It has been found that the MNF based FCC captures spectral variability in a much efficient way compared to the popularly used schemes. The Lowell target constitutes of massifs of anorthosites (un-shocked/shocked/Mg-spinel bearing), Lacus Veris basalts and mature soils. The crater wall is largely noritic with intermittent anorthositic and Mg-spinel rich areas. The crater floor is mostly occupied with gabbroic melts and the surface irregularities show distinct clinopyroxene signatures. A part of the proximal ejecta in the NW and NE also shows presence of clinopyroxene. The central peak shows distinct compositional asymmetry (Figure 11).

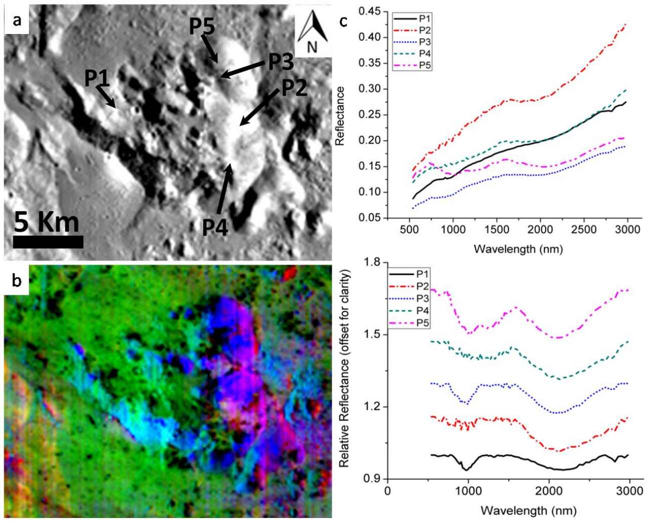

Figure 11: a) A blown-up view of the central peak from 750 nm M^3 data showing sites for which spectra have been plotted in ‘c’; b) Corresponding MNF based FCC showing compositional W-E asymmetry. Here, gabbroic/basaltic occur as green/black, noritic areas as blue and various types of anorthosites occur as magenta and red; c: Reflectance spectra for selected locations on the central peak depicting compositional diversity. Here, P5 corresponds to the olivine rich boulders.

The lithology on the West is gabbroic whereas on the East, mostly coinciding with the slumped zone, they are largely noritic and Mg-spinel bearing. A few zones of olivine rich boulders are present on the central peak that possibly represents exposures of undifferentiated mantle of the Moon, as predicted earlier by our group. These observations from the Lowell crater indicate that the Lowell impact event would have exhumed stratigraphically uplifted mantle rocks, excavated a deep seated gabbroic pluton and Orientale ejecta of anorthositic - noritic composition.

(N. Srivastava)

Evidence of subsurface ice in Zephyria Planum region

Using the Shallow Radar (SHARAD) on Mars Reconnaissance Orbiter (MRO), we have detected significant subsurface reflections in the Zephyria Planum region (1° N; 154.5° E). Earlier, images taken from the Mars Express spacecraft of the nearby Elysium Planitia region showed that there is presence of ash covered with water ice. Our recent SHARAD based finding of subsurface reflectors in this region further strengthen the previous observations and hence extend the observations by providing an indication that there are hydrous elements deposited in the subsurface of Zephyria Planum. We have analyzed the SHARAD radargrams of this region and we found the presence of substantial amounts of ice preserved in the subsurface. On the basis of morphology and slope formation, we hypothesize that most of the sinuous ridges in the Zephyria Planum region is likely formed by aqueous surficial flow. The subsurface reflections are diffused in nature thereby indicating that the upper few hundred meters of the Zephyria Planum is highly porous. As a radar wave travels through a deposit, the power is lost through attenuation and scattering, resulting in weaker subsurface echo; similar to what we observe in the NPLD basal region. A real permittivity value of 3.15 produces a depth profile (Figure 12) with flat and oriented towards the southern region, which further substantiates that the subsurface material permittivity is same as that of ice. In summary, we infer that the material preserved beneath the Zephyria Planum region is composed of pure ice.

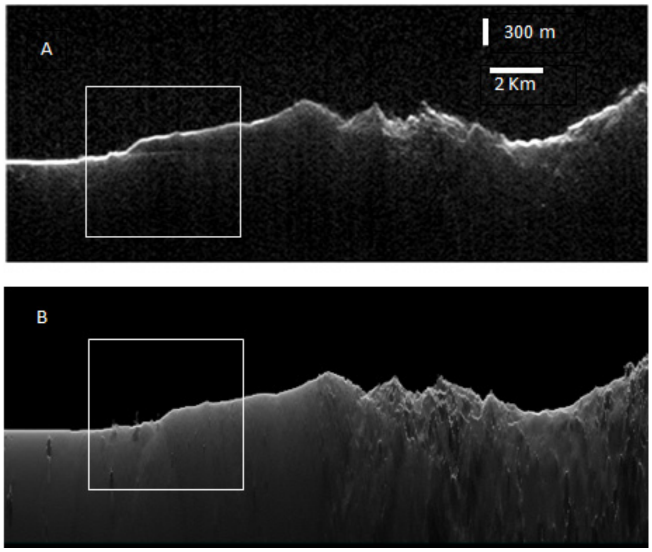

Figure 12: SHARAD radar observation 0505401 crossing Zephyria Planum. (a) Depth corrected radargram with bright subsurface reflection in square box. (b) Clutter simulation showing echoes resulting only from surface topography.

(R. R. Bharti, R. K. Sinha, S. Vijayan)

Evidence for extensive debris-covered glaciation and preservation of Late Amazonian ice in the Tanaica Montes region of Mars

The morphological resemblance of lobate debris apron/lineated valley fill (LDA/LVF) landforms to terrestrial debris-covered glacial landsystems has improved our understanding of the nature of Late Amazonian climate. Therefore, finding another region on Mars that has been previously unidentified for preserving LDA/LVF landforms and then detecting ice beneath these landforms will definitely advance our understanding of Martian paleoclimate and is crucial for assessing ice-related interactions over Mars’ Late Amazonian history. In this study, we have discovered a new region (Tanaica Montes; 39.55 N, 269.17 E) spanning over $\sim$150 $\times$ 200 km^2, wherein extensive glacial deposits similar to LDA/LVF have been observed. From our observations and analysis, we report (1) typical down-gradient flow of ice-debris mixture resulting from accumulation-ablation of ice over the Montes flanks that merge in the downstream to form large piedmont lobe. (2) Significant presence of ring-mold craters over LDA/LVF. (3) The best-fit timing of glacial activity that formed LDA/LVF in the region is ∼0.1-1 Ga. (4) Interaction between craters' ejecta overtopping Montes with the LDA/LVF layers that resulted in formation of numerous sublimation tills in the region. (5) Evidence of buried ice beneath LDA/LVF surface as detected by SHARAD (depth ∼300 meters).

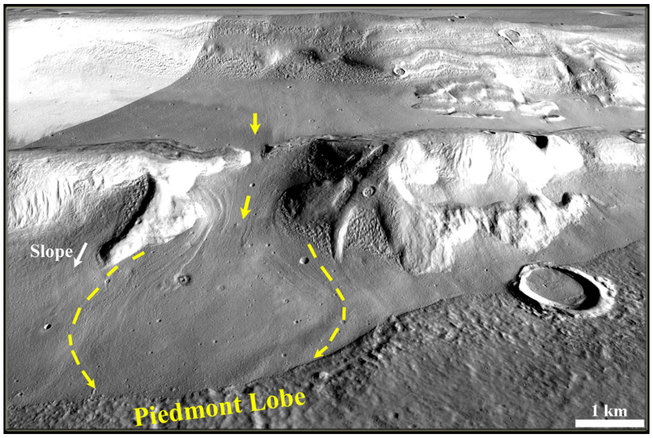

Figure 13: The figure depicts a distinct group of LFV flow lineations, which terminate downslope of the montes flanks in the form of expanded, large piedmont lobe.

We conclude that Tanaica Montes has been a region in the volcanic provinces of Mars that has preserved ice in the subsurface of LDA/LVF resulting from the debris-covered glaciation of an extensive glacial phase (∼0.1-1 Ga) during the Late Amazonian history of Mars.

(R. K. Sinha, S. Vijayan, R. R. Bharti)

Geomorphic evidence for moderate debris covered glaciation in Newton basin, Mars

Geomorphic evidence indicates that, as the regional glaciation transitioned from major-moderate-minor periods, glacial landforms of varying scales were emplaced in stratigraphy, such that the gully and polygonal features superpose the lobate debris-covered glaciers in the downstream, indicating temporal relationships. A change in the climate cycle has thus been interpreted that has influenced the nature and extent of ice accumulation and flow. In this study, we focused our geomorphic observation to Newton basin (40.50°S, 201.97°E; ∼300 km) to primarily demonstrate that the craters formed in the basin interior have preserved intriguing evidence for lobate flow features (LFF). Further, our observations and analysis signifies that (1) crater diameter has been a key factor in controlling the flow extent of LFFs; (2) the LFFs preserved in the interior of basin crater's are of moderate debris-covered glacial origin; (3) LFFs originate only from the pole-facing slope of the craters; and (4) the pattern of ice accumulation and flow in this region (i.e. the pole-facing preference) has not varied, at least for the past ∼100 Ma. Taken together, we conclude that the glacial period during which LFF was emplaced could be interpreted as an obvious episodic shift in the Late Amazonian glacial history that led to formation of these moderate scale glacial features within Newton basin.

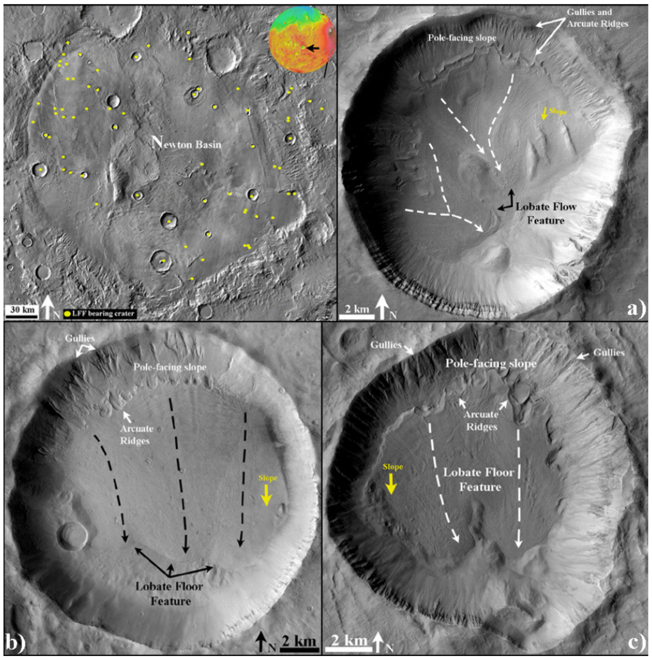

Figure 14: Regional survey of Newton basin for identification of LFF bearing craters in the region. The 'yellow circle' represents detection of a host crater in the interior of which we found LFF. Note the typical pole-facing orientation preference and integrated flow pattern displayed by each of the LFFs. Gullies and arcuate ridges formed in recent time-scales (past 10 Ma), with similar pole-facing orientation preferences, superpose LFF.

(R. K. Sinha, S. Vijayan)

Terrestrial Rock Glaciers are a Potential Analog for Lobate Flow Features (LFF) on Mars

Rock glaciers, regarded as cryospheric ice/water resource in the terrestrial-glacial systems based on their tongue/lobate-shaped flow characteristic and subsurface investigation using ground-penetrating radar.

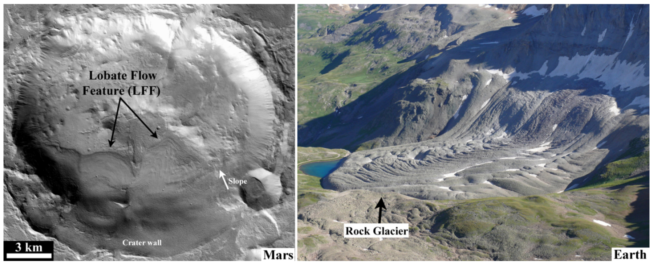

Figure 15: MRO CTX image of a crater with lobate flow feature (LFF) preserved in the interior. An example for ice-debris mixture flow on Earth. Note that as the ice-debris mixture slowly moved downslope, it is emplaced as a tongue shaped debris-covered rock glacier or as a lobate rock glacier at the foot of steep walls.

In this study, we have examined the subsurface, geomorphology, climate-sensitivity and thermophysical properties of a Lobate Flow Feature (LFF) on Mars (30°,60° N&S hemispheres) to compare/assess the potentials of rock glaciers as an analog in suggesting LFFs to be a source of subsurface ice/water. LFFs are generally observed at the foot of impact craters' wall. HiRISE/CTX imageries from MRO spacecraft were used for geomorphological investigation of LFF using ArcMap-10.0 and subsurface investigation was carried out using data from MRO-SHARAD (shallow radar) after integrating with SiesWare-8.0. ENVI-5.0 was used to retrieve thermophysical properties of LFF from nighttime datasets (12.57 μm) acquired by THEMIS instrument-onboard the Mars Odyssey spacecraft and derive LFFs morphometry from MOLA altimeter point tracks onboard MGS spacecraft. Integrating crater chronology tool (Craterstats) with Arc Map, we have derived the formation age of LFF. Our investigation and comparison of LFF to rock glaciers revealed: (1) LFFs have preserved ice at depth ∼50m as revealed from SHARAD radargram and top-layer composed of rocky-debris material with thermal inertia (∼300-350 $\mathrm{Jm}^{-2}\mathrm{K}^{-1}\mathrm{s}^{-1/2}$). (2) LFF formation age (∼10-100 Ma) corresponds to moderate scale debris covered glaciation of a shorter-span suggesting high sensitivity to obliquity-driven climatic shifts. (3) Presence of polygon cracks and high linear-arcuate furrow-and-ridges on the surface indicates presence of buried ice. This work is a significant step towards suggesting LFF to be a potential source of present-day stored ice/water on Mars.

(R. K. Sinha, S. Vijayan, R. R. Bharti)

Gullies in Ladakh, India: Potential Analogs for Martian Gullies

Ladakh Himalaya, being situated in the rain shadow zone of the Great Himalayan Range, is characterized by cold-arid desert landscape having rainfall <100 mm and low temperatures (below freezing point during winters).

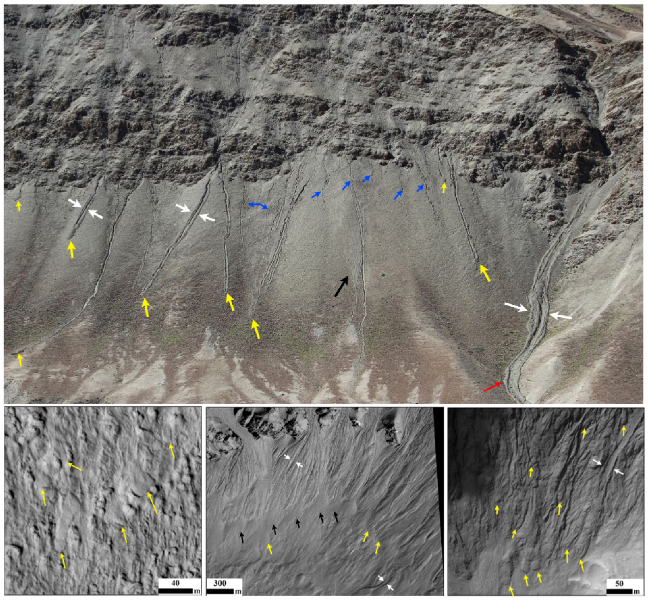

Figure 16: (Top) An example of gully system from Ladakh Range presenting debris flow lobe and gully-channel relationships. (Bottom) Example images of Martian gullies to represent features analogous to Ladakh gully. 'Yellow' arrows- individual lobate flow deposits with gully-channels formed through them; 'White' arrows- clearly defined leve deposits; 'Black' arrows- pre-existing gully fan crosscut by younger gullies; 'Blue' arrows- relatively fresh gully channels; 'Red' arrow- lobate deposits through the pre-existing gully.

There are multiple, episodic gullies and channels carved on the glacial and paraglacial sediments such as moraines, alluvial fan and debris flow. Despite being benefitted by the geographical location, its regional elevation (relative relief of 1000-2000 m, with few peaks >7000 m), and insolation conditions that elucidate well its contemporary arid to hyper-arid climate, Ladakh gullies, have not been assessed to explore their relative importance in understanding Martian gullies. In this study, we have carried out field investigation of morphology of terrestrial gully analogs from Ladakh Range to provide some insights on the origin of Martian gullies, using field data measurements, ground level photography, and orbital imagery. The noteworthy morphological element observed from field photographs was presence of lobate debris-flow deposits on the wall of cliffs flowing downslope from the top. We noticed that there were (i) individual lobate flow deposits; (ii) gully-channel through lobate deposits with clearly defined levée deposits; (iii) fresh gully-channel systems that flow individually and/or merge/superimpose with the pre-existing gullies; and (iv) lobate deposits through the pre-existing gully. From the orbital imagery (MRO HiRISE) of selected Martian gullies for comparison, we noticed several gullies associated with lobate debris-flow deposits. We believe that from our integrated field and orbital image investigations, Ladakh could emerge as a potential Earth-analog for understanding the key aspects involved in gully formation on Mars.

(R. K. Sinha, A. D. Shukla, S. Vijayan, F. Bhattacharya)

Reflectance spectroscopy of Planetary Analogues

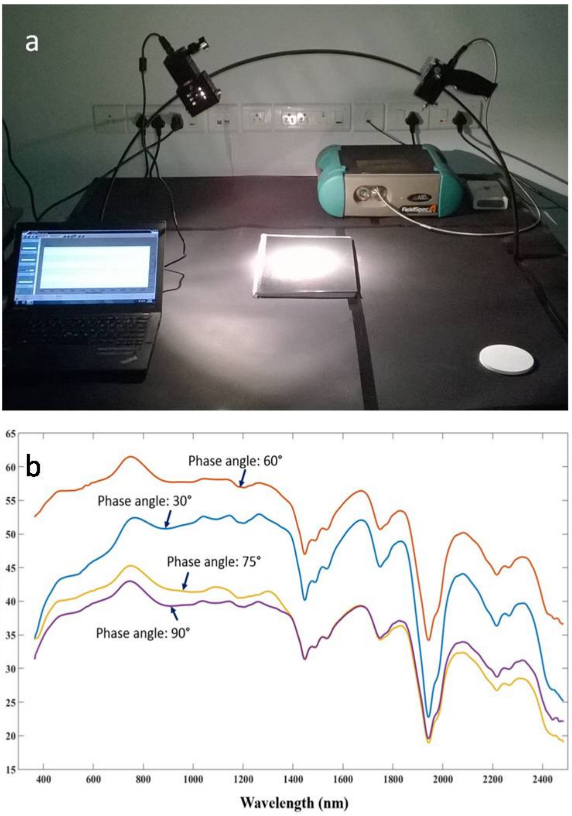

Figure 17: The experimental setup; b. The bidirectional reflectance spectra of a hydrous sulphate measured at various phase angles. The characteristic absorption features are centered at $\sim 1.75\mu, 2.2\mu and \sim 2.3\mu$

Remotely acquired spectral reflectance in the UVVISNIR region provides mineralogical information since minerals exhibit distinct spectral response as a function of their composition and crystal structure. Most planetary missions (for e.g. Chandrayaan -1 (2008), Dawn (2007), MRO (2005), Rosetta (2004)) carry reflectance spectrometers onboard for studies of mineralogical composition of planetary surfaces. However, interpreting them is a complex task since numerous parameters such as viewing geometry, grain size etc. influence composition dependent reflectance values. Therefore, it is imperative to carry out spectral reflectance studies of planetary samples and their analogues under simulated conditions in laboratory. In this study, we have carried out bi-directional reflectance measurements of analogues for Mars such as olivine samples, basalts and hydrous sulphate using recently acquired ASD Fieldspec 4 Hi-Res. A custom made in-plane goniometer has been realized for bidirectional measurements under varying viewing geometry (Figure 17).

(N. Srivastava)

Geomorphic characterisation of Late Hesperian Reuyl crater, Mars: Implications for episodic fluvial processes within crater

Despite numerous evidence of water related activity reported on Mars through the presence of valleys/channels, gullies, Recurring Slope Lineae and hydrous minerals, either inside craters or over plains, the quest for their source remains unresolved. Significant questions about the period over which the aqueous activity persisted was bracketed to Noachian epoch, however there are episodic localised activities and such localised post Noachian flows seek consistent explanation. In line to the history of fluvial activity, craters have played a key role in their initiation (groundwater/hydrothermal), as a sink (lacustrine) and often acted as a base for assessing the features (channel/fan, ridge/esker etc.) preserved over the floor/rims resulted from prevailing fluvial activities. Geomorphic analysis of the features preserved in the craters is one of the primordial importance, primarily for understanding the past environmental conditions. Reuyl, a ∼85 km diameter crater located (9.5°S, 167°E) west of Apollinaris Mons, has preserved diverse geomorphological features like delta/fans over its floor, central mound and layered ejecta. With these noteworthy features, the salient questions we are attempting to answer through this crater are characterisation of the fluvial process, the activity period and possible origin of source. Geomorphologic characterisation was carried out, using MRO-CTX/HiRISE images. The best-fit formation age of crater from crater counts is ∼3.5 Ga, suggesting Late Hesperian (LH). Our observations infer 1) numerous dendritic channels emerging from almost all sides of the wall that terminated over the floor with fans, 2) Some channels on the floor portray meandering ridges with high degree of sinuosity and delta associated at the termini, 3) Presence of desiccated polygons within the channelized zones suggests possible evidence for sustained aqueous activity, 4) The central peak, ∼2.8 km height is blanketed by layered deposits with overlying channels and 5) Multiple-layered ejecta with ground hugging flow could be possible due to subjected presence of subsurface volatile during crater formation. The existence of complex delta network on Reuyl implies that climatic condition during Hesperian epoch, within this crater, supported possible aqueous activity on localised scale.

(S. Vijayan, R. K. Sinha)

Thermophysical characteristics of selected sols from Mars Science Laboratory Curiosity rover measurements in Gale crater

On Mars, Thermal inertia (TI) estimation for any surface provides insights into their thermophysical characteristics and geological properties. In situ measured surface temperature, relative humidity, wind velocity and surface pressure from Rover Environmental Monitoring Station (REMS) of the Mars Science Laboratory (MSL) mission for ten sols were utilized to estimate the Surface Energy Budget (G) for Gale crater. A one-dimensional heat conduction equation was used to model subsurface temperatures and the heat flux (G*). Subsequently, 'TI' was derived by best fitting 'G' and 'G*'. Further, the KRC numerical thermal model was utilized to estimate the 'TI' for first order comparison. Selected sols were divided into four classes based on their surface texture, viz. sandy, rocky, rover track altered surface, and mixed (sandy and rocky) regions. The 'G' estimates reveal significant influence of seasons in terms of least surface forcing from winter season, and reaches maximum during summer. The mean 'TI' estimates for the sandy and rocky –regions are ∼230 and ∼478 Jm^{-2}K^{-1}s$^{-1/2}$, respectively. For rover track altered surfaces and mixed regions 'TI' estimates are ∼222 and ∼330 Jm^{-2}K^{-1}s$^{-1/2}$, respectively. Our 'TI' estimates provide physical basis to the corresponding MSL Navcam images and expands the relative importance of surface associated geological properties, previously predicted from orbiters at regional/global scales. Rover track altered surface portrays low albedo, with possibly disturbed thermal gradient having lowest estimated 'TI'. The high resolution insitu meteorological data measured by Curiosity REMS has allowed an in-depth thermophysical study of the Gale crater floor. This study brings out how the insitu measured temperature, their diurnal/seasonal variation and the derive TI can help us to understand the local scale thermophysical properties. This study brings out the need for detailed 'TI' estimation for the MSL sols to improve our understanding of the influence of prevailing physical and environmental conditions on the geological properties of the Gale crater.Thermal inertia provided a physical meaning to studied sols in context with rover optical images and agrees with the thermophysical nature of the area under study.

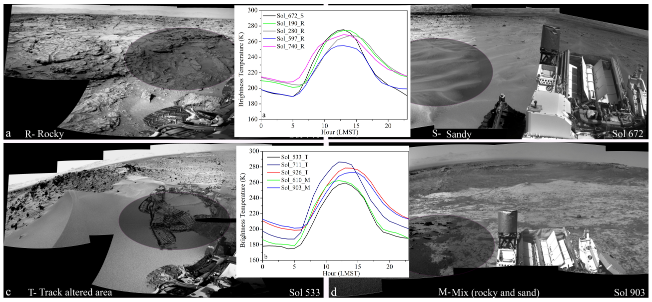

Figure 18: Thermophysical characteristics of selected sols from MSL curiosity in Gale crater

(S. Bose, S. Vijayan, R. K. Sinha, A. Sarkar, J. P. Pabari, D. Banerjee)

Geologic investigation of layered mound of Henry Crater, Mars: Implications for history of ancient hydrological activities in the region

Craters around the Schiaparelli Basin (∼460 km diameter; 2.71°S 16.77°E) on Mars are infilled with mound on their floors. These mounds have preserved intriguing layers in stratigraphy that has exposed pristine sets of geomorphic and geochemical signatures bearing strong implications towards understanding geological history of Mars. Detailed remote analysis of stratigraphy of layers exposed over Henry crater's (∼150 km diameter; 10.79°N 23.45°E; 500 km northeast of Schiaparelli Basin) mound (rising ∼2 km from floor) is carried out to infer the origin and episodes of geological events occurred in this region. Using crater counting technique the age of the topmost surface of the crater mound is found to be 3.64 billion years since the exposure of this strata post complete infilling.

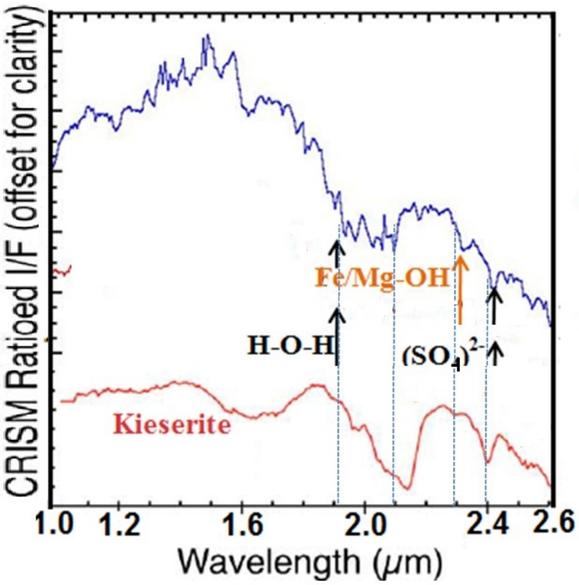

Figure 19: CRISM processed mineral spectra (blue) shows spectacular similarity with laboratory spectra (red) of hydrated sulphate Kieserite. Thermodynamically, kieserite is not stable in deposits that have experienced surface cycles of hydration and desiccation.

The stratigraphy of consistent and conformable layers in the crater interior acts as a proxy of the long-lived event of sediment deposition in a rather quiescent condition. Distinct layering can be traced across the crater from the mound to the crater wall across the floor. Using MRO HiRISE & CTX images, distinct spatial distribution of morphological features distributed in stratigraphy is observed that reveals the dominant geological agents behind their formation, viz. temporal hydrological and aeolian processes forming differential erosional structures across the basin. MRO CRISM based mineralogical investigation reveals diagnostic signature of the hydrated sulphate mineral Kieserite. Based on the thermodynamic properties of Kieserite and apparent lack of desiccation cracks in the scale of observation, it is inferred that the water level inside the crater did not experience fluctuation. Rather on systematic compilation of the mineralogical and morphological data, it is inferred that the mound formation process was gradual and can be correlated with the water level inside the crater at various stages during the recession stage.

(S. Sarkar, R. K. Sinha, S. Vijayan, D. Banerjee)

Payload Development and Instrumentation

Alpha Particle X-ray Spectrometer on-board Chandrayaan-2 Rover: The new configuration

Alpha Particle X-ray Spectrometer (APXS) is one of the instruments being developed at PRL to study the elemental composition of Lunar rock and soil onboard Chandrayaan-2 rover by irradiation the lunar surface with alpha particles and X-rays using radio-active alpha source. The working principle of APXS involves measuring the intensity of characteristic X-rays emitted from the sample due to Alpha Particle Induced X-ray Emission (PIXE) and X-ray florescence (XRF) processes using ^{241}Am alpha source which allows us to determine of elements from Na to Br, spanning the energy range of 0.9 to 16 keV. The electronics design of the APXS experiment has been completed and shown that the developed system provides energy resolution of ∼150 eV @ 5.9 keV which is comparable to off-the-shelf Silicon Drift Detector (SDD) based X-ray spectrometers. The developed system has been characterized for various other performance requirements such as energy resolution versus temperature, shaping time and count rate. XRF measurements were also carried out using Fe-55 X-ray source and measured XRF for various metal and rock samples. Our initial plan was to use Cm-244 alpha source which provides high specific activity due to shorter half life (18.1 years) compared to other alpha sources. Recently, the Russian company has agreed to provide the Cm-244 alpha source for our APXS experiment. We are also closely working with BARC, Mumbai for making the alternate alpha source Am-241 and its qualification for space use is in progress.

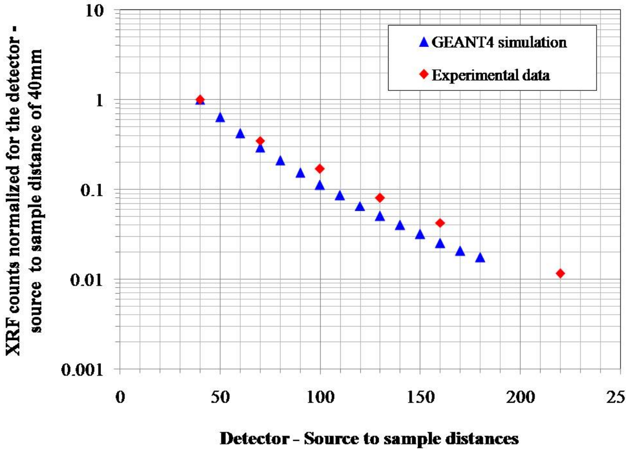

Figure 20: XRF signal measured for various detector - source to sample distances

In the earlier APXS configuration, the APXS instrument was mounted under the rover chassis in the front side of the rover at an height of 180 mm from the lunar surface. This was due to the mass and power constraints to implement the robotic arm to carry the APXS instrument close to the lunar surface. Mounting the APXS under rover chassis at an height of 180 mm requires several hours of integration time to acquire the desired data. The recent XRF measurements using Fe-55 X-ray sources suggest that the signal yield decreases to ∼2 orders of magnitude when the detector-source to sample distance is increased from 40 mm to 180 mm. This has been confirmed with GEANT4 simulation as shown in Figure 20. These results were presented in the payload review and the review committee suggested lowering the APXS payload closer to the lunar surface to reduce the integration time, and at the same time carry out multiple lunar sample measurements instead of being fixed in one location for longer durations. In view of this, it is decided to change the APXS configuration and lower the detector-source close to the lunar surface to get higher yield. The modified APXS mechanical configuration is as shown in Figure 21. In this configuration, APXS detector-source will be placed at an height of 50-70 mm from the lunar surface during the measurement. We are working towards completion of this new version of the APXS design and proceed with qualification and flight models.

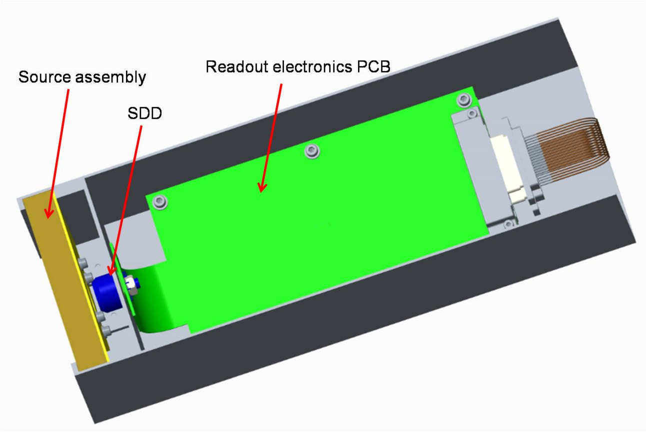

Figure 21: Mechanical design of the new APXS configuration

(M. Shanmugam, S. K. Goyal, A. Patel, T. Ladiya, S. V. S. Murty, S. V. Vadawale)

Solar X-ray Monitor for Chandrayaan-2 Orbiter

The Solar X-ray Monitor (XSM) is one of the instruments onboard Chandrayaan-2 orbiter designed to provide the real time solar X-ray spectrum input to the companion instrument Chandra's Large Area Soft X-ray Spectrometer (CLASS). The CLASS instrument is a large area X-ray spectrometer viewing moon from the orbiting satellite to detect the XRF from the lunar surface with wide field of view and this instrument is being developed at ISAC, Bangalore. Carrying out X-ray fluorescence spectroscopy from an orbiting satellite using Solar X-ray as exciting radiation provides possibility of generating global maps of individual elemental abundances though at relatively coarse spatial resolution. Since the flux of fluorescent X-ray lines critically depend on the flux and spectrum of the incident solar X-rays, it is essential to have simultaneous and accurate measurement of X-ray from both Moon and Sun. Thus a typical remote X-ray fluorescence experiment consists of two components, a Moon viewing X-ray detector to measure the fluorescent spectra and a Sun viewing X-ray detector to measure direct solar X-ray spectra. At PRL, we are involved in developing XSM payload for Chandrayaan-2 Orbiter.

XSM instrument is designed with two packages namely XSM sensor package and XSM processing electronics package. XSM sensor package consists of Silicon Drift Detector (SDD) coupled with front-end electronics for signal readout. This package also incorporates a stepper motor based moving mechanism to control the incident solar flux during the large class flares and also has provision for mounting calibration source for the instrument calibration. The XSM processing electronics consist of Field Programmable Gate Array (FPGA) based payload control and data acquisition system and the DC-DC converter for supplying the power to the XSM payload. The XSM front-end electronics is optimized to handle large count rates up to 100 k counts/s with reasonability good energy resolution. The front-end electronics is also has provision for counting the X-ray event rates more than 100 k counts/s. The overall size of the XSM sensor package is about 70 $\times$ 140 $\times$ 60 mm^3 with mass of 600 gm and the size of processing electronics is 130 x 130 x 45 mm^3 with mass of $\sim$900 gm. The engineering model of XSM instrument has been completed and tested for various performance characteristics and shown to meet the scientific requirements of the payload. The photographic view of XSM sensor package is shown in Figure 22 and the XSM processing electronics package is shown in Figure 23. The detailed instrument calibration is in progress. The qualification and flight model fabrication has been initiated.

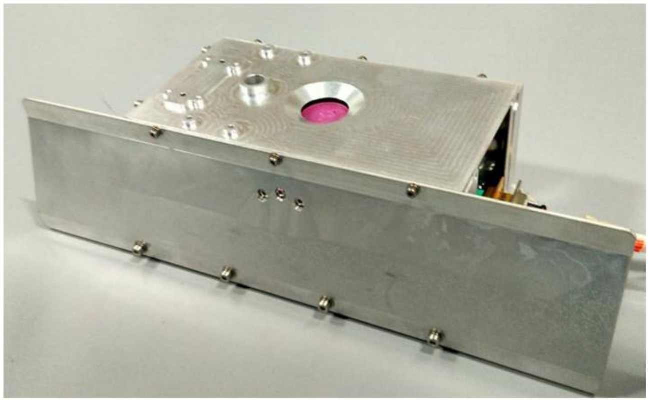

Figure 22: Photographic view of XSM sensor package

Figure 23: Photographic view of XSM processing electronics package, FPGA (left), DC-DC converter (right)

(M. Shanmugam, A. Patel, S. K. Goyal, T. Ladiya, S. V. Vadawale)

Prototype Development of Mars Orbit Dust Experiment (MODEX) for Mars-2 Orbiter

Recent observations of high altitude Martian dust from about 150 to 1000 km height from the surface by the LPW instrument on MAVEN mission has not been explained, and the source of such dust is not understood. To study origin, abundance, distribution and seasonal variation of Martian dust, a Mars Orbit Dust Experiment (MODEX) is proposed for future Mars orbiter.

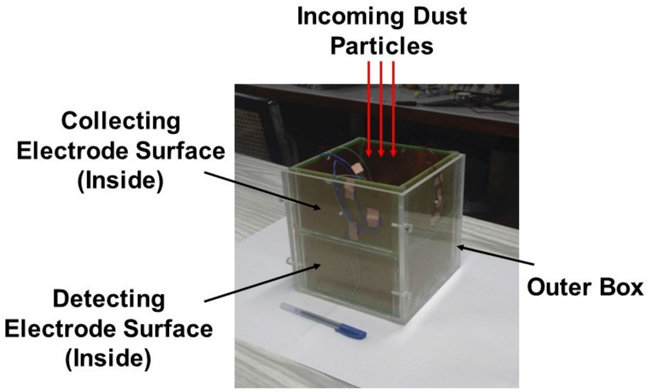

Figure 24: Snapshot of a prototype dust detector

The additional objective is to measure interplanetary dust particle (IDP) during cruise phase of MOM-2 for enhancing understanding of the dynamical evolution. A prototype design of impact ionization dust detector and its electronics have been initiated at PRL. The preliminary circuit of front end electronics has been designed, implemented and tested successfully.

Figure 24 show a snapshot of the prototype detector, while Figure 25 depicts the preliminary design blocks of the front end electronics of the MODEX prototype.

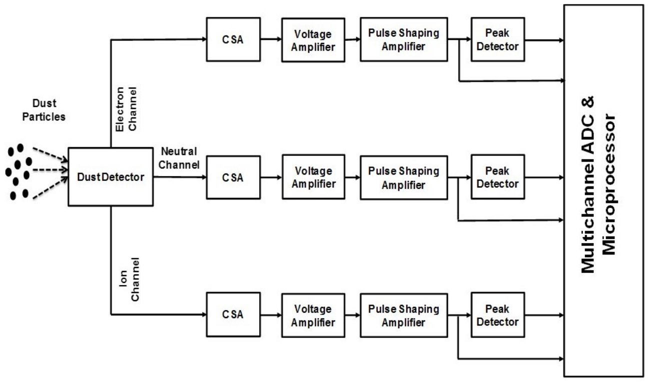

Figure 25: Preliminary design of front end electronics of the prototype dust detector

The ballistic limit in the hyper velocity event represents the thickness necessary for the target plate of the impact ionization dust detector. We have computed the ballistic limit for the gold target dust detector and the results are shown in Figure 26.

Since, the smaller dust particles travel faster while the bigger particles travel smaller, the ballistic limit for the detector may remain within a few mm range for the practical application. Further work in this direction is underway.

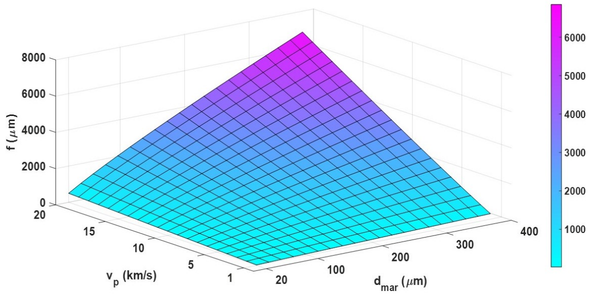

Figure 26: Ballistic limit for the hypervelocity event, representing the thickness needed for the detector target plate

(J. P. Pabari, D. K. Patel, A. Bogavelly)

Estimation of High Altitude Martian Dust Parameters

The study of high altitude Martian dust is found in literature for many years. Recently, dust has been detected at orbital altitudes by the MAVEN mission. However, the source of such dust is not understood. The mathematical modelling helps understand physical parameters and behavior of the Martian dust, beforehand. The estimation of high altitude Martian dust parameters has been carried out using the modelling. Figure 27 show the expected random velocity of dust particles around the Mars. The lifetime of dust particles around the Mars has been computed for the dust particles coming from the Phobos and Deimos, and the results are shown in Figure 28 and Figure 29, respectively. The results are summarized in Table 1. Further work in this direction is underway.

Table 1: High altitude Martian dust parameters

Parameter	Value
Size	10 to 200 μm
Mass	10^{-7} to 10^{-11} kg
Particle Random Velocity	1 to 17 km/s
Particle Number Density	10^{-3} to 10^{-6} #/m^3
Particle Lifetime	0.4 to 4500 years

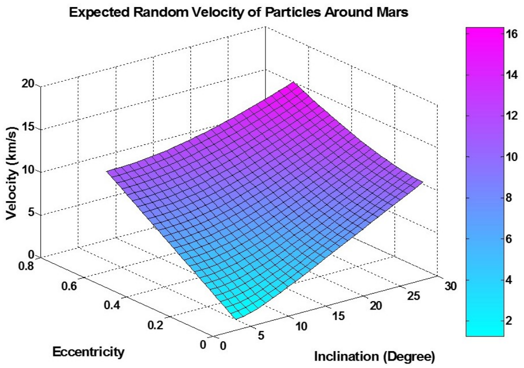

Figure 27: Expected random velocity of the dust particles around the Mars

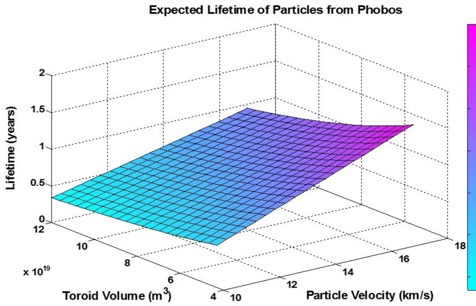

Figure 28: Expected lifetime of the dust particles coming from the Phobos and remaining around the Mars

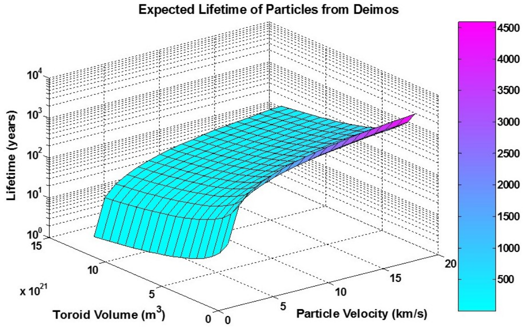

Figure 29: Expected lifetime of the dust particles coming from the Deimos and remaining around the Mars

(J. P. Pabari, P. J. Bhalodi)

Lunar Electrostatic and Dust Levitation Modeling

The surfaces of airless, non-magnetized bodies like the Moon are directly exposed to solar wind and ultraviolet radiation, causing surface dust grains to be electrically charged and levitated, whenever electric fields exceed the surface forces and gravity. For an improved understanding of the lunar dust environment, we have studied the surface charging processes using the electrostatic modelling. We apply Gauss's law to examine the dust levitation and compare the implications with those obtained using free-space capacitance of the particle. Calculating grain charge on surface by assuming its free-space capacitance is erroneous and is therefore inapplicable. The daytime surface potential during high solar activity is estimated to be $\sim$20 V, while the nighttime potential can be as high as –3.8 kV. The maximum radius of levitating particles is greatly affected by the method used to model the dust levitation. Using Gauss's approach, it comes out to be in the picometre range, where matter is usually found in the form of gas or molecule and it may be difficult to explain the dust levitation process. These results are in contrast to the existing calculations which estimate the grain radius to be in the nanometre to micrometer range. The LDEX provided no indication of 0.1 μm-sized particles near the terminator, as suggested previously from Apollo observations. This result is not inconsistent with our predictions based on Gauss's law. Hence, it still remains an open question whether dust levitation occurs on the Moon or not, and experiments are necessary on future lunar lander mission which provide direct measurement of surface potential and near-surface charged dust particles to confirm the same. A Moon Electrostatic Potential and Dust Analyzer (MESDA) may be used on future lunar lander to confirm the dust levitation process, and also to measure the lunar surface potential as well as dust particles near the lunar surface.

(J. P. Pabari, D. Banerjee)

Supra Thermal & Energetic Particle Spectrometer (STEPS) - Subsystem of ASPEX payload

Aditya Solar wind Particle EXperiment (ASPEX) is one of the scientific experiments onboard the Aditya - L1 mission, the first Indian solar mission. The primary scientific objective of the ASPEX experiment is to carry out in-situ, multi-directional measurements of solar wind ions in the energy range of 100 eV/n to 5 MeV/n. ASPEX instrument is configured with two subsystems namely Solar Wind Ion Spectrometer (SWIS) and Supra Thermal & Energetic Particle Spectrometer (STEPS). SWIS will measure the angular and energy distribution of solar wind ions in the energy range of 100 eV to 20 keV and STEPS will measure the energy spectrum of high energetic particles from six directions covering the energy range of 20 keV/n to 5 MeV/n. The scientific objective of the STEPS is to investigate the origin of the supra thermal particles and their relationship with the primary solar wind constituents by measuring the spectrum of protons, alpha and other heavier particles with a narrow conical field of view.

STEPS subsystem is configured into three packages: STEPS-1, STEPS-2 and processing electronics package. Breadboard model of the developed electronics is shown in Figure 30. Si PIN detector is procured from the Micron semiconductor. The CSPA is AC coupled amplifier with 2N4416 FET at the input followed by LM6172 operational amplifier.

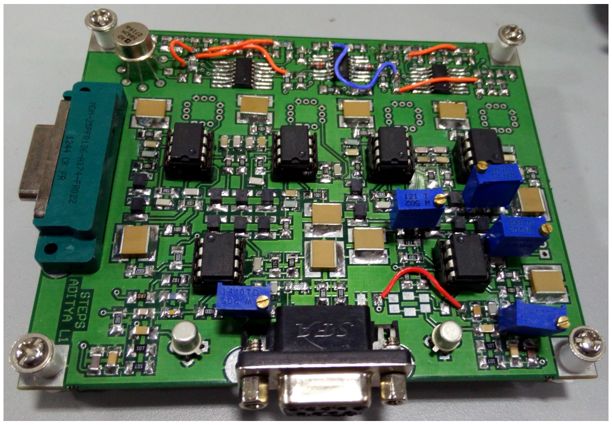

Figure 30: Front end electronics (PCB size 90 x 110 mm^2)

The output of CSPA is further amplified and shaped using shaping amplifier of 3 μs peaking time. The spectrum acquired using ^{241}Am and ^{109}Cd X-ray radioactive sources (Figure 31) shows that low energy threshold ($<$ 20 keV) is achieved using in-house developed electronics, which is essential for the STEPS subsystem.

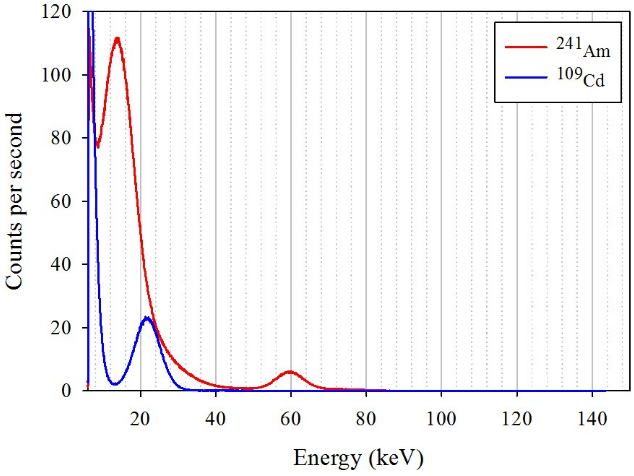

Figure 31: X-ray spectrum

Si Photomultiplier (SiPM) is procured from SensL. Active area of SiPM is 3 x 3 mm^2 with total package size of 4 x 4 mm^2. There are total 4774 pixels of 35 micron each. The dark count rate is 300 kHz. PCB for the array of SiPM is fabricated, which will be used for the photons readout from the plastic scintillator (BC408), shown in Figure 32, 33 and 34. STEPS processing electronics takes 9 parallel inputs from the silicon detectors and other 3 parallel inputs from the scintillator detectors. It controls the analog multiplexer for selection of the energy range, takes inputs of health parameters of the payload as well as interface with the BDH & TM/TC.

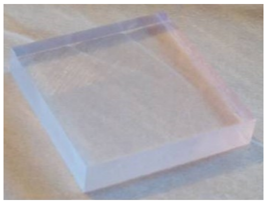

Figure 32: Plastic scintillator

Figure 33: Single SiPM

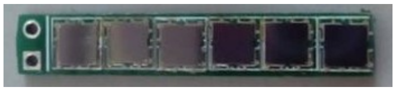

Figure 34: PCB for 1x6 array of SiPM (PCB size 28 x 5 mm^2)

The PCB fabricated for the STEPS processing electronics is shown in Figure 35. SAC, Ahmedabad is also involved in the development of certain aspects of the payload.

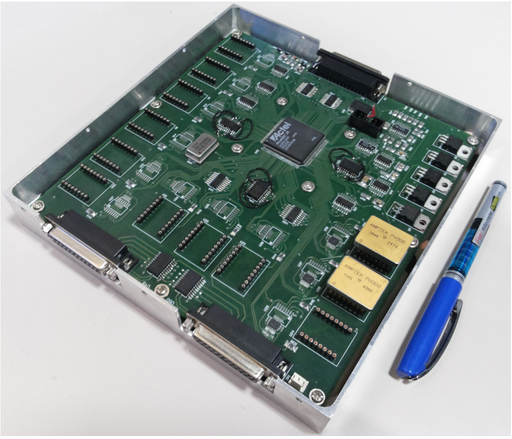

Figure 35: PCB for STEPS processing electronics (PCB size 220 x 220 mm^2)

(S. K. Goyal, M. Shanmugam, A. R. Patel, T. Ladiya, N. K. Tiwari, S. V. Vadawale, P. Janardhan, D. Chakrabarty, A. Sarkar)

Development of Gamma Ray Spectrometer (GRS) using HPGe detector for future Mars orbiter

One of the basic keys to an understanding of the formation and evolution of any planet is the knowledge of the elemental composition of its surface. Gamma spectroscopy on Mars orbiter provides a unique opportunity to measure the elemental composition of its surface, with an atmosphere thin enough to allow detection of gamma rays produced from the near surface rock and soil materials. We are developing a gamma ray spectrometer using High Purity Germanium (HPGe) detector for future Mars orbiter mission. The scientific objective of the instrument is to map the naturally occurring radioactive elements (Th, U, and K) and other major elements (Fe, Mg, Cl, Al, Si, S, Mg, Cl) over the entire Martian surface with a spatial resolution of better than 250 km. The gamma ray spectrometer will also have Anti - Coincidence Shield (ACS) detector for background subtraction from the surrounding material. GEANT4 simulation has been carried out to study the design requirements for a gamma ray spectrometer on a future Mars orbiter mission. This includes the selection of the size of HPGe detector, selection of the detector material and thickness for the ACS detector. We have chosen a 3 inch (diameter) x 3 inch (length) HPGe detector which will be covered with 0.5 inch thick Ge ACS from all sides except from the front side (Field of View side). The cooling of HPGe is planned using Ricor make cryo - cooler. This cooler will be thermally connected to the cold finger of HPGe detector. This is an active cooling mechanism and takes around 5 minutes to reach to 77 K temperature from the room temperature. The effect of Martian atmosphere on the transmission of gamma rays has also been simulated. Figure 36 shows the transmission efficiency plotted with the energy of gamma rays. This has been plotted with 8 different cases. It is clear from this plot that gamma rays are mostly attenuated in the top 20 km altitude. The transmission factors are 15 % at 0.5 MeV, 25 % at 1.0 MeV, and 59 % at 7.0 MeV.

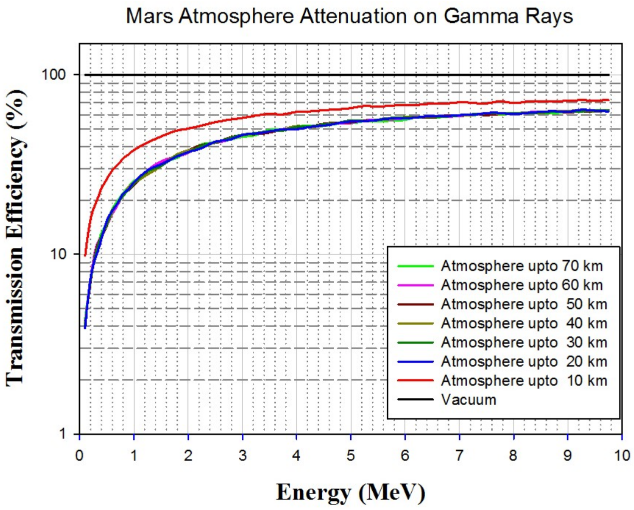

Figure 36: Transmission of gamma rays through the Martian atmosphere

We have procured off the shelf Germanium detector from M/s Canberra. It is a p type co-axial HPGe detector of 5 % efficiency (Figure 37). The crystal diameter is 44 mm, and the length is 30.8 mm. It is presently connected to a 30 ltr dewar for the cooling using LN_2. The output of the Charge Sensitive Pre-Amplifier (CSPA) is connected to the Ortec shaping amplifier. The peaking time of the Gaussian shaping amplifier is set to 2 μs. Uni-polar shaping output is given to the Ortec make Multi Channel Analyzer (MCA).

Figure 37: HPGe detector with 30 ltr LN_2 dewar

Figure 37 shows the Ge detector with LN_2 dewar and Figure 38 shows spectrum obtained using ^{22}Na radioactive source. FWHM obtained at 122 keV (^{57}Co) and 1.332 MeV (^{60}Co) energy lines are 0.8 keV and 1.7 keV respectively. These tests are done using commercially available electronics. We are in the phase of development of electronics for this detector. The Ricor make cryo-cooler has been procured and expected to be available soon.

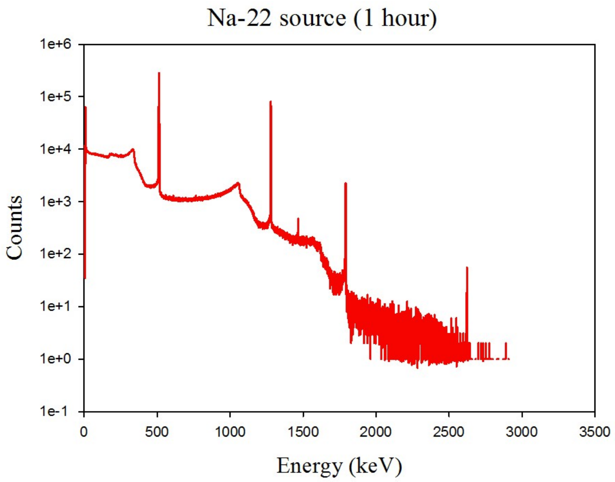

Figure 38: Spectrum using ^{22}Na radioactive source

(S. K. Goyal, D. Banerjee, D. K. Panda, A. R. Patel, T. Ladiya, S. Vadawale)

Development of $LaBr_3$:Ce and $CeBr_3$ for space applications

Elemental composition of a planetary surface can be deduced from in-situ measurements, remote sensing techniques, and by laboratory analysis of returned samples. Gamma ray and neutron spectroscopy comprise some of the basic tools for mapping of planetary surfaces. We are developing a gamma ray spectrometer (GRS) for future planetary orbiter missions for global mapping of U, Th, K, Fe and other major elements on moon and Mars, and the feasibility of using a $CeBr_3$ detector for measuring individual concentrations of ^{40}K, ^{238}U and ^{232}Th in laboratory samples using gamma ray spectra. This paper presents the development of GRS and results of calibration tests of the $LaBr_3$:Ce and $CeBr_3$ conducted using different radioactive sources.

We have previously developed a $LaBr_3$:Ce gamma ray spectrometer, and the energy resolution of the GRS developed using in-house front-end and processing electronics at 511 and 1274 keV is estimated to be 4.1% and 2.5 % respectively. Different individual subsystems including shaping amplifier, peak detection, analog to digital conversion and high voltage unit have been developed. The control signal for peak detector and ADC are being generated through FPGA program. Along with the FPGA, the processing electronics sub-system consists of a discriminator unit for synchronization of shaping pulses with digital acquisition, a reference generator unit for ADC, line drivers for the signal compatibility of FPGA and 13-bits parallel ADC. The ADC digitized data are readout using Data Acquisition Software developed in Labview. The intrinsic activity count-rate for our 3”× 3” $LaBr_3$:Ce gamma ray spectrometer was observed to be ~61 counts s^{-1} (~0.18 counts s^{-1} cm^{-3}) for the ^{40}K energy window (1400-1520 keV) and ~3.4 counts s^{-1} for the ^{232}Th (2550-2700 keV) energy window. Although this large intrinsic activity of the $LaBr_3$:Ce crystal inhibits estimation of the concentrations of Th and K, our attempts using a newly developed $CeBr_3$ gamma ray spectrometer were more successful. A 1 × 1 inch $CeBr_3$ crystal coupled with a 2 inch PMT was procured subsequently. The energy resolution for $CeBr_3$ detector connected with in-house electronics is observed to be ∼2.6 % at 1274 keV. The intrinsic activity count-rate for our $CeBr_3$ based GRS was observed to be significantly lower than $LaBr_3$:Ce and is ∼0.03 counts s^{-1} (0.002 counts s^{-1} cm^{-3}) for the ^{40}K energy window (1400-1520 keV), and ∼0.001 counts s^{-1} for the ^{232}Th (2550-2700 keV) energy window. The next experiments will involve estimation of Th, K and U using the $CeBr_3$ detector.

(D. K. Panda, D. Banerjee, S. K. Goyal, A. R. Patel, A. D. Shukla, T. Ladiya)

Design & development of Hard X - ray imaging detector using Scintillator and Si Photomultiplier

Silicon Photomultiplier (SiPM) is a new development in the field of photon detection and can be described as 2D array of small (hundreds of μm^2) avalanche photodiodes. The Avalanche Photo Diodes (APD) operate in Geiger mode, where the output is independent of the number of incoming photons. The gain of each APD is $\sim 10^5$ - 10^6 electrons.

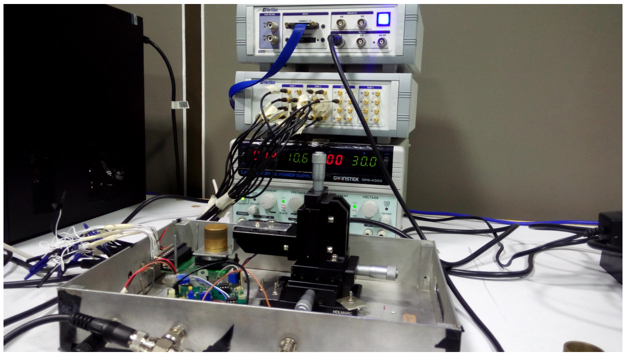

Figure 39: Test setup for measurement of X Y position for the incoming X ray

When a photon creates a photoelectron through the photoelectric effect in one of such APD microcells, a large breakdown current is produced. This current through APD is controlled using in-built quenching resistor. The current flow through the parallel combination of APDs is linearly proportional to the number of incoming photons. Hence the SiPM is a linear amplifier device, where the amount of output charge is linearly proportional to the number of incoming photons, as long as these numbers of incoming photons does not exceed the total number of APDs in detection area. SiPM is an alternate option of using conventional PMTs (Photo Multiplier Tubes), as this offers comparable photon detection efficiency, small size, feasibility of compact array, low cost, low operating voltage and insensitivity to the external magnetic field.

We are developing a hard X - ray imaging detector using Scintillator and SiPM devices. In our experiment, we are using CsI Scintillator crystals of size 15 mm x 15 mm x 3 mm, which is optically coupled to SiPM array of size 4 x 4. We are using this setup in two different modes; 1) Total charge output of all SiPMs added together to get the energy information. 2) In the imaging mode to get the X - Y position of the incoming X - ray. Figure 39 shows the test setup for the CsI Scintillator and SiPM and Figure 40 shows the Gaussian fit output of the 4 x 4 array.

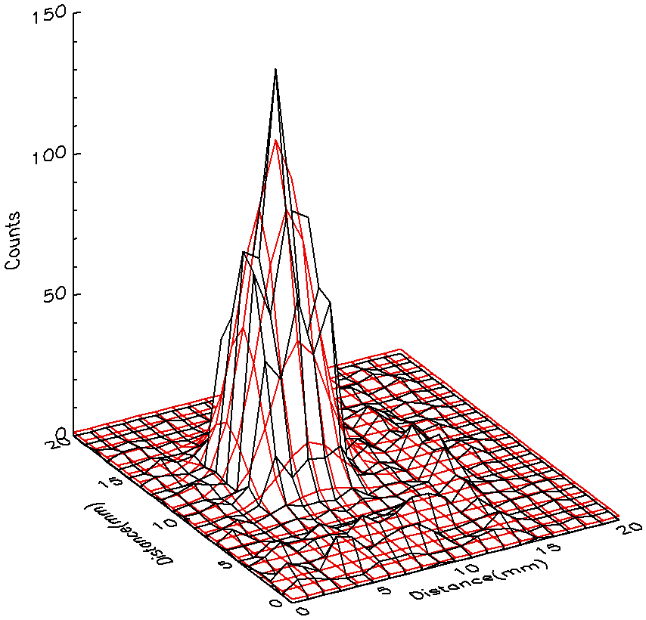

Figure 40: Gaussian fitted data for the 4 x 4 array

We achieved ± 0.5 mm movement using this setup. 60 keV X ray energy line (^{241}Am) is used for the experiment. The processing of the 16 parallel analog chains is done using Vertilon setup. We are developing our own parallel processing system for this.

(S. K. Goyal, S. Vadawale, A. R. Patel, Mithun N. P. S., T. Ladiya, N. K. Tiwari)

Investigation of Gamma ray radiation effects on the Silicon Drift Detector on-board Chandrayaan-2 Mission

It is well known that the Earth is surrounded by extremely intense radiation regions known as Van Allen radiation belts which consists of highly energetic electrons and protons trapped within the Earth's magnetosphere. Such harsh radiation environment is known to adversely affect the performance of X-ray detectors. Forth coming Chandrayaan-2 mission, the second Indian mission to the Moon will have two X-ray spectrometer experiments using Silicon Drift Detectors (SDD) namely Solar X-ray Monitor (XSM) and Alpha Particle X-ray Spectrometer (APXS). Silicon detectors are sensitive to displacement damage which is due to the Non Ionizing Energy Loss (NEIL) of charged and neutral particles. The displacement damage leads to increase in the detector leakage current and thus degrades the energy resolution. Thus in order to estimate the end-of-life performance, it is necessary to carry out the radiation damage tests. The total radiation dose encountered by the SDD module was estimated for both the passage through radiation belts during Earth to the Moon as well as solar protons during the life time of two years. The fluence of trapped protons en-route to the Moon similar orbital profile as Chandrayaan-1 mission, was estimated using ESA software suit SPENVIS and NSSDC AP-8 model. Total solar proton fluence during two year mission life around the Moon was estimated using the JPL-91 solar fluence model. The NIEL function in SPENVIS was used to estimate the equivalent fluence of 10 MeV protons considering the model incident proton spectra as well as total effective shielding. The total radiation dose at the end of two year mission life was estimated to be ∼10 krad which is about ∼4x10^{9} protons/40 mm^{2} area SDD.

We have used the ^{60}Co gamma ray source to simulate the proton induced radiation damage in the SDD as the particle accelerators are less accessible. The SDD irradiated using ^{60}Co with photon energies of 1.17 MeV and 1.33 MeV produces scattered Compton electrons having energies of a few hundred keV and these electrons cause displacement damage. The NIEL scaling hypothesis is based on the assumption that the displacement damage is linearly dependent on the amount of energy imparted in displacing collisions which is independent of particle type.

To compare the damage produced by different type's particles at various energies, the particle fluence Φ of particular irradiation is usually related to a reference value of 1MeV neutrons by introducing a hardness factorκ. The 1 MeV equivalent neutron fluence Φ_{eq} is given by $\Phi_{eq} = \kappa\Phi$. The value of the hardness factor based on the NIEL scaling hypothesis is the ratio of damage displacement function $\{\mathrm{D}_i\,(\mathrm{E})\}$ for the particle (i) with energy $(\mathrm{E})$to the displacement damage function of 1MeV neutrons ($D_{neutron}$ for 1 MeV = 95 MeV mb). Based on the NIEL scaling hypothesis, the hardness factor is about 2 orders of magnitude lower for electrons at 1 MeV compared to that of a proton with energy at 10 MeV. To estimate the scattered Compton electron interactions in a 40 mm^{2} area SDD, we have carried out a GEANT4 simulation for the gamma ray irradiation environment with 10^{9} photons. This gives ∼2.5x10^{5} scattered Compton electron interactions depositing a total dose of ∼0.025 rads. The ^{60}Co gamma ray chamber provides ∼3.26 rads/s, which is ∼3.23x10^{7} electron interactions/second. The 10 MeV equivalent total proton fluence of ∼4x10^{9} protons/40 mm^{2} provides the cumulative dose of ∼10 krad with each proton depositing ∼5 MeV in a 450 micron thick SDD. To achieve the same dose through gamma irradiation requires ∼1x10^{11} gamma induced Compton electron interactions.

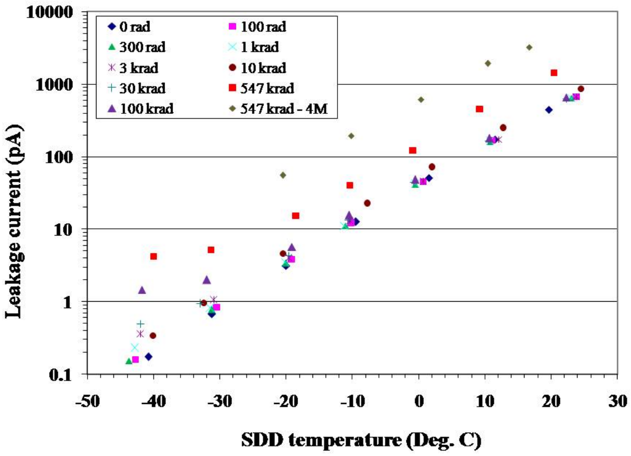

Figure 41: Leakage current for various gamma ray doses

The SDD detector is irradiated in steps of desired dose levels over a period of five days in passive mode. After each dose, the detector leakage current and the energy resolution is measured. The initial irradiation study is targeted for the gamma ray dose up to ∼10 krad for the Chandrayaan-2 mission requirement and subsequently extended our irradiation studies up to ∼547 krad. It is shown that the measured increase in leakage current is ∼0.35 pA at -40^{o}C, ∼50 pA at 0^{o}C and ∼450 pA at 20^{o}C for the gamma ray dose of ∼10 krad and at ∼547 krad, the leakage current increased to ∼4 pA at -40^{o}C, ∼80 pA at 0^{o}C and 1.4 nA at 20^{o}C as shown in Figure 41.

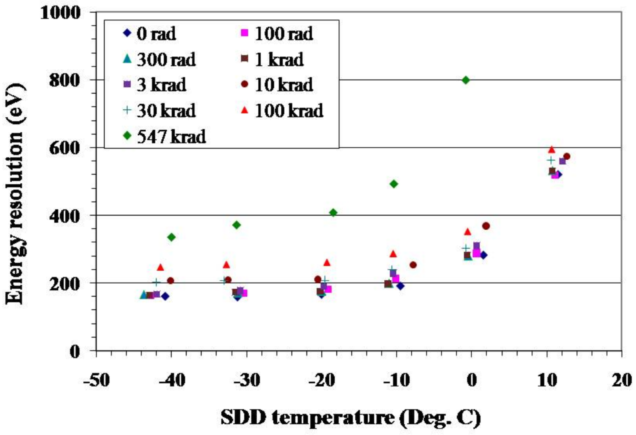

Figure 42: Energy resolution for various gamma ray doses with detector operating temperature

Leakage current is also measured 4 months after irradiation by preserving the SDD module in the laboratory environment and found that the increase in leakage current is ∼40 pA at ∼-20^{o}C compared to the leakage current measured just after irradiation of ∼547 krad. The SDD module could not be cooled below -20^{o}C, this could be due to permanent damage to the peltier cooler inside the SDD module. It is shown that there is no significant degradation in the energy resolution for the gamma ray doses up to 3 krad, and the energy resolution degrades to ∼210 eV at 10 krad which is expected during the Chandrayaan-2 life time of two years. The energy resolution degrades to ∼250 eV at 100 krad and ∼340 eV at 547 krad for the detector operating temperature of ∼ -40^{o}C as shown in Figure 42. This irradiation measurement shows that these SDD modules can survive ∼20 years in the lunar environment providing the required energy resolution.

(M. Shanmugam, Y. B. Acharya, S. V. Vadawale, A. Patel, S. K. Goyal, T. Ladiya)

A novel technique for measuring the Leakage current and its usage as a calibration tool for the Silicon Drift Detector based X-ray spectrometers for on-board applications

In recent years, Silicon Drift Detector (SDD) based X-ray spectrometers are widely flown on-board space/planetary missions due to the superior spectroscopic performance of SDD. Several planetary missions such as Mars Exploration Rover (MER), Mars Science Lab (MSL), Changé-3 and Rosetta have employed SDD based X-ray spectrometer to measure the X-ray fluorescence from the planetary surfaces. There are two SDD based X-ray instruments are planned on-board Chandrayaan-2 mission which are being developed at PRL.

The energy resolution of the SDD based spectrometer primarily depends on the detector leakage current and the baseline noise associated with the charge readout & signal processing electronics. The SDD leakage current on-board X-ray spectrometer varies with detector operating temperature and increases with radiation dose absorbed by the detector in the space environment. The baseline noise associated with the charge readout and signal processing electronics is not expected to change significantly due to the virtue of using space qualified and radiation hardened electronic components.

Thus the degradation in the energy resolution of the SDD can be estimated if it is possible to measure the detector leakage current. However, the leakage current measurement typically involves a different measurement setup with access to the bare detector chip. Hence, the conventional methods of measuring detector leakage current cannot be implemented in the on-board electronics. Thus it becomes essential to have a dedicated calibration source or target, typically requiring a separate moving mechanism, in order to keep track of the performance degradation of the SDD in space. Such a moving mechanism is heavy and consumes more power which is not desirable for space payload design.

We proposed an alternate technique for calibrating the SDD based X-ray spectrometers by measuring the detector leakage current on-board and hence the energy resolution. We adapted a simple technique to measure the detector leakage current by measuring the reset frequency of the reset-type charge sensitive pre-amplifier (CSPA). The output of reset-type CSPA will be in the form of ramp signal as shown in Figure 43.

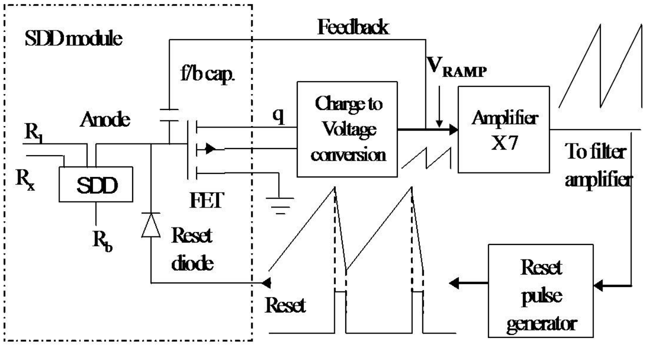

Figure 43: Block schematic of pulsed reset type Charge Sensitive Pre-Amplifier (CSPA) design

The ramp signal frequency at the output of the CSPA will depend on the magnitude of the leakage current generated by the SDD in the absence of any photon interacting with the detector. In the presence of photon interactions, the ramp signal frequency varies with energy and rate of photon interacting with the detector and they appear as step pulses on the ramp signal. The leakage current is obtained using the relation $\mathrm{I}_o = \mathrm{C}_f \times \mathrm{V}_{\mathrm{RAMP}}/\mathrm{T}_{\mathrm{RAMP}}$, where C_f is the charge integrating feedback capacitor, $\mathrm{V}_{\mathrm{RAMP}}$ is the ramp signal amplitude and $\mathrm{T}_{\mathrm{RAMP}}$ is the ramp signal period. By measuring $\mathrm{T}_{\mathrm{RAMP}}$, one can estimate the SDD leakage with the known values of C_f and $\mathrm{V}_{\mathrm{RAMP}}$.

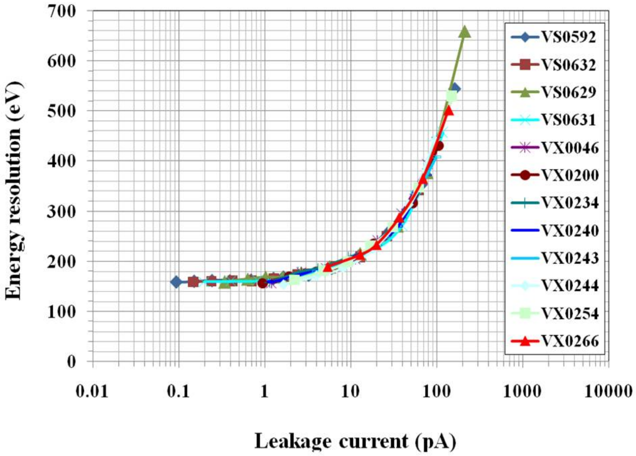

Figure 44: Leakage current measured for large sample of SDDs versus measured energy resolution

This technique does not require any additional electronics hardware except a counter which can be part of spectrometer digital data acquisition system and thus can be easily implemented for any number of detectors. Using this technique, the leakage current is measured for large samples of SDDs having two different active areas of 40 mm^2 and 109 mm^2 with 450 micron thick silicon. These measurements are carried out in the temperature range of -50^{o}C to 20^{o}C. At each step energy resolution is measured for all SDDs using Fe-55 X-ray source and shown (Figure 44) that the energy resolution varies systematically with the leakage current irrespective of the difference among the detectors of the same as well as different sizes. The energy resolution of the developed spectrometer degrades for the detector leakage currents greater than 1 pA and degrades from $\sim$150 eV for the detector leakage current of $\sim$1 pA to 200 eV at 10 pA and 400 eV at 100 pA. It can be clearly seen that the energy resolution does not improve for the leakage currents $<$ 1 pA. For the smaller leakage currents $<$ 1 pA, the spectrometer system noise is dominant and hence the spectral energy resolution is constant at $\sim$150 eV at 5.9 keV for the pulse peaking time of $\sim$3 s. Using this technique, one can estimate any performance degradation to the SDD based X-ray spectrometer when used in the space missions where in the leakage current increases with temperature and space radiation.

(M. Shanmugam, Y. B. Acharya, S. V. Vadawale, A. Patel, S. K. Goyal, T. Ladiya)

Front-End Electronics Development for ChaSTE Payload onboard Chandrayaan-2 Lander

Lunar subsurface heat flow measurements are often perturbed by external thermal forcing due to solar insolation. Therefore, precise estimation of equilibrium balance between external (solar) and internal (due to radioactive decay and accretion) heat fluxes is needed for estimating the thermal state of the Moon. To address this aspect, PRL, Ahmedabad and SPL/VSSC, Trivandrum have proposed and jointly developing ChaSTE (Chandra's Surface Thermo physical Experiment) payload that will be flown on Chandrayaan-2 Lander.

ChaSTE will help measure the vertical temperature gradient and thermal conductivity within the top 10 cm of the regolith. The experiment contains a thermal probe which will be deployed up to ∼10 cm into the lunar regolith at the Landing site. Harness running from the probe will connect the probe to the electronics placed inside the lander. One of the important aspects of the payload is the design of a precise and wide-range temperature measurement front-end (FE). This includes selection of an appropriate sensor and meticulous design of front-end electronics. After detailed theoretical and experimental evaluations, a custom developed Platinum RTD, PT1000, has been selected as sensing element. The front-end electronics is responsible for exciting RTD sensors by current source, acquiring analog voltages from the sensors and converting the acquired analog signals to digital signals by Analog to Digital Converter (ADC). Several designs have been evaluated including the conventional bridge approach for front-end electronics design. Finally, a new signal conditioning approach operating in constant current excitation mode followed by an analog multiplexer has been adopted to cater the experimental requirements. A low noise, precision, Rail to Rail op-amp has been chosen for this purpose. In this scheme, a change in RTD resistance produces a linear change in gain of the amplifier, and hence the change in output voltage of the amplifier is proportional to the temperature sensed by RTD. An additional gain stage is provided to have wide dynamic range and a better resolution. The present design provides measurement capability of temperature between -250^{o}C to 250^{o}C with a resolution of 10 mV/^{o}C. In final configuration when the landing site is finalized, we expect to have ΔT of ∼300^{o}C thus improving the resolution to ∼16 mV/^{o}C. The block schematic of the adopted approach is shown in Figure 45.

A laboratory verification model (LVM) of the system has been developed to demonstrate the proof of concept of the experiment. The performance of LVM was evaluated under, laboratory, field and simulated lunar environments and results were satisfactory. Engineering model (EM) PCB is currently under fabrication. A 3D CAD view EM PCB is shown in Figure 46. After successful testing and evaluation of EM, we plan to proceed for the qualification model.

This work is done in collaboration with SPL (VSSC), Thiruvananthapuram.

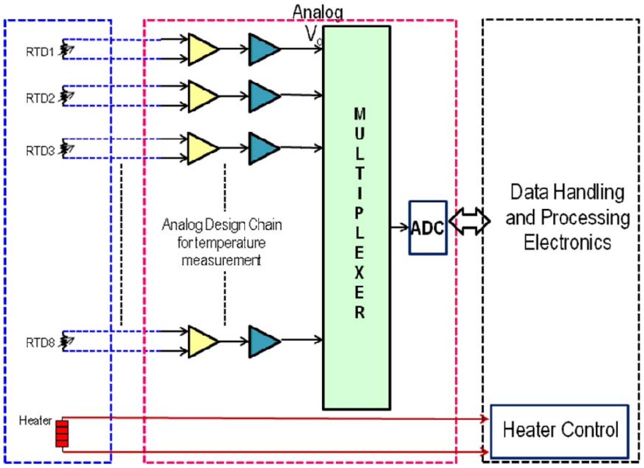

Figure 45: ChaSTE Front-End (FE) Electronics Block Schematic.

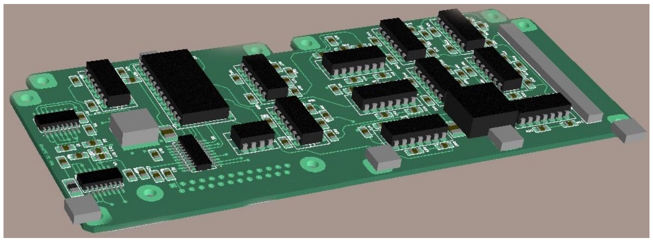

Figure 46: 3D CAD view of FE PCB using the adopted scheme.

(K. D. Prasad, C. Kumar, A. Patel, T. Ladiya, M. Shanmugam, S. V. S.Murty, V. K. Rai)

Development and evaluation of a 3D surface thermo physical model of the Moon

Systematic measurements of heat loss from lunar interior and its spatial variation are needed to estimate the net heat flow on the Moon. Thermal measurements of the Moon gained importance in light of recent results from various instruments on board lunar missions such as LRO, GRAIL and Chandrayaan-1. Although heat flow measurements will be of top priority for future in situ geophysical exploration of the Moon, no such mission is in the offing at least for the next decade. At this point, the only way we can improve our current understanding about these aspects is through laboratory experiments and numerical simulations.

A three-dimensional finite element model to understand the thermo physical behaviour of the lunar surface has been developed and evaluated using COMSOL software. The model is designed to account for complex geometry, different size, irregular meshing, parametric based variation in physics and boundary conditions. A schematic of the developed model is shown in Figure 47.

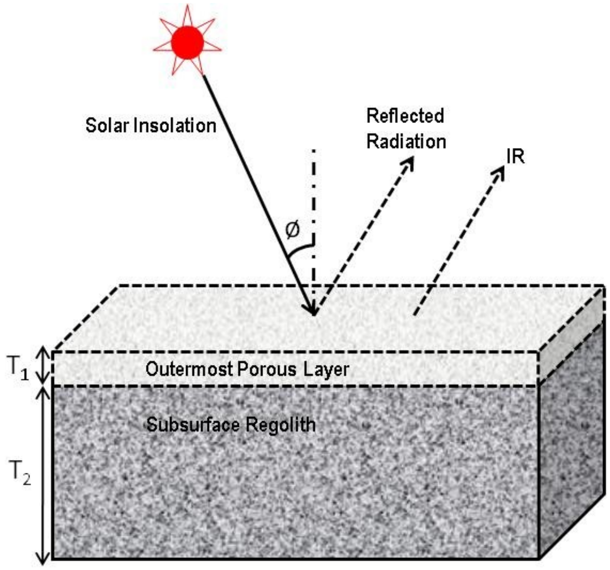

Figure 47: Schematic of 3D-Lunar Surface Model for two layers.

Using the model, simulations have been carried out for diurnal and annual cycles for all latitudes. The model results have been validated against laboratory experiments, in-situ data and earlier models and are in good agreement. Figure 48 shows a comparison of diurnal variation of surface and subsurface temperatures (at a depth of 17 cm) obtained from the model and Apollo 17 heat flow probe data. It can be clearly seen that the model derived diurnal variation in surface and subsurface temperatures are in good agreement with Apollo 17 in situ data. For a depth of 17 cm, two scenarios were considered for model simulations.

The first scenario is a porous material and second scenario mimics Apollo 17 heat flow probe deployment, where the sensor at 17cm of Apollo heat flow probe is hanging at the centre of the bore stem and not in contact with regolith. This implies that the sensor is measuring the radiated heat within the bore stem. It is clearly seen that the model derived plot using second scenario better mimics (within model uncertainties) the Apollo in situ data at that depth. These results thus validate the credibility of the developed model to simulate the realistic conditions on the Moon. Using the model, the subsurface temperatures at various latitudes have been systematically estimated. Further improvements of the model to incorporate local terrain effects (particularly for high latitudes) are in progress.

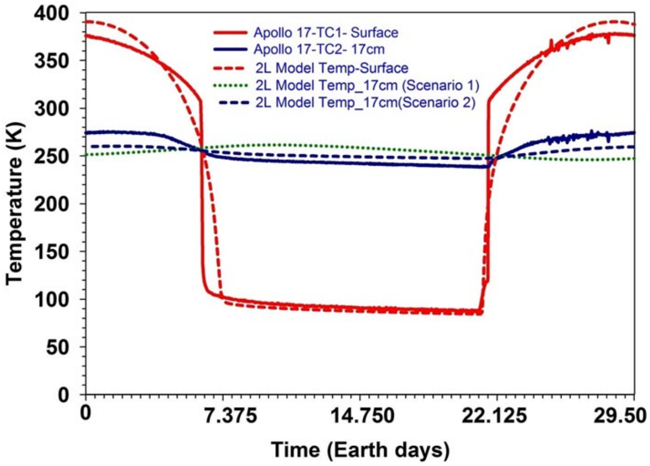

Figure 48: Comparison of Model derived surface and subsurface temperature with Apollo 17 in situ data.

(K. D. Prasad, V. K. Rai, S. V. S. Murty)

Science

Space and Atmospheric Sciences

Aerosol Radiative Forcing Surface Reflectance

Aerosol radiative forcing depends not only on the type of aerosols (scattering or absorbing) but also on whether they are present over lower (ocean) or higher reflectance (land, desert and snow) surfaces (Figure 1). At the outset, aerosol radiative forcing is higher for higher values of aerosol optical depth (AOD) and single scattering albedo (SSA) (Figure 1).

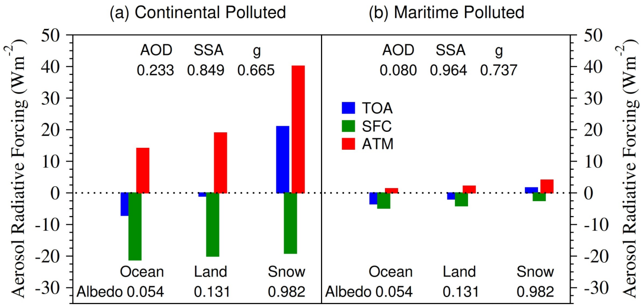

Figure 1: Aerosol radiative forcing (Wm^{-2}) at the top of the atmosphere (TOA), at the surface (SFC) and in the atmosphere (ATM) derived for surface reflectance (or albedo) values of ocean, land and snow for (a) Continental Polluted and (b) Maritime Polluted aerosols. AOD, SSA and g at 550 nm for Continental and Maritime Polluted aerosols are given in the figure. Surface reflectance at 550 nm for ocean, land and snow are also mentioned in the figure.

For the same aerosol properties aerosol radiative forcing increases as surface reflectance increases (Figure 1) for continental and marine aerosols. Over higher reflectance surfaces (land and snow) the surface radiation reflected from the surface below would again interact with the aerosols above. As the surface reflectance increases the top of the atmosphere (TOA) forcing becomes less negative (land) or becomes positive (snow) when compared to ocean. This is in contrast to the greenhouse gases whose TOA forcing is always positive. The atmospheric forcing significantly increases as the TOA forcing becomes less negative or positive. The reduction and/or the sign change in TOA is a consequence of higher surface albedo and higher amount of absorbing aerosols (especially black carbon) leading to lower SSA over the continent. This study highlights that accurate determination of surface reflectance is essential not only for accurate retrieval of aerosol parameters but is also crucial to reduce the uncertainty in aerosol radiative forcing and climate change.

(S. Ramachandran)

Characteristics and source apportionment of black carbon aerosols over urban region

Black carbon (BC) produced from incomplete combustion of fossil fuel and biomass burning are optically absorbing particles. Aethalometer based source apportionment model using the measured aerosol absorption coefficients at different wavelengths is used to determine the contribution of fossil fuel and wood burning sources to the total BC mass concentrations over an urban region. Temporal and seasonal variabilities in BC mass concentrations, equivalent BC from fossil fuel (BC$_{ff}$) and wood burning (BC$_{wb}$) are investigated using seven wavelength aethalometer. BC mass concentrations, BC$_{ff}$ and BC$_{wb}$ exhibit strong diurnal variation and are mainly influenced by atmospheric dynamics (diurnal evolution of atmospheric boundary layer and meteorology). Maximum and minimum BC mass concentrations are observed during the month of December (11.1 $\mu g/m^3$) and July (1.6 $\mu g/m^3$) respectively. The corresponding observed maximum BC$_{ff}$ and BC$_{wb}$ values are 8.5 and 3.1 $\mu g/m^3$, while the minimum values are 1.4 and 0.2 $\mu g/m^3$ respectively (Figure 2). The observed contributions of BC$_{ff}$ in total BC dominates throughout the year, and is highest BC$_{ff}$ (87%) in July. During the monsoon season major contribution of BC in the atmosphere arises from fossil fuel as biomass burning is minimal. During postmonsoon and winter higher BC along with its equivalent components occur due to shallow atmospheric boundary layer, long-range transport associated with low wind speeds, and significant increase in the amount of biomass burning. The anthropogenic activity and atmospheric dynamics governs the contribution of BC$_{ff}$ and BC$_{wb}$ to total BC (Figure 2). Annual mean BC$_{ff}$ and BC$_{wb}$ contributions to total BC are 80 and 20% respectively (Figure 2) confirming that fossil fuels dominate the BC mass concentrations over Ahmedabad.

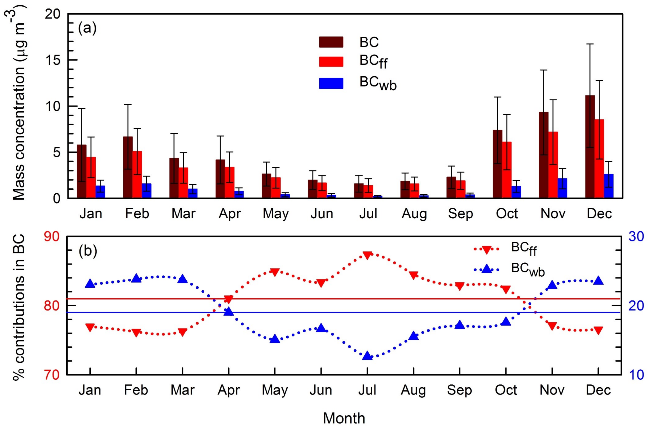

Figure 2: Monthly mean (a) black carbon (BC) mass concentrations, equivalent black carbon concentrations from fossil fuel (BC$_{ff}$) and wood burning (BC$_{wb}$) and (b) percentage contributions of BC$_{ff}$ and BC$_{wb}$. Solid red and blue lines correspond to annual mean percentage contributions of BC$_{ff}$ and BC$_{wb}$ respectively. Vertical bars indicate $\pm 1\sigma$ variation from the mean.

(T. A. Rajesh, S. Ramachandran)

Aerosol sampling system to quantify Influence of relative humidity on aerosol properties

Aerosols undergo hygroscopic growth in the ambient atmosphere and their optical properties (e.g. aerosol scattering coefficient (β_{scat}) strongly depend on the ambient relative humidity (RH). An aerosol sampling system has been developed to sample atmospheric aerosols sequentially at ambient relative humidity and in dry air condition to quantify the effect of RH on aerosol properties (Figure 3a). The ambient atmospheric aerosols are sampled through an inlet manifold, processed and fed to the aerosol sampling instrument through outlet manifold (Figure 3a). The manifold has temperature and relative humidity sensors to monitor the air temperature and humidity at the inlet and outlet of the aerosol sampling system. Aerosols are fed to one of the two parallel stainless steel cylinders C1 and C2 through straight 0.75 inch bore electrical actuated ball valves V1 and V2 respectively (Figure 3a). The sampling cylinder C1 is filled with Silica beads and houses 9 aerosol ducts made up from stainless steel (SS 316) wire mesh. The Silica beads are used to remove the moisture content in the ambient air sample. The ambient sampling cylinder C2 is used to sample the ambient aerosol without any RH conditioning. The valves are electronically controlled through a microcontroller and have been programmed to sample air in a predefined sequential condition. β_{scat} at 550 nm is found to decrease by about 25% when RH reduces by the same amount from 74% (ambient) to 50% (conditioned) (Figure 3b).

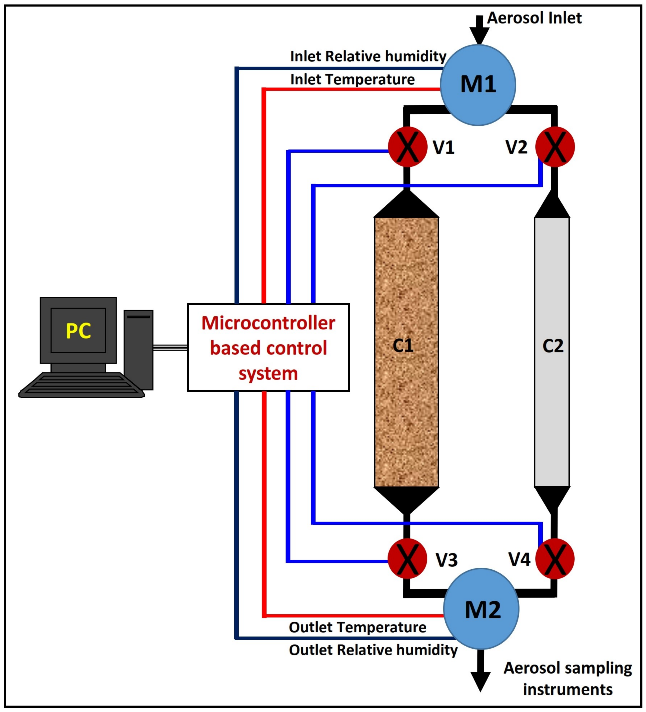

Figure 3: (a) Schematic of the aerosol sampling system displaying the cross sectional view of sampling cylinders (C1-C4) and the operational condition of electrically actuated valves (V1-V4).

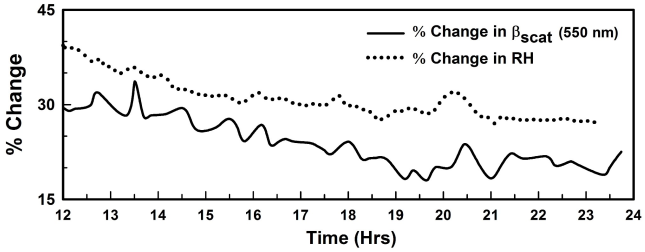

Figure 3: (b) Percentage change in β_{scat} determined using the aerosol sampling system during the day along the change in relative humidity (%).

(S. Ramachandran, T. A. Rajesh)

Effect of relative humidity on aerosol optical characteristics

Measurements of near surface aerosol scattering (β_{scat}) and absorption coefficients (β_{abs}) are being made in Ahmedabad. β_{scat} values during January are about a factor of 4 higher than September (Figure 4). The atmospheric boundary layer is shallow during winter resulting in trapping of pollutants in a lesser volume which leads to higher β_{scat}. During September an increase in atmospheric boundary layer height, surface temperature, convective activity, and rainfall result in lower β_{scat} values. β_{scat} are about 75 Mm^{-1} in September (southwest monsoon), while β_{scat} was higher than 300 Mm^{-1} in January (northeast monsoon) (Figure 4). As β_{scat} depends strongly on the ambient relative humidity (RH), the β_{scat} values are corrected for the variation in the ambient RH using hygroscopic scaling factor estimated using an aerosol optical properties model (OPAC). β_{scat} shows maximum percentage change during September (>40%) due to higher RH (83%) during this month. The ratio of aerosol absorption to scattering coefficients (ASR) can be to quantify the role of scattering vs. absorbing type aerosols in the atmosphere. ASR is maximum during October (0.4) indicating the dominance of absorbing type aerosols, and is minimum in January (0.14) suggesting the dominance of scattering type aerosols (Figure 4). Variations in ASR suggest that the sources are common for scattering and absorbing type aerosols over the study location. Maximum and minimum monthly mean RH corrected single scattering albedo (SSA) are found to be in January (0.88) and October (0.70) the corresponding maximum and minimum monthly mean SSA values without relative humidity correction (RHC) are 0.89 and 0.74 respectively at 550 nm (Figure 4). The study highlights the importance and significance of RH correction on β_{scat} and SSA over an urban region. This study quantifies the effect of RH on aerosol optical characteristics and can be used in estimating SSA more accurately which in turn will reduce the uncertainty in aerosol radiative forcing estimates.

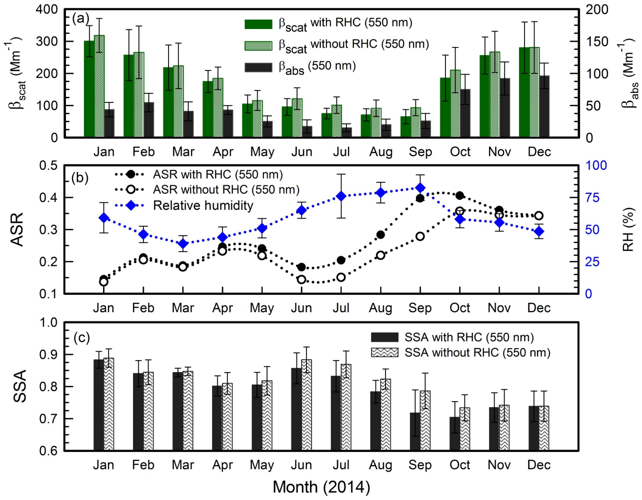

Figure 4: Monthly variations of (a) aerosol scattering coefficient (β_{scat}) with and without relative humidity corrections (RHC) along with aerosol absorption coefficient (β_{abs}), (b) absorption to scattering coefficient ratio (ASR) with and without RHC at 550 nm along with ambient relative humidity (RH), and (c) single scattering albedo (SSA) with and without relative humidity corrections (RHC) at 550 nm over Ahmedabad during 2014. Vertical bars represent $\pm 1\sigma$ variation from the mean.

(T. A. Rajesh, S. Ramachandran)

Seasonal variation in aerosol single scattering albedo over urban region

Simultaneous measurements of columnar optical aerosol characteristics and size distribution are being conducted over Ahmedabad, an urban region in western India since 2014 using skyradiometer that measures direct solar irradiance and radiances. Single scattering albedo (SSA) at 500 nm is lowest in December (0.82) and is highest during June-September (0.95) consistent with the type of aerosols that dominate the urban atmosphere in these months. Frequency distribution histograms of SSA revealed that >50% of measured SSA values are higher than 0.9 during monsoon and postmonsoon seasons, while during winter and premonsoon 50% SSA values are lower than 0.90. Seasonal mean SSA over Ahmedabad are 0.88 (winter), 0.87 (premonsoon), 0.95 (monsoon) and 0.91 (postmonsoon) respectively. During winter absorbing aerosols (black carbon) emitted from fossil fuel and biomass burning dominate the urban atmosphere and give rise to lower SSA. During premonsoon winds from the surrounding arid/semiarid regions transport mineral dust and black carbon at elevated altitudes which reduce the columnar SSA. During monsoon removal of absorbing aerosols and increase in relative humidity give rise to increase in scattering contribution which in turn results in higher SSA. This analysis will be useful to delineate the manmade contribution from the natural sources of aerosols and its influence on aerosol characteristics over urban regions.

(S. Ramachandran, T. A. Rajesh, S. Jose)

Sources of atmospheric VOCs and effect of marathon events at an urban site of Ahmedabad in India

Measurements of atmospheric volatile organic compounds (VOCs) using a high resolution proton transfer reaction-time of flight-mass spectrometer (PTR-TOF-MS) were made at Ahmedabad city in India during winter 2014. The time series of VOCs exhibit strong diurnal and large day-to-day variations. Oxygenated-VOCs (OVOCs) such as methanol, acetone, acetaldehyde, etc. were the most abundant VOCs. Among the major VOCs, the OVOCs contributed up to about 85% of total measured VOCs with methanol being the most abundant (Figure. 5).

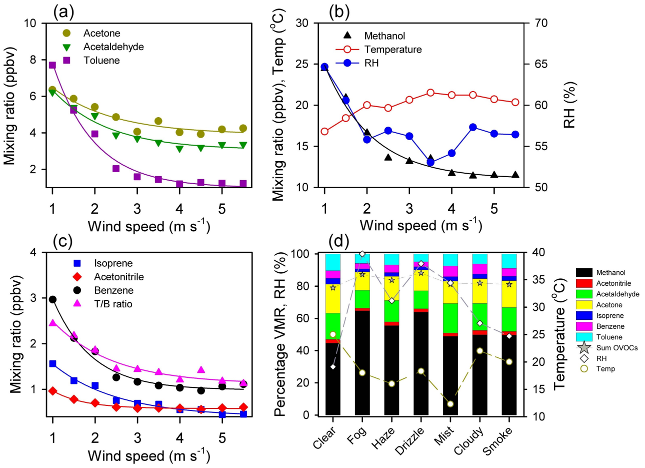

Figure 5: Dependence of mixing ratios of VOCs on wind speed (a, b and c) and percentage contribution of different compounds to the total measured VOCs under different weather conditions (d).

The level and variations of VOCs showed strong dependence on weather conditions. It is observed that the mixing ratios of primary VOCs (anthropogenic) such as benzene and toluene decrease more rapidly compared to those of OVOCs with increase in wind speed. Although vehicular emissions are major sources of VOCs at Ahmedabad, the emission ratios (ERs) of several VOCs indicate significant contribution from biogenic emissions in the daytime. During the marathon (5 Jan 2014) and cyclothon (19 Jan 2014) events, levels of anthropogenic VOCs were 2-10 times higher compared to a normal weekend. The ERs of VOCs, estimated based on nighttime data, fall within the range reported for several major cities of the world. Overall, the primary anthropogenic emissions of acetaldehyde, acetone and isoprene were about 44%, 45% and 63%, respectively. The increase in anthropogenic contribution to acetaldehyde (∼10%), acetone (9%) and isoprene (30%) during cloudy days was due to the reduction in biogenic emissions and photochemical production of these compounds.

(L. K. Sahu, R. Yadav, D. Pal)

Temporal variations of C_2-C_7 NMHCs at an urban site of western India. Measurements using GC-TD-FID technique

Measurements of C_2-C_7 non-methane hydrocarbons (NMHCs) were made at an urban site of Udaipur (26.58°N, 73.68°E) in western India. The air samples were collected during February 2015-January 2016 and analyzed using a thermal desorption-gas chromatograph equipped with flame ionization detector (TD-GC-FID). The mixing ratios of C_2-C_7 NMHCs show peaks during the morning and evening rush hours and lowest in the afternoon hours. In winter season, average mixing ratios of aromatic compounds benzene (C_6H_6) and toluene (C_6H_7) were 1.6 ppbv and 2.5 ppbv, respectively. Measurements in the monsoon season do not show significant diurnal dependence. Anthropogenic NMHCs show strong seasonal variation with the highest during winter and lowest during the monsoon season. Local emission, transport and boundary layer height were important factors in controlling the diurnal and seasonal variations of anthropogenic NMHCs. The good correlations ($r^2 > 0.5$) between the mixing ratios of different NMHCs indicate their emissions from common or co-located sources. The emission of natural gas and use of liquid petroleum gas (LPG) contribute to the elevated levels of ethane and propane. Emissions from vehicles are the dominant sources of ethene, propene, acetylene, benzene and toluene.

(R. Yadav, D. Pal, L. K. Sahu)

Vertical and seasonal variations of carbon monoxide over an urban region in peninsular India

The vertical profiles of carbon monoxide (CO) measured over Chennai region in peninsular India during March 2012 to June 2013 were analyzed. In-situ profiles were measured under the Measurements of Ozone aboard Airbus In-service Aircraft (MOZAIC) program. Monthly mean profiles of CO show significant vertical and temporal variations in the troposphere. In the PBL region, level of CO was the highest of 190±68 ppbv in winter and lowest of 124±33 ppbv during monsoon. The vertical distributions of CO during the monsoon and post-monsoon months were influenced by strong convective activity. The Chemistry Climate Model (CCM2) and Model for Ozone And Related Chemical Tracers (MOZART-4) provide reasonable agreement with the measurements from winter to pre-monsoon season. However, simulations failed to capture the vertical variability of CO in the post-monsoon season. In the free troposphere, the levels of CO measured during the pre-monsoon 2012 (mild El Niño) were 15-20 ppbv higher than the values during the pre-monsoon 2013 (normal ENSO). However, both CCM2 and MOZART-4 could not reproduce the difference in profiles of CO measured during the pre-monsoon of 2012 and 2013. Long-range transport of pollutants and emissions from biomass burning sources play important role in seasonal variation of CO. The profiles of CO during monsoon and post-monsoon seasons were significantly influenced by the convective dynamics and prevailing ENSO conditions.

(L. K. Sahu, V. Sheel)

Comparison of CO_2 observations with a model simulation

The in situ measurements of CO_2 using a laser based Cavity Ring Down Spectroscopic (CRDS) technique are being made at PRL since November 2013. The analyser is calibrated using three calibration standards following the World Meteorological Organisation (WMO) CO_2 scales, supplied by the National Oceanic and Atmospheric Administration (NOAA), Boulder, USA. The observations show large diurnal, day to day and seasonal variability, which can be linked to emissions from fossil fuel burning, sources and sinks from the terrestrial ecosystem, and meteorological conditions, e.g., the planetary boundary layer height and wind speed and direction. The fossil fuel emissions can be estimated in a better way than the biogenic sources/sinks, which are relatively more uncertain. We have tried to understand these process using a state of the art atmospheric general circulation model (AGCM)-based chemistry-transport model (ACTM), which incorporates various components of CO_2 fluxes (biospheric, oceanic and anthropogenic) from JapanAgency for Marine-Earth Science and Technology (JAMSTEC).

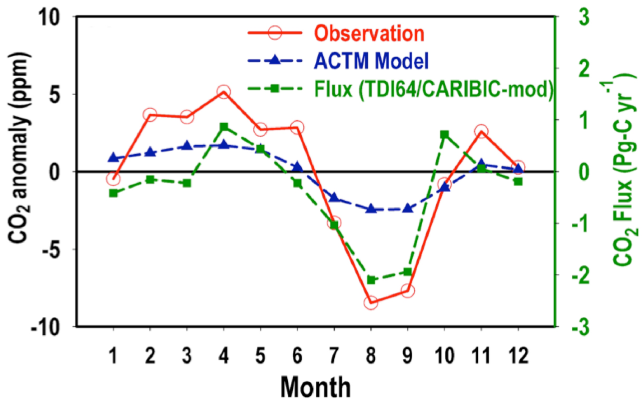

Figure 6: Mean seasonal cycles of CO_2 concentrations using afternoon values, based on the measurements over Ahmedabad (red circles) and the ACTM simulation (blue triangles). The seasonal variation of CO_2 flux over South Asia as estimated using an inverse model (green squares) is also shown.

The CO_2 seasonal cycle, which is calculated after subtracting the annual mean from the afternoon average values of each month for the observations and model simulation, is shown in Figure 6. The afternoon values, used as the signals from the local anthropogenic sources and biospheric fluxes, are well mixed through the greater depth of the planetary boundary layer and thus more regionally representative. The model reproduces the observed seasonal cycle in CO_2 fairly well but with much low seasonal amplitude of about 4.15 ppm compared to the 13.6 ppm from the observations. Positive bias during the summer monsoon season depicts the underestimation of biospheric productivity as simulated by the terrestrial ecosystem model of Carnegie-Ames-Stanford Approach (CASA). The seasonal variation of CO_2 fluxes using an inverse model, which uses aircraft measurements over the Indian subcontinent, is also shown in Figure 6 to understand the role of the biosphere. Positive and negative values of flux show the net release and net sink by the land biosphere over the South Asia region. This comparison shows an almost one-to-one correlation in the monthly variation of CO_2, and suggests that the lower levels of CO_2 during August-September and the higher levels in April-May are due to the strong sink and moderate source, respectively. Significant correlation ($r^2 = 0.88$) between the South

Asian CO_2 fluxes from inversion and monthly mean CO_2 for daytime suggest that observations over the region is extremely important for tracking the seasonal carbon cycling in our biosphere.

This work is done in collaboration with Dr. P. K. Patra of JAMSTEC, Japan.

(N. Chandra, S. Venkataramani, S. Lal)

First observations of trace gases over a high altitude site in Southern India

Rapidly developing economy of the Indian subcontinent leads to increasing anthropogenic emissions of ozone precursors. Over a long period of time, these emissions invariably alter the regional background concentrations of various trace gases. Southern part of India is relatively less affected by anthropogenic emissions since this region has lesser anthropogenic emission sources and is also flushed by marine winds. However, the emissions from the Indo-Gangetic belt can still affect south India during winter as the north-east monsoon winds carry the pollutants to this region through the northern Bay of Bengal. Realizing the absence of the regionally representative observations of trace gases in southern Indian region, an environmental laboratory was set-up at Ooty (11.4°N, 76.7°E, 2520 m amsl), a hill station in Tamil Nadu, in collaboration with TNAU (Tamil Nadu Agricultural University), Coimbatore under the Atmospheric Trace Gases and Modelling (ATCTM) project of Indian Space Research Organisation-Geosphere Biosphere (ISRO-GBP) programme. As the site is in the free troposphere most of the time, measurements from this place are representative of this region. Continuous measurements of ozone, CO, NOx are being made at this site for the last 3-4 years. In addition to these insitu measurements, ambient air samples have been collected at two hours interval continuously for 2 to 3 days once in 2 months in glass sampling tubes using an air compressor. These samples are analysed for non-methane hydrocarbons (NMHCs) at PRL, Ahmedabad using a gas chromatographic system. The lowest concentrations of NMHCs are observed during the monsoon season and are also lower than those observed over the central Himalayan region.

This work is done in collaboration with Prof. C. Udayasooriyan, Tamil Nadu Agricultural University (TNAU), Coimbatore.

(S. Venkataramani, S. Lal)

Effects of convection and long-range transport on tropospheric carbon monoxide over India

Variability in the tropospheric distributions of carbon monoxide (CO) over five selected regions of India has been studied using the MOPITT data for the period of 2001-2014. The average seasonal profiles show highest mixing ratios at 900 hPa in the boreal winter and lowest in the Indian summer monsoon over all the study regions. We observe a slight increase in CO levels from 500 hPa to 200 hPa over all the locations. The CO mixing ratios are found to be higher by about 10-40% around 300-200 hPa as compared to 900 hPa over Ahmedabad, Hyderabad and Trivandrum during monsoon period. This could be due to lifting of polluted air by convection and getting trapped in the anticyclonic winds over the Indian region during the monsoon. Most of the 7 day back trajectories over these regions show transport of the polluted air mass from the major biomass burning regions of central Africa and SE Asia. The results show dominance of the seasonal amplitude at 900 hPa over all the regions, while inter-annual variability dominates mostly over Ahmedabad, Hyderabad and Trivandrum at 300 hPa. In order to check the ability of different models in capturing the observed variability, the results have been compared with simulations from two chemistry transport models (MOZART and EMAC). This comparison shows that both the models perform reasonably well in simulating the basic features such as annual variation as well as increase in CO around 300-200 hPa due to convection during the monsoon season.

(N. Chandra, S. Venkataramani, V. Sheel)

Effect of relative humidity on SOA formation

Carbonaceous species in PM10 and PM2.5 samples, collected from an urban location at Ahmedabad in India during summer, were analyzed to study variability in water-soluble organic carbon (WSOC) and secondary organic carbon (SOC) along with atmospheric water vapor content. Analysis suggests that higher atmospheric water vapor content is not favorable for SOA formation in the range of observed RH during daytime in summer. In order to study the cause for this, we simulated OH, CO and NO_x concentrations using MOZART-4 (Model for Ozone and Related chemical Tracers, version 4). Our study shows that influence of wind regime and source strength of VOCs is minimal on the observed trend between atmospheric water vapor and SOA. We find that the temporal variation of MOZART simulated OH radical concentration exhibits similar trend as that of water vapor content. The average values of O_3 and NO_x mixing ratios also do not show significant variability during the observation period. This suggests that, concentrations of oxidizing species in ambient air are increasing during our observation from March to June 2007, and not the limiting factor for VOC oxidation processes for SOA formation. Hence, ambient water vapor content possibly causes a decrease in SOA formation during daytime at lower RH range ($<$40%). At higher RH range ($>$40%) a direct relation of VOC oxidation and/or SOA formation with ambient water vapor content is not evident (as observed during nighttime as well as during monsoon period).

This work is done in collaboration with A. K. Sudheer and R. Rengarajan from GSDN.

(V. Sheel)

Space Weather

Sudden turnings of IMF-Bz with enhanced solar wind velocity and density are associated with geomagnetic storms and electric fields of magnetospheric origin that affect the ionosphere globally. Case studies of sudden southward or northward turnings of IMF-Bz or slow long duration changes of IMF-Bz were made using the geomagnetic and ionosonde data at low latitude stations in different longitudes. The super geomagnetic storm of 6 April 2000 and its effects on the ionosphere at Thumba, India and at Jicamarca, Peru are studied. The event was unique with IMF-Bz steady and southward for about 6 hours and later turning from -30 nT at 2300 UT to 10 nT at 02 UT and large fluctuations around 1200 UT on 7 April 2000. The southward turning of IMF-Bz on the night of 06-07 April inhibited the development of spread-F irregularities at Thumba. The large excursions of IMF-Bz on 7 April 2000 inhibited the Es-q at Thumba. At Jicamarca the southward turning of IMF-Bz on 6 April caused a large enhancement of EEJ current and strong Es-q. The northward turning of IMF-Bz on 7 April 2000 is associated with large rise of F-layer around midnight and spread-F was seen at 0100 LT, however later the F-layer descended and inhibited the spread-F irregularities. Thus the effect on equatorial ionosphere at different longitudes depends on the local solar time of the event.

(R. G. Rastogi, H. Chandra)

Equatorial electrojet

As part of the study of the equatorial electrojet currents in the south Atlantic anomaly region, geomagnetic field deviations at African stations Addis-Ababa (AAE) and Freetown (FTN) for three years 1962-64 were examined. Hourly values of the deviations in the geomagnetic X and Y field at FTN on the eastern part and AAE on the western part are studied. The declination is almost along the geographic N-S at AAE and 14° towards west of the geographic N-S at FTN. The annual mean daily range in X is around 80 nT at FTN and 70 nT at AAE with peak around 11 hrs. Deviations in Y at FTN show a broad minimum of about -20 nT around noon while the decrease is much smaller at AAE with a minimum of 5 nT at noon. Seasonal mean variations of the daily range in X show almost equal peaks during D and E-months at FTN but at AAE it is highest during equinoctial months and lowest during J-months. The seasonal asymmetry at FTN could be due to large declination. The equinoctial peak in February-March is higher than the peak in September-October at both the stations. Another notable feature at FTN is the steady increase in deviation in X from about -10 nT at 18 hrs to 10 nT at 06 hrs. The study complements the recent studies from South American sector based on stations in Peru and east Brazil.

(R. G. Rastogi, H. Chandra)

Tropical spread F

Tropical spread F studies over Ahmedabad in the past had shown high occurrence during high sunspot years particularly during equinoxes. These events were shown to be associated with the equatorial spread F. However, during the low sunspot years, high occurrence was noted during June solstices when the equatorial spread F is restricted to a narrower latitudinal belt. Finer characteristics of the spread F echoes from ionograms could not be studied earlier due to the wide pulse of the transmitter High resolution ionograms obtained from Digisonde at Ahmedabad during July 2012 were examined and it was shown that several off-vertical reflections, prior to onset of spread F, are seen in the ionograms. This suggests the role of the travelling ionospheric disturbances from mid latitudes and subsequent local generation of the irregularities during June-solstices of low sunspot years.

(R. G. Rastogi, H. Chandra)

Equatorial Electrojet during the geomagnetic storm of 13-14 November 1998

The geomagnetic storm of November 1998 is unique event where IMF-Bz remained southward with values exceeding -15 nT for more than a day. The SYM-H index decreased from about 07 h on 13 November 1998 reaching a minimum of about -120 nT around midnight of 13-14 November 1998. Features of the equatorial electrojet in the Indian region are studied during the geomagnetic storm event of 13-14 November 1998 based on the geomagnetic data from the chain of observatories in India. Sudden northward turning of IMF-Bz for a very short duration around 08 h on 13 November 1998 resulted in a small and very short duration counter electrojet. A strong (-50 nT) and a long duration counter electrojet right from 08 h to 13 h on 14 November 1998 was observed resulting in the absence of the equatorial Es at Thumba. Absence of the equatorial ionization anomaly was also observed as seen from the ionograms over Thumba and ionspheric data from Ahmedabad. The delayed effect on 14 November 1998 is due to the disturbance dynamo effect.

This work was done with collaboration of R. K. Choudhary of SPL, VSSC.

(H. Chandra, R. G. Rastogi, S. K. Sharma)

First three dimensional wave characteristics in the daytime upper atmosphere derived from ground-based multiwavelength oxygen dayglow emission measurements

The importance of neutral wind and wave dynamics in contributing to the day-to-day, diurnal, and seasonal behaviour of the upper atmosphere is well known. It can be appreciated that, unlike winds which can be measured by both ground-based and satellite-based platforms, scale sizes of neutral waves in the daytime can only be obtained by ground-based observations of optical airglow emissions that are carried out over a large field of view (FOV). In the present study, we have used a high spectral resolution large FOV imaging slit spectrograph in zonal and meridional directions and obtained thermospheric daytime airglow emission intensities simultaneously at multiple wavelengths. For this study, oxygen dayglow emissions at 557.7 nm, 630.0 nm, and 777.4 nm that originate from around 130 km, 230 km, and 300 km (peak of the F region) were used. From this information on the dayglow emission intensities in the orthogonal directions, wave features in the horizontal directions at these three altitudes of emissions have been obtained through spectral analysis. Such measurements on horizontal scale sizes (in two dimensions) have hitherto been not reported. Moreover, the measured values have been used in conjunction with the gravity wave (GW) dispersion relation proposed by Hines to calculate the plausible wave features in the vertical direction as well. Thus, in this investigation the first results on the three-dimensional wave characteristics at different altitudes in the daytime upper atmosphere were obtained. Figure 7 shows the propagation of wave fronts on 19 May 2015 in the meridional and zonal directions at the three emission wavelengths (Top row: OI 777.4 nm, middle row: OI 630.0 nm; bottom row: OI 557.7 nm). In general, a southward and westward directed propagation can be seen in the gravity waves of daytime upper atmosphere. The horizontal scale sizes of GWs, their time periods, phase propagation angle (counterclockwise from east), and phase speeds are found to vary in the range of

27-227 km, 32-70 min, 207°-253°, and 6-76 ms^{-1}, respectively.

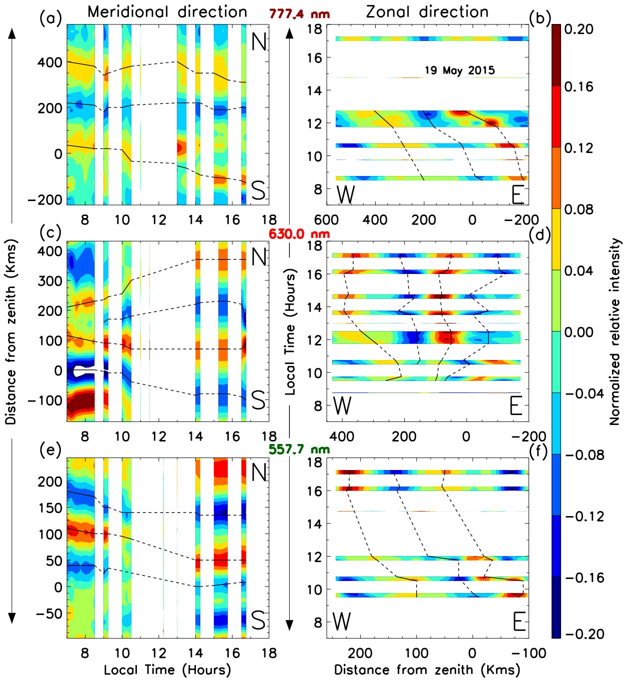

Figure 7: Normalized relative dayglow intensity variations obtained using band-pass filter centered on the dominant scale sizes obtained for 19 May 2015. Left/right columns correspond to meridional/zonal scales. (Top row: OI 777.4 nm, middle row: OI 630.0 nm; bottom row: OI 557.7 nm). Westward and southward phase propagations can be seen.

(D. Pallamraju, D. K. Karan, K. A. Phadke)

Electrodynamic control on the neutral daytime oxygen emission airglow intensity distributions

Daytime airglow emission intensity measurements at three wavelengths OI 777.4 nm OI 630.0 nm, and OI 557.7 nm are being carried out from a low latitude location, Hyderabad as part of PRL-JNTUH collaboration. As the production mechanisms of the dayglow emissions are mainly solar zenith angle dependent, it is expected that the diurnal intensity distribution of the daytime oxygen emission intensity variations show a symmetric behaviour with respect to the local noon. However, it was found that on several occasions the emission pattern was deviating from this behaviour. The plausible reason for this has been investigated and it is found that the equatorial electrodynamics is the casue for the observed asymmetric behaviour. These electrodynamical phenomena contribute to the movement of plasma from the equator to low-latitudes, thereby giving rise to the asymmetric behaviour. Supporting magnetic, ionospheric and model wind data on the days with asymmetric behaviour in neutral optical mesurements confirm that this behaviour in optical emissions is due to electrodynamics and rules out other causes (e.g., neutral winds). Figure 8 shows example of the contrasting behaviour in the dayglow emissions and neutral winds and electrojet strengths. It can be seen that as the neutral wind magnitudes are smaller on the day with asymmetric behaviour as compared to the day with symmetric intensity distribution, neutral winds can not bring about the asymmetric nature. In contrast, the electrojet strength is greater on the day that showed asymmetric behaviour as compared with the day with symmetric behaviour. This cause has been ascertained further using ionospheric data from Trivendrum and Ahmedabad. This study thus emphasizes the coupled nature of the neutral and plasma processes, especially in the low- and equatorial-latitudes.

This work is done in collaboration with T. Vijayalakshmi and M. Anjireddi at JNTU, Hyderabad.

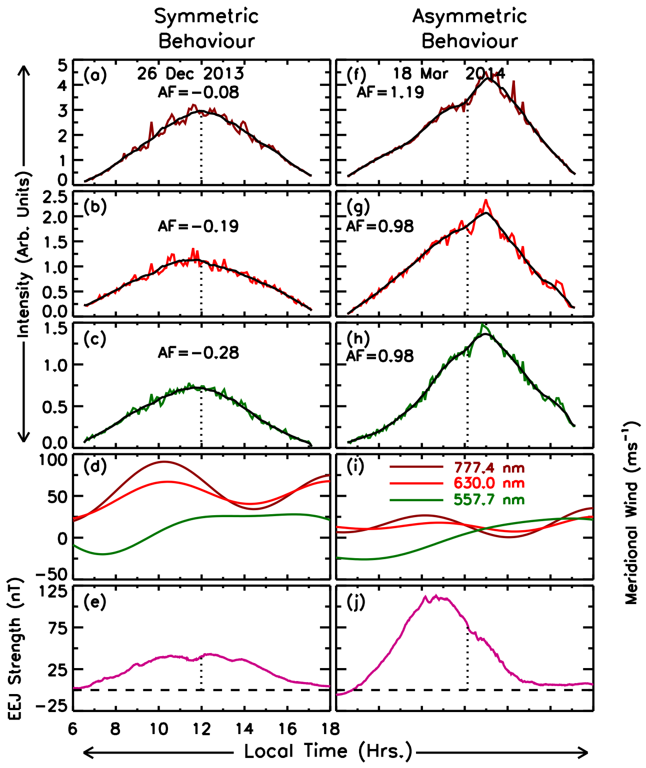

Figure 8: Top row (a,f) show the diurnal variability in OI 777.4 nm on two selected days. Plots (b,g) show the behaviour of OI 630.0 nm, and (c,h) OI 557.7 nm on the same days. Plots (d,i) show the HWM14 meridional wind magnitudes corresponding to all these altitudes. Plots (e,j) show the electrojet strengths. The plots in the left column show symmetric behaviour in the diurnal pattern, while the right column represents the days with asymmetric behaviour.

(D. K. Karan, D. Pallamraju, K. A. Phadke)

Vertical wavelength of gravity waves in the mesosphere measured using O_2 and OH nightglow emissions

Airglow intensity and temperature variations in time and space have been used to understand the complex mesospheric dynamics at their altitudes of emissions. It is now understood that waves of different scales, such as planetary waves, tides, and Gravity Waves (GWs) play an important role in the energy and momentum transfer between various atmospheric layers. These waves modulate density and temperature while passing through the airglow emitting altitudes. To investigate the vertical wave characteristics at mesospheric heights we have used simultaneous measurements of high cadence observations of O_2 (0-1) and OH (6-2) band intensities which emanate from 87 km and 94 km altitudes. These measurements were carried out using the in-house built Near Infrared Imaging Spectrograph (NIRIS) from the optical aeronomy observatory in Gurushikhar, Mount Abu. In order to obtain the periodicities of GW scale sizes, residuals have been obtained by subtracting a 4-hour running average from the original data. The residuals so obtained on the night of 4 May 2013 in O_2 and OH intensities are shown in Figures 9a and 9b. It can be clearly seen that there is downward phase propagation in the variation of residuals of the nightglow emission intensities on this night (marked by green lines). To ascertain if the fluctuations seen in the intensities at both the altitudes are due to the same GW, the wave periodicities (τ) for these residuals have been obtained and are shown in Figure 9c along with the respective 90% false alarm limit values (dotted lines). It can be seen that periodicities of around 1.8 hours is statistically significant and is coherent in both O_2 and OH nightglow intensities. By using cross correlation analysis between residuals of O_2 and OH intensities seen in Figures 9a and 9b, the phase offset time (Δ_t) is found to be 0.5 hours. As the difference between O_2 and OH emission layer heights (Δ_z) is 7 km, the vertical phase speed ($c_z = \Delta_z/\Delta_t$) and vertical wavelength ($\lambda_z = \tau . c_z$) have been calculated to be 3.9 ms^{-1} and 25.2 km. This method is being used to characterize GW behaviour of mesosphere with an aim to address the mesosphere lower thermosphere dynamics.

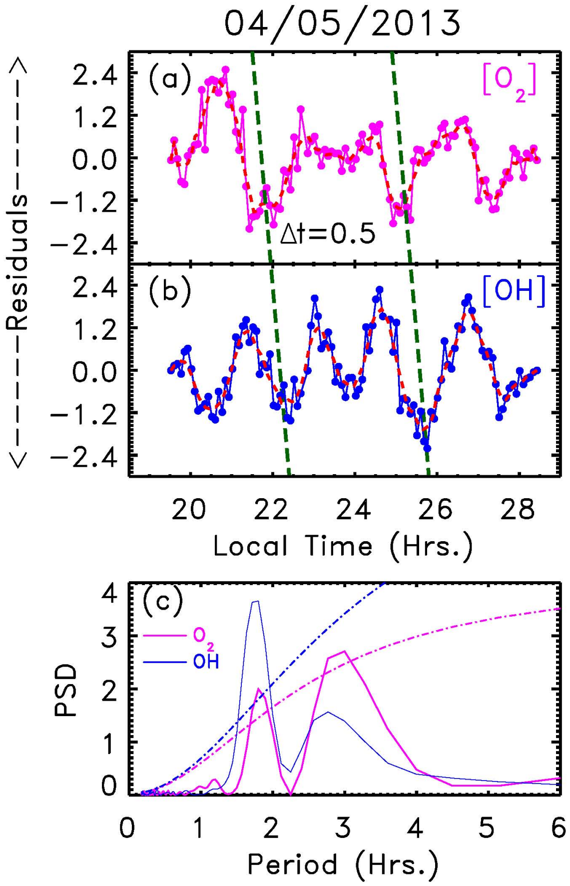

Figure 9: (a, b) Residulas of O_2 and OH airglow intensities on the night of 4 May 2013 showing a downward phase propagation, and (c) Result of the spectral analysis showing the coherent wave period of ∼1.8 hours at these two emission altitudes.

(R. P. Singh, D. Pallamraju)

Derivation of meridional scale sizes of gravity waves in the mesosphere

NIRIS (Near InfraRed Imaging Spectrograph) is a large FOV (80°) instrument which is presently being operated along the meridional (north-south) orientation from Gurushikhar in Mt. Abu. Therefore, by using the information on emission intensity variability that originates from different directions along the meridian it is possible to derive the meridional component (λ_y) of the gravity waves (GW) that exist in the mesosphere. At the O_2 and OH emission altitudes (94 km and 87 km) the range covered by of NIRIS is 155 km and 145 km, respectively. Hence, according to the Nyquist criterion GWs having wavelengths smaller than 77.5 km and 72.5 km at O_2 and OH emission altitudes are reliable. After commissioning NIRIS for field operations in Gurushikhar, angle calibration of NIRIS has been performed by taking series of spectral images by allowing only a small portion of the diffused light from known angles to fall on to the CCD chip. The meridional variations of the O_2 and OH intensities for every individual observation throughout the night are shown in Figures 10a and 10c for the night of 4 May 2013. The vertical scale is for the bottom-most intensity variation and the subsequent plots are shifted by 0.15 arbitrary units. The start and end times of the observations are 19.50 hours and 28.50 hours (0430 LT of 5 May). The horizontal axis shows the north-south range covered at the respective emission altitudes and the dashed vertical line indicates the zenith location.

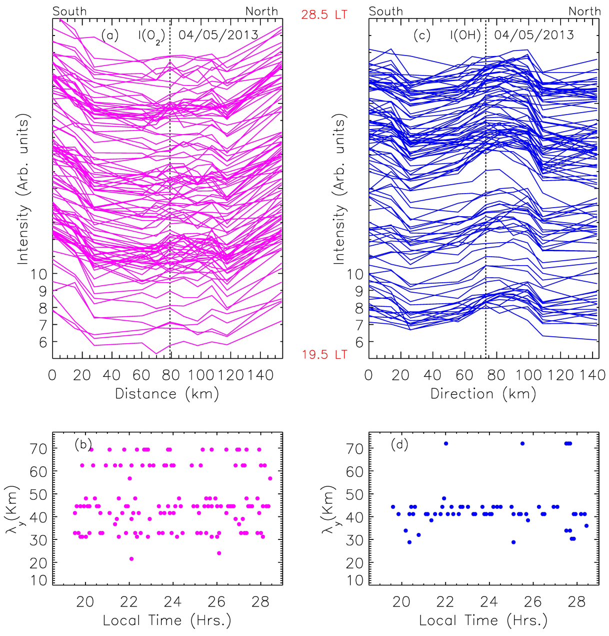

Figure 10: (a, b) Meridional variation in O_2 and OH emission intensities on the night of 4 May 2013, and (c, d) the Meridional scale sizes derived from O_2 and OH intensity measurements.

Large scale wave structures in the intensity variations are quite evident throughout the night in both O_2 and OH intensities in addition to small scale fluctuations. Wave number spectral analyses have been performed on the intensity variations at these two emission wavelengths which yields information on GW wavelengths along the north-south meridian (λ_y). Statistically significant meridional wavelengths (which are greater than 90% false alarm limit) for every observation are obtained throughout the night are shown in Figures 10b and 10d for O_2 and OH emission altitudes. The x- and y- axes show local time and scale sizes in km. It can be noted that the ranges in the observed meridional wavelength, λ_y, are greater at O_2 emission altitudes as compared to that of the OH, however, 40-50 km wavelengths are observed at both altitudes. In addition to this 30-35 km and 60-70 km meridional wavelengths are observed only at O_2 emission altitude throughout the night. This wide range of meridional scales in O_2 emission as compared to OH could be due to the proximity of O_2 emission height to the Mesopause height and the ensuing dynamics. This aspect is currently under investigation.

(R. P. Singh, D. Pallamraju)

Study of Stratospheric Sudden Warming (SSW) over Tropical and Sub-Tropical Regions of India using Rayleigh Lidar

The Stratospheric Sudden Warming (SSW) is one of the most spectacular phenomena in the atmosphere and has impacts on the Earth‘s lower, middle and upper atmospheres. In this study, two major SSW episodes associated with vortex displacement and vortex splitting occurred in year 1998 and 1999 respectively are investigated first time over Mt. Abu using lidar observations. Analyses show that ground based lidar and satellite observations from Halogen occultation experiment (HALOE) onboard upper atmospheric research satellite (UARS) are able to capture effect of SSW events. Lidar measurements are able to capture SSW warming and its decay very accurately. Impact of SSW is further investigated in the European Centre for Medium-Range Weather Forecasts (ECMWF) Interim reanalyzed potential vorticity. Moreover, a detailed study has been presented to understand the latitudinal variation of SSW warming and associated mesospheric cooling over Indian region. Analyses showed that warming is more at high latitude like Kashmir region (35°N, 77°E) and lowest in the equatorial Indian Ocean region (5°N, 77°E).

(S. K. Sharma, H. Chandra)

Evaluation of Inter-hemispheric Characteristics of the Tropopause-Stratopause-Mesopause over Sub-tropical regions

The transition regions in thermal structure viz. Tropopause, Stratopause and Mesopause play a vital role in the vertical coupling of the Earth‘s atmosphere. For the first time, inter-hemispheric characteristics of the transition regions over two subtropical regions are studied using temperature observations from SABER onboard TIMED satellite and ERA Interim reanalysis during year 2002 to 2015. Results show that Tropopause height is higher over Reunion Island (21.11°S, 55.53°E) in the Southern Hemisphere (SH) as compared to Mt. Abu region (24.59°N, 72.70°E) in the Northern Hemisphere (NH). Temporal variation of Tropopause temperature reveals a decreasing ($\sim$4 K) trend from year 2002 to 2008 and beyond this, an increasing ($\sim$1.5 K) trend is found in Tropopause temperature. These features are reinforcing for Mesopause as compared to Tropopause temperature. The SH shows stronger variations in Mesopause temperature ($\sim$7 K) compared to NH during year 2002 to 2008. The occurrence frequency of Mesopause and Stratopause height show that the maximum occurrence frequency ($\sim$60%) of Mesopause at $\sim$100 km in NH, while frequency is found to be $\sim$55% in the SH. Results show that Stratopause (Mesopause) is cooler (warmer) in NH as compared SH. Moreover, Lomb Scargle Periodogram and wavelet transform techniques are used to investigate the periodicity of Mesopause, Stratopause and Tropopause temperatures and heights. Investigations revealed prominent annual oscillations in Tropopause and Stratopause temperatures in both the hemispheres. These findings will be of immense use for the vertical and inter-hemispheric atmospheric coupling studies.

This work has been done in collaboration with LACY, University of Reunion, France.

(S. K. Sharma, R. Vaishnav)

Evaluation of Cloud Base Height measurements from Ceilometer CL31 and MODIS satellite over Ahmedabad, India

Clouds play a tangible role in the Earth‘s atmosphere and in particular, the cloud base height (CBH) which is linked to cloud type is one of the important characteristic to describe the influence of clouds on the environment. In present study, CBH observations from ceilometer CL31 have been extensively studied during May 2013 to January 2015 over Ahmedabad (23.03°N, 72.54°E), India. A detail comparison has been performed with the use of ground-based CBH measurements from ceilometer CL31 and CBH retrieved from MODIS (Moderate Resolution Imaging Spectroradiometer) onboard Aqua and Terra satellite. Some interesting features of cloud dynamics viz. strong downdraft and updraft have been observed over Ahmedabad which revealed different cloud characteristics during monsoon and post-monsoon periods. CBH shows seasonal variation during Indian summer monsoon and post-monsoon period. Results indicate that ceilometer is one of the excellent instruments to precisely detect low and mid-level clouds and MODIS satellite provides accurate retrieval of high-level clouds over this region. The CBH algorithm used for MODIS satellite is also able to capture the low-level clouds.

(S. K. Sharma, R. Vaishnav, S. Lal, Y. B. Acharya)

An evidence for prompt electric field disturbance driven by changes in the solar wind density under northward IMF Bz condition

Before the onset of a geomagnetic storm on 22 January, 2012 (Ap=24), an enhancement in solar wind number density from 10 /cc to 22 /cc during 0440-0510 UT under northward interplanetary magnetic field (IMF Bz) condition is shown to have enhanced the high latitude ionospheric convection and also caused variations in the geomagnetic field globally. The latitudinal variation of the amplitude of the northward component of the geomagnetic field (ΔX) variation during 0440-0510 UT is shown to be consistent with the characteristics of prompt penetration electric field disturbances. Most importantly, the density pulse event caused enhancements in the equatorial electrojet strength and the peak height of the F-layer (hmF2) over the Indian dip equatorial sector. Further, the concomitant enhancements in electrojet current and F layer movement over the dip equator observed during this space weather event suggest a common driver of prompt electric field disturbance at this time. Such simultaneous variations are found to be absent during magnetically quiet days. In absence of significant change in solar wind velocity and magnetospheric substorm activity, these observations point towards perceptible prompt electric field disturbance over the dip equator driven by the over-compression of the magnetosphere by solar wind density enhancement.

This work is done in collaboration with the scientists from the Space Physics Laboratory, VSSC, Indian Institute of Geomagnetism, India, Los Alamos National Laboratory and Virginia Tech, USA, Nagoya University, Japan.

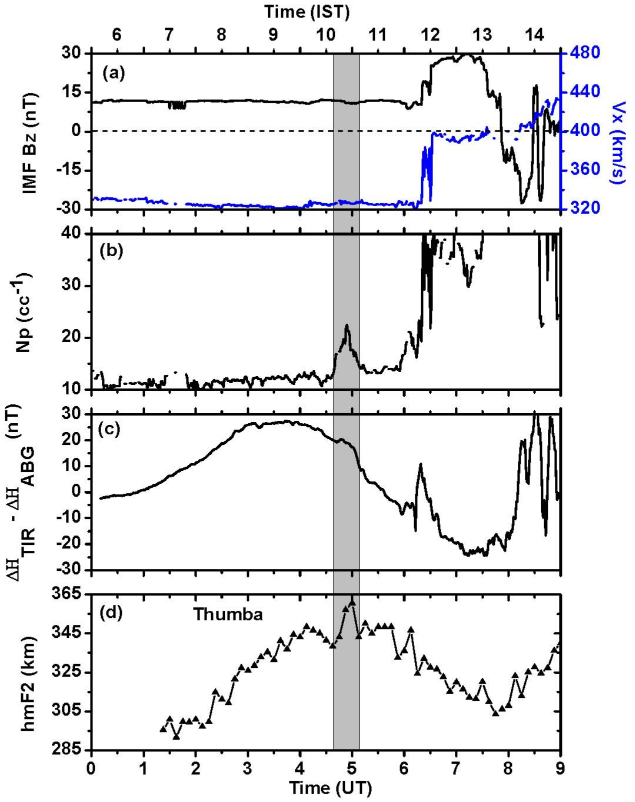

Figure 11: Variations in (a) Z-component of interplanetary magnetic field (IMF Bz, in black) and solar wind velocity (Vx, in blue), (b) Solar wind proton density (Np), (c) EEJ strength (ΔH_{TIR}-ΔH_{ABG} parameterized by the base line corrected horizontal magnetic field (H) values over a dip equatorial (Tirunelveli or TIR) and off-equatorial (Alibag or ABG) stations, and (d) the maximum height of the F layer (hmF2) over Thumba (Trivandrum). The rectangular grey box highlights the interval when solar wind density changes (but not IMF Bz or velocity) and simultaneous fluctuations are observed in EEJ strength and hmF2 suggesting prompt electric field disturbance.

(D. Rout, D. Chakrabarty, R. Sekar)

Prompt penetration electric field disturbances in the equatorial ionosphere during Co-rotation Interaction Region (CIR) events in the minimum of solar cycle 23

The fast solar streams coming from the solar coronal holes interact with the background slow solar wind in the interplanetary medium leading to the generation of Co-rotation Interaction Regions (or CIRs). These events that predominantly occur during solar minimum can be identified by various solar wind parameters. It is also known that CIRs produce weak to moderate geomagnetic storms when they encounter terrestrial magnetosphere. In order to characterize the prompt electric field disturbances in the equatorial ionosphere during these events in the minimum of solar cycle 23, solar wind and ionospheric data are analyzed for 46 events spanning over five years starting from 2006 to 2010. The analyses suggest that the frequency response of the shielding region at the inner edge of the ring current plays an important role in filtering out a number of frequency components in IMF Bz during the passage of CIR.

(D. Rout, D. Chakrabarty, P. Janardhan, R. Sekar)

Role of IMF By in the Prompt Electric Field Disturbances over Equatorial Ionosphere During a Space Weather Event

During a space weather event, prompt electric field perturbations of opposite polarities are observed over two conjugate dip equatorial stations on a few occasions. Both IMF Bz and By changed polarities occasionally with comparable variations in magnitudes during this event. Interestingly, the zonal electric field is found to be of similar polarity over these conjugate stations during a particular interval. This is in contrast with the general expectation wherein opposite polarities of prompt penetration electric field is expected over conjugate sectors. It is suggested that IMF By has played an important role in causing the electric field perturbations of same polarity over both the places at this time.

This work is done in collaboration with the scientists from the Indian Institute of Geomagnetism, India and Los Alamos National Laboratory, USA.

(D. Chakrabarty, D. Hui, D. Rout, R. Sekar)

Estimation of nighttime dip-equatorial E-region current density using measurements and models

The existence of the possible ionospheric current during nighttime over low-equatorial latitudes is one of the unresolved issues in ionospheric physics and geomagnetism. A detailed investigation is carried out to estimate the same over Indian longitudes using in situ measurements from Thumba (8.5°N, 76.9°E), empirical plasma drift model and equatorial electrojet model developed in PRL. This investigation reveals that the nighttime E-region current densities vary from $\sim$0.3 to $\sim$0.7 A/km^2 during pre-midnight to early morning hours on geomagnetically quiet conditions. The nighttime current densities over the dip equator are estimated using three different methods (discussed in methodology section) and are found to be consistent with one another within the uncertainty limits. Altitude structures in the E-region current densities are also noticed which are shown to be associated with altitudinal structures in the electron densities. The horizontal component of the magnetic field induced by these nighttime ionospheric currents is estimated to vary between $\sim$2 and $\sim$6 nT during magnetically quiet periods. This investigation confirms the existence of nighttime ionospheric current and opens up a possibility of estimating base line value for geomagnetic field fluctuations as observed by ground-based magnetometer.

(K. Pandey, R. Sekar, B. G. Anandarao, S. P. Gupta, D. Chakrabarty)

Analysis of GPS/GNSS data using newly developed software

A web-based novel GUI application software used for analysis and display of various parameters derived from the data received from

GPS (GSV4004B) and GNSS (PolaRxS) receivers as a function of time is developed in-house.

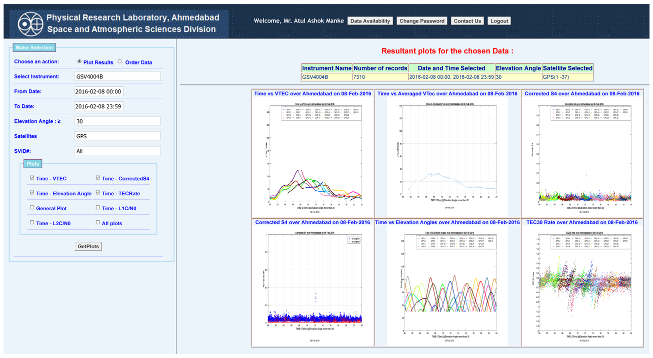

Choose an action: ● Plot Results ○ Order Data

Select Instrument: GSV4004B

From Date: 2016-02-08 00:00

To Date: 2016-02-08 23:59

Elevation Angle : ≥ 30

Satellites GPS

SVID#: All

☑ Time - VTEC ☑ Time - CorrectedS4

☑ Time - Elevation Angle ☑ Time - TECRate

☐ General Plot ☐ Time - L1C/N0

☐ Time - L2C/N0 ☐ All plots

Resultant plots for the chosen Data :

Instrument Name	Number of records	Date and Time Selected	Elevation Angle	Satellite Selected
GSV4004B	7310	2016-02-08 00:00, 2016-02-08 23:59	30	GPS(1 -37)

Figure 12: A screenshot of the web-based novel GUI application software used for analysis and display of various parameters derived from the data received from GPS (GSV4004B) and GNSS (PolaRxS) receivers as a function of time.

The software allows the user to seamlessly combine and compare the Total electron content (TEC), ionospheric scintillation index (S4) and also other parameters in real time and make these available to the registered users. The software package is designed and developed using various web-utilities like Apache (Web Server), PHP scripts, J-Query, and My-SQL. The software uses MATLAB for plotting the parameters and produce browser compatible output. This analysis tool brings out a number of features associated with the electrodynamics of the low latitude ionosphere.

(A. A. Manke, D. Chakrabarty)

Impact of the perturbation zonal velocity variation on the spatio/temporal occurrence pattern of L-band scintillation - a case study

The earlier evolved method for the forecast of the spatio-temporal variation of L band scintillation based on the expected variation of the perturbations, under favourable ionospheric/thermospheric conditions, has been refined by duly accounting for the local time variation of the zonal velocity of the perturbations. The unique combination of the two geostationary satellites (GSAT-8 and GSAT-10) over the Indian zone has been used to estimate the typical local time dependence of the perturbation velocities by closely following identifiable features in the scintillation pattern. The measured velocities, that registered a steady decrease with the progression of night, had been shown to significantly alter the forecast pattern of the scintillations with respect to longitude and local time. The significant improvement in the forecast pattern has been demonstrated through a case study putting the forecast method on a firmer footing.

This work was carried out in collaboration with Mala Bagiya of IIG, Surendra Sunda of AAI on deputation to SAC, Tarun K Pant and Rajkumar Chaudhary of SPL, VSSC.

(R. Sridharan)

Nonlinear wave-wave interactions in the middle atmosphere over low latitude stations

The low latitude diurnal tide amplitude exhibits clear intermittent modulation at periods of planetary waves in the mesosphere and lower thermosphere (MLT).

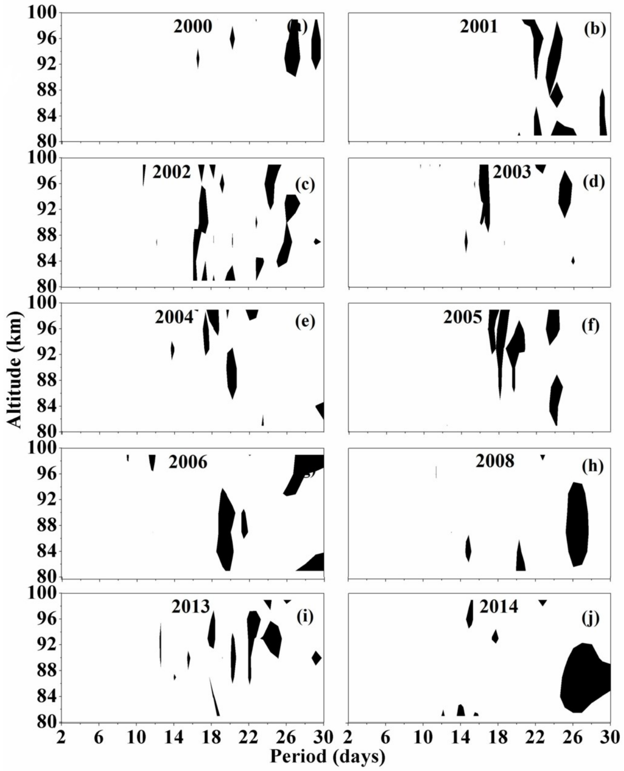

Figure 13: Lomb-Scargle periodogram of powers greater than 95% confidence value estimated from the QTDW amplitude are shown in the MLT for the years (a) 2000, (b) 2001, (c) 2002, (d) 2003, (e) 2004, (f) 2005, (g) 2006, (h) 2008, (i) 2013, (j) 2014. Clear modulation in the long periods ($>$ 10 days) is noticeable.

An indication of coupling of the diurnal tide with the intraseasonal oscillations is noticed at various times of the year. Modulation of the quasi-2-day wave (QTDW) amplitude in the periods of planetary wave is found (Figure 13) implying nonlinear interactions between the QTDW and longer period waves. The strong quasi-2-day wave activity, as observed at this location, has potential to cause significant effect on the overlying ionosphere and hence the atmosphere-ionosphere dynamical coupling.

The above work is carried out in collaboration with P. P. Batista and B. R. Clemesha, National Institute for Space Research, Brazil.

(A. Guharay)

Refinement of the background ionospheric conditions and plausible explanation based on neutral dynamics for the occurrence/non-occurrence of L-band scintillation patches against forecast

The recently evolved L-band scintillation forecast mechanism based on the characteristic features of the daytime F-region electron density fluctuations and also on the basic ionospheric conditions had been successful to a reasonable extent in forecasting the spatio-temporal map of scintillation patches. There had been a few non-compliances in the expected pattern within/outside the forecast windows. Attention has been paid to such non-compliances and a plausible explanation based on neutral dynamics, especially the local time variation of vertical winds over the magnetic equator has been offered, while at the same time refining the earlier stipulated background ionospheric conditions. With the above refinements, it is anticipated that the forecast mechanism would become very robust. The present results highlight the importance of the neutral dynamical parameters and the urgent need to concentrate on the efforts to make systematic measurements of the same in order to characterize their variability.

This work was carried out in collaboration with Mala Bagiya of IIG, Surendra Sunda of AAI on deputation to SAC, Tarun K. Pant and Rajkumar Chaudhary of SPL, VSSC.

(R. Sridharan)

Spatio-temporal forecast model for L-band scintillation Vs in-situ measurements by C/NOFS satellite- a case study

The spatio-temporal maps generated in the recent times to forecast the occurrence pattern of plasma density irregularities that cause ionospheric scintillations based on the characteristic features of the daytime F-region electron density fluctuations had been put to further test by directly comparing the forecast with the in-situ measurements by the Communication/Navigation Outage Forecasting System (C/NOFS) satellite.

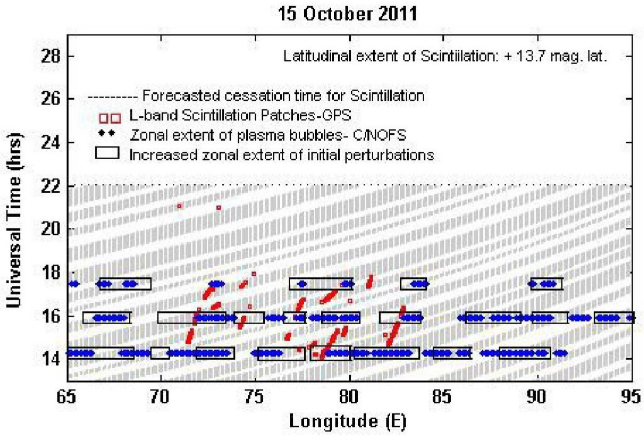

Figure 14: Spatio-temporal forecast map for ionospheric irregularities and the consequent L-band scintillations for 15 October, 2011 over the Indian longitudes (65-95°) after accounting for the representative zonal velocity variations. The shaded region represents the scintillation prone areas. Thick dotted line indicates the plasma bubbles as observed by C/NOFS. Open circles represent the S_4 index as derived from GPS measurements over the Indian region. The boxes indicate the representative extension of the zonal extent due to the mushrooming effect of the plasma bubble undergoes during its evolution.

Though the overall comparison had been good, the present results highlight the need to account for the increase in the zonal extent of a plasma bubble as it evolves from the base of the F-region extending well into the topside of the F-region of the ionosphere. The forecasts based on i) the temporal variation of the density perturbations derived from the F-region peak plasma densities taken to represent the fluctuations in the base of the F-region over a single location and ii) a-priori knowledge of the zonal velocity of the perturbations, have been found to reasonably agree with the actual measurements by C/NOFS. The current study, while validating the earlier assumptions in the forecast scheme, further demonstrates the need to account for all the relevant parameters that control the evolution of the plasma bubble which serves as the seat for the generation of the medium scale irregularities responsible for the L-band scintillations.

This work was carried out in collaboration with Surendra Sunda of AAI on deputation to SAC and with Tarun K Pant of SPL, VSSC.

(S. Yadav and R. Sridharan)

The impact of the 17 March 2015-St. Patrick‘s Day storm on the evolutionary pattern of Equatorial Ionization Anomaly over the Indian longitudes using high resolution spatio-temporal TEC maps-New insights

The inherent advantage of a ground based SBAS (Satellite Based Augmentation System) enabled receiver to yield 2-D (lat x long) TEC maps at unprecedented spatial and temporal resolution has been put to effective use in bringing out the impact of St. Patrick‘s Day storm, that occurred on 17^{th} - 18^{th} March 2015 on the major equatorial electro-dynamical process viz., the Equatorial Ionization Anomaly (EIA). The time evolution of i) the impact, ii) the spatial (lat x long) variation in its magnitude, iii) the inhibition of EIA followed by iv) its recovery etc., have been brought out for the first time through these unique TEC maps. The signatures of wave number 4 (WN4) structure of the EIA and its variability during different phases of a geomagnetic storm within the narrow vicinity of 40° longitude emerge as a notable outcome. Results reveal the complete reversal in the longitudinal structure of EIA during the recovery phase of the storm as compared to the quiet day indicating the possible distortion of WN4 longitudinal structure of the EIA by the storm associated processes. They can be explained in the light of the combined effects of, i) the penetration electric fields of magnetosphere origin, ii) activation of the storm induced disturbance dynamo and, iii) the consequent thermospheric winds, effectively distorting the longitudinal WN4 structure of the EIA. It has been shown for the first time that even a separation of few degrees in longitude could experience significantly different forcings. The relevance and the far reaching consequences of the study in the light of the current trends and requirements for reliable satellite based navigation are highlighted.

This work was carried out in collaboration with Surendra Sunda of AAI on deputation to SAC.

(S. Yadav and R. Sridharan)

SBAS derived TEC maps-a new tool to forecast the spatial maps of maximum probable scintillation Index (S_{4max}) over Indian region

Realizing the importance of satellite based navigation in life critical applications like civil aviation, and its vulnerability to the ionospheric scintillations, as the latter could cause loss of lock of the satellite signal thus affecting the accuracy and availability of vital position information, forecasting the occurrence pattern of the ionospheric scintillation along with its maximum probable intensity has become of paramount importance. Once indicative forecasts have become available, it would serve as a warning to the user so as to be prepared well in time to take counter measures. By making use of the established relation between the dusk time vertical TEC (TEC_{1930}) and the maximum probable S_{4max} and also employing the innovative method of retrieving spatio-temporal TEC data from the ionospheric delay information generated and transmitted in real time by an SBAS for the use of navigators, S_{4max} maps generated as early as 1930 LT and that which would be valid for the whole night have successfully been generated. Except on a very few occasions the actual scintillation intensity had turned out be lesser than what has been forecast for S_{4max}. Further, the spatial pattern of the scintillations is also noticed to be well aligned with the TEC distribution. The present study presents an integrated picture and demonstrates that a viable forecast map indicating not only the spatial occurrence pattern but also the intensity of maximum probable scintillations is becoming a reality. With the superposition of the perturbation pattern on the maps, the temporal variation of the occurrence pattern could be delineated, highlighting the scintillation and no-scintillation zones at any given instant.

This work was carried out in collaboration with Surendra Sunda of AAI on deputation to SAC.

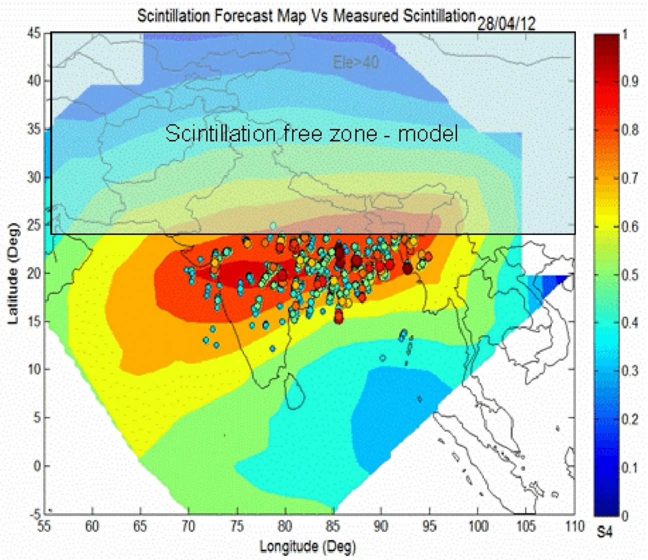

Figure 15: The occurrence pattern of L band scintillation in the back drop of the forecast model contours. The actual occurrence is well aligned to the forecast pattern and the intensity is consistently less than the model forecast and the model forecasts well the upper latitudinal limit for the scintillations taking it one step closer to operational forecasting for satellite navigation purposes.

(S. Yadav and R. Sridharan)

Observation of Neon at mid and high latitudes in the sunlit Lunar Exosphere: Results from CHACE aboard MIP/Chandrayaan-1

The distribution of neutral Neon at the mid and high latitudes in the sunlit lunar exosphere observed by CHandra‘s Altitudinal Composition Explorer (CHACE) aboard the Moon Impact Probe (MIP) of the Chandrayaan-1 has been estimated. The CHACE observations were made when the Moon was in the Earth‘s magneto-tail. The upper limits of the surface number density is found to vary from (7-22) × 10^3 cm^{-3} at the pole, to (3-5) × 10^3 cm^{-3} in mid (50_S) latitudes and to (0.5-1.1)× 10^3 cm^{-3} in lower (20_S) latitudes. The surface number densities estimated at lower latitudes from CHACE observations are found to be consistent with the LADEE Neutral Mass Spectrometer (NMS) observations providing an independent confirmation.

This work has been carried out in collaboration with Tirtha Pratim Das, Smitha Thampi and Anil Bhardwaj of SPL, VSSC, and Syed Maqbool Ahmed of Central University, Hyderabad.

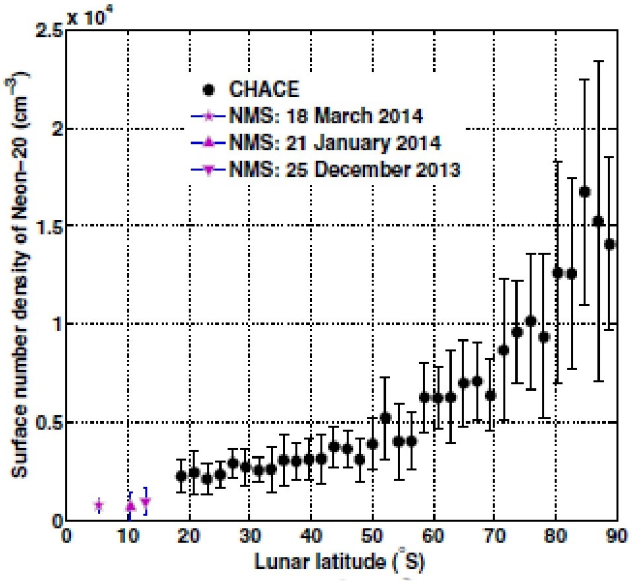

Figure 16: Variation of surface number density of neon with latitude in southern hemisphere of the Moon as observed by CHACE on the moon impact probe of Chandrayaan-1 (filled circles). The measurements from the Neutral Mass spectrometer on board LADEE space craft from low latitudes is also shown for comparison.

(R. Sridharan)

Dust storm and electron density in the D region ionosphere of Mars and Earth

We report the first model result for dust densities and electron densities in the D-region ionosphere of Mars for aerosol particles of different sizes during major dust storm that occurred in Martian Year 25 at low latitude. These calculations are made at latitude 10°S and Solar Longitude = 200°, 220°, 250° and 280° for high, medium, low and absence of dust storms respectively. Four corresponding dust layers were found at 55 km, 50 km, 38 km and 25 km during these events (Figure 17). During high dust storm period the optical depth and dust density increased by a factor of ∼20 from its normal condition. The electron densities estimated for the D region ionosphere of Mars for submicron sized dust particles are largest as compared to that estimated for larger particles. The electron density reduced by ∼2 orders of magnitude during high dust storm. The estimated electron density of Mars is compared with measurements of Earth‘s ionosphere at nearly the same geophysical condition. In comparing D region ionosphere of Mars with Earth‘s ionosphere we have considered the electron density peak estimated in the clear atmosphere (τ = 0.1 and dust size = 0.2 μm) of Mars as being suitable for comparison with rocket measurements on Earth. We found that the estimated peak densities in the clear atmosphere of Mars are lower by factors of 2-5 from the measurements on Earth. The peak heights of calculated electron densities on Mars are lower by factor of $\sim$3 with respect to the measurements on Earth.

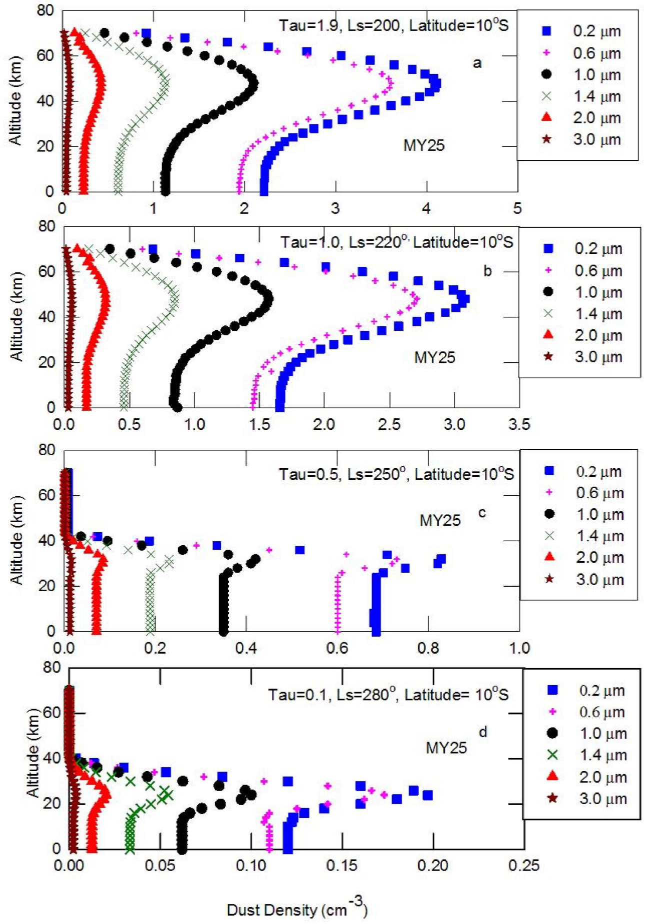

Figure 17: Altitude profiles of dust densities at 10°S for different size of aerosol particles in the spring season of MY25 at (a) Ls=200°, (b) Ls= 220°, (c) Ls=250° and (d) Ls=280°.

(S. A. Haider, V. Sheel and Y. S. Siddhi)

Flare X-ray photochemistry of the E region ionosphere of Mars

Based on electron density profiles obtained from the Mars Global Surveyor we report X- ray flare responses in the E region ionosphere of Mars during six events that occurred on 28 March and 6 April, 2001; 17, 18 March and 21 April, 2003 and 19 February, 2005. We have developed a time dependent Analytical Yield Spectrum model to calculate a time series of photoionization rate, photoelectron impact ionization rate, photoelectron flux, ion density, electron density and Ionospheric Electron Content (IEC) of the E region for each flare day. The estimated production rate, flux and densities increase by 1-2 orders of magnitude due to effect of these flares in the E region ionosphere of Mars. The estimated IEC are compared with the measured IEC. It is found that the normalized IEC of the simulated E layer increased by a factor of 5-10 at the flare time compared to a factor of 2 enhancements in the normalized IEC of the corresponding MGS profiles. The time dependent ionospheric calculations in the E region were not carried out earlier. For the first time we have developed this model. Our model is useful for studying the time dependent aeronomical processes due to the effect of X-ray flares in the E region ionosphere of Mars.

(S. A. Haider, Y. S. Siddhi and P. Thirupathaiah)

Chemistry and Seasonal Variability of O_3 in the lower atmosphere of Mars

We have estimated density profiles of O_3 from Global Circulation Model in the lower atmosphere of Mars between solar longitude 0° and 360° at different altitudes, latitudes and longitudes. These density profiles are integrated from 0 to 70 km to obtain the column density of O_3. These calculations were carried out for Martian Year 29. Recently the SPICAM UV spectrometer onboard Mars Express observed the seasonal variability of the column density of O3. We have processed these data for modeling studies of O_3 variability with seasons in northern and southern hemisphere of Mars. The estimated column density of O_3 is compared with the SPICAM observations. We have also calculated production rates of O_3^+ at different latitude, longitude and seasons. The ion production rate of ozone is calculated by using energy loss model. In this calculation the impact ionization source is taken as galactic cosmic rays. The model calculation shows that the production rates of ozone are maximum in winter and minimum in summer. Ozone is produced minimum in summer, indicating an efficient O_3 destruction by the HO_x radical released from large amount of water vapor and sunlight. Ozone is large near the surface of Mars because it is created from three body reaction due to combination of O, O_2, and CO_2, where the densities are high. At high altitudes, production of O_3 decreases with the density and the balance between O and O_3 move toward O from the photolysis of O_3 (O_3 +hν O + O_2). This process is decreasing O_3 by increasing O at high altitude. There is a distinct peak in the density of O_3 at about 50 km. This peak is formed when loss of O_3 is low by HO_x radical due to lack of H_2O in that region.

(S. A. Haider and Y. S. Siddhi)

Modeling of CO Cameron band emission intensities in the dayside atmosphere of Mars: MEX and MAVEN observations

We have developed a model to calculate the photoelectron energy fluxes and emission intensities of the CO Cameron bands in the upper atmosphere of Mars between solar zenith angles 0° to 90°. The production and loss mechanisms of CO($a^3\Pi$) are incorporated in the model. The atmospheric neutral parameters are adopted from the Mars Climate Database (v5.2). The required solar EUV fluxes are taken from the Solar 2000 model (v2.37) and scaled to Mars. The photoelectron fluxes are calculated at different solar zenith angles using an analytical yield spectrum approach based on the Monte Carlo method. In this model we have assumed that crustal magnetic fields are horizontal in direction. Thus, photoelectrons are losing their energy at the same height where they are produced. This assumption is valid at mid and high latitudes where magnetic fields are mostly horizontal. We have also developed a coupled chemistry model to calculate the ion and electron density at different solar zenith angles, which are used in the airglow model. The model results are compared with the observations provided by the SPICAM/MEX and IUVS/MAVEN. Our model reproduces the observed intensity profiles quite well. The CO($a^3\Pi$) is produced due to photoelectron excitation/dissociation, photodissociation, and dissociative recombination processes. It is destroyed by CO_2, CO and radiative decay. It is found that photon and photoelectron dissociations are dominant production processes of CO($a^3\Pi$), while radiative decay is a major loss mechanism of this state. The estimated photoelectron fluxes, production rates and intensities are decreasing with increasing solar zenith angles.

(S. A. Haider and P. Thirupathaiah)

Response of dust storm to radiative transfer modelling for infrared thermal emission on Mars: PFS/MEX observation

We have developed a radiative transfer model for dusty atmosphere of Mars. This model is used to estimate thermal emission spectra for Martian Year (MY) 28 before and after the dust storm season at low latitude region between 0°-10°, 10°-20° and 20°-30° respectively. The atmospheric inputs are taken from Mars Climate Database (MCD v5.2) for dust season of MY 28. We have estimated dust profiles empirically for different size of aerosol particles of radius $\leq 3\ \mu$m. We have retrieved brightness temperatures from thermal emission spectra obtained from the averaged PFS data. The CO_2 has very high absorption around wave number 667 cm^{-1}. The spectral region from 250 to 500 cm^{-1} is determined by H_2O, which produces a continuum emission. The absorption of dust is observed between wave number 900 cm^{-1} and 1200 cm^{-1} at low latitude in southern hemisphere. The maximum brightness temperature ∼280 K is measured at Ls=240° when Mars received a large amount of solar radiation at perihelion. The minimum brightness temperature ∼220 K is observed at Ls=320° in the absence of dust storm. The suspended dust causes the heating of atmosphere by absorbing the solar radiation. As a result, thermal emission spectra and brightness temperature showed absorption features around 1080 cm^{-1} in for Ls 280° and Ls 300° respectively. We concluded that in the presence of dust storm, brightness temperature are reduced by a factor of ∼2 within the 900 cm^{-1} - 1200 cm^{-1} in comparison to that observed in the absence of dust storm.

(S. A. Haider and M. P. Jethwa)

Spatio-temporal variability of ozone on Mars: Observations vs. Model

The trace species ozone (O_3) is an effective probe of atmospheric chemistry as it is lost by reaction with the active HOX radicals which are produced from water vapour. The hydrogen chemistry stabilizes the CO_2 atmosphere of Mars. Thus ozone measurements offer a powerful constraint for photochemical models. We have studied the spatio-temporal variability of ozone by developing a retrieval algorithm to retrieve total columnar ozone from radiances observed by the SPICAM (Spectroscopy for Investigation of Characteristics of the Atmosphere of Mars) instrument on board Mars Express. We also compare these retrieved observations with the three-dimensional LMDZ photochemistry-coupled general circulation model simulations. The retrievals were done for the Martian years 27 to 30. The comparison of observed and modeled ozone is reasonable except for mid-latitudes. In equatorial region the seasonal variation of ozone shows three peaks, compared to polar regions. Very often an anti-correlation of ozone with water vapour (from GCM) is observed. During the Martian year 28 (MY28), high ozone values are observed during the global dust storm of MY28.

(V. Sheel and A. Modak)

Science

Geosciences

Spatial variation of amount effect over peninsular India and Sri Lanka: Role of seasonality

The monthly amount-weighted mean stable oxygen isotope ratio (δ^{18}O) of tropical rain is negatively correlated with monthly rainfall, where the typical relationship is $\sim$-1.5 ‰ change in δ^{18}O per 100mm of rain. This so-called "amount effect" is exploited for the reconstruction of past monsoon rainfall from δ^{18}O of cave calcites and tree rings from the tropics. The δ^{18}O variations of such proxies are also interpreted in terms of past monsoon intensity. The amount effect is known to exhibit a large spatial variation. Causes include complex cloud-rainout processes and differences in the sources of moisture. Peninsular India and Sri Lanka receive both the Indian summer monsoon (ISM, JuneSeptember) and northeast monsoon (winter monsoon or NEM, OctoberDecember). Over the east peninsular Indian coast and Sri Lanka, NEM is the dominant source of rain, while over the rest of peninsular India, ISM dominates. During the ISM, driven by south westerly winds, the moisture source of rainfall lies in the Arabian Sea and southern Indian Ocean, while during the NEM, north easterly winds bring moisture mainly from the Bay of Bengal (BoB). In southwest India, the local rain amount plays a weaker role in determining δ^{18}O of monsoon rain compared to moisture recycling associated with the large scale convective systems. The seasonal shift in the source of moisture and the associated change in δ^{18}O of the incoming vapor further complicate the rainfall- δ^{18}O correlation. With an aim to optimally choose ^{18}O-based monsoon proxy sites from this region, given the abundant teak trees and limestone caves that possibly house climate archives, we investigated (i) the spatial variation of the amount effect and (ii) the causes for the seasonal difference in δ^{18}O of rainfall in NEM and ISM in peninsular India and Sri Lanka that leads to a stronger amount effect. Analysis of new (and published) data of the δ^{18}O of monsoon rains and vapor at nine stations shows that in regions of distinct seasonality in precipitation (e.g., peninsular India), the noise in such reconstructions can be minimized by a careful selection of sites. Peninsular India receives rain from both the Indian summer monsoon (ISM) and the northeast monsoon (NEM). Significant amount effect is observed only where the NEM rainfall is larger than or comparable to ISM rainfall. This is due to the higher quantity of NEM rain with more depleted ^{18}O relative to ISM rain. NEM rain is more depleted in ^{18}O because of cyclonic activity over Bay of Bengal, and the ^{18}O depletion of Bay of Bengal surface waters due to post-ISM river runoff.

(P. R. Lekshmy, M. Midhun, R. Ramesh)

Intra-event isotope and raindrop size data of tropical rain reveal effects concealed by event averaged data

Evaporation of rain is known to contribute water vapor, a potent greenhouse gas, to the atmosphere. Stable oxygen and hydrogen isotopic compositions (δ^{18}O and, δD, respectively) of precipitation, usually measured/presented as values integrated over rain events or monthly mean values, are important tools for detecting evaporation effects.The slope $\sim$8 of the linear relationship between such time-averaged values of δD and δ^{18}O (called the meteoric water line) is widely accepted as a proof of condensation under isotopic equilibrium and absence of evaporation of rain during atmospheric fall. Here, through a simultaneous investigation of the isotopic and drop size distributions of seventeen rain events sampled on an intra-event scale at Gadanki (13.5°N, 79.2°E), southern India, we demonstrate that the evaporation effects, not evident in the time-averaged data, are significantly manifested in the sub-samples of individual rain events. We detect this through (1) slopes significantly less than 8 for the δD-δ^{18}O relation on intra-event scale and (2) significant positive correlations between deuterium excess (*d*-excess=δD-8$*\delta^{18}$O; lower values in rain indicate evaporation) and the mass-weighted mean diameter of the raindrops (D*m*). An estimated $\sim$44$\%$ of rain is influenced by evaporation. This study also reveals a signature of isotopic equilibration of rain with the cloud base vapor, the processes important for modeling isotopic composition of precipitation; *d*-excess values of rain are modified by the post-condensation processes and the present approach offers a way to identify the *d*-excess values least affected by such processes. Isotope-enabled global circulation models could be improved by incorporating intra-event isotopic data and raindrop size dependent isotopic effects.

This work was done in collaboration with NARL and Pondicherry University.

(R. A. Jani, R. Ramesh)

Validation of δ^{18}O as a proxy for past monsoon rain by multi-GCM simulations

Stable oxygen isotope ratios (δ^{18}O) of tree cellulose and speleothem carbonate are useful proxies for past monsoon rain in many tropical regions, as a decrease in rain δ^{18}O is observed with increase in rainfall on a monthly time scale. This amount effect varies spatially; therefore a local calibration, with actual measurements of rain amount and its δ^{18}O is required. Such observations, however, are quite limited in space and time. To circumvent this difficulty, many isotope enabled general circulation models (GCMs) are used to aid the interpretation of ^{18}O proxies; nevertheless, *all such simulations* taken together are yet to be evaluated against observations over the Indian summer monsoon (ISM) region. Here we examine ten such GCM simulations archived by the stable water isotope Intercomparison Group, phase 2. The spatial patterns of simulated ISM rainfall and its δ^{18}O are in good agreement with the limited observations available. Simulations nudged with observed wind fields show better skill in reproducing the observed spatio-temporal pattern of rainfall and its δ^{18}O. A large discrepancy is observed in the magnitude of the simulated amount effect over the Indian subcontinent between the models and observation, probably because models simulate the spatial distribution of monsoon precipitation differently. Nudged simulations show that interannual variability of rainfall δ^{18}O at proxy sites are controlled by either regional (rather than local) rainfall or upstream rain out. Interannual variability of rainfall δ^{18}O over the East Asian region is well correlated with ENSO, while it is only weakly correlated over the Indian sub-continent.

(M. Midhun, R. Ramesh)

Long-term patterns of net phytoplankton and hydrography in coastal SE Arabian Sea: What can be inferred from genus level data?

Based on 21 years of phytoplankton and environmental monitoring data from the surface water of coastal southeast Arabian Sea, we demonstrate a shift in phytoplankton community towards higher sample genus richness and diatom abundance during the two decades of observations. Analyses were based on 587 water samples collected between 1990 and 2010 and additionally revealed marked long-term changes in sea surface temperature (SST), sea surface salinity (SSS) and turbidity (Secchi depth). The abundances of dinoflagellate genera were positively correlated to SST, particularly during and after the 1997-1998 El Ni$\sim$no Southern Oscillation event. Several diatom genera increased in abundances with decreasing turbidity around and after 1995-2000, mainly the large celled genera *Coscinodiscus spp*, *Odontella spp* and *Ditylum spp*. In 1996-2000, sample genus richness increased from mean of 8-14, and decreased to 11 thereafter. The increase in sample genus richness was linked to the more frequent presence of most taxa during 1996-2000. Increasing Secchi depth and abundance of frequently encountered large-celled diatoms concurrent with decreasing abundances of Trichodesmium spp might signal the alleviation of the nitrogen limitation in the region, favouring diatoms.

This work was done in collaboration with University of Gothenburg and Karnataka University.

(R. Ramesh)

Dissolved Iron (DFe) distributions in the Arabian Sea during post southwest monsoon

Arabian Sea (AS) is one of the highly productive basins in the world Oceans and is characterized by the presence of perennial intense oxygen minimum zone in intermediate water. High resolution DFe distribution in the Arabian Sea during post southwest monsoon period of 2015 is obtained as a part of GEOTRACES-INDIA programme. A total of 18 full vertical profiles were measured onboard along the cruise track in the western Arabian Sea.

DFe concentrations ranges from 0.3 nM to 6 nM in this section with the high values observed in the shelf region of eastern AS indicating release of iron from the highly reductive shelf sediments and low values were noticed along western AS. Elevated concentrations of DFe (1.8 nM) have been observed in the OMZ region and along the Carlsberg Ridge. Atmospheric deposition, upwelling of subsurface waters along with the presence of Fe binding ligands in the AS waters are resulting in the elevated concentrations. The hydrothermal vent fields along Carlsberg Ridge are also contributing to the DFe concentrations in the Arabian Sea. The lower Fe/NO_3 seems to be responsible for HNLC (High nutrient low chlorophyll) region in the western AS during post southwest monsoon period when winds are not favourable for atmospheric deposition.

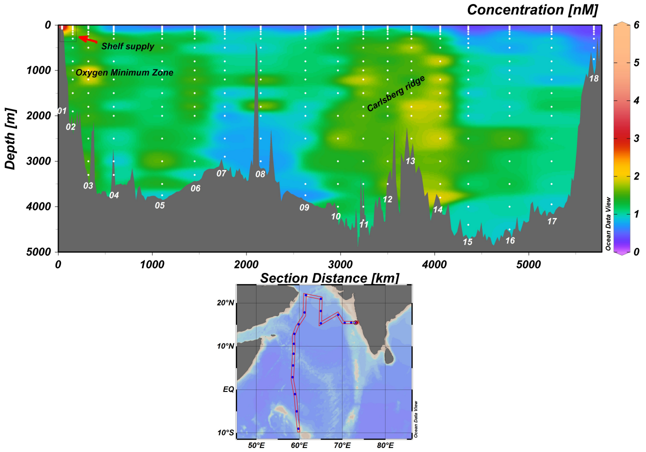

Figure 1: Distributions of DFe along the cruise track in western Arabian Sea during SK-324.

(V. Chinni, S. K. Singh)

REEs in the Arabian Sea water column

To construct the water masses and the potential sources of trace elements in the Arabian Sea (AS) water column, water samples were collected at 14 stations from AS during summer (April-May) 2012 (Fig. 2) and analyzed for their REE abundances.

REE concentrations are higher in the AS surface waters, minimum at top of the OMZ and maximum at the deeper depth. The higher concentration of REEs in surface waters is consistence with the atmospheric inputs. In subsurface waters, the REE concentrations are depleted compared to surface waters. Ce abundance is increased in the OMZ due to reduction of its oxidation state. REE concentrations except Ce display a systematic enhancement with depth below the OMZ.

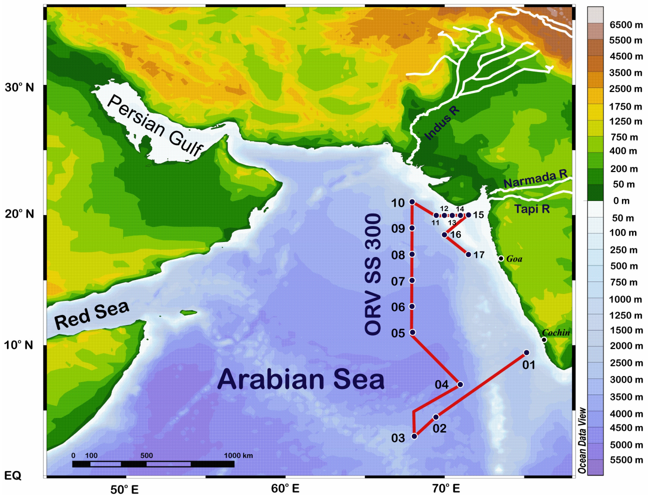

Figure 2: Sample location along the cruise track in the Arabian Sea during summer (April-May)2012.

(K. Damodararao, S.K. Singh)

REEs and $\varepsilon_{\mathrm{ND}}$ in estuaries of the East Coast of India

The hydrographical and morphological properties alongwith Eh - pH conditions of estuaries play a key role in removal and/or release of trace elements in the mixing zones.Distributions of REEs along with Nd isotope composition both in particulate and dissolved phases have been measured along the salinity gradients in the Hooghly, the Mahanadi, the Godavari and the Krishna Estuaries along the east coast of India. All these estuaries experience large release of REEs in the mid salinity region after their initial loss in lower salinity ranges. In the Hooghly estuary, the observed REEs abundances are $\sim$18 times higher compared to their Riverine abundances due to their release from suspended particulate matter in mid salinity region.The release of REEs is associated with higher concentration of dissolved Mn, lower abundance of Oxygen and decrease in $\varepsilon_{\mathrm{ND}}$ of particulates matters suggesting release of REEs from Fe-Mn oxyhydroxide and from dissolution of silicate phases of the particulates. Such particulate release could contribute one order of magnitude higher REEs compared to their riverine fluxes to the Global oceanic budget.

(K. Damodararao, S. K. Singh)

Archean crustal evolution in the Bundelkhand Craton, India: constraints from whole rock Sr-Nd, zircon U-Pb/Hf and titanite U-Pb isotopes

To understand the evolution and reworking of the continental crust we measured in situ zircon U-Pb (13 granitoids) and Hf (9 granitoids), *in situ* titanite U-Pb (9 granitoids) and combined it with *whole-rock* Sr and Nd analyses for Archean TTGs (16 samples) and geochemically variable high-K granitoids (45 samples) from the Bundelkhand Craton, India.UPb zircon ages reveal that the TTGs were emplaced at 3.42 Ga, 3.33 Ga and 2.72 Ga, while the high-K granites, including sanukitoids, were emplaced between 2.57 Ga and 2.54 Ga.The U-Pb titanite ages corroborate with the zircon emplacement ages for high-K granitoids (ca 2.5 Ga) while in case of TTGs they point towards a much younger event at $\sim$2.5 Ga (probably resetting due to emplacement of high-K granites). The high-K granitoids with higher ^{87}Sr/^{86}Sr (0.71734 - 1.62493) and lower εHf (from -8.9 to +0.4) values have ^{143}Nd/^{144}Nd ratio in the range of 0.51034 - 0.51209 as compared with the TTGs which have lower ^{87}Sr/^{86}Sr (0.72066 - 0.80386) and higher εHf (from -1.6 to +5.9) values while their ^{143}Nd/^{144}Nd ratios are in the range of 0.51016 - 0.51108 respectively. The Hf depleted mantle model ages calculated for high-K granitoids are 3.19-2.86 Ga and for TTGs 3.71-3.48 Ga. The U-Pb ages and chondritic to superchondritic εHf values of the TTGs provide evidence for a long-term episodic growth of juvenile crust from depleted mantle reservoirs between 3.4 and 2.7 Ga. The strongly negative εHf values of the high-K granitoids, together with geochemical features (variable compatible and incompatible elements) indicate that they were a result of multi-stage reworking of the Paleo- to Neoarchean crust and mixing with magmas extracted from an enriched mantle source during a relatively short-lived tectonic event at the end of the Archean that led to the stabilization of the craton.

(B. K. Joshi, S. K. Singh)

Temporal variation in provenance of the Quaternary deposits of the Ganga Plain

Several sediment cores have been drilled in the Ganga Plain traversing from Garhmuktershwar, near the foothills of the Himalaya to the Farakka, near its outflow in India to study the paleo-erosion over the Himalaya and their relation with climate and tectonics. One of the objectives of this study is to constrain the timing of migration of course of the Yamuna River using geochemical and Sr-Nd isotopes proxies. Two sediment cores, from Garhmukteshwar and Kalpi have been dated using OSL in quartz mineral to better constrain the age of sedimentation. 3 samples of Garhmukteshwar core (42 m long) and 10 samples of Kalpi core (50 m long), which were raised from the upper and middle Ganga Plain respectively, have been dated. The age of Garhmukteshwar core ranges from 1.5±.03 Ka (at 5 m depth) to 14±1.3 Ka (at 42 m depth) and Kalpi core from 0.1±.01 Ka (at 1.4 m depth) to 88±3.1 Ka (at 51 m depth). Long hiatus in sedimentation in the Kalpi core has been observed between 26 and 3 Ka. Significant variation in the major element composition of the sediments with depth observed in the Kalpi section suggests variation in their provenances under the influence of climate. Sediment samples are under processing for measurement of their Sr and Nd isotope compositions to better understand the timing of shift in course of the Yamuna River and depositional history during Late Holocene in the Ganga Plain.

This work is being done in collaboration with Wadia Institute of Himalayan Geology.

(S. Ali, S. K. Singh, A. K. Singhvi)

Provenance of the mid-Holocene sediments in the Great Rann of Kachchh, India

The decline of the Harappan Civilization, one of the earliest urban civilizations, has been linked to the demise of a mythical perennial river that originated from the Himalayas and flowed through the Thar Desert. To test this hypothesis we have determined geochemical provenance of sediments, deposited during 5.5 to 1.0 ka in the Great Rann of Kachchh, an uplifted former gulf of the Arabian Sea that housed the purported delta of the river. We find that apart from the river Indus and the Thar Desert, a sub-Himalayan river system had contributed significantly to the basin. Sediments from the Indus Delta were routed through long-shore currents and storm tides, whereas the sub-Himalayan contribution was channelized through the ephemeral Ghaggar-Hakra-Nara streams, during monsoonal flooding. The fact that sedimentation persisted until $\sim$1.0 ka suggests that drying up of the sub-Himalayan fluvial system was not the primary cause for the decline of the civilization.

(A. Chatterjee, J. S. Ray, A. D. Shukla, N. Juyal)

^{40}Ar/^{39}Ar geochronology of Andaman Ophiolite

A geochronological study the Andaman ophiolite was performed along a $\sim$120 km corridor on the eastern margin of the Andaman Islands, which forms part of the Andaman-Nicobar accretionary wedge. This Cretaceous ophiolite sequence occurs as imbricate thrust wedges overlying the Paleogene flysch and Neogene pelagic sediments. Incremental heating ^{40}Ar/^{39}Ar dating of three pillow basalts and a peridotite samples reveals that the ophiolite has a composite thermal history. Apparent age spectra of all the samples suggest a clear two stage evolution, with the high temperature steps (1000 to 1400°C) and the lower temperature steps (400-950°C) showing a staircase pattern and a plateau-like pattern, respectively. The apparent ages of the highest temperature steps vary from 135 Ma to 97 Ma, which appear to suggest multiple crystallization ages. Interestingly, the plateau-like spectra for the lower temperature steps yield indistinguishable ages, although with very high errors (as high as 67% at 1σ), across all the samples. The isochron ages too overlap with the plateau-like ages. Thus the weighted average of the plateau-like ages of 0.9 ± 0.3 (2σ) Ma most likely represents the timing of the latest thermal resetting. Based on the above information we conclude that while different units of the Andaman ophiolite may have been formed at different times, all had seen a major thermal resetting. Considering the position of these rocks vis-à-vis the structural configuration of the Andaman-Nicobar accretionary wedge we infer that there was a mega thrusting event in the region at $\sim$0.9 Ma which was possibly responsible for exhumation of the current outcrops of the ophiolite sequence along the east coast of the Andaman Islands.

This work was done in collaboration with K. Pande, IIT Bombay

(J. S. Ray)

Provenance of sediments in the Neoproterozoic Marwar Basin, Western India

The Marwar Super group of Rajasthan is one of the important Proterozoic sedimentary successions of India. Deposited in an intracratonic basin, the supergroup contains unmetamorphosed and undeformed fluvial siliciclastics, marine carbonates, and minor volcaniclastics. Formed above the $\sim$750 million year old Malani igneous complex and bounded by Proterozoic mountain belts at the eastern boundary, the sedimentary history of the basin would most likely have recorded the post-Rodinian tectono-climatic evolution of the Indian shield. In addition, owing to its continuity well into the early Cambrian, these deposits are believed to hold clues to the early evolution of animal life. To understand the evolutionary history of the basin, we determined the provenance of siliciclastic sediments using geochemical and isotopic tracers.

We find that most of the sandstone and shale formations show trace element patterns (e.g., LREE enrichment) and key trace element ratios (Th/Sc = 3.51, Eu/Eu* = 0.64, $f_{Sm/\mathrm{Nd}}$= -0.44) akin to those of the upper continental crust. They possess very low $\varepsilon_{\mathrm{N}d}(0)$ (-22.4 to -9.1) and T_{DM} in the range of 2.8 to 1.2 Ga, with a mode at 2.0 Ga; which clearly suggest derivation of these sediments from Precambrian crustal rocks. A closer scrutiny reveals that most of these sources are located within the Delhi Fold Belt, located to the southeast of the basin, which themselves were derived from the sources in the $\sim$1.7 Ga Sandmata Complex ($\varepsilon_{\mathrm{N}d}(0)$ = -30.5 to -17.8; T_{DM} = 3.0 to 2.6 Ga). Mixing models suggest that the other younger crustal source component is the $\sim$850 Ma Erinpura Granites ($\varepsilon_{\mathrm{N}d}(0)$ = -16.7 to -6.4; T_{DM} = 2.1 to 1.4 Ga). Interestingly, there exists little evidence to suggest that the basin basement, the Malani Igneous Complex, had ever been a significant sediment source, except for the bottommost sandstone formation. These results support the idea that the Marwar craton had already amalgamated with the Aravalli craton at its western boundary and that their relative positions have not changed since then. We speculate that since the rocks of the Delhi Fold Belt also contributed to the Vindhyan Basin located to its southeast, the initiation of deposition in the Marwar Basin to its northwest (i.e., $\leq$635 Ma) might represent the timing of cessation of deposition in the Vindhyan Basin in Rajasthan.

(B. G. George, J. S. Ray)

A comparative study of two- versus three-sequence multidynamic modes for ^{142}Nd analyses by TIMS

Alkaline rocks from Khariar(India) were reported to possess ^{142}Nd anomaly as low as -13 ppm (Upadhyay et al. 2009), which was subsequently questioned by Roth et al. (2014). The latter study was based on a 2-sequence multidynamic analysis on TIMS, of same samples, corrected for mass dependent fractionation using exponential law only, whereas the previous study had used power law normalized exponential law (Upadhyay et al., 2009). We revisited the issue by analyzing new samples from the same locations from Khariar using both the methods. In addition, we also used a simple exponential fractionation law to correct our 3-sequence data. The results of our study (Fig. 3) not only confirm the observations made by Roth et al. (2014) but also reveal that a simple exponential fractionation law correction to the 3-sequence data would yield similar result. This would mean that the data generated in a 3-sequence analysis need not be corrected for relative fractionation rate as prescribed in (Roth et al. 2014).

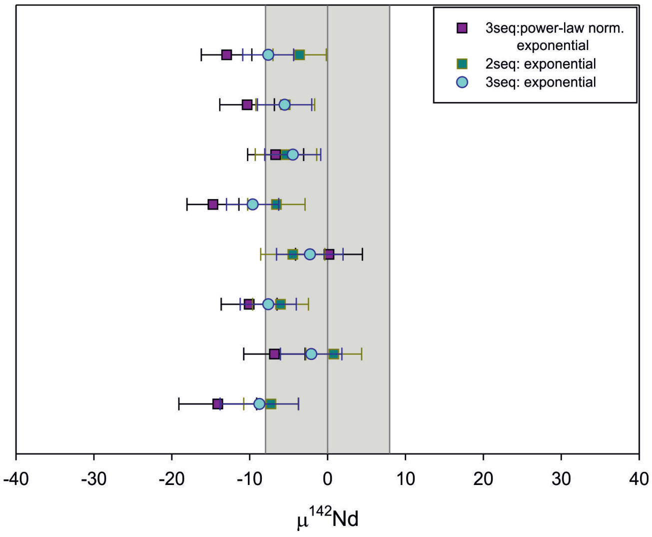

Figure 3: μ^{142}Nd of alkaline rocks from Khariar relative to Ames Nd standard (^{142}Nd/^{144}Nd=1.1418373 with 2RSD=7.97; n=78)

(I. Gautam, J. S. Ray)

Studies on stable isotopic composition of daily rainfall from Kozhikode, Kerala, India

The stable isotopic composition of 113 major daily rain fall samples collected from Kozhikode in Kerala, India for the year 2010, representing the pre-monsoon, southwest and northeast monsoon seasons was examined. The ranges of isotopic variations in daily rainfall during pre-monsoon period were: δ^{18}O: -4.4 ‰ to 2 ‰ ; δ^{2}H: -25.3 ‰ to 13.8 ‰ and d-excess: -2.4 ‰ to 15.3 ‰. During the southwest monsoon period, the ranges of isotopic variations in daily rainfall were: δ^{18}O: -9.7 ‰ to -0.6 ‰ δ^{2}H: -61.7 ‰ to 5.3 ‰ and d-excess 5.8 ‰ 17.4 ‰. During the northeast monsoon period, the ranges of isotopic variations in daily rainfall were: δ^{18}O -11.3 ‰ to -1.4 ‰ ; δ^{2}H: -75.3 ‰ to 0.9 ‰ and d-excess: 8.8 ‰ to 21.3 ‰.

This study showed that daily rainfall events during the two monsoon periods had distinct range of isotopic composition and distinguishable pattern of periodic variations which reveals underlying processes. The stable isotopic content of rainfall during the southwest monsoon period oscillates in a periodic manner, with typical amplitude of $\sim$-2-4 ‰ in δ^{18}O. The δ^{18}O of rainfall during the four months (June, July, August and September) of the southwest monsoon period does not show any correlation with d-excess, which suggests that evaporation from falling rain drop may not be the principal factor behind observed isotopic variation in rainfall.

The northeast monsoon rains were characterised by consistently higher *d-excess*, suggesting moisture contribution from multiple continental sources including locally recycled moisture. The isotopic composition of northeast rainfall oscillates with amplitude of $\sim$9 ‰ , from low δ^{18}O values ($\sim$ -11 ‰) to high ($\sim$ -2 ‰). It is to be noted that range of variation in δ^{18}O values in the northeast rainfall ($\sim$9‰) is considerably larger than that for the southwest monsoon rainfall ($\sim$3 ‰). Most of the rainfall events in northeast monsoon season have significantly higher ($>$15 ‰) *d*-excess values compared to the southwest monsoon.

This study analyzing the stable isotopic characteristics of individual rain events in southern India which is influenced by dual monsoon rainfall will aid in better understanding processes and mechanisms of rain formation in southern India.

This work was done in collaboration with U. Warrier, CWRDM, Kozhikode, Kerala and team

(R. D. Deshpande)

Estimation of snow and glacier melt contribution to Liddar stream in a mountainous catchment, western Himalaya: an isotopic approach

Snow-and glacier-dominated catchments in the Himalayas are important sources of fresh water to more than one billion people. However, the contribution of snowmelt and glacier melt to stream flow remains largely unquantified in most parts of the Himalayas. We used environmental isotopes and geochemical tracers to determine the source water and flow paths of stream flow draining the snow- and glacier-dominated mountainous catchment of the western Himalaya. The study suggested that the stream flow in the spring season is dominated by the snowmelt released from low altitudes and becomes isotopically depleted as the melt season progressed. The tracer-based mixing models suggested that snowmelt contributed a significant proportion (5 - 66%) to stream flow throughout the year with the maximum contribution in spring and summer seasons (from March to July). In 2013 a large and persistent snowpack contributed significantly ($\sim$51%) to stream flow in autumn (September and October) as well. The average annual contribution of glacier melt to stream flow is little (5%). However, the monthly contribution of glacier melt to stream flow reaches up to 19% in September during years of less persistent snow pack.

The tracer-based three component mixing model was used to separate hydrographs into different components. The results suggest that snowmelt dominantly (47%) contributes to average annual stream flow, with the maximum contribution in July (64%). The monthly contribution of rain to stream flow is high in April (17%) and August (18%). The average annual contribution of glacier melt to stream flow is meagre (5%) with a maximum contribution in September (19%). The study also revealed significant correlation (R2=0.98) between simulated glacier discharge (hydrograph separation method) and observed discharge, suggesting the validity of isotope-based hydrographic separation in snow and glacierized mountainous catchments.

This work was done in collaboration with Gh. Jeelani, Kashmir University, Srinagar, J&K and team

(R. D. Deshpande, V. R. Padhya)

Oxygen isotope in archaeological bioapatites from India: Implications to climate change and decline of Bronze Age Harappan civilization

The oxygen and hydrogen isotope data of precipitation at Hissar in Haryana, generated as part of the IWIN National Programme, was used in one of the collaborative studies dealing with climate change and decline of Bronze age Harappan civilization. This study was initiated by IIT, Kharagpur with PRL as one of the collaborators. This study is summarised in the following.

The antiquity and decline of the Bronze Age Harappan civilization in the Indus-Ghaggar-Hakra river valleys is an enigma in archaeology. Weakening of the monsoon after ∼5 ka BP (and droughts throughout the Asia) is a strong contender for the Harappan collapse, although controversy exists about the synchroneity of climate change and collapse of civilization. One reason for this controversy is lack of a continuous record of cultural levels and palaeomonsoon change in close proximity.

A high resolution oxygen isotope (δ^{18}O) record of animal teeth-bone phosphates from an archaeological trench at Bhirrana, NW India, preserving all cultural levels of this civilization, was constructed in this study. Bhirrana was part of a high concentration of settlements along the dried up mythical Vedic river valley 'Saraswati', an extension of Ghaggar river in the Thar Desert. Isotope and archaeological data suggest that the pre-Harappans started inhabiting this area along the mighty Ghaggar-Hakra rivers fed by intensified monsoon from 9 to 7 ka BP. The monsoon monotonically declined after 7 ka yet the settlements continued to survive from early to mature Harappan time. This study suggested that other cause like change in subsistence strategy by shifting crop patterns rather than climate change was responsible for Harappan collapse.

This work was done in collaboration with A. Sarkar, IIT, Kharagpur and team

(R.D. Deshpande, N. Juyal)

Sulphur isotopes as tracers for sea level variability in southern Saurashtra coast, Gujarat, Western India

Sedimentary Sulphur (S) isotopic variability provide clues to oxygenation history of depositional environments. Depleted δ^{34}S values (-20-30‰) indicate pyrite formation environments under bacterial sulphate reduction (BSR). In contrast, sea water sulphates are enriched and δ^{34}S of present day sea water is typically ∼21.0‰ worldwide. Modern sediments (shale), surface soils and atmospheric particulates typically show δ^{34}S values between ∼3-6 ‰ . In coastal environments, δ^{34}S could reveal past sea level variability vis-à-vis anoxic bacterially mediated biogeochemistry.Based on this assumption, relict (Vasoj: VV) and active mudflats (Diu:DV ; Rohisa:RH) of Southern Saurashtra coast, Gujarat, Western India were investigated to decipher mid-late Holocene sea level variability. Present study is a first attempt to use the sulphur isotopes as a proxy for sea level variability.

In this study, we report δ^{34}S depth profiles of ^{14}C dated three mudflat sections from southern Saurashtra coast covering mid-Holocene to present. Based on redox sensitive elements (RSE), total sulphur (TS) and δ^{34}S, two major shifts in sea level regressions ∼3200 and ∼1500 cal yr BP are inferred, which appear to have transformed the studied site from coastal lagoon to mudflat region with a shift in δ^{34}S from -30 ‰ to 11 ‰ . Saurashtra coast being tectonically active region, inferred sea regressions could be localised in nature, requiring more spatial geomorphic evidences. Nonetheless above findings encourage exploitation of sedimentary δ^{34}S as a potential tracer of past sea level changes.

This study was carried out in collaboration with Dr. Rajesh Agnihotri, Birbal Sahni Institute of Paleosciences, Lucknow and Prof. A.J.T. Jull, NSF-AMS Facility, University of Arizona, Tucson, USA.

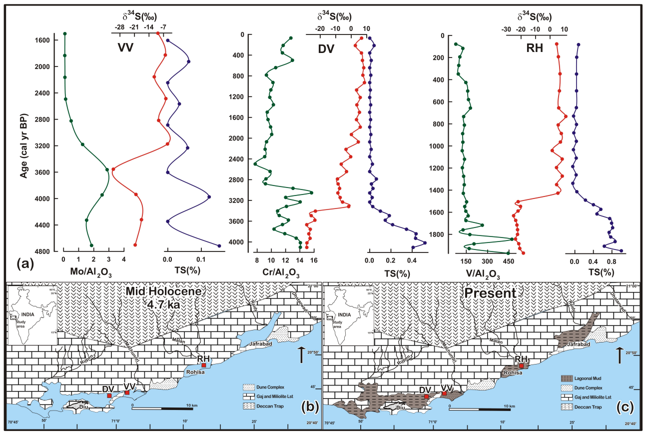

Figure 4: (a) Downcore variation of RSE, δ^{34}S and TS. Two shifts inδ^{34}S viz. ∼3200 and ∼1500 cal yr BP suggest transformation of lagoon to mudflat. (b) shows coastal lagoon during 4.7 ka, while (c) represents extend of present day mudflats along southern Saurashtra coast.

(U. S. Banerji, R. Bhushan, N. Khonde)

Reconstruction of redox conditions in paleolagoon of Vasoj, Southern Saurashtra coast, Gujarat, Western India

The coastal lagoon experiences nutrient input from both land and sea therefore, they are highly productive and eutrophic zones along the coast. Enhanced productivity causes oxygen deficiency thereby forming reducing conditions in the water column and sediment-water interface. Present study attempts to reconstruct paleoredox conditions persisted in the paleolagoon of Vasoj village near southern Saurashtra coast of Gujarat, India based on geochemical proxies. Present study attempts to reconstruct the paleo-lagoonal conditions based on redox sensitive and geochemical proxies. The presence of *Turritella* shells and mangrove pollens in the Vasoj relict section suggests high sea level with a regressive trend (Banerji et al., 2015). The variation of redox sensitive elements suggest that anoxic conditions persisted during 4710-4000 cal yr BP, followed by euxinic conditions from 4000-3200 cal yr BP. Post 3200 cal yr BP, the water column remained oxic till 1500 cal yr BP, when the sedimentation ceased. This study further points that the euxinic conditions during 4000-3200 cal yr BP was not triggered by the intense TOC degradation but was a resultant of sea level lowering, caused by stagnation of water or reduced ventilation of water and thereby developed euxinic conditions. The results further suggest that it was after 3200 cal yr BP that the lagoon got transformed into coast/mudflat

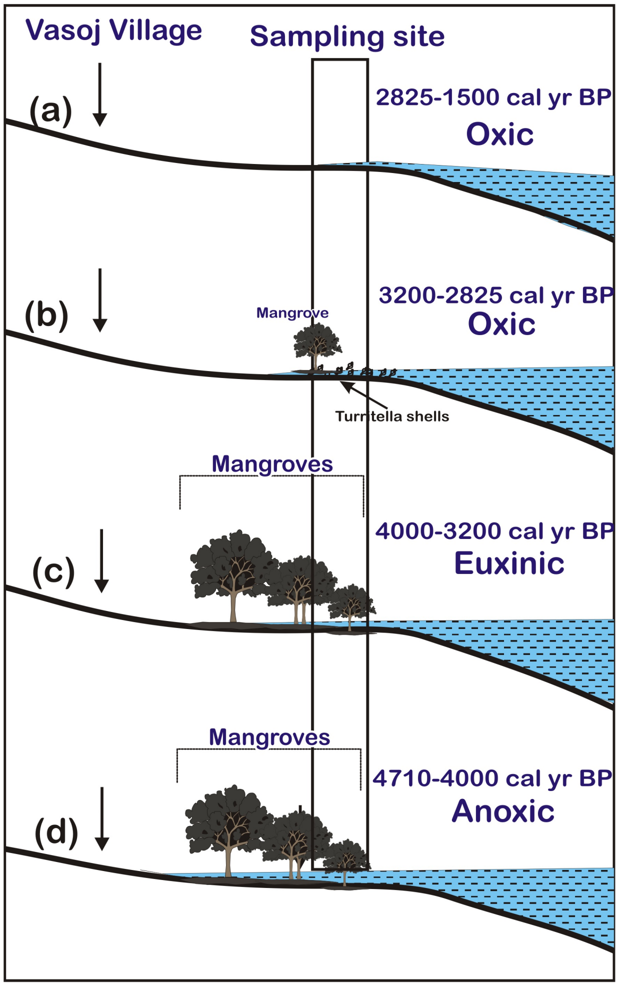

Figure 5: Phases of paleoredox conditions reconstructed for the relict mudflat of Vasoj, Southern Saurashtra coast. Anoxic conditions (d) resulted due to intense *in-situ* productivity by mangrove forest, while euxinic (c) caused by water stagnation/reduced ventilation resulted from sea regression. The region experienced oxic conditions (a and b) since 3200 cal yr BP.

(U. S. Banerji, R. Bhushan)

Coastal Pollution history of the last century from marine sediment records of the Arabian Sea along the Western Indian Coast

Eastern Arabian Sea sediments can provide clues to past monsoon changes in terms of surface productivity, sub-surface denitrification, bottom water redox-conditions and measure of contamination. A sediment core (SM-29-13-03) recovered from the south-eastern Arabian Sea coast was analysed for various major and trace elements. The chronology of this core was ascertained by ^{210}Pb dating technique. This core site is influenced by rivers coming from west coast of India along with many industrial units disposing waste may also have impact on this core site. Thus, this core would provide the anthropogenic influence in coastal cores of Arabian Sea during the last century. To deduce measure of contamination in this coastal cores, other parameters of pollutions like Enrichment Factor (EF), Contamination factor (CF) and Geoaccumulation Index (I_{geo}) were derived. From this study we observed that Cr shows moderately contaminated state while other elements like Pb, Ni and Cu shows uncontaminated to moderately contaminated state. The source for this moderately higher Cr source is not completely understood but this may had come through erosion of soils from mining areas. As Cr shows moderately contaminated state throughout last 120 years but its enrichment have increased in last 20 years. Further studies are going on to understand its possible source and its influence on climate.

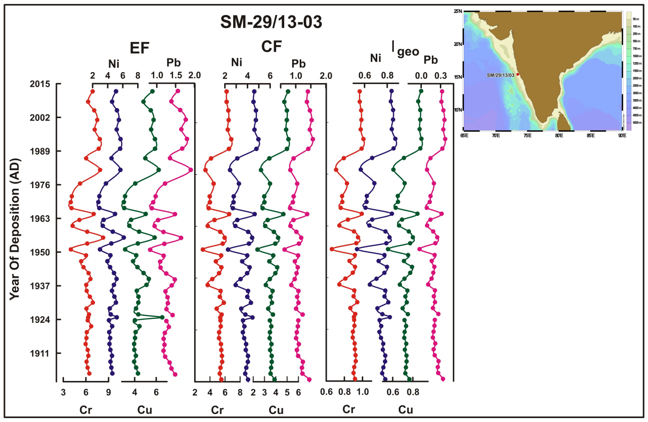

Figure 6: Core location and downcore variation of various pollution indexes for the sediment core SM/29/13/03 retrieved from SE Arabian Sea

(C. Shah, R. Bhushan, U.S. Banerji)

Late Quaternary Nitrate utilisation as recorded by sedimentary nitrogen isotope in the equatorial Indian Ocean

The nutrient availability in the near-surface ocean plays a vital role in controlling the over-head productivity, whose variability had altered major biogeochemical cycles during the past. The equatorial oceanic regions are known for equatorial upwelling process thereby witnessing high productivity leading to enhanced nutrient utilisation. The equatorial Indian Ocean is unique as it witnesses seasonally reversing monsoon associated with high winds thereby causing changes in circulation pattern of surface waters. The present study aims to reconstruct paleo-productivity variations during the last 25 ka in the intermixing zone of Bay of Bengal and Arabian Sea from the equatorial Indian Ocean. Towards this, a sediment core from the equatorial Indian Ocean off southern Srilanka was investigated for various paleo-productivity proxies. The equatorial oceanic regions are known for increased siliceous productivity during enhanced upwelling as a resultant of nutrient utilisation process. The isotopic changes are related to changes in water circulation and surface productivity between glacial-interglacial periods. The Holocene period shows increase in biogenic silica content from 3 to 10% and high Si/OC and Si/N suggests high relative utilisation of silicic acid: nitrate ratio and thus high productivity due to intensification of monsoon.

This study was carried out in collaboration with Dr. Rajesh Agnihotri, Birbal Sahni Institute of Paleosciences, Lucknow and Prof. A.J.T. Jull, NSF Arizona AMS Laboratory, University of Arizona, Tucson, AZ 85721, USA.

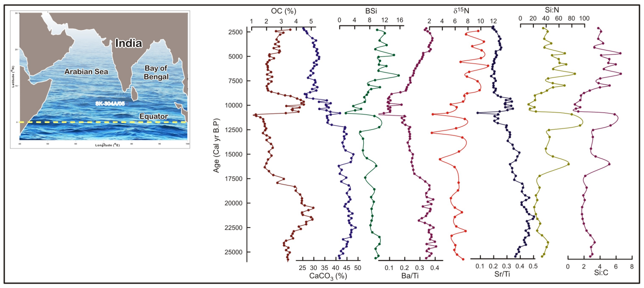

Figure 7: Down core variation of productivity proxies during last 25 ka for the sediment core raised from the equatorial Indian ocean.

(K. R. Chandana, R. Bhushan)

Productivity induced stable isotope variations in the northern Arabian Sea during the last 35 ka

Stable isotopic composition in organic matter is mainly controlled by the nutrient availability, source of nutrient and productivity. The palaeo-productivity record has been investigated along with stable isotopic composition of organic matter for the last 35 ka using radiocarbon dated sediment core from Northern Arabian Sea. Stable isotopic composition of organic carbon and nitrogen has been used to understand the biogeochemical changes associated with palaeo-productivity variations. The sediment record shows contrasting biogenic composition at glacial and interglacial periods with two contrasting phases clearly visible in the down core profiles (Fig. 8).

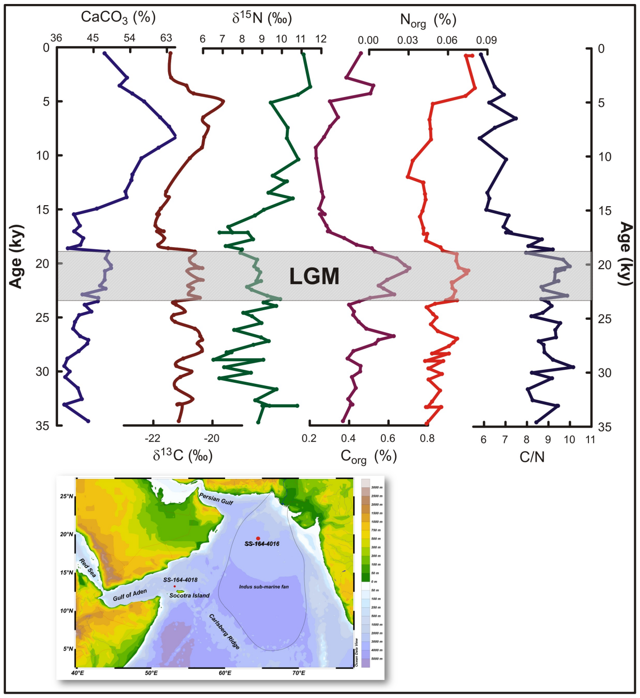

Figure 8: Down core record of productivity proxies in sediment core 4016 retrieved from northern Arabian Sea. Last glacial maximum is shown by grey background.

Preglacial and glacial periods (35 to 19 ka BP) were indistinguishable in the proxy records and post glacial period i.e. 19 ka BP to present shows a different scenario in the proxy records. Besides these observations, Last Glacial Maximum (LGM; 23-19 ka BP) is characterised by high concentration of organic carbon and nitrogen which indicates high productivity in northern Arabian sea during this period. Molar ratio of organic carbon to nitrogen also shows two distinct values before and after the termination of last glacial maximum. Nutrient availability in northern Arabian Sea is mainly controlled by lateral advection of upwelled water along the Omani coast during southwest monsoon and vertical mixing during winter monsoon. The post-glacial increase in stable nitrogen isotope values is attributed to increase in surface productivity and/or decrease in nutrient availability.

This study was carried out in collaboration with Mr. Balaji D. and Prof. L.S. Chamyal, from Department of Geology, the M.S. University of Baroda, Vadodara and Prof. A.J.T. Jull, NSF-AMS Facility, University of Arizona, Tucson, USA

(R. Bhushan, S. Kumar)

Late Quaternary paleoclimatic and paleoproductivity changes in Oxygen Minimum Zone (OMZ) of Eastern Arabian Sea

A sediment core (SK-304/02) raised from sediment-water interface at the Oxygen Minimum Zone (OMZ) of the eastern Arabian Sea at $\sim$760m water depth off Mangalore was investigated. The chronology of this core was ascertained using select planktonic foraminifera species (e.g. *G. menardii, G. ruber, G. sacculifer*) by ^{14}C dating using AMS.

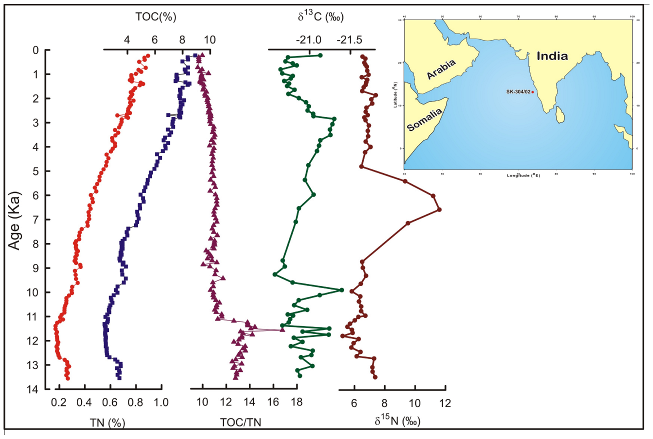

Figure 9: Down core variations in elemental and isotopic geochemical proxies in sediment core (SK-304/02) in the eastern Arabian Sea.

This core records history of past $\sim$15 ka before present. The CaCO$_3$ varies from 13 to 40% throughout the core section and remains below 20% during the Younger Dryas (YD) event corroborating with the low organic content and total nitrogen in the sediments whereas, the C/N ratio is characteristically higher up to 14 to 17 during this time. The δ^{13}C values vary from -20.8 to -21.2 ‰ indicating organic matter predominantly of marine origin and δ^{15}N values of 5.2 to 7.5 ‰ suggesting enhanced denitrification. This suggest that the relatively less intensified OMZ during this period which is also supported by the low TOC, TN, $CaCO_3$ content and high CN values. Thereafter since YD to 9 ka the δ^{13}C largely fluctuates in a narrow range from ~ -20.6 to -21.4 ‰ suggesting marine source for organic matter throughout the deposition of these sediments whereas δ^{15}N shows marginal increase from 6-7 ‰ . The calcareous productivity sharply increases ~11ka to 9 ka on account of the early Holocene monsoon intensification as recorded here. Similar changes are clearly evident in increased preservation in the total organic carbon (3-4%) and total nitrogen (0.2 to 0.4%) content. The C/N ratio on decreased from ~16 to 11 and remains more or less stable throughout the core section. Another important observation to note here is the increased TOC content from 4 to 9% throughout past ~9 ka which indirectly suggests the intensification of the oxygen minimum zone during this period. The highest values of δ^{15}N from ~7 to 11 occur between 9 to 5 ka before present.

This study was carried out in collaboration with Dr. F.J. Santos of Centro Nacional de Aceleradores, University of Sevilla, Spain.

(N. Khonde, R. Bhushan, S. Kumar)

Sedimentation rate variability due to transport of sediments by longshore currents within the continental margin along the Eastern Arabian Sea

There has been a significant amount of studies pertaining to estimation of sedimentation rates in the off shore region of the Arabian Sea. However, there exists a knowledge gap for the ascertaining the sedimentation rates along the western Indian coast. Since the industrial era, both natural and anthropogenically induced climatic perturbation has taken place which are preserved in the coastal sediments of Arabian Sea.

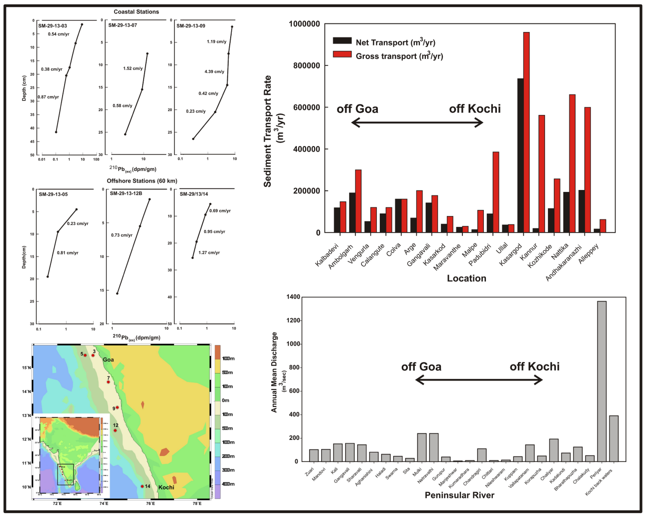

Figure 10: Increased longshore currents with enhanced river flux from off Goa to off Kochi along the western coast of India.

Therefore, the utmost requirement for the reconstruction of paleo environmental conditions is to ascertain the sedimentation rates along the coastal Arabian Sea. Generally, when considering the sedimentation rates and age during the last 100 years, the applicability of ^{210}Pb is evident due to its short half-lives of nearly 22.4 years. Therefore nearly six sediment cores were raised from the coastal Arabian Sea during On-board Sagar Manjusha-29 and the sedimentation rates were estimated using ^{210}Pb dating technique. The present study indicated that there is increased sedimentation rate from north (off Goa) to south (off Kochi). Such increased sedimentation rates has resulted due to high riverine flux towards southern coast compared to the northern part of the study area. Study has indicated that along the western Indian coast, the longshore sediment transport rates has been observed to be mostly towards the south and in the present study, a high sediment rate has been observed at Kerala coast compared to Goa and Karnataka which could have resulted due to southwards sediment transport longshore current.

(C. Shah, U. S. Banerji, K. R. Chandana, R. Bhushan)

Installation of Graphite preparation system from inorganic/organic samples

PRL has procured Accelerator Mass Spectrometer (AMS) and one of its basic requirements for measurement of carbon samples for ^{14}C by AMS is preparation of graphite for both organic and inorganic carbon.

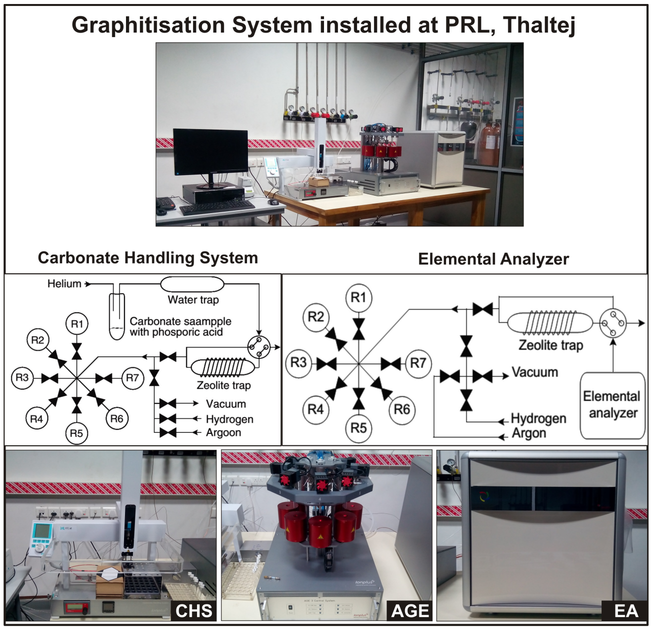

Figure 11: AGE3 Graphitisation system along with CHS and EA as part of AMS Lab installed at PRL, Thaltej.

The organic/inorganic carbon samples to be measured with high precision Accelerator Mass Spectrometry (AMS) measurements are converted in to graphite and this process is known as graphitisation. Therefore, in order to process the samples, Automated Graphitisation Equipment (AGE3) has been installed at PRL, Thaltej campus. The AGE3 system is interlinked with Elemental Analyser (Vario Micro Cube, Elementar) for conversion of CO_2 from organic samples and Carbonate Handling System (CHS) for CO_2 from inorganic samples. The CO_2 thus produced is further transferred to AGE3 through a zeolite trap. Later, the zeolite trap is heated to 450°C for release of CO_2 to be contained in pyrex tube for graphitisation. In AGE3 system, sample CO_2 is mixed with hydrogen in 1:3 proportions in presence of Iron powder acting as a catalyst at ~600°C and graphite is produced in 2 hours, which can be directly used for the measurement in AMS. The AGE3 system has been successfully tested for graphite preparation using CHS and Elemental Analyser. The AGE3 system is capable of converting <1mg of carbon to graphite without any external contamination in short duration.

(R. Bhushan, M. G. Yadava)

Mean residence time of organic carbon in forest soils

To assess the extent of decomposition by microbes and effect of percolation of fresh organic matter into deeper soil layers, two soil sections Kotumsar and Tirathgarh from karst area of Chhattisgarh state in a tropical reserve forest in central India were investigated for soil organic carbon (SOC) content, its mean residence time (MRT) and the evolution of stable carbon isotopic composition (δ^{13}C). Results show that SOC stocks in the upper 30 cm of soil layers are ~5.3 kg/m^2 and ~3.0 kg/m^2; in the upper 110 m are ~10.7 kg/m^2 and ~7.8 kg/m^2 at Kotumsar and Tirathgarh, respectively. Bomb radiocarbon signature is still retained in the upper ~10 cm of soil layers while δ^{13}C values of SOC increase with depth. Organic matters in the top soil layers (0-10 cm) have MRT values of the order of a century which increases gradually with depths, reaching 3500-5000 yrs at ~100 cm.

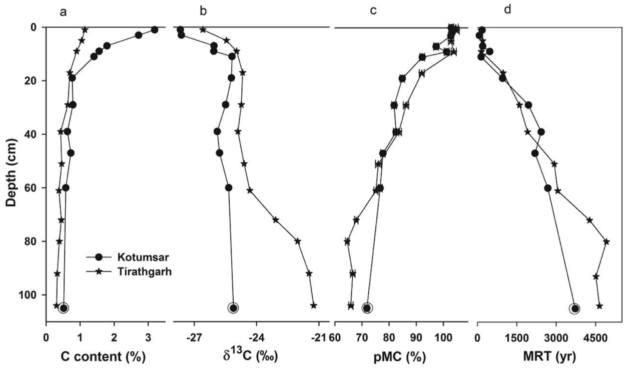

Figure 12: (a) Organic carbon contents in weight%, (b) δ^{13}C of soil organic carbon, (c) Percentage Modern Carbon (pMC) and (d) mean residence time (MRT) of the soil organic carbon in the two profiles. Encircled points at the bottom of the Kotumsar profile are measured values for organic carbon in bedrocks.

(A. H. Laskar, R. Ramesh, M. G.Yadava)

Isotopic composition of seepage water and rainwater in a Karst area

Numerous studies have shown that δ^{18}O of tropical speleothems may serve as a proxy of local precipitation if the local meteorology permits a persistent and a long-term 'amount effect' in the local precipitation. Stalagmites from Belum Cave in Kurnool district of peninsular India have a great potential for reconstructing monsoon for over a million year timescale. We initiated a programme to collect seasonal samples of drip and rain water samples from cave area to verify suitability of the Belum stalagmites for precipitation reconstruction. Based on sampling of drip water during 2007-2009 and 2011 CE, and rain water from May 2010 to Jan 2011 CE, we found that their δ^{18}O values indeed exhibit a significant negative correlation with the amount of the local rain. Changes in δ^{18}O and δD values of drip water samples confirm that the cave drip water do respond to the amount-dependent isotopic changes in local precipitation. Additionally, we found that the *d*-excess of the rain water samples shift from ~10 ‰ during the initial phase to ~30 ‰ during the final phase of the southwest monsoon. This study has demonstrated that Belum stalagmites have potential to reconstruct past monsoon and therefore will be useful to the ongoing efforts from several groups working with speleothems from the Kurnool area.

The work was carried out in collaboration with University of Hyderabad.

(R. A. Jani, R. Ramesh, M. G. Yadava)

Particulate organic carbon export flux in the Bay of Bengal and the Indian Ocean using ^{234}Th-^{238}U and ^{210}Po-^{210}Pb disequilibria

The naturally occurring radionuclide tracers, ^{234}Th-^{238}U and ^{210}Po-^{210}Pb pairs, were measured in the Bay of Bengal and the Indian Ocean along a N-S transect from 20°N to 25°S during March to April 2014 (SK-311) as a part of the Indian GEOTRACES program to evaluate export variability of organic carbon in the Euphotic zone.

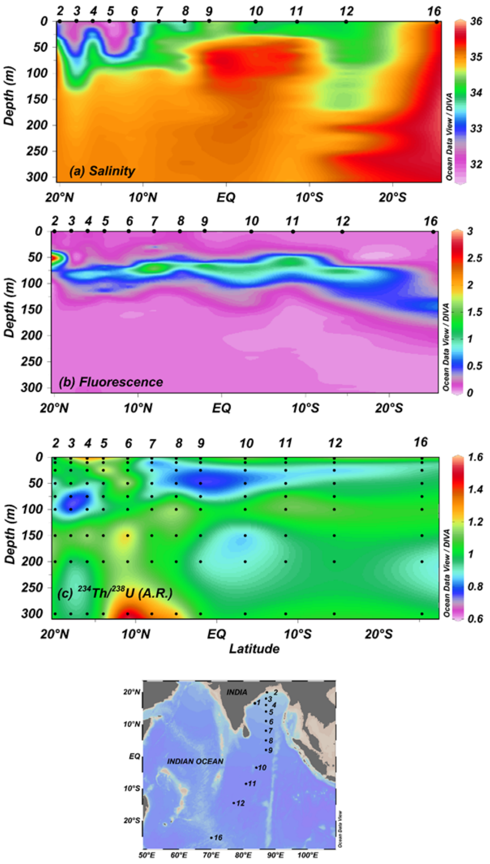

Figure 13 :Distribution of (a) salinity, (b) fluorescence and (c) ^{234}Th/^{238}U in the upper 300 m in the section along 87°E from the Bay of Bengal and the Indian Ocean during March-April 2014.

Seawater profiles for total (dissolved + particulate) activities of ^{234}Th and ^{210}Po-^{210}Pb were measured at 13 and 7 stations, respectively. Particulate organic matter was collected at 200 m depth and measured for organic carbon and activity of ^{234}Th, ^{210}Po and ^{210}Pb.

Chlorophyll concentration varied between 0.5 - 2.5 mg m^{-3} at all stations and the peak value occurred at 20°N in the Bay of Bengal.Chlorophyll peaks were found between 50-100 m depth except at a station at 25.3°S. Euphotic depth varied mostly from 50 to 110 m. Primary productivity varied from 13.2 to 173.8 mmol m^{-2} d^{-1}. Oxygen profiles revealed that the water column was hypoxic to anoxic at depths where ^{234}Th was released. Excess of ^{234}Th immediately below the surface deficit are indicative of particle remineralization by heterotrophic bacteria and zooplankton.In general, ^{234}Th was released in the water column below the chlorophyll peak.In the southern Bay of Bengal, in addition to microbial degradation of organic matter, ^{234}Th was also released from waters below 300 m (3.86-3.59 dpm L^{-1}), possibly due to episodic export events and/or intrusion of high saline seawater to the Bay of Bengal at 300 m depth, thus transporting particulate carbon from regions of high export.POC measured at 200 m depth ranged from 0.45-1.78 μM L^{-1} and organic carbon export flux varied from $\sim$0 to 7.7 mmol m^{-2} d^{-1}; maximum POC and organic carbon export occurred at 2°N.Shoaling of thermocline in the thermocline ridge located in the tropical Indian Ocean influences primary productivity by supplying nutrients to the upper layers (Fig.13). Though northern Bay of Bengal showed more particulate organic carbon (0.65 - 0.93μM L^{-1}) most of the carbon was utilized at the sub-surface depths by microbes and no significant amount was exported to the bottom.

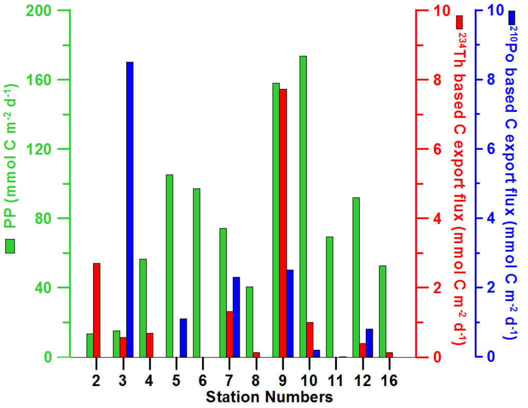

Figure 14: Primary Productivity and carbon export fluxes based on both ^{234}Th-^{238}U and ^{210}Po-^{210}Pb disequilibria.

Profiles of ^{210}Po - ^{210}Pb measured simultaneously at alternate stations showed high ^{210}Pb (19.82 dpm 100 kg^{-1}) in surface waters of northern Bay of Bengal (18°N). ^{210}Po based organic carbon export flux varied from $\sim$0 to 8.5 mmol m^{-2} d^{-1}. High organic carbon export (8.5 mmol m^{-2} d^{-1}) at 18 °N was not captured by ^{234}Th:^{238}U disequilibrium technique due to high riverine sediment flux (Fig.14).Considerably less POC export flux was found at other stations.

This work was carried out in collaboration with Dr. V.V.S.S. Sarma, Regional Centre, National Institute of Oceanography, Vishakhapatnam.

(R. Rengarajan, S. S. Anand, P. Dhruv)

Effect of nutrient stoichiometry on nitrogen assimilation rates

Our knowledge of nitrogen (N) and carbon (C) cycling, particularly N uptake dynamics and its dependence on N and phosphorus (P) distribution in tropical estuaries and the adjacent coastal waters remains rudimentary. Detailed knowledge in this regard is of utmost importance to develop mitigation strategies to restore and save the estuarine-coastal coupled systems from eutrophication.In the recent past, we have performed experiments to quantify rates of $NO_3{}^{-}$, $NH_4{}^{+}$, and C uptake along with N_2 fixation rates in the Cochin Estuary and coastal Arabian Sea using stable isotopes tracer techniques. We observed significant negative correlations of $NH_4{}^{+}$ uptake and N_2 fixation rates with TN:TP during pre-monsoon, which failed during monsoon and post-monsoon. This observation motivated us to carry detailed experiments to examine the N uptake rates at different TN:TP ratios, where we manipulated TN:TP ratios as ambient, 1:1, 5:1, 16:1, and 30:1. Experiments were performed at 8 stations in the Cochin estuary. Results indicate the enhancement in the $NH_4{}^{+}$ uptake rates at TN:TP close to 16:1 (Redfield ratio) at four stations (Fig. 15) and at 30:1 at the other two. Due to inherent affinity of autotrophs in eutrophic estuaries towards $NH_4{}^{+}$, nitrate uptake rates were suppressed and did not show any relationship with varying TN:TP.

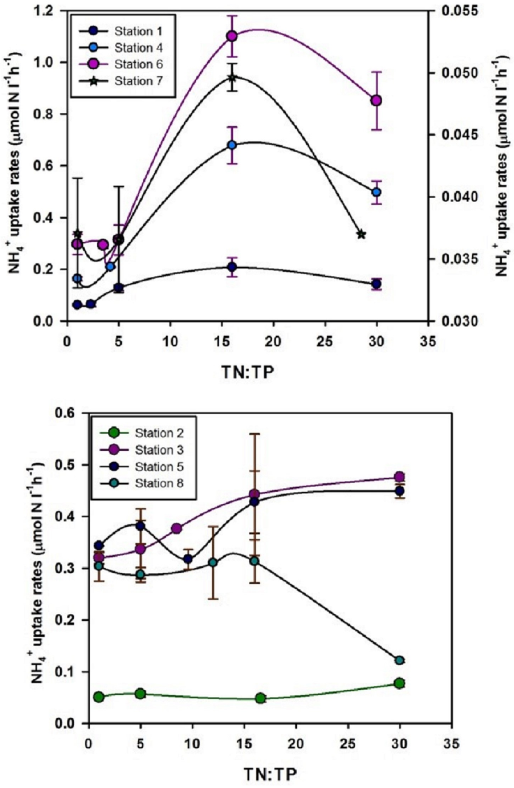

Figure 15: Nitrogen uptakes rates under varying TN: TP. Right hand side in upper panel refers to station 7 only.

(P. S. Bhavya, S. Kumar)

Biogeochemistry of the Chilika Lake

Chilika Lake, a brackish water lagoon (64.3 km long and 20.1 km wide) located on the east coast of India, is one of the important ecosystems economically as well as ecologically.This lake also acts as the largest wintering ground for the variety of migratory birds in the Indian subcontinent.Now a day the lake is suffering from eutrophication problem owing to natural (tidal) and anthropogenic (riverine inputs) forcings. To account for the high productivity, we measured dissolved inorganic nitrogen uptake rates along with N isotopic composition of particulate matter at sixteen locations within the lake during 16-29th June, 2015 (premonsoon). Ammonium uptake rates in the Chilika Lake ranged from 0.30 to 5.76 μmolN l^{-1}h^{-1} with an average of 2.44$\pm$0.20 μmolN l^{-1}h^{-1}, whereas NO_3^- uptake rates ranged from 0.005 to 1.57 μmolN l^{-1}h^{-1} with an average of 0.54$\pm$0.05 μmolN l^{-1}h^{-1}. Ammonium uptake rates were significantly higher than the nitrate uptake rates. The results show that biogeochemical rates, in general, were higher near the terrestrial side compared to the marine end. Spatial distribution of particulate matter N isotopic composition varied from 1.34 ‰ to a maximum 8.31 ‰ showing signatures of both terrestrial as well marine origins.

(R. Mukherjee, S. Kumar)

Gross nitrogen mineralization rates in forest soils of India

In past few decades, human activities have altered many terrestrial ecosystems by increasing human derived nitrogen (N) inputs which has caused shift in natural cycling of elements. This has eventually affected carbon (C) fluxes and C storage capacity of soils, providing positive feedbacks to climate change. As N acts as an important growth limiting nutrient for plants and the biogeochemical cycles of N and C are coupled, it is important to understand N cycling in forest ecosystems in order to develop proper forest management practices. Production of NH_4^+ in soils can be studied by determining either net rates which shows the amount of nutrient remaining after consumption; or gross rates which allows quantification of total mineralized N. So far, many studies have been conducted on net rates of mineralization as it is considered to be the principal step which determines plant productivity but few studies exists vis-à-vis gross mineralization rates worldwide. We performed experiments to measure gross mineralization rates of N by using ^{15}N isotope dilution method in order to understand plant growth and nutrient availability in tropical forest soils of Kerala. The mineralization rates in soils of managed, unmanaged and commercially used land were measured and preliminary results indicated that the shift in land use pattern, particularly use of a single plant for long time can affect the rates of mineralization. The results indicated that there is almost same rate of mineralization among soils of managed forests whereas large intra-site variability was observed for unmanaged forest soils.

(N.Sharma, S. Kumar)

Revisiting the N_2 fixation rates in the Eastern Arabian Sea

Biogeochemical implications of global imbalance between the marine N_2 fixation and denitrification have spurred us to undertake this study in the eastern Arabian Sea, which is a major ocean basin that contributes to global nitrogen budget. Using $^{15}N_2$ enriched isotope labeling incubation experiments during the spring 2010, we estimated N_2 fixation to be 11 Tg N yr^{-1}, which is less than that observed in the preceding year (15 Tg N yr^{-1}, spring 2009) in the same region. Our maximum areal rates (8 mmol N m^{-2} d^{-1}) were the highest ever rates observed anywhere in world oceans. High N_2 fixation rates were observed with dark incubations, indicating the presence of heterotrophic diazotrophs that have recently discovered to fix significant amount of N_2.

(P. K. Kumar, A. Singh, R. Ramesh)

Real-time characteristics of Brown Carbon over the central Indo-Gangetic Plain during winter

Carbonaceous aerosols are ubiquitous in the Earth's atmosphere and they have been extensively studied in recent years. A large fraction (20-80%) of carbonaceous aerosols is water soluble, which can promote cloud formation and thus, affects climate cooling and hydrological cycle. However, certain types of organic carbon (OC) absorb radiation efficiently in the near-UV and visible ranges and termed as Brown Carbon (BrC). Major fraction of BrC is reported to be water-soluble. However, the extent of light absorbing properties of OC and its direct and indirect warming effects on climate are poorly understood due to lack of studies that can unravel the variability and complexity of BrC mixtures on temporal and spatial scale. The main focus of this study is to understand the characteristics of water soluble BrC and its role in radiative forcing in the atmosphere over the Indo-Genetic-Plain (IGP). The study area is located in the IGP, a region known to be highly polluted by industries, vehicular emission and biomass burning emissions. Real time analysis of water soluble organic carbon (WSOC) and BrC was carried out using Particle into liquid sampler (PILS) coupled with liquid wave guide capillary cell (LWCC) and total organic carbon (TOC) analyzer during winter season (December, 2015 to February, 2016). The light-absorbing coefficient per unit ambient WSOC mass (at 365 nm) i.e., mass absorption efficiency (MAE), ranges from 0.7 - 2.1 m^{2}g^{-1}. Further, WSOC concentrations exhibited strong correlation (r^2=0.70) with absorption coefficient at 365 nm (Abs$_-$365), attesting that a significant fraction of WSOC is BrC. During fog events, both WSOC and BrC values show decreasing trends. This is attributed to their hygroscopic nature. Further, fog processed aerosols, after fog dissipation, show enhancement in light absorption, which reduces subsequently as day progresses. This observation indicates that BrC is photosensitive and/or volatile.

This study was carried out in collaboration with Prof. S.N. Tripathi, IIT, Kanpur.

(R. V. Satish, N. Rastogi)

Brown carbon characteristics over the northwestern Indo-Gangetic Plain during paddy residue burning

This study was carried out before, during, and after a large scale paddy-residue burning over Patiala (30.2°N, 76.3°E), Punjab, located in the northwestern Indo-Gangetic Plain (IGP) during October-November, 2014. A total of about seventy filter-based $PM_{2.5}$ samples (day/night pairs) were collected and analyzed for their chemical composition and absorption properties. $PM_{2.5}$ mass concentrations ranged from $\sim$90 to 500 μg m^{-3} during the study period. Average K^+/EC ratio ($\sim$0.5) during study period suggests that emissions from biomass burning are dominant over those from fossil fuel burning over the study site. The absorption signal measured at 365 nm in aqueous extracts of aerosols shows a linear increase with WSOC and K$^+$ concentration (Fig.16), indicating the role of emissions from biomass burning on BrC abundances over the IGP. Abs_365/WSOC ratio depicts considerable enhancement during biomass burning relative to pre- and post-burning period, suggesting that biomass burning is a prominent sources of BrC. Further, nighttime BrC was higher than that during daytime.

Logistic support for the sample collection was provided by Mr. Atinderpal Singh and Prof. Darshan Singh (Punjabi University, Patiala).

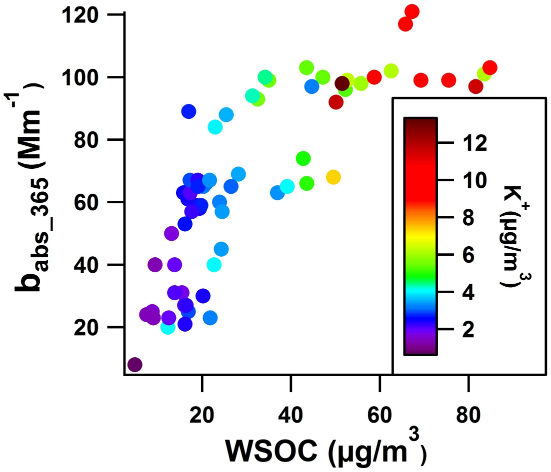

Figure 16: Relationship between WSOC and Abs_365 as a function of K$^+$.

(R. V. Satish, N. Rastogi)

Brown carbon abundances over a semi-arid region in western India

Real-time semi-continuous measurements of BrC have been carried out using PILS-LWCC-TOC system (defined above) over Ahmedabad during February-April and November 2015 to investigate the sources and characteristics of BrC over a semi-arid region. In contrast to that observed over the IGP region, Abs_365 was poorly correlated with WSOC during February-April (r^2= 0.32) and November (r^2= 0.26), suggesting the differences in absorption properties of organic aerosols over the IGP and western India. BrC concentrations were higher during winter period (MAE= ~0.7 m^2g^{-1}) in comparison to that during February-April (MAE= ~0.6 m^2g^{-1}). There were evidences that BrC is of both primary and secondary origin over the study region. High concentration of BrC was observed during 'Holika Dehan' night, suggesting its major contribution from wood burning. In parallel to BrC, carbon monoxide (CO) and nitrogen oxides (NO_x = NO_2 + NO) were also measured. Relationship between Abs_365 and WSOC as a function of CO and NO_x suggests that BrC from combustion sources is relatively more absorbing (Fig. 17 & 18). Diurnal trends of WSOC and BrC showed increase in concentrations in morning hours likely due to photochemistry and decrease in afternoon due to photo bleaching of BrC. Concentrations further increase in evening hours to late night (rush hours) due to fossil fuel combustion and boundary layer dynamics.

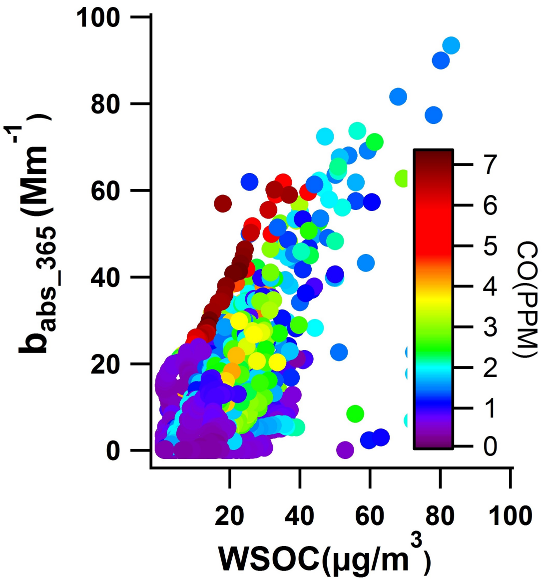

Figure 17: Relationship between WSOC and Abs_365 as a function of CO and NO_x.

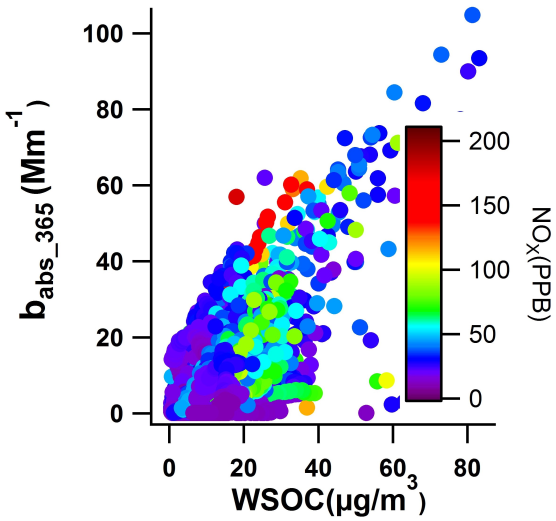

Figure 18: Relationship between WSOC and Abs_365 as a function of CO and NO_x.

(R. V. Satish, N. Rastogi)

Oxidative potential of ambient fine aerosols over the Indo-Gangetic Plain

Epidemiological studies show the aerosols to be well associated with morbidity and mortality, which necessitates the need of understanding the mechanism that how aerosol species causes toxicity. It is now known that when molecular oxygen undergoes reduction in situ, various reactive oxygen species (ROS) are produced, where particulate matter (PM) acts as catalyst. Capacity of aerosols to generate ROS is called as their oxidative potential (OP), which in turn reflects their toxicity. Production of ROS not only affects human health but also secondary aerosols formation processes in the ambient air. Widely proposed mechanism on how aerosol affect health is that ambient aerosols enter in lungs through breathing and fine/ultrafine aerosols can go deep down into lungs where they may produce ROS. These ROS affect epithelial cells which may cause oxidative stress, inflammation or even cell death. In spite of being so important, the OP of aerosols has not yet been documented in India. Measurements of the OP of ambient aerosols using most widely used dithiothrietol (DTT) method have been started at PRL. Here, the OP is described as consumption of μM DTT per minute in presence of PM. Several $PM_{2.5}$ samples have been collected from Patiala, located in the Indo-Gangetic Plain (IGP) during winter 2014. $PM_{2.5}$ mass concentration varied from 33 to 313 μg m^{-3} during the study period. On average, the $PM_{2.5}$ were composed of ∼31% water soluble inorganic species, 31% organic matter, 5% Elemental Carbon and remaining fraction was unidentified. The OP of aerosols has been estimated per unit volume of filtered air as well as per unit mass of collected aerosols. OP/(m^3 of air) varies from 0.1 to 2.2 and OP/(μg of $PM_{2.5}$) varies from 2.4 to 15.3 over the study region during winter time. The OP/(μg of $PM_{2.5}$) has been shown to be more reliable unit for OP in our study. Such studies are very important in understanding the effects of aerosols on the air quality and atmospheric chemistry.

Logistic support for the sample collection was provided by Mr. Atinderpal Singh and Prof. Darshan Singh (Punjabi University, Patiala).

(A. Patel, N. Rastogi)

Anthropogenic trace metals in the Continental outflow to the Bay of Bengal

Atmospheric ^{210}Pb and trace metals (Pb, Cd, Cu, Mn, Cr, Co, Ni and Zn) were studied in fine mode aerosols ($PM_{2.5}$) from a sampling site (Kharagpur: 22.3°N, 87.3°E) in the Indo-Gangetic Plain (IGP) during the continental outflow (November-March) to the Bay of Bengal (BoB). The aerosol ^{210}Pb activity (1.3-6.6 mBqm^{-3}) is significantly high in the wintertime (December-January) compared to model based data in the literature. The cause for higher ^{210}Pb activity is attributed to enhanced ^{222}Rn emanation from Alluvium in the IGP and lower boundary layer height. The trace metal concentrations (ng m^{-3}) also exhibit pronounced temporal variability (Pb: 8-296, Mn: 8-568, Cr: 4.5-33, Cu: 2.1-29.3, Ni: 2.3-14.3, Co: 0.5-1.6 and Cd: 1-29.5) and are of comparable magnitude with those documented over the BoB, suggesting dominant impact of IGP-outflow on marine atmospheric boundary layer. The enrichment factors (EFcrust) of Pb, Cd, Cu, Mn, Cr, Co and Ni in $PM_{2.5}$ relative to upper continental crust, varied as 105-1561, 1265-24006, 13-87, 3-99, 7-27, 3-19 and 9-27, respectively. Significant linear relationship among trace metals and chemical species (non-sea-salt-K^+, nss-$SO_4{}^{2-}$ and EC) emphasizes their anthropogenic source. The high concentrations and EFcrust of Pb, Cd and Cu in the IGP-outflow has implications to increase in the aerosol toxicity and impact on biogeochemistry of ocean surface waters via air-sea deposition.

(B. Srinivas, M. M. Sarin and V. Chinni)

Emission budget of carbonaceous species from biomass burning emissions in the Indo-Gangetic Plain

The large-scale biomass burning emissions, mainly from post-harvest agricultural-waste burning, in the Indo-Gangetic Plain (IGP) addresses the issue of contribution from secondary organic aerosols (SOA) and potential loss of atmospheric chemical constituents (O_3, NO_x and OH radical) via chemical reactions. The emission budget of carbonaceous species, studied from two distinct agricultural-waste (paddy- and wheat-residue) burning in the IGP, reveals that organic carbon (OC) and elemental carbon (EC) account for 505±68 Gg/y and 59±2 Gg/y, respectively. From a global perspective, crop-residue burning in the IGP contributes nearly 20% of both OC and EC to the total emission budget from the agricultural-waste burning.

(P. Rajput, M. M. Sarin)

Surface Active substances in atmospheric aerosol

Uncertainty is assessing aerosol-cloud-interaction and the influence of atmospheric aerosol on precipitation as well as hydrologic cycle is mainly due to difficulties in realistically describing the cloud droplet nucleation and growth, at fundamental level. Classical equilibrium Köhler theory is generally used to predict the soluble aerosol that act as cloud condensation nuclei (CCN). A major portion of organic aerosol is water soluble and contributes to CCN which makes their representation more complex, due to poor characterization of numerous individual compounds of organic aerosol and assumption on surface tension of droplet. Neglecting surface partitioning of surface active substances (SAS) leads to an overestimation of critical super saturation. Hence, measurement of surface active characteristics of soluble organic matter in the ambient aerosol, in order to document their abundances and possible influence on CCN activation, is essential for a better assessment of aerosol-cloud interactions. SAS can be quantified in aqueous solutions by electrochemical method, in which, the capability of their spontaneous adsorption at different phase boundaries is exploited. The interface between a mercury electrode and electrolyte solution can serve as an ideal surface to study adsorption characteristics and determine organic SAS due to their hydrophobic expulsion properties. With this perspective, aerosol samples were collected from Ahmedabad (a representative urban location) using high-volume sampler during December 2012 for the measurement of SAS. The SAS was measured in these samples with a Metrohm 797 VA voltammetry system equipped with three electrode system. Hanging mercury drop electrode (HMDE) with approximate surface area 0.01 cm^2 was used as working electrode; Ag/AgCl/3M KCl and platinum electrodes were used as reference electrode and auxiliary electrode, respectively. Water extract of aerosol sample was mixed with saturated solution of NaCl so that the final solution is ∼0.55M NaCl. Voltage sweep was done from -0.6 V to -1.8 V against Ag/AgCl applying AC voltage and current was recorded at a phase difference of 90°. Decrease in capacitance current at -0.6V, for standard (Titron-X100) solution with respect to blank is used for constructing the calibration curve, based on which measurement of SAS in sample is performed. The preliminary results show that, SAS concentration in $PM_{2.5}$ ranges from 1.5 to 4 μg m^{-3}, with an average value of ∼2.2 μg m^{-3} (equivalent of TX-100) during winter at Ahmedabad. The estimated surface tension corresponding to the observed levels of SAS during activation process is ∼38 mNm^{-1}. This reduction in surface tension from that of pure water (72 mNm^{-1}) can cause substantial change in critical super saturation necessary for droplet activation, and has profound implication in estimation of cloud droplet population and albedo.

(A. K. Sudheer)

Sr Isotope Composition of Mineral aerosol over north-western India and Arabian Sea

A comprehensive study involving chemical and isotopic composition of mineral dust is essential in order to improve our understanding of their sources, transport, deposition and biogeochemical impact on Surface Ocean. Towards this, Sr isotopic compositions of silicate fraction aerosol have been analysed from marine boundary layer of Arabian Sea and two continental locations, Ahmedabad and Jodhpur. Preliminary results of Sr isotopic composition of aerosol over Arabian Sea exhibits spatial variation from 0.7110 to 0.7120 (concentration varies from 7 ng m^{-3} to 31 ng m^{-3}). ^{87}Sr/^{86}Sr ratio at Jodhpur, a major source region of dust in arid region, ranges from 0.7137 to 0.7323 which is significantly different from aerosol over Arabian Sea. ^{87}Sr/^{86}Sr ratio at Ahmedabad varies from 0.7112 to 0.7187 over a year, which is having a distinct seasonal cycle. The labile fraction of aerosol separated by leaching aerosol filter samples from Ahmedabad with 0.6N HCl exhibits average ^{87}Sr/^{86}Sr ratio of 0.7098 ranging from 0.7092 to 0.7106.

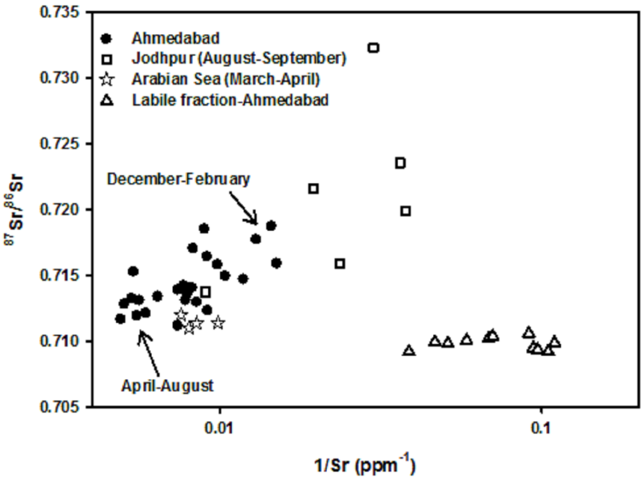

Figure 19: ^{87}Sr/^{86}Sr in aerosol samples collected from continental and marine atmosphere.

(A. K. Sudheer, S. K. Singh, R. Rengarajan, V. K. Rai, R. Bhushan)

Carbon isotopic composition of atmospheric aerosol over north-western India: Implication to sources

Carbon isotopic composition of atmospheric aerosol is a useful tracer to evaluate the contribution of various sources as well as photochemical aging of carbonaceous aerosol, but, complexities arise due to wide range of δ^{13}C values as well as potential alteration of isotopic composition during atmospheric processes. Hence, source apportionment studies involving δ^{13}C and carbonaceous species in regional scale is highly demanding. In this context, δ^{13}C of total carbon (excluding carbonate carbon) been studied along with various constituents like water soluble organic carbon (WSOC), elemental carbon (EC), organic carbon (OC) and water soluble inorganic ions over two location in western India (Ahmedabad and Jodhpur) during May-September, 2012, in order to assess their origin and transport.δ^{13}C of total carbon δ^{13}C values of TC varied from -31‰ to -27.1‰ at Ahmedabad with an average value of -28.9‰ . These values are more depleted compared to those previously reported from coastal locations in western India, Mumbai and Goa. Scatter plots between δ^{13}C and sea-salt constituents (Na^{+}, Mg^{2+} and Cl^{-}) exhibit a trend, indicating that increase in sea-salt contribution is associated with more depleted values of δ^{13}C. δ^{13}C value of OC in seawater generally ranges from -22 ‰ to -20 ‰ in low and mid-latitudes. Hence, contribution of marine dissolved organic carbon to the aerosol measured at Ahmedabad may be negligible even though carbonaceous aerosol at Ahmedabad is influenced by transport from oceanic region during this season. Since fossil fuel emissions generates carbonaceous aerosol with δ^{13}C of TC typically between -28 to -25 ‰ , contribution from ship emissions can be insignificant. The observed δ^{13}C at Ahmedabad is likely due to contribution from secondary aerosol. The average δ^{13}C value of TC at Jodhpur is -27.5 ‰ and ranged from -29.6 ‰ to -25.8 ‰ . The air mass sampled over Jodhpur is transported from marine environment in western region until 2 September 2011, after which shifted towards eastern region. For the samples during 2-31 August 2011, linear correlation between δ^{13}C and WSOC/EC ratio suggests aging of carbonaceous aerosol. Dominant portion of organic carbon exists in coarse particles and concentration as well as isotopic composition of carbonaceous aerosol is likely to be influenced by the local/regional emission sources rather than long-range transport at Jodhpur. When winds were easterly, generally the concentration of organic aerosol is relatively high and δ^{13}C is more depleted. Comprehensive data on carbonaceous species, water soluble ions and δ^{13}C from two locations suggest that strong heterogeneity exists in sources of carbonaceous aerosol over this region.

This work was done in collaboration with Prof. J.S. Rathore from J.N.V. University, Jodhpur.

(A. K. Sudheer, R. Rengarajan, R. Bhushan, S. K. Singh, S. Kumar)

Science

Theoretical Physics

Thermal suppression of phase separation in condensate mixtures

We examine the role of thermal fluctuations in binary condensate mixtures of dilute atomic gases. In particular, we use the Hartree-Fock-Bogoliubov theory with the Popov approximation to probe the impact of noncondensate atoms to the phenomenon of phase separation in two-component Bose-Einstein condensates. We demonstrate that, in comparison to $\mathrm{T} = 0$, there is a suppression in the phase separation of the binary condensates at $\mathrm{T} \neq 0$. This arises from the interaction of the condensate atoms with the thermal cloud. We also show that, when $\mathrm{T} \neq 0$, it is possible to distinguish the phase-separated case from the miscible from the trends in the correlation function. However, this is not the case at $\mathrm{T} = 0$.

(A. Roy and D. Angom)

Triple excitations in perturbed relativistic coupled-cluster theory and electric dipole polarizability of group-IIB elements

We use the perturbed relativistic coupled-cluster (PRCC) theory to compute the electric dipole polarizabilities α of Zn, Cd, and Hg. The computations are done using the Dirac-Coulomb-Breit Hamiltonian with the Uehling potential to incorporate vacuum polarization corrections. To assimilate the self-energy corrections we use the model self-energy operator of Shabaev *et al.* [Phys. Rev. A 88, 012513 (2013)]. The triple excitations are included perturbatively in the PRCC theory and nonperturbatively in the unperturbed sector. Our results for for all three elements are in excellent agreement with the experimental data. The other highlight of the results is the orbital energy corrections from Breit interactions. In the literature we could only get the data of Hg [E. Lindroth et al., J. Phys. B 22, 2447 (1989)], which are a near perfect match with our results. We also present the linearized equations of the cluster amplitudes, including the triple excitations, with the angular factors.

(S. Chattopadhyay, B. K. Mani, D. Angom)

Fluctuation-driven topological transition of binary condensates in optical lattices

We show the emergence of a third Goldstone mode in binary condensates at phase separation in quasi-one dimensional (quasi-1D) optical lattices. We develop the coupled discrete nonlinear Schrödinger equations using Hartree-Fock-Bogoliubov theory with the Popov approximation in the Bose-Hubbard model to investigate the mode evolution at zero temperature, in particular, as the system is driven from the miscible to the immiscible phase. We demonstrate that the position exchange of the species in the ^{87}Rb-^{85}Rb system is accompanied by a discontinuity in the excitation spectrum. Our results show that, in quasi-1D optical lattices, the presence of the fluctuations dramatically changes the geometry of the ground-state density profile of two-component Bose-Einstein condensates.

(K. Suthar, A. Roy, D. Angom)

Dissipative properties of hot and dense hadronic matter in an excluded-volume hadron resonance gas model

We estimate dissipative properties, viz., shear and bulk viscosities of hadronic matter using relativistic Boltzmann equation in relaxation time approximation within the framework of excluded-volume hadron resonance gas (EHRG) model. We find that at zero baryon chemical potential the shear viscosity to entropy ratio decreases with temperature while at finite baryon chemical potential this ratio shows the same behavior as a function of temperature but reaches close to the Kovtun-Son-Starinets (KSS) bound. Further along the chemical freezeout curve, the ratio of shear viscosity to entropy density is almost constant apart from small initial monotonic rise. This observation may have some relevance to the experimental finding that the differential elliptic flow of charged hadrons does not change considerably at lower center-of-mass energy.We further find that bulk viscosity to entropy density decreases with temperature while this ratio has higher value at finite baryon chemical potential at higher temperature. Along the freezeout curve bulk viscosity to entropy ratio decreases monotonically at lower center-of-mass energy and then saturates.

(G. Kadam and H. Mishra)

Medium modification of hadron masses and the thermodynamics of the hadron resonance gas model

We study the effect of temperature and baryon density dependent hadron masses on the thermodynamics of hadronic matter.We use linear scaling rule in terms of constituent quark masses for all hadrons except for light mesons. cw temperature and chemical potential dependent constituent quark masses and the light meson masses are computed using 2+1 flavor Nambu-Jona-Lasinio (NJL) model.We compute the thermodynamical quantities of hadronic matter within excluded volume hadron resonance gas model (EHRG) with these T- and -dependent hadron masses. We confront the thermodynamical quantities with the lattice quantum chromodynamics (LQCD) at zero baryon density. Further, we comment on the effect of temperature and density dependent hadron masses on the transport properties near the transition temperature.

(G. Kadam, H. Mishra)

Estimating transport coefficients in hot and dense quark matter

We compute the transport coefficients namely, coefficients of shear and bulk viscosity as well as thermal conductivity for hot and dense quark matter. The calculations are performed within the Nambu Jona Lasinio (NJL) model. The estimation of the transport coefficients is made using a quasi particle approach of solving Boltzmann kinetic equation within the relaxation time approximation. The transition rates are calculated in a manifestly covariant manner to estimate the thermal averaged cross sections for quark quark as well as quark anti-quark scattering. The calculations are performed for finite chemical potential also. Within the parameters of the model, the ratio of shear viscosity to entropy density has a minimum at the Mott transition temperature. At vanishing chemical potential, the ratio of bulk viscosity to entropy density, on the other hand, decrease with temperature with a sharp decrease near the critical temperature and vanishes beyond it. At finite chemical potential, however, it increases slowly with temperature beyond the Mott temperature. The coefficient of thermal conductivity also shows a minimum at the critical temperature.

(P. Deb, G. Kadam, H. Mishra)

Looking for bSM physics using top-quark polarization and decay-lepton kinematic asymmetries

The work explores beyond Standard Model (bSM) physics signatures in the lepton+jets channel of $t\bar{t}$ pair production process at the Tevatron and the LHC.It studies the effects of bSM physics scenarios on the top-quark polarization and on the kinematics of the decay leptons.To this end, certain asymmetries are constructed using the lepton energy and angular distributions.Further, their correlations with the top polarization, net charge asymmetry and top forward backward asymmetry are determined and it is shown that used together, these observables can help discriminate effectively between SM and different bSM scenarios which can lead to varying degrees of top polarization at the Tevatron as well as the LHC.Two types of coloured mediator models are used to demonstrate the effectiveness of proposed observables, an s-channel axigluon model and a u-channel diquark model .

This work was done in collaboration with Rohini M. Godbole and Gaurav Mendiratta of CHEP, Indian Institute of Science, Bengaluru.

(S. D. Rindani)

Polarization of top quark as a probe of its chromomagnetic and chromoelectric couplings in $t\mathrm{W}$ production at the LHC

This work studies the sensitivity of the Large Hadron Collider (LHC) to top quark chromomagnetic (CEDM) dipole moments and $\mathrm{W}tb$ effective couplings in single-top production in association with a Wboson, followed by semileptonic decay of the top. The $\mathrm{W}t$ single-top production mode helps to isolate the anomalous ttg and Wtb couplings, in contrast to top-pair production and other single-top production modes, where other new-physics effects can also contribute. The top polarization and the effects of these anomalous couplings on it are calculated at two centre-of-mass energies, 8 TeV and 14 TeV. As a measure of top polarization, decay-lepton angular distributions in the laboratory frame, without requiring reconstruction of the rest frame of the top have been examined,and also the effect of the anomalous couplings on these distributions. Certain asymmetries to study the sensitivity of these distributions to top-quark couplings are constructed. Limits on the dominant couplings, viz., the real part of the CMDM Re ρ_2,the imaginary part of the CEDM Im ρ_3, and the real part of the tensor $\mathrm{W}tb$ coupling Re $f_{2\mathrm{R}}$,which may be obtained by utilizing these asymmetries at the LHC, have been estimated.

This work was done in collaboration with Pankaj Sharma and Anthony W. Thomas of COEPP, Adelaide University.

(S. D. Rindani)

Unravelling the CP phase of top-Higgs coupling in associated production at the LHC

This is a study of the sensitivity of top polarization observables to the CP phase ζ_t in the top Yukawa coupling in the process $pp \to th+$ jet at the 14 TeV high-luminosity run of the Large Hadron Collider. The top polarization in this process as well as an azimuthal asymmetry of the charged lepton arising from the decay of the top in the lab frame have been calculated. It is found that the dependence of this lab-frame azimuthal asymmetry on the phase ζ_t closely resembles the dependence of the top polarization on ζ_t.As compared to the cross section, which is sensitive to ζ_t for larger values, the lepton azimuthal asymmetry can provide a sensitive measurement of ζ_t for smaller values.

This work was done in collaboration with Pankaj Sharma of COEPP, Adelaide University and Ambresh Shivaji of INFN Pavia.

(S. D. Rindani)

Memory Function Approach to Correlated Electron Transport: A Comprehensive Review

Memory function formalism or projection operator technique is an extremely useful method to study the transport and optical properties of various condensed matter systems. A recent revival of its uses in various correlated electronic systems is being observed. It is being used and discussed in various contexts, ranging from non-equilibrium dynamics to the optical properties of various strongly correlated systems such as high temperature superconductors. However, a detailed discussion on this method, starting from its origin to its present day applications at one place is lacking. We wrote a comprehensive review of the memory function approach focusing on its uses in studying the dynamics and the transport properties of correlated electronic systems.

(N. Das, P. Bhalla, N. Singh)

Generalized Drude Scattering rate from the memory function formalism.

An explicit perturbative computation of the Moris memory function was performed by Goetze and Woelfle (GW) to calculate Generalized Drude scattering (GDS) rate for the case of electron-impurity and electron-phonon scattering in metals by assuming constant electronic density of states at the Fermi energy. In the present investigation, we go beyond this assumption and extend the GW formalism to the case in which there is a gap around the Fermi surface in electron density of states. The resulting GDS is compared with a recent one by Sharapov and Carbotte (SC) obtained through a different route. We find good agreement between the two at finite frequencies. However, we find discrepancies in the dc scattering rate. These are due to a crucial assumption made in SC. No such high frequency assumption is made in the memory function based technique.

(P. Bhalla and N. Singh)

Moment Expansion to the Memory Function for Generalized Drude Scattering rate

The memory function formalism is an important tool to evaluate the frequency dependent elec-tronic conductivity. It is previously used within some approximations in the case of electrons interacting with various other degrees of freedom in metals with great success. However, one needs to go beyond those approximations as the interaction strengths become stronger. In this work, we propose a systematic expansion of the memory function involving its various moments. We calculate the higher order contribution to the generalized Drude scattering rate in case of electron-impurity interactions. Further we compare our results with the results from previously studied lowest order calculations. We find larger contributions from the higher moments in the low frequency regime and also in the case of larger interaction strength.

(P. Bhalla, N. Das, N. Singh)

Hot-electron relaxation in metals within the Goetze-Woelfle memory function formalism

We consider non-equilibrium relaxation of electrons due to their coupling with phonons in a simple metal. In our model electrons are living at a higher temperature than that of the phonon bath, mimicking a non-equilibrium steady state situation. We study the relaxation of such hot electrons proposing a suitable generalization of the memory function formalism formulated by Goetze and Woelfle. We derive analytical expressions for both dc and optical scattering rates in various temperature and frequency regimes. Limiting cases are in accord with the previous studies. An interesting feature, that the dc scattering rate at high temperatures and optical scattering rate at high frequencies, are independent of the temperature difference between the electrons and the phonons is found in this study. The present formalism forms a basis which can also be extended to study hot-electron relaxation in more complex situations.

(N. Das and N. Singh)

Determination of the 2-3 mixing angle and CP phase in the neutrino sector

The octant of the 2-3 leptonic mixing angle and the CP phase are two of the major unknown neutrino oscillation parameters at the present moment. The precise determination of these parameters is difficult because of the the octant-CP degeneracy.We studied the potential of the DUNE experiment at FermiLab to determine these parameters. In particular, we explored the role of anti-nutirnos in DUNE in detail and find that antineutrinos can play an important role even when there are degeneracies associated with these probabilities. This happens becuase of the (i) broad-band nature of the beam so that even if there is degeneracy at a particular energy bin, over the whole spectrum the degeneracy may not be there; (ii) the enhanced matter effect due to the comparatively longer baseline which creates an increased tension between the neutrino and the antineutrino probabilities which raises the overall sensitivity in case of combined runs. This feature is more prominent for IH since the antineutrino probabilities in this case are much higher than the neutrino probabilitiesdue to matter effects.The main role of antineutrinos in enhancing CP sensitivity is their ability to remove the octant-CPdegeneracy. However even if one assumes octant to be known the addition of antineutrinos can give enhanced cp sensitivity in some parameter regions due to the tension between the neutrino and antineutrino contributions.We determine the optimal combination of neutrino and antineutrino runs that can give maximum CP coverage.

(S. Goswami, N. Nath, M. Ghosh)

The Scalar Triplet Contribution to Lepton Flavour Violation and Neutrinoless Double Beta Decay in Left-Right Symmetric Model

We analyse in detail the scalar triplet contribution to the low-energy lepton flavour violating (LFV) and lepton number violating (LNV) processes within a TeV-scale left-right symmetric framework. We show that in both type-I and type-II seesaw dominance for the light neutrino masses, the triplet of mass comparable to or smaller than the largest right-handed neutrino mass scale can give sizeable contribution to the LFV processes,except in the quasi-degenerate limit of light neutrino masses, where a suppression canoccur due to cancellations. In

back to contents

particular, a moderate value of the heaviest neutrino toscalar triplet mass ratio is still experimentally allowed and can be explored inthe future LFV experiments. Similarly, the contribution of a relatively light triplet to the LNV process of neutrinoless double beta decay could be significant, disfavouring a part ofthe model parameter space otherwise allowed by LFV constraints. Nevertheless, we findregions of parameter space consistent with both LFV and LNV searches, for which the values of the total effective neutrino mass can be accessible to the next generation ton-scale experiments. Such light triplets can also be directly searched for at the LHC, thusproviding a complementary probe of this scenario. Finally, we also study the implicationsof the triplet contribution for the left-right symmetric model interpretation of the recent diboson anomaly at the LHC.

This work was done in collaboration with Manimala Mitra from University of Durham and P.S.B. Bhupal Dev from University of Manchester.

(S. Goswami, G. Bambhaniya)

Exploring decaying atmospheric neutrinos at INO

Neutrino oscillation solution to atmospheric neutirno problem is well established now and the focus has shifted to probe if subdominat solution to oscillations can be constrained from future data. We explore the situation where one of the neutrino states decayso that one can have both decay and oscillations. At the analytical level the problem is interesting because the Hamiltonian in presence of decay is non-hermitian. We have worked on finding the methodology of diagonalizing such Hamiltonians. We have also studied the constraints that can be obtained on the neutrino decay parameter from atmospheric neutrinos at the ICAL detector of India-Based Neutrino Observatory (INO).

This work is done in collaboration with Sandhya Choubey from Harish-Chandra Research Institute and Tarak Thakore from Louisianna State University, US.

(S. Goswami, C. Gupta, L. S. Mohan)

Constraints on just enough inflation preceded by a thermal era

If the inflationary era is preceded by a radiation dominated era in which the inflaton too was in thermal equilibrium at some very early time then the CMB data places an upper bound on the comoving temperature of the (decoupled) inflaton quanta. In addition, if one considers models of “just enough” inflation, where the number of e-foldings of inflation is just enough to solve the horizon and flatness problems, then we get a lower bound on the Hubble parameter during inflation, $\mathrm{H}_{\mathrm{inf}}$, which is in severe conflict with the upper bound from tensor perturbations. Alternatively, imposing the upper bound on $\mathrm{H}_{\mathrm{inf}}$ implies that such scenarios are compatible with the data only if the number of relativistic degrees of freedom in the thermal bath in the pre-inflationary Universe is extremely large (greater than 10^9 or 10^{11}). We are not aware of scenarios in which this can be satisfied.

This work was done in collaboration with Gaurav Goswami of Ahmedabad University, Suratna Das of IIT Kanpur and Jayanti Prasad of IUCAA, Pune.

(R. Rangarajan)

Vacuum stability and unitarity constraint in a left-right symmetric model

ATLAS and CMS data indicated narrow range of SM Higgs at 125-126 GeV. With existing values of top mass and strong coupling constant, SM Higgs quartic coupling may run into negative values at a scale below the Planck scale. This vacuum stability problem can be avoided by introducing physics beyond the Standard Model (BSM) in a intermediate scale before Planck scale. We examine the usefulness of the unitarity conditions in a left-right symmetric model which can translate into giving a stronger constraint on the model parameters together with the criteria derived from vacuum stability and perturbativity. In this light, we demonstrate the bounds on the masses of the physical scalars present in the model and find the scenario where multiple scalar modes are in the reach of the Large Hadron Collider. We also analyze the additional conditions that can come from charge breaking minima in this context.

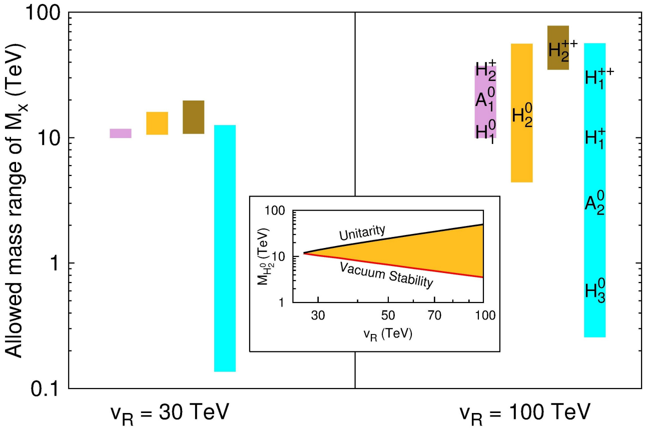

Figure 1: Allowed mass range for four sets of heavy scalar states after imposing all constraints coming from vacuum stability, unitarity, as well as perturbativity at each scale all the way up to Planck scale. Two different sets of the left-right symmetry breaking scale is considered, which are 30 TeV and 100 TeV.

(T. Mondal, U.K. Dey, P. Konar)

Hints of a reconstructible seesaw model at the LHC

We study the production of heavy neutrinos at the Large Hadron Collider through the dominant s-channel production mode as well as the vector boson fusion process. We consider the TeV scale minimal linear seesaw model containing two heavy singlets with the opposite lepton number. This model is fully reconstructible from oscillation data apart from an overall normalization constant which can be constrained from the metastability of the electroweak vacuum and bounds coming from lepton flavor violation searches. The Dirac nature of heavy neutrinos in this model implies suppression of the conventional same-sign-dilepton signal at the Large Hadron Collider. We analyze the collider signatures with the trilepton final state and missing transverse energy as well as vector boson fusion type signals which are characterized by two additional forward tagged jets. Our investigation reveals that due to stringent constraints on light-heavy mixing coming from lepton flavor violation and metastability bounds, the model can be explored only for a light to moderate mass range of heavy neutrinos. We also note that in case of a positive signal, flavor counting of the final trilepton channel can give information about the mass hierarchy of the light neutrinos.

(G. Bambhaniya, S. Goswami, S. Khan, P. Konar, T. Mondal)

Constraints on a seesaw model leading to quasidegenerate neutrinos and signatures at the LHC

We consider a variant of TeV-scale seesaw models in which three additional heavy right-handed neutrinos are added to the standard model to generate the quasidegenerate light neutrinos. This model is theoretically interesting since it can be fully rebuilt from the experimental data of neutrino oscillations except for an unknown factor in the Dirac-Yukawa coupling. We study the constraints on this coupling coming from metastability of electroweak vacuum. An even stronger bound comes from the lepton flavor violating decays on this model, especially in a heavy neutrino mass scenario which is within the colliders reach. Bestowed with these constrained parameters, we explore the production and discovery potential coming from these heavy neutrinos at the 14 TeV run of the Large Hadron Collider. Signatures with trilepton final state together with backgrounds are considered in a realistic simulation.

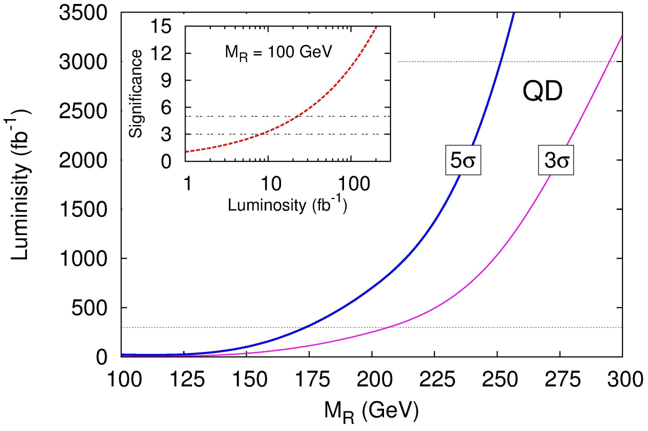

Figure 2: Contours of constant significance the 14 TeV LHC in terms of heavy neutrino mass $\mathrm{M_R}$ and integrated luminosity considering the trilepton signals to probe the heavy neutrino.

(G. Bambhaniya, S. Khan, P. Konar, T. Mondal)

Non-commutative geometry at linear collider

The idea of field theories on the noncommutative(NC) space-time is old, introducing a fundamental length scale in the model consistent with the symmetry. This outlook is further revived after realisation of their possible connection with quantum gravity, where NC is perceived as an outcome of certain string theory embedded into a background magnetic field. Theoretically NC scale is unknown, but one can try to extract the lower bounds directly from the collider experiments by looking at the characteristic signals this framework can provide. We study the associated Higgs production with Z boson at future linear colliders in the framework of the minimal noncommutative standard model. We also consider the effect of earths rotation on the orientation of noncommutative parameters with respect to the laboratory frame and thus on the total cross-section, its azimuthal distribution and rapidity distribution for the machine energy ranging from 0.5 TeV to 3 TeV corresponding to the noncommutative scale $\Lambda \geq$ 0.5TeV.

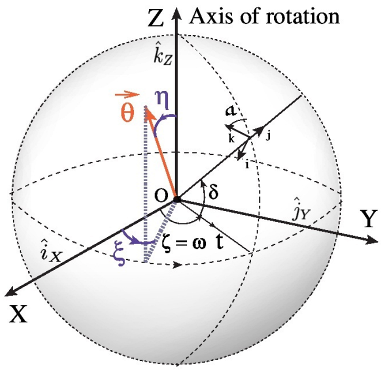

Figure 3: The primary coordinate system (XYZ) with the Z-axis along the earth axis of rotation and the laboratory coordinate system for an experiment on the earth are shown.

This work was done in collaboration with J. Selvaganapathy, P.K. Das of BITS Pilani, Goa campus.

(P. Konar)

Semi-invisible production at LHC exploring constrained variables

The mass-constraining variable $\mathrm{M_2}$, a (1+3)-dimensional natural successor of extremely popular $\mathrm{M_{T2}}$, possesses an array of rich features having the ability to use on-shell mass constraints in semi-invisible production at a hadron collider.

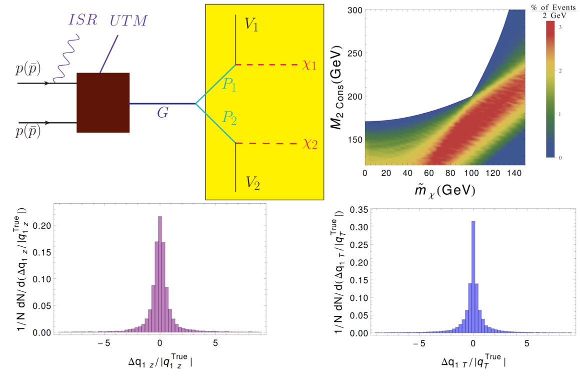

Figure 4: (Upper-Left) Representative for a simple antler topology produced at the Large Hadron Collider. (Upper-Right) Density of events as a percentage of total data contributing to $\mathrm{M_2}$ distributions as a function of the trial invisible mass $m_{\tilde{\chi}}$. The presence of the kink can be clearly seen from the figure, and it is solely because of the on-shell heavy resonance constraint. (Lower plots) Representing the capability of reconstructing missing daughter momenta using this constrained variable for transverse and longitudinal momentum.

In this work, we investigate the consequence of applying a heavy resonance mass-shell constraint in the context of a semi-invisible antler decay topology produced at the LHC. Our proposed variable, under additional constraint, develops a new kink solution at the true masses. This enables one to determine the invisible particle mass simultaneously with the parent particle mass from these events. We analyze in a way to measure this kink optimally, exploring the origin and the properties of such interesting characteristics. We also study the event reconstruction capability inferred from this new variable and find that the resulting momenta are unique and well correlated with true invisible particle momenta.

(P. Konar, A. K. Swain)

Compressed Supersymmetric Spectrum in the light of 125 GeV Higgs boson

A compressed spectrum was initially proposed as an explanation for the elusiveness of low-energy supersymmetry (SUSY). Some characteristic signals at the Large Hadron Collider (LHC), such as mono-jet + , had been propounded as its trademark signals. However, later investigations suggested that lower limits on the supersymmetric particle masses would be quite stringent in spite of compression. Also, most compressed SUSY scenarios studied so far are only partially compressed. In this backdrop, we make an exhaustive analysis of the compressed SUSY scenarios for the 13 TeV run of LHC, keeping the level of compression in the entire spectrum as high as possible.

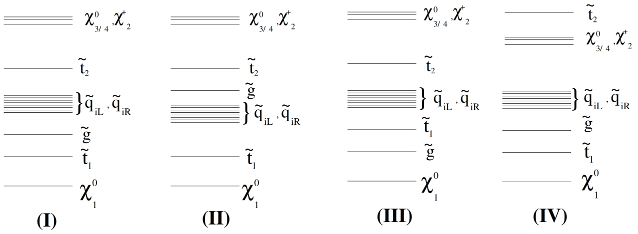

Figure 5: Different benchmark scenarios for compressed spectrum considered in our study: Type I (BP1,BP3, BP5, BP10), Type II (BP4, BP7, BP8, BP9), Type III (BP2) and Type IV (BP6).

A broad class of benchmark spectra are thus considered, after ensuring consistency with the observed Higgs mass as well as the dark matter constraints. The rates of observable events in the high-energy run are obtained through detailed simulation, for both the multi-jet + and mono-jet + final states. Our conclusion is that the former is still more efficient to reveal a compressed SUSY spectrum first, while the latter can serve as a useful confirmatory channel.

This work was done in collaboration with J. Dutta, S. Mondal, B. Mukhopadhyayaa, S.K. Rai of HRI, Allahabad.

(P. Konar)

A proposal for unambiguous detection of nuclear anapole moments in the Fr isotopes

By carrying out calculations of the parity non-conserving electric dipole amplitudes for the $7s\ {}^2\mathrm{S}_{1/2} \rightarrow 6d\ {}^2\mathrm{D}_{5/2}$ transitions in the Fr isotopes, it is shown that these amplitudes, sensitive only to the nuclear spin dependent effects, are larger than the low-lying $\mathrm{S}-\mathrm{D}_{5/2}$ transitions in the Ba$^+$ and Ra$^+$ ions owing to the very large contributions from the electron core-polarization effects in Fr. This translates to a relatively large and, in principle,measurable induced light shift, which would be a signature of nuclear spin dependent parity nonconservation effect primarily caused by the nuclear anapole moment. A plausible scheme to measure this quantity using the Cyclotron and Radioisotope Center (CYRIC) facility at Tohoku University, Japan has been demonstrated.

This work was done in collaboration with T. Aoki University of Tokyo, Japan, B. P. Das of Tokyo Institute of Technology,Japan and Y. Sakemi of Tohoku University, Sendai, Japan.

(B. K. Sahoo)

Explaining inconsistencies among the measured and theoretically determined lifetimes of the $5d\ {}^2\mathrm{D}_{3/2,5/2}$ states in Cs

Disagreements between the theoretically evaluated lifetimes of the $5d\ {}^2\mathrm{D}_{3/2}$ and $5d\ {}^2\mathrm{D}_{5/2}$ states in Cs with their experimental values were reported earlier in [Phys. Rev. A 57, 4204(R) (1998)]. By employing an all order perturbative relativistic coupled-cluster method, we were able to address this issue. We found inclusion of the higher order correlation effects arising through the non-linear terms and relativistic corrections due to the Breit and QED interactions in the many-body theory are the decisive factors to explain the measurements.

(B. K. Sahoo)

Hyperfine splitting to detect nuclear octupole moment of ^{211}Fr

Considering preliminary value of nuclear octupole moment, Ω, from the nuclear shell-model, its contributions to the hyperfine splitting of many low-lying states in ^{211}Fr were estimated. Accuracies of atomic wave functions to determine these values were verified by comparing the calculated magnetic dipole and electric quadrupole hyperfine structure constants using these wave functions with the available high precision experimental results. In this assessment, hyperfine transitions with enhanced contributions from Ω were identified and their measurements have been recommended for inferring precise value of Ω.

(B. K. Sahoo)

Magic wavelengths in the alkaline-earth-metal ions for high precision measurements

Magic wavelengths for the S - P and S - D transitions in the Mg$^+$, Ca$^+$, Sr$^+$ and Ba$^+$ alkaline earth-metal ions, at which the differential Stark shifts are nullified, were determined for linearly polarized lights by carrying out high accuracy dynamic electric dipole polarizabilities in the above ions. Accuracies of these quantities were validated by comparing their static electric dipole polarizabilities with the experimental results. Moreover, we were also able to reproduce the recently measured few magic wavelengths in the Ca$^+$. Knowledge of these magic wavelengths are propitious to carry out many proposed high precision measurements trapping the above ions in the electric fields with the corresponding frequencies.

This work was carried out in collaboration with J. Kaur, S. Singh and B. Arora of Department of Physics, Guru Nanak Dev University, Punjab, India.

(B. K. Sahoo)

Electric dipole moment of ^{225}Ra due to parity and time reversal symmetry violating weak interactions

Electric dipole moment (EDM) of ^{225}Ra due to parity and time-reversal violating tensor-pseudotensor (T-PT) and nuclear Schiff moment (NSM) interactions are obtained as $d_a = -10.01 \times 10^{-20} \mathrm{C_T} \langle \sigma_n \rangle$ e-cm and $d_a = -6.79 \times 10^{-17} \mathrm{S}/(|e| fm^3)$, respectively, with the T-PT coupling constant $\mathrm{C_T}$ and NSM S. These values for the corresponding T-PT and NSM interactions are reduced by about 45% and 23%, respectively, compared to the previously carried out calculations. The validity of our calculations were vindicated by comparing results with the earlier studies at the zeroth order Dirac-Fock method and all order random-phase approximation. The first measurement of ^{225}Ra EDM is reported recently in [Phys. Rev. Lett. 114, 233002 (2015)]. In this paper, the authors claim that the systematic uncertainties and statistical sensitivity of their measured value will be improved drastically in near future. Thus, our calculations in combination with these improved measurement may provide more accurate limits on the electron-quark T-PT interaction coupling coefficient and Θ_{QCD} parameter when the experiment comes into fruition. These results are essential to probe particle physics beyond the Standard Model.

(B. K. Sahoo, Y. Singh)

Asymmetries and observables for $\Lambda_b \to \Lambda \ell^+ \ell^-$

The semi-leptonic $b \to s$ decays provide a unique opportunity to test physics beyond the standard model. Experiments have provided some hints of discrepancies between the theoretical predictions and observations. The baryonic decay, $\Lambda_b \to \Lambda \ell^+ \ell^-$ has been studied in detail and new angular observables have been proposed which can test the standard model and also help discriminate different new physics models.

(G. Kumar, N. Mahajan)

$\mathrm{B}^- \to \mathrm{D}^{(*)} \tau \bar{\nu}$ excesses in ALRSM constrained from B, D decays and D^0-$\bar{\mathrm{D}}^0$ mixing

Many experiments in the flavour sector are hinting at some new physics beyond the standard model. Within the context of a specific left-right symmetric model, various anomalies have been shown to have a consistent explanation after imposing stringent constraints from many different flavour observables.

(C. Hati, G. Kumar, N. Mahajan)

Light neutrino contribution: is it all there is to neutrinoless double beta decay?

Perturbative one loop QCD corrections to the light neutrino contribution to neutrinoless double beta decay are considered for the first time and large enhancement to the rate are found. QCD corrections also generate structures which mimic new physics contributions that usually arise in many extensions of the standard model. Within some approximations, the net effect seem to almost saturate the experimental limits, and therefore seems to imply that there may not be much room for new physics beyond the standard model in explaining neutrinoless double beta decay.

(N. Mahajan)

Constraints on Scalar Leptoquark from Kaon Sector

The flavour anomalies, as observed by various experiments, could possibly be addressed by a scalar leptoquark. The constraints on such a leptoquark couplings to the standard model particles from the kaon decays and mixing have been considered for the first time. It is found that the model can be tightly constrained, and at the same time the different set of couplings involved yield similar or tighter constraints than those from bottom meson decays.

(G. Kumar)

Precise determination of the low-energy hadronic contribution to the muon g–2 from analyticity and unitarity

The two-pion low-energy contribution to the anomalous magnetic moment of the muon brings a relatively large contribution to the theoretical error. By exploiting analyticity and unitarity of the pion electromagnetic form factor, an attempt is made to derive stringent constraints on the two-pion contribution. The results seem to be optimal for a given input and do not depend on the unknown phase of the form factor above the inelastic threshold. The present work improves a previous analysis based on the same technique, including more experimental data and employing better statistical tools for their treatment.

This work was done in collaboration with B.Ananthanarayan, Irinel Caprini, I. Sentitemsu Imsong.

(D. Das)

Shear Viscosity of Turbulent Chiral Plasma

Chiral plasmas are known to have an instability arising due to difference in the chemical potentials of right-handed and left-handed particles. The instability can drive the turbulent transport and the collisionality between the particles can increase due to the instability driven fluctuations. Using the Berry-curvature modified kinetic equation and resonance broadening theory for strong turbulence, we calculate the coefficient of shear viscosity. We obtain an explicit relationship between the coefficient of shear viscosity, chiral-chemical potential and the decorrelation time.

(A. Kumar, J. R. Bhatt, A. Das, P. K. Kaw)

back to contents

Reason for T2K to run in dominant neutrino mode for detecting CP violation

The long-baseline experiment T2K in Japan has collected data in the neutrino mode and currently it is running in the antineutrino mode. The main aim of the antineutrino run is to measure the leptonic phase which may help in understanding the matter-antimatter asymmetry of the universe. We show that in T2K, antineutrinos are required only for removing the wrong octant solutions which in turn improves the CP sensitivity. If however the octant is known then pure neutrino run is capable of giving the maximum CP sensitivity. If we divide the total true parameter space into eight sets, then we find that T2K antineutrino run helps in improving the CP sensitivity for only two sets while for the remaining six combinations pure neutrino run gives the best CP sensitivity. Thus if the neutrino run is replaced by the antineutrino run then it causes a reduction in the CP sensitivity in 75% of the true parameter space due to lesser statistics. Thus it is worthwhile to study if the T2K antineutrino run can be reduced by the antineutrino runs of the other experiments, so that T2K can run in dominant neutrino mode to extract the best CP sensitivity. In this work we explore the possibility of the antineutrino component of NOVA and the atmospheric neutrino experiment ICAL@INO for compensating the antineutrino run of T2K.

(M. Ghosh)

Understanding the Masses and Mixings of One-Zero Textures in 3+1 Scenario

We present a detailed analysis and phenomenological consequences of neutrino mass matrix, with one-zero texture in the flavor basis where the active neutrino sector is extended by one sterile neutrino (3+1 case). In particular, our aim is to explore behaviour of the sterile mixing parameters in detail when one of the elements of the neutrino mass matrix goes to zero. To study this, we consider two distinct mass spectrum of the active neutrinos: (i) completely hierarchical mass spectrum with a vanishing neutrino mass and (ii) completely quasidegenerate mass spectrum. In 3+1 scenario, the low energy neutrino mass matrix, is a 44 matrix and has 10 independent elements. Thus it can have 10 possible one-zero textures. From the earlier studies it can be inferred that, if one assumes one vanishing neutrino mass, then only seven of these are phenomenologically allowed by the current neutrino oscillation data. On the other hand, if the neutrinos are quasidegenerate then there are eight phenomenologically viable one-zero textures. In this present work, we study the correlations between the sterile mixing parameters for each of these allowed textures for both mass spectrum and also their implications on the effective Majorana mass.

This work is done in collaboration with Shivani Gupta of Center of Excellence in Particle Physics (CoEPP), University of Adelaide, Adelaide SA 5005, Australia.

(M. Ghosh, N. Nath)

Science

Atomic, Molecular and Optical Physics

Generation of "perfect" vortex of variable size and its effect in angular spectrum of the down−converted photons

The "perfect" vortex is a new class of optical vortex beam having ring radius independent of its topological charge (order). One of the simplest techniques to generate such beams is the Fourier transformation of the Bessel−Gauss beams. The variation in ring radius of such vortices require Fourier lenses of different focal lengths and or complicated imaging setup. Here we report a novel experimental scheme to generate perfect vortex of any ring radius using a convex lens and an axicon. As a proof of principle, using a lens of focal length f $=$ 200 mm, we have varied the radius of the vortex beam across 0.3−1.18 mm simply by adjusting the separation between the lens and axicon. This is also a simple scheme to measure the apex angle of an axicon with ease. Using such vortices we have studied non−collinear interaction of photons having orbital angular momentum (OAM) in spontaneous parametric down−conversion (SPDC) process and observed that the angular spectrum of the SPDC photons are independent of OAM of the pump photons rather depends on spatial profile of the pump beam. In the presence of spatial walk−off effect in nonlinear crystals, the SPDC photons have asymmetric angular spectrum with reducing asymmetry at increasing vortex radius.

(M. V. Jabir, A. N. Chaitanya, A. Aadhi, G. K. Samanta)

High−power, high−repetition−rate, Yb−fiber laser based femtosecond source at 355 nm

We have developed a high−power, high−repetition−rate, fiber laser based source of ultrafast ultraviolet (UV) radiation. Using single−pass second−harmonic generation and subsequent sum−frequency generation (SFG) of an ultrafast ytterbium fiber at 1064 nm in 1.2 and 5 mm long bismuth triborate (BIBO) crystals, respectively, we have generated UV output power as high as 1.06 W at 355 nm with single−pass near−infrared−to−UV conversion efficiency of $\sim 22\%$. The source has output pulses of temporal and spectral widths of ~ 576 fs and 1.6 nm, respectively, at 78 MHz repetition rate. For given crystals and laser parameters, we have experimentally verified that the optimum conversion efficiency of the SFG process requires interacting pump beams to have the same confocal parameters. We also present a systematic study on the power ratio of pump beams influencing the overall conversion of the UV radiation. The UV source has a peak−to−peak short−term power fluctuation of $<$ 2.2%, with a power drift of 0.76%/h associated to different loss mechanisms of the BIBO crystal at UV wavelengths. At tight focusing, the BIBO crystal has a broad angular acceptance bandwidth of ($\sim 2mrad \cdot cm$) for SFG of the femtosecond laser.

(A. N. Chaitanya, A. Aadhi, M. V. Jabir, and G. K. Samanta)

Frequency−doubling characteristics of high−power, ultrafast phase singular optical beams

We have demonstrated frequency−doubling characteristics of high−power, ultrafast optical vortex beams in a nonlinear medium. Based on single−pass second−harmonic generation (SHG) of optical vortices in 1.2 mm long bismuth triborate (BIBO) crystal, we studied the effect of different parameters influencing the SHG process in generating high power and higher−order vortices. We observed a decrease in SHG efficiency with the order, which can be attributed to the increase of the vortex beam area with order. Like a Gaussian beam, optical vortices show focusing−dependent conversion efficiency. However, under similar experimental conditions, the optimum focusing condition for optical vortices is reached at tighter focusing with orders. We observed higher angular acceptance bandwidth in the case of optical vortices than that of a Gaussian beam; however, there is no substantial change in angular acceptance bandwidth with vortex order. We also observed that in the frequency−doubling process, the topological charge has negligible or no effect in temporal and spectral properties of the beams. We have generated ultrafast vortices at 532 nm with power as much as 900mW and order as high as 12. In addition, we have devised a novel scheme based on linear optical elements to double the order of any optical vortex at the same wavelength.

(A. N. Chaitanya, A. Aadhi, M. V. Jabir, G. K. Samanta)

Fibre coupled biphoton source for quantum information processing

Photon modes have an important role in characterizing the quantum sources of light. The two main pre−detection factors affecting the biphoton mode coupling in SPDC are the pump beam focusing parameter and the crystal thickness. We present the numerical and experimental results on the effect of pump focusing on conditional down−converted photon modes for a Type−I BBO crystal. We experimentally verify that biphoton coupling efficiency decreases asymptotically with pump beam focusing parameter. We attribute this behaviour to (a) the asymmetry in the spatial distribution of down−converted photons with the pump beam focusing parameter and (b) the ellipticity of biphoton modes introduced due to the focusing of the pump beam. We also show the ellipticity experimentally as well as quantify it with the focusing parameter. These results may be useful in selecting optimum conditions for generating efficient fiber coupled sources of heralded single photons and entangled photons for quantum information applications.

(A.Anwar, P. Chithrabhanu, S. G. Reddy, S. Prabakar, and R. P. Singh)

Non−coaxial superposition of vector vortex beams

Vector vortex beams are classified into four types depending upon spatial variation in their polarization vector. We have generated all the four types of vector vortex beams by using a modified polarization Sagnac interferometer with a vortex lens. Further, we have studied the non−coaxial superposition of two vector vortex beams. It is observed that the superposition of two vector vortex beams with same polarization singularity leads to a beam with another kind of polarization singularity in their interaction region. The results may be of importance in ultrahigh security of the polarization−encrypted data that utilizes vector vortex beams and multiple optical trapping with non−coaxial superposition of vector vortex beams. We verified our experimental results with theory.

(A. Aadhi, P. Vaity, P. Chithrabhanu, S. G. Reddy, S. Prabakar, R. P. Singh)

Polarization state transformation using two quarter wave plates: application to Mueller polarimetry.

We show that there are a number of ways to transform an arbitrary polarization state into another with just two quarter wave plates (QWPs). We have verified this geometrically using the trajectories of the initial and final polarization states corresponding to all the fast axis orientations of a QWP on the Poincarè sphere. The exact analytical expression for the locus of polarization states has also been given, and describes the trajectory. An analytical treatment of the equations obtained through matrix operations corresponding to the transformation supports the geometrical representation. This knowledge can be used to obtain the Mueller matrix by just using QWPs, which has been shown experimentally by exploiting projections of the output states on the input states.

This work was done in collaboration with R. Simon of Institute of Mathematical Sciences, Chennai.

(S. G. Reddy, S. Prabhakar, P. Chithrabhanu, R. P. Singh, R. Simon)

Polarization properties of the Airy beam

Airy light beam has unusual and interesting properties and their applications have been the subject of numerous investigations. These properties include self−healing, auto−focusing, and self−acceleration. On the other hand it's polarization properties have not yet received much attention. We have, therefore, studied polarization of paraxial Airy beam solutions of Maxwell's equations and its evolution with propagation. We experimentally demonstrate the existence of the cross−polarization component of the Airy beam, typical of non−planar phase fronts, and study its evolution with propagation.

This work was done in collaboration with Sean Nomoto, Reeta Vyas and Surendra Singh of Department of Physics, University of Arkansas, USA.

(A. Aadhi, S. Prabhakar, R. P. Singh)

Divergence of optical vortex beams

We show, both theoretically and experimentally, that the propagation of optical vortices in free space can be analyzed by using the width of the host Gaussian beam and the inner and outer radii of the vortex beam at the source plane. We also studied the divergence of vortex beams, considered as the rate of change of inner or outer radius with the propagation distance, and found that it varies with the order in the same way as that of the inner and outer radii at the source plane. These results may be useful in designing optical fibers for orbital angular momentum modes that play a crucial role in quantum communication.

(S. G. Reddy, P. Chithrabhanu, S. Prabhakar, A. Anwar, J. Banerji, R. P. Singh)

Non−diffracting speckles of a "perfect" vortex beam

We generate "perfect" optical vortex (POV) beams, whose intensity distribution is independent of the order, and scatter them through a rough surface. We show that the size of produced speckles is independent of the order of the POV and their Fourier transform gives the random non−diffracting fields. The invariant size of speckles over the free space propagation verifies their non−diffracting or non−diverging nature. The size of speckles can be easily controlled by changing the axicon parameter, used to generate the Bessel−Gauss beams whose Fourier transform provides the POV. These results may be useful in applications of POV for authentication in cryptography.

(S. G. Reddy, P. Chithrabhanu, P. Vaity, A. Aadhi, S. Prabhakar, R. P. Singh)

"Three−photon hyper−entanglement: teleportation and quantum key distribution"

We present a scheme to generate three−particle hyper−entanglement utilizing polarization and orbital angular momentum (OAM) of photons. We show that the generated state can be used to teleport a two−qubit state described by the polarization and the OAM. The proposed quantum system has also been used to describe a new efficient quantum key distribution (QKD) protocol. We give a sketch of the experimental arrangement to realize the proposed teleportation and the QKD.textit

This work was done in collaboration with Goutam Paul of Indian Statistical Institute, Kolkata.

(P. Chithrabhanu, A. Aadhi, S. G. Reddy, S. Prabhakar, G. K. Samanta, R. P. Singh)

Recovering the vorticity of a light beam after scattering

We generate optical vortices and scatter them through a rough surface. However, the scattered light passing through a lens shows the same vorticity when probed at the Fourier plane. The vorticity is measured using a nonseparable state of polarization and orbital angular momentum of light as it cannot be confirmed by the standard interferometric technique. The observed vorticity is found to be independent of the amount of scattered light collected. Therefore, vortices can be used as information carriers even in the presence of scattering media. The experimental results are well supported by the theoretical results.

(S. G. Reddy, P. Chithrabhanu, S. Prabhakar, A. Anwar, R. P. Singh)

Scattering of non−separable states of light

We experimentally show that the non−separability of polarization and orbital angular momentum present in a light beam remains preserved under scattering through a random medium like rotating ground glass. We verify this by measuring the degree of polarization and observing the intensity distribution of the beam when projected to different polarization states, before as well as after the scattering. We extend our study to the non−maximally non−separable states also.

(P. Chithrabhanu, S. G. Reddy, A. Anwar, A. Aadhi, S. Prabhakar, R. P. Singh)

Design and fabrication of flight model of SWIS instrument in ASPEX payload of Aditya−L1 mission

The proof−of−concept of the SWIS instrument was successfully completed last year. The extension of this to the realization of the flight model was undertaken in last year. Extensive simulations were performed using an ion trajectory simulation software for maximizing the energy and mass resolution for ion energies ranging from 100 eV to 20 keV. The electric field between the top hat analyzer (THA) and the magnetic mass separator (MMS) was reconfigured by insertion of a biased wire−mesh grid in between them. The voltage on the grid is proportional to the ramp HV voltage applied to the inner dome of the THA for scanning the ion energy. Further, the rectangular magnets are replaced by trapezoidal ones for achieving uniform magnetic field all along the deflected ion trajectories inside the MMS. All the parts have been machined with tight tolerances and high degree finish and are assembled. The performance of the flight model will be studied in the laboratory using ions from an ion gun with ion energies in the range of few hundreds of eV to 5 keV. The model also will be subjected to structural and thermal tests to be qualified for the flight model.

This work was done in collaboration with B. Bapat of IISER, Pune and A.R. Srinivasan and Piyush Shukla of SAC, Ahmedabad.

(P. Kumar, S. B. Banerjee, K. P. Subramanian)

A new algorithm for improving the accuracy of position encoding using resistive anode encoder

A resistive anode encoder (REA) to be used along with an 80 mm diameter multichannel plate (MCP) ion detector is being developed for imaging the energy and mass selected ions in the SWIS instrument of ASPEX Payload. The position sensitivity of the device was tested by placing a mask over the detector with a tiny aperture above a designated region of the resistive anode. The position encoding is done using the differential charge measurement at the resistive chain terminals. The signals are shaped and charge−amplified using appropriate sensitive electronic circuits, which were developed in the lab. The position detection efficiency depends on a number of parameters such as the total resistance of the resistive chain anode, inter−track resistances etc. The performance is also found to depend on the detector characteristics, such as the pulse height distribution (PHD). Maximum position encoding accuracy is obtained when the overlap between PHD and the 'gain curve' of the electronic circuit is maximized. However large jitters in the PHD is an inherent problem due to attenuation of the signal on varied resistive paths, which badly affects the position resolution of the detector. An algorithm has been developed to correct this jitter, by which the position accuracy has been improved substantially.

(P. Adhyaru, K. Baladaniya, S. B. Banerjee, P. Kumar, K. P. Subramanian)

Dependence of transition probability on impact energy during dissociative double ionization of N_2 and CO

Experimental and computational analysis of dissociative double ionization of N_2 and CO molecules under electron impact at 1, 3, and 5 keV electron energies indicate observable changes in the kinetic energy release (KER) distribution spectra., KER distributions corresponding to charge symmetric dissociation channels of N_2^{2+} and CO^{2+} at these impact energies exhibit an approximately linear trend between the transition energy and the expected KER values. The same trend was inferred by analysing the dissociation process using the calculated potential energy curves of the dications. The results indicate that the transition probability for excitation to different molecular ion states is not only a function of energy difference between the ground and excited states, but also a complicated function of the impact energy. In addition, nature of the observed trend in the differential KER cross sections differs significantly from their differential transition probability, which are calculated using inelastic collision model for fast−electron−impact case.

This work was done in collaboration with B. Bapat of IISER Pune.

(A. Pandey, P. Kumar, S. B. Banerjee, K.P. Subramanian)

Energy−selective fragment spectra: a probe for high−lying dications

The lifetime of transient molecular ions are very small; therefore study of various highly excited states involved in the fragmentation process is rather impossible. This limits our knowledge of their dynamical evolution and the parameters governing the dissociation.The large density of high−lying states and crossing of states makes theoretical interpretation of fragmentation a tedious task. The contributions from different states to the fragment kinetic energy distributions cannot be separated. Consequently, the exact nature of the evolution remains elusive. In this context, we have performed kinematic analysis of the dissociation dynamics of di−cations of N_2 and CO formed by photoionisation. The energy of the transient molecular ions is estimated from the correlated fragment ion momenta, measured in coincidence with energy−analyzed ejected electrons. These measurements bring out the differences in kinematics of the fragmentation of transient molecular ions having different internal energies. The study indicates that highly excited states decay primarily to their own asymptotic limits with only weak coupling to states decaying to lower asymptotes.

This work was done in collaboration with B. Bapat of IISER Pune and K. Saha of Weizmann Institute of Science, Israel.

(A. Pandey, K. Saha, B. Bapat, P. Kumar, S. B. Banerjee, K. P. Subramanian)

Vacuum Ultraviolet Photoabsorption Spectra of Nitrile Ices for their Identification on Pluto

Icy bodies, such as Pluto, are known to harbour simple and complex molecules. The recent New Horizons flyby of Pluto has revealed a complex surface composed of bright and dark ice surfaces, indicating a rich chemistry based on nitrogen (N_2), methane (CH_4) and carbon monoxide (CO). Nitrile (CN) containing molecules such acetonitrile (CH_3CN), propionitrile (CH_3CH_2CN), butyronitrile ($CH_3CH_2CH_2CN$) and isobutyronitrile ($(CH_3)_2CHCN$) are some of the nitrile molecules that are known to be synthesized by radiative processing of such simple ices. Through the provision of a spectral atlas for such compounds we propose that such nitriles may be identified from the ALICE payload onboard New Horizons.

The first VUV photoabsorption spectra of nitrile bearing molecules such as aceto, propio, butyro and iso−butyronitrile molecules are reported for ices prepared at 10 K and at higher temperatures. The spectral signatures of all the nitrile ices were found to be similar in the 110 to 145 nm region with subtle changes in the absorption intensity due to morphology changes (amorphous to crystalline) upon warming the ice to higher temperatures. Comparison of the nitrile spectra with the spectra of several of the simpler and dominant molecules on Pluto (N_2, CH_4 and CO) and other possible trace species such as water and oxygen, suggest that the detection of continuous absorption in the 150 nm to 175 nm region may be a good indicator of the detection of nitrile molecules in the surface ice of Pluto (Figure 1).

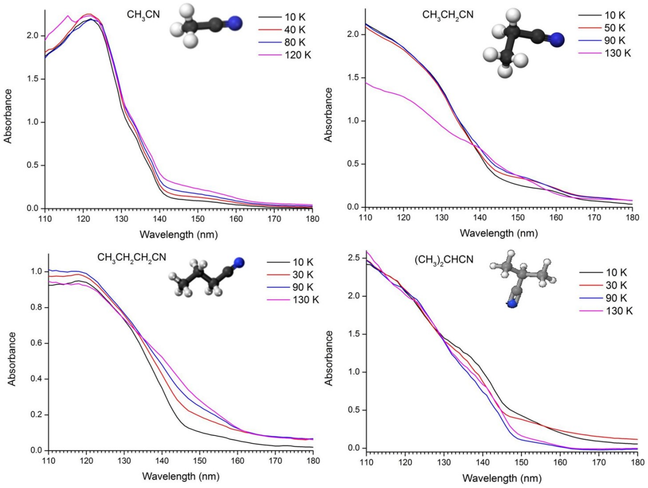

Figure 1 : VUV photoabsorption spectra of acetonitrile, propionitrile, butyronitrile and isobutyronitrile ices as a function of temperature. Note baselines are displaced to show spectra at different temperatuers.

This is done in colloboration with NSRRC and OU.

(B. Sivaraman)

Component specific analysis of Optically Stimulated Luminescence (OSL) using an in−house developed GUI application for the same

Mathematical equation expressing the decay of the optically stimulated luminescence (OSL) of quartz as a function of stimulation time is widely accepted as being the sum of a number of exponentials. Using computer generated synthetic OSL decay curves we had developed rigorous statistical procedures to determine the number of components that best fit the curves. In this study we had included Poisson noise and random instrumental background in synthetic OSL decay curves and a multi−exponential decay curve was fitted to the decay curves to deconvolute them into several components. The fitting algorithm was critically dependent on signal−to−noise ratio and therefore a method of retrieving the intensities of the components from OSL signals with poor signal−to−noise ratios was developed and tested. We have now developed a user−friendly software that would enable anyone to carry out the component specific analysis.

The ability of the procedure to retrieve the intensities of these components was examined in case of real samples using a decay curve comprising three known components. Rigorous comparison of the results of palaeodose based on fast component extracted from individual OSL decay curves with the Paleodose values from standard SAR protocol (using both the early and late light subtraction) on samples from diverse depositional environment indicated that paleodoses based on fast components SAR were invariably lower compared to those from the usual SAR protocol. The underestimation ranged from about 7% to 53%. Interestingly, in all the samples, dose recovery test yielded comparable results from fast component dose and the SAR protocol. This suggested robustness of our de−convolution procedure and implies caution in conventional SAR based ages.

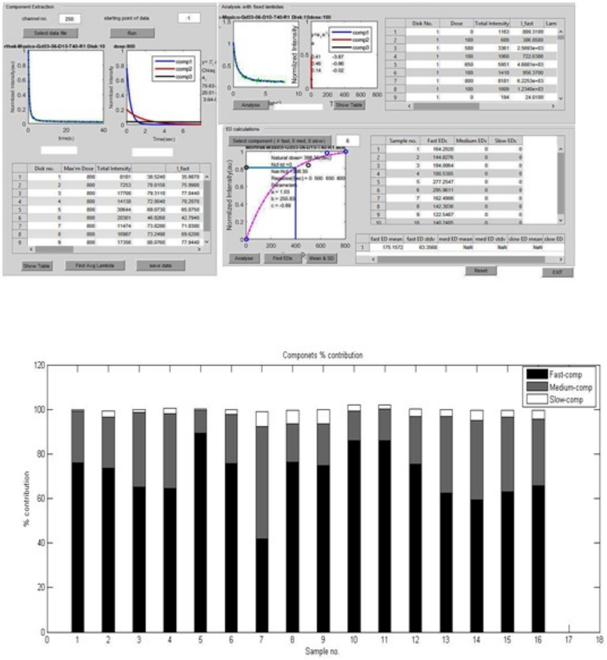

Figure 2: Top: Snapshot of the component analysis software. Bottom: The contribution of components for different samples and for different environment. Sample (1−2) Aeolian, (3−6) Desert, (7−8) River, (9−12) lake and (13−16) coastal environments.

(V. Kumar, M.K. Murari, A. K. Singhvi)

Optical dating of sediments from the palaeochannels of the Ghaggar river of Haryana

Remote sensing and GIS studies have helped identify palaeochannels of Ghaggar River (often discussed as the mythical Saraswati?) in various parts of Haryana. The buried channels are considered to be the bed of a mighty river that once sustained hundreds of Harappan sites along its channel. The view has constantly been challenged and debated.

In this study an attempt is being made to synthesize the existing chronometric data on sites along the course of palaeo−Gagghar and supplement these with optically stimulated luminescence (OSL) dates on quartz from sediments obtained from stratigraphic sections of deep wells in the palaeo−channels of the Ghaggar River near Hissar in Haryana. Preliminary data suggest that micaceous sands of Himalayan origin were replaced by red sands of Thar deserts sometime around 20 ka, much prior to the times of Harappans. The effort is aimed to develop an insight into the hydrological regime of the river and the contemporary climatic conditions to help elucidate the settlement pattern and the *raison d etre* for the sustenance of the Harappan sites in this region.

(A. K. Dave and A. K. Singhvi)

Chronology of Desert Margin in Western India

This study is an attempt to provide improved chronology for ∼ 30 m sediment section located in Mahi river basin near Rayka. The sequence has preserved a near continuous record of climate change since the Last Interglacial. An earlier study by Juyal et al 2000 based on feldspar IRSL chronology shows a combined effect of anomalous fading and unbleached components resulting in age inversions. In present work the possibility of using blue light stimulated luminescence (BLSL) of quartz, infra−red stimulated luminescence (IRSL) of feldspar and the newly developed methodologies, like natural correction factor based single aliquot regeneration (NCF−SAR) protocol and decision making schemes based on distribution of doses and beta heterogeneity concept for luminescence dating of sediments were explored. Observations suggested that quartz which is considered a better mineral compared to feldspar in terms of its luminescence behavior and bleachability suffered from significant sensitivity changes during natural signal measurement and partial bleaching. A combination of NCF−SAR protocol and sample specific equivalent dose computation helped in arriving at better age estimate for present samples. The study also compares the criteria for the selection of different age models that are used at present. The ages of the alluvial sequence is now bracketed between 10 ka (upper aeolian unit) and 75 ka (lowermost fluvial unit)

This work is carried out in collaboration with P. Morthekai, BSIP.

(N. Chauhan and N. Juyal)

Optical Dating of Termite

Small ants of termites are considered as one of the important factors for controlling global methane fluxes. Termite ants form colonies and build mounds that are several meter high. We examined the luminescence of quartz grains from selected location in mounds and their source region to understand their formation dynamics. Luminescence of single grains of quartz from each strategically located horizon was analyzed from six termite mounds were. As expected the dose distribution was complex but a pattern in the dose progression with termite height was seen and this indicated the manner in which the mounds form and how these mounds could be reliably dated. A series of modern and ancient mounds were dated and the oldest age was 4ka. The data analysis also suggested that termite mound formation occurred in episodes of favorable climate.

This work is being done in collaboration with R.J. Wasson of National University, Singapore and S. Garnet, Charles Darwin University, Australia.

(H.M. Rajapara, N. Chauhan, A. K. Singhvi)

Sensitivity changes during natural measurement in single grains of quartz

It has been observed that luminescence sensitivity of the quartz changes significantly during measurement of natural OSL signal. Conventionally used SAR protocol is expected to correct for sensitivity changes during the measurement sequence, however, it cannot correct for sensitivity changes during measurement of natural signal. Earlier, we proposed a methodology to correct for sensitivity changes via natural correction factor (NCF that ratio of sensitivity of sample as received and the same sample with first cycle of preheat and OSL readout) for single aliquots. Variations in sensitivity changes in single grains of 90−150 μm diameter were examined for possible correlation between luminescence sensitivity of individual grains and their NCF. Several hundred grains from samples of diverse depositional environment, were measured in order and preliminary results suggest that with for samples with higher sensitivity, the NCF factor approaches unity.

(N. Chauhan and A. K. Singhvi)

Optical dating of neotectonic events in Central Indian shield zone.

ENEWSW trending Gavilgarh Fault Zone (GFZ) is an important tectonic lineament within the Central Indian shield. Geomorphological mapping and spatial analyses of rivers, by Delhi University scientists helped elucidate the imprints of active tectonics on the fluvial systems of this region. Sinuosity index, width–depth ratio of river valleys, longitudinal profile, SL index and hypsometric index of the rivers flowing from north to south across the GFZ lineament suggested that the northern side of GFZ was tectonically uplifted. Luminescence dating of sediments from river terraces enabled calculation of knick−point migration rates in the rivers. These indicated multiple neotectonic events in GFZ at ca. 65-80 ka, ca. 50 ka, ca. 30–40 ka, and ca. 14 ka. This evidence of neotectonic activity, presence of active geothermal springs, and recent earthquakes along GFZ suggest that this lineament is tectonically active and there is a need for proper seismic monitoring of this fault zone.

This work was done in collaboration with D. Bhattacharjee, V. Jain, A. Chattopadhyay of Delhi University.

(R. H. Biswas and A. K. Singhvi)

Reconnaissance Optical dating of coastal, fluvial and aeolian carbonate sequences of Saurashtra

Saurashtra coast and its interior regions in Western India host bioclastic carbonate deposits (termed as the miliolites after *sp. miliolidae*). These span an area of about 28,000 km^2 and were formed due to combination of near shore marine, inter−tidal, backshore, fluvial and aeolian processes. Considerable debate on their formation processes, chronology and presence deep inland in the region, have existed for decades. Such debates arose due partly to questionable chronologies based on, i) inappropriate sampling strategies and, ii) the use of ^{230}Th/^{234}U and ^{14}C ages on the bulk carbonates (that are invariably contaminated by detritus and altered during post depositional diagenetic processes). Use of such diagenetically altered ages of formation to date e.g. aeolian processes that build carbonate dunes lead to avoidable confusion. In the present study traces (<1%) of quartz grains trapped in carbonate were used for Optically Simulated Luminescence (OSL) dating. The basic premise was that the quartz grains were syn−sedimentary to the carbonate deposition at a given site (either pristine or aeolian transported grain) and that, methodologically, the ages were not affected by diagenetic and cementation processes. In general, the optical ages were lower compared to the existing radiometric ages and suggested that previously argued correlation of aeolian deposition with low sea stands only was not tenable. OSL ages also suggested that inland carbonate deposits were result of re−working of older carbonate sediments that were transported as grains during increased aridity. These ages accord with geomorphic processes and suggest that previously suggested tectonic uplift of the entire region by up to 40−50 m at an average rate of 0.23 to 2.2 mm/year was incorrect. Overall the OSL ages settle the existing debates on miliolites, their origins, and their climate/tectonics connections.

This work was done in collaboration with Nilesh Bhatt, MS University of Baroda and D.K. Cheong of Kangwon National University, South Korea.

(K. Sharma, A. D. Shukla, A. K. Singhvi)

Electron Irradiation of Carbon dioxide−Carbon disulphide Ice Analog and its Implication on the Identification of Carbon disulphide on Moon

Carbon dioxide (CO_2) and carbon disulphide (CS_2) molecular ice mixture was prepared under low temperature (85 K) astrochemical conditions. The icy mixture irradiated with keV electrons simulates the irradiation environment experienced by icy satellites and Interstellar Icy Mantles (IIM). Upon electron irradiation the chemical composition was found to have altered and the new products from irradiation were found to be carbonyl sulphide (OCS), sulphur dioxide (SO_2), ozone (O_3), carbon trioxide (CO_3), sulphur trioxide (SO_3), carbon subsulphide (C_3S_2) and carbon monoxide (CO). Results obtained confirm the presence of CS_2 molecules in Lunar south pole probed by the Moon Impact Probe (MIP) (Figure 3).

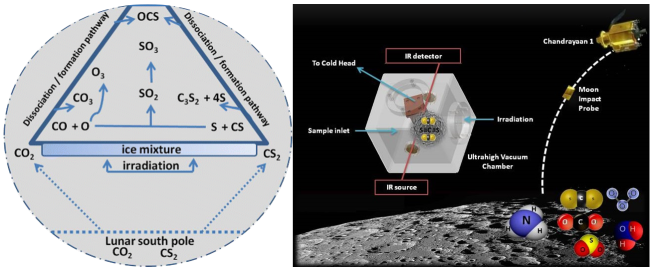

Figure 3: (Left) Reaction schema for the synthesis of SO$_x$ and OCS from CO_2-CS_2 ice mixture. (Right) Simulating the colder lunar south pole in laboratory conditions.

(B. Sivaraman, R. Sridharan)

A Rare Impact Event of Space Origin in Vellore District in India

Bharathidhasan Engineering College (BEC) located in Natrampalli, Vellore district (Tamilnadu, India), came under the limelight after an incident on 6^{th} February 2016 due to a report of bolide trail (extending several km) and possible fall in which a bus driver was killed. The event left a crater of diameter $\sim$ 1.2 m and depth $\sim$ 0.34 m, is till date disputed whether it is related to an impact of space related object or a land based explosion. The deceased person was found to have 19 rib bones broken and no damage to the long bones. Damages were also observed in the college premises and its surrounding area. Bomb squad had dismissed the possibility of any man made explosive. Detailed analysis of the damage that had occurred along with video footage evidences and scientific questioning, rather all of them, lead us towards one surprising conclusion that the event is, in fact, an unique and extremely rare impact event of an object of space origin, travelling at high velocities. Disintegration of the impacting material is expected at such high velocities, making it hard to be found in the BEC landscape. It was later reported in NASA Fireball and Bolide report page that, on the same day, an explosion equivalent to 13 kT (rare event) took place at $\sim$ 31 km altitude over the South Atlantic Ocean (30.4 °S, 25.5 °W) (Figure 4).

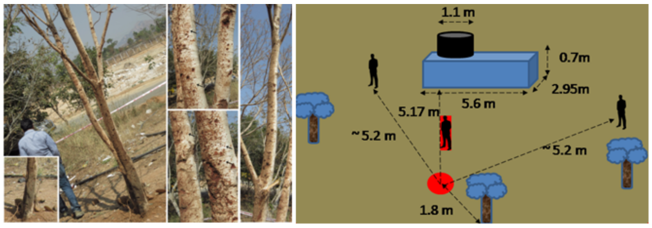

Figure 4: (a) Ejecta on tree present at 1.8 m from centre of crater. (b) Showing the relative distances and the positions of the deceased (in red rectangle) and injured persons with respect to the impact crater (red circle).

(B. Sivaraman, S. Vijayan, R. Ramachandran, H. Shankar, A. D. Shukla, R. Mahajan, D. Ray)

Interstellar Monohydric Alcohols and their Thiol Analogs

It has been pointed out by various astronomers that in accordance to the spectroscopic behaviours and chemical abundances, very interesting relationship exist between interstellar alcohols and their corresponding thiols (sulfur analogue of alcohols).

In the the monohydric alcohols: methanol, ethanol are widely observed whereas 1−propanol is recently claimed in Orion KL. Among the monohydric thiols, methnanethiol (chemical analog of methanol), has already been firmly detected in Orion KL and Sgr B2(N2) and ethanethiol (chemical analog of ethanol) has been claimed to observe in SgrB2(N2) though the confirmation of this detection is yet to come. It is very likely that higher order thiols could be observed around these sources. In this attempt, here we study the formation of monohydric alcohols and their thiol analogues. Based on our quantum chemical calculation and chemical modelling, we find that 'Tg' conformer of 1−propanethiol is a good candidate of astronomical interest. We present various spectroscopic information of this molecule for its future detection in the Interstellar medium (ISM) (Figure 5).

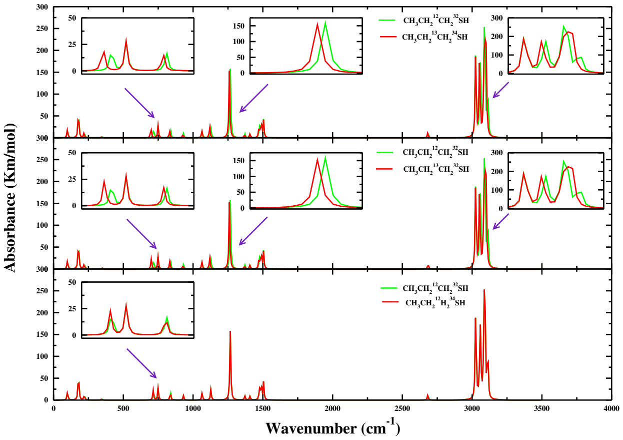

Figure 5: Isotopic variation of 1−propanethiol.

This work is carried out in collaboration with Dr. Ankan Das, Indian Center for Space Physics, Kolkatta.

(B. Sivaraman)

Vacuum Ultraviolet Photoabsorption of Prime Ice Analogs of Pluto and Charon

New Horizons being the first dedicated mission to explore the icy Pluto and its moons has been returning data from the scientific payloads onboard. Well before the New Horizons encounter, it was widely known about the chemical composition of the larger bodies of the Pluto system, Pluto and Charon, were dominated by the presence of simple ices such as nitrogen/methane/carbon monoxide and ammonium hydroxide, respectively. From ***New Horizons*** flyby, water was found to be a component of icy Pluto and pure ammonia to exist in Charon system.

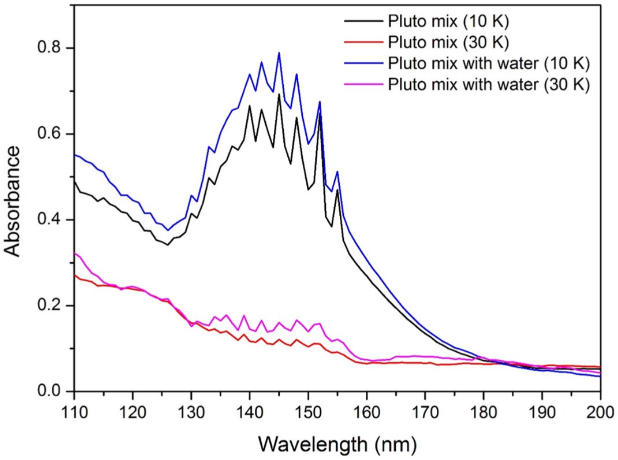

Figure 6 : VUV Photoabsorption spectra of Pluto ice mixtures at 10 K and warmed to 30 K.

Nitrogen (N_2), carbon monoxide (CO) and methane (CH_4) molecules were mixed in gas phase in the ratio 100:1:1 and was inlet into the UHV chamber to condense on the LiF substrate at 10 K to mimic the surface ices of Pluto. The Pluto mixture was then mixed with water in the ratio N_2:CO:CH_4:H_2O = 100:1:1:3 to realise the effect of water in the VUV spectra from the surface of Pluto. In the next experiment, ammonia (NH_3) and water (H_2O) molecules were mixed in gas phase in the ratio 1:1 and made to condense in the LiF substrate at 10 K to mimic the surface ices of Charon. A temperature dependent study of these Pluto and Charon ice analogs were also studied (Figure 6).

This is done in colloboration with NSRRC and OU.

(B. Sivaraman)

Using Hartley band to detect the ozone precursor on icy satellites

To−date Hartley band (220 nm −310 nm) of ozone is widely used to detect the presence of ozone. Recently the Vacuum UltraViolet (VUV), 110 nm −190 nm, photoabsorption spectra of pure solid ozone revealed the absence of Hartley band while ozone concentrations are low. This could be one reason for the weak absorption in the Hartley band in Iapetus while it was intense in Rhea and Dione. Yet, due to strong absorption of other simple molecular ices, such as H_2O / CO_2 etc., in the VUV region unambiquous identifcation of ozone could not be made. Therefore, Hartley band is the only wavelength that is available to−date for the identification of ozone elsewhere, which demands sufficient ozone concentration. It is surprising to note that there was only two experiments to−date that had reported the Hartley band of pure solid ozone synthesized from O_2 / CO_2 ices under astrochemical conditions. Though the ozone synthesizers are considered simple molecular species the chemical complexity and different range of temperatures that prevails on icy bodies, indeed, demands more investigation. This is important especially when there could be absorption, from another molecule like SO_2, at similar wavelength.

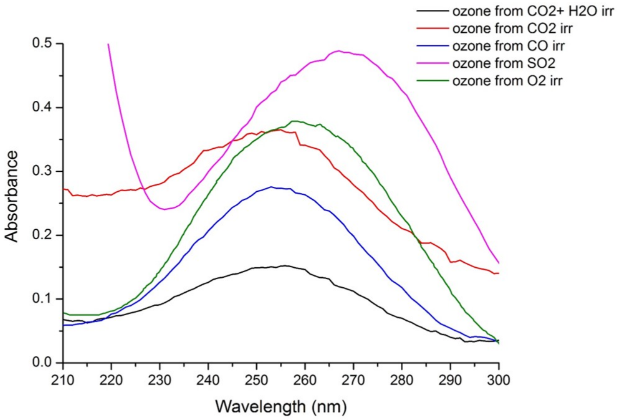

Figure 7: Hartley band observed after in−situ ozone synthesis in different ozone precursor molecular ices.

Here, we propose using the Hartley band in identifying the ozone precursor molecule on the icy satellites based on a series of experiments carried out on simple ozone precusor ice analogs. Upon irradiation of O_2, CO, CO_2, CO_2+H_2O, SO_2, NO, N_2O and NO_2 ices and subsequent recording of spectra strong absorption in the Hartley band was observed (Figure 7). This confirms the presence of ozone in the icy analogues. After VUV irradiation spectra were also recorded as a function of temperature until the sublimation of majority of ozone molecules observed by the reducing intensity of Hartley band. Depending on the icy analogue the peak of the observed Hartley band was found to vary from 255 −270 nm (Figure 7). Therefore, the implication of this experimental data could lead to the identification of ozone precursor molecules on icy satellites by observing the Hartley band, where many of the icy satellites are known to harbour a variety of ozone precursors, simple oxygen bearing molecules.

This is done in colloboration with NSRRC and OU.

(B. Sivaraman)

Landslide phenomena on Saturn's icy moon: Rhea

Rhea, the second largest satellite of Saturn has undergone the geological activity at larger scale for longer period of time. Airless moon of Saturn shows numerous stratigraphic features which were analysed earlier from Voyager mission. The geological landform includes presence of lineaments, scarps, grabens, ridges, fault lines, grooves etc. Through the treasure of high resolution data provided by Cassini mission on multiple flybys of Rhea starting from 2005, it is possible to sneak into this icy moon in more efficient way.

Figure 8: Part of Nishanu crater acquired from ISS NAC with product id N1665994776, approximately ranging from 10°N to 277.2°E. The image resolution is approx. 257 m/pixel. The white arrows indicated the area of landslide.

Landslide is one of the most common geological activity seen on the surface of the earth till day. However, this activity is already observed on a large scale on other planets like Mars, Moon, Venus and few icy satellites like Iapetus, Io and Rhea. The presence of mass wasting on these planets shows some activity similar to the surface of earth. Additionally, mass wasting on one of the youngest crater called Inktomi shows that the surface of Rhea was active till few years back.

Add−on to this, on the basis of age difference between Kuma crater and landslide, it is possible to have deep understanding regarding formation of mass wasting; whether it is a result of impact effect or any weathering process. If any physical weathering process is associated with it then what are the feasible driving factor behind it, and how it form. The author is taking this idea further by mapping the landslide location on Rhea through which it will be possible to get the understanding of surface composition and its structure.

(R. Parek, S. Vijayan, B. Sivaraman)

Low velocity impact experimental facility in PRL

Impact processes are considered to be the reason behind the formation of large sized objects and are also responsible for the dusty environment that are found in several regions in our Solar System. Experimental evidences had shown that low velocity impacts, 0.1 to 1 km s^{-1}, played major role in producing planetesimals and cometesimals. Indeed, lower velocity impacts are the secondary impact process that is a result of any hypervelocity impact on to a solid/icy surface. In the case of Jovian and Saturnian satellites such low velocity impact processes in low temperature ice targets explains both the accretion and surface evolution of icy planetary bodies. Numerous laboratory experiments had been performed to study effect of impact on to solid surfaces in order to estimate the strength of a given material for space applications. Simultaneously experiments were also performed to understand the crater formation on atmosphereless objects (such as asteroids) and icy bodies (Jovian and Saturnian satellites). However most of the experiments were focused in simulating and scaling the amount of damage that can be brought by impacting projectiles, where the experiments were carried out by firing single projectile on to the target. Our experiments on low velocity impact studies are carried out using a table top manually operated shocktube that can propel multiple projectiles at an average velocity up to 220 m s^{-1}. Using our new experimental facility we carry out impact experiments at low velocities using sand and fullerene soot particles on water and dry ice to investigate the ice assisted sticking and growth of planetesimals.

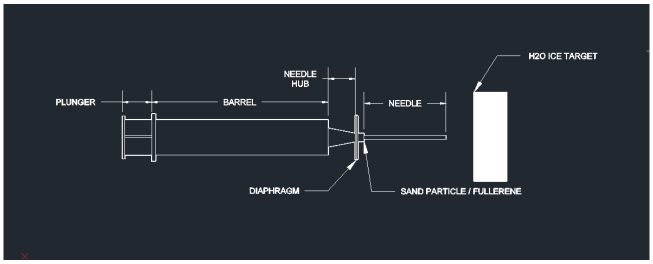

Figure 9: Schematic of the basic Reddy Tube setup. A larger version of this is used to simulate low velocity impact experiments on ice targets.

(B. Sivaraman, M. Jaya Krishna S. Vijayan)

Electron Irradiation of N_2O - CS_2 ice mixtures in astrochemical conditions

Experiments were carried out in the experimental chamber housed in the laboratory for low temperature Astrochemistry at Physical Research Laboratory (PRL), India. An UltraHigh Vacuum (UHV) chamber, that can reach base pressures up to 10^{-10} mbar, containing a cold head with Zinc Selenide (ZnSe) substrate cooled down to 85 K. An all metal leak valve was used to introduce gases to form molecular ices on to the cooled ZnSe substrate at 85 K.

N_2O and CS_2 molecules were mixed in the gasline and deposited on the ZnSe substrate at 85 K. An IR spectrum was recorded at 85 K. The ice mixtures were irradiated with 1 KeV electrons for 30 minutes and another IR spectrum was recorded as shown in Figure 9. The main products found to appear after irradiation were C_3S_2 at 2055 cm^{-1} and SO_2 at 1150 and 1154 cm^{-1} as shown in Figure 9.

SO_2 can be formed via the following reactions (a, b and c); C_3S_2 can be formed by reaction (d):

(a) $CS_2 \rightarrow CS + S$

(b) $S + O \rightarrow SO(+O) \rightarrow SO_2$

(c) $S + O_2 \rightarrow SO_2$

(d) $3CS_2 \rightarrow C_3S_2 + 4S$

N_2O - CS_2 ice mixture, kept at 85 K, upon electron irradiation was found to synthesis C_3S_2 and SO_2. From the experiments carried out we could clearly see that carbon and sulphur bearing molecules were synthesized in larger amounts. The available S atoms from the CS_2 and O atoms from N_2O were found to react readily in synthesizing SO_2. Therefore, we propose SO_2 to be one of the largely available molecules on cometary nucleus rich in CS_2 and oxygen bearing simple molecules.

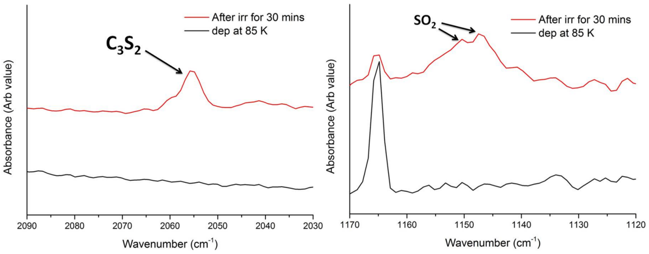

Figure 10: Infrared spectra of the ice mixture before and after irradiation (left) C_3S_2 observed after irradiation at 2055 cm^{-1} and (right) SO_2 after irradiation at 1150 and 1154 cm^{-1}.

(S. Pavithraa, S. Raman, B. Sivaraman)

Publications

Publications in Journals

Astronomy and Astrophysics

1. Banerjee, D. P. K., Nuth, J. A., III, Misselt, K. A., Varricatt, W. P., Sand, D., Ashok, N. M., Su, K. Y. L., Marion, G. H. and Marengo, M., 2015, *“Evolution of the Dust in V4332 Sagittarii”*, ApJ, v. 814, p. 109-117.
2. Banerjee, D. P. K., Srivastava, M. K., Ashok, N. M. and Venkataraman, V., 2016, *“Near-infrared studies of the carbon monoxide and dust-forming Nova V5668 Sgr”*, MNRAS Lett., v. 455, p. 109-113.
3. Chandra, S., Zhang, H., Kushwaha, P., Singh, K. P., Bottcher, M., Kaur, N. and Baliyan, K. S., 2015, *“Multi-wavelength Study of Flaring Activity in BL Lac Object S5 0716+714 during the 2015 Outburst”*, ApJ, v. 809, pp. 1-9.
4. Chattopadhyay, T., Vadawale, S. V., Goyal, S. K., Mithun, N. P. S., Patel, A. R., Shukla, R., Ladiya, T., Shanmugam, M., Patel, V. R. and Ubale, G. P., 2016, *“Development of a hard x-ray focal plane compton polarimeter: a compact polarimetric configuration with scintillators and Si photomultipliers”*, Exp Astron, v. 41, p. 197-214.
5. Epili, P., Naik, S. and Jaisawal, G. K., 2016, *“Broad-band spectroscopy of the transient X-ray binary pulsar KS 1947+300 during 2013 giant outburst : Detection of pulsating soft X-ray excess component”*, Res. Astron. Astrophys., v. 16, pp. 1-10.
6. Fischer, D. A., Anglada-Escude, G., Arriagada, P., Baluev, R. V., Bean, J. L., Bouchy, F., Buchhave, L. A., Carroll, T., Chakraborty, A., Crepp, J. R., Dawson, R. I., Diddams, S. A., Dumusque, X., Eastman, J. D., Endl, M., Figueira, P., Ford, E. B., Foreman-Mackey, D., Fournier, P., Fursz, G., Gaudi, B. S., Gregory, P. C., Grundahl, F., Hatzes, A. P., Hbrard, G., Herrero, E., Hogg, D. W., Howard, A. W., et al., 2016, *“State of the Field: Extreme Precision Radial Velocities”*, PASP, v.128, p. 66001-66043.
7. Gehrz, R. D., Evans, A., Helton, L. A., Shenoy, D. P., Banerjee, D. P. K., Woodward, C. E., Vacca, W. D., Dykhoff, D. A., Ashok, N. M., Cass, A. C., Carlon, R. L., Corgan, D. T., Eyres, S. P. S., Joshi, V., Keller, Luke D., Krautter, J., Liimets, T., Rushton, M. and Starrfield, S., 2015, *“The Early Infrared Temporal Development of Nova Delphini 2013 (V339 DEL) Observed with the Stratospheric Observatory for Infrared Astronomy (SOFIA) and from the Ground”*, ApJ, v. 812, p. 132-143.
8. Hsiao, E. Y., Burns, C. R., Contreras, C., Hflich, P., Sand, D., Marion, G. H., Phillips, M. M., Stritzinger, M., Gonzlez-Gaitn, S., Mason, R. E., Folatelli, G., Parent, E., Gall, C., Amanullah, R., Anupama, G. C., Arcavi, I., Banerjee, D. P. K., et al., 2015, *“Strong near-infrared carbon in the Type Ia supernova iPTF13ebh”*, A & A, v. 578, p. 9-26.
9. Jaisawal, G. K. and Naik, S., 2015, *“Detection of fundamental and first harmonic cyclotron line in X-ray pulsar Cep X-4”*, MNRAS Lett., v. 453, p.L21-L25.
10. Jaisawal, G. K., Naik, S. and Epili, P., 2016, *“Suzaku view of the Be/X-ray binary pulsar GX 304-1 during Type I X-ray outbursts”*, MNRAS, v. 457, p. 2749-2760.
11. Janardhan, P., Bisoi, S. K., Ananthakrishnan, S., Sridharan, R. and Jose, L., 2015, *“Solar and Interplanetary Signatures of a Maunder-like Grand Solar Minimum around the Corner - Implications to Near-Earth Space ”*, Sun and Geosphere, v. 10, p. 147-156.

12. Janardhan, P., Bisoi, S. K., Ananthakrishnan, S., Tokumaru, M., Fujiki, K., Jose, L. and Sridharan, R., 2015, *"A Twenty Year Decline in Solar Photospheric Magnetic Fields: Inner-Heliospheric Signatures and Possible Implications? "*, J. Geophys. Res. Atmos., v. 120, p. 5306-5317.
13. Joshi, V., Banerjee, D. P. K., Ashok, N. M., Venkataraman, V., Walter, F. M., 2015, *"Infrared studies of Nova Scorpii 2014: an outburst in a symbiotic system sans an accompanying blast wave"*, MNRAS, v. 452, p. 3696-3703.
14. Kane, S. R., Wittenmyer, R. A., Hinkel, N. R., Roy, A., Mahadevan, S., Dragomir, D., Matthews, J. M., Henry, G. W., Chakraborty, A., Boyajian, T. S., Wright, J. T., Ciardi, D. R., Fischer, D. A., Butler, R. P., Tinney, C. G., Carter, B. D., Jones, Hugh R. A., Bailey, J., OToole, S. J., 2016, *"Evidence for Reflected Light from the Most Eccentric Exoplanet Known."*, ApJ, v. 821, pp. 1-12.
15. Kantharia, N. G., Dutta, P., Roy, N., Anupama, G. C., Ishwara-Chandra, C. H., Chitale, A., Prabhu, T. P., Banerjee, D. P. K. and Ashok, N. M., 2016, *"Insights into the evolution of symbiotic recurrent novae from radio synchrotron emission: V745 Scorpii and RS Ophiuchi"*, MNRAS Lett., v. 456, p. 49-53.
16. Raj, A., Banerjee, D. P. K., Ashok, N. M., Kim, Sang Chul 2015, *"Near-infrared studies of nova V5584 Sgr in the pre-maximum and early decline phase."*, Research in A & A, v. 15, p. 993-1005.
17. Rao, J. A., Vadawale, S. V., Mithun, N. P. S. and Misra, R., 2016, *"Investigating the Connection between Quasi Periodic Oscillations and Spectral Components with NuSTAR Data of GRS 1915+105"*, ApJ, v. 817, pp. 1-7.
18. Srivastava, M. K., Ashok, N. M., Banerjee, D. P. K., Sand, D., 2015, *"Near-infrared studies during maximum and early decline of Nova Cephei 2014 and Nova Scorpii 2015"*, MNRAS, v. 454, p. 1297-1309.
19. Vacca, W. D., Hamilton, R. T., Savage, M., Shenoy, S., Becklin, E. E., McLean, I. S., Logsdon, S. E., Marion, G. H., Ashok, N. M., Banerjee, D. P. K., Evans, A., Fox, O. D., Garnavich, P., Gehrz, R. D., Greenhouse, M., Helton, L. A., Kirshner, R. P., Shenoy, D., Smith, N., Spyromilio, J., Starrfield, S., Wooden, D. H. and Woodward, C. E., 2015, *"Observations of Type Ia Supernova 2014J with FLITECAM/SOFIA"*, ApJ, v. 804, p. 66-74.
20. Vadawale, S. V., Chattopadhyay, T., Rao, A. R., Bhattacharya, D., Bhalerao, V. B., Vagshette, N., Pawar, P. and Sreekumar, S. 2015, *"Hard X-ray polarimetry with Astrosat-CZTI"*, A & A, v. 578, pp. 1-7.
21. Valtonen, M. J., Zola, S., Ciprini, S., Gopakumar, A., Matsumoto, K., Baliyan, K.S., Kaur, N., Sameer and Ganesh, S., et al. 2016, *"Primary Black Hole Spin in OJ 287 as Determined by the General Relativity Centenary Flare"*, ApJL , v. 819, pp.1-6.

Solar Physics

22. Joshi, B., Bhattacharyya, R., Pandey, K. K., Kushwaha, U. and Moon, Y. 2015, *"Evolutionary aspects and north-south asymmetry of soft X-ray flare index during solar cycles 21, 22, and 23"*, A & A, v. 583, p. 1-11.
23. Kumar, S., Bhattacharyya, R. and Smolarkiewicz, P. K. 2015, *"On the role of topological complexity in spontaneous development of current sheets"*, Phys. Plasmas, v. 22, 082903, p. 1-15
24. Kumar, S. and Bhattacharyya, R. 2016, *"Continuous development of current sheets near and away from magnetic nulls"*, Phys. Plasmas, v. 23, 044501, p. 1-4
25. Mishra, W.,Srivastava, N. and Singh, T. 2015, *"Kinematics of interacting CMEs of 25 and 28 September 2012"*, J. Geophys. Res. Space Physics, v. 120, p. 10221-10236
26. Mishra, W. and Srivastava, N. 2015, *"Heliospheric tracking of enhanced density structures of the 6 October 2010 CME"*, J. Space Weather Space Clim., v. 5, A20, p. 1-12

Planetary Sciences and PLANEX Program

27. Banerjee, R., Ray, D. and Ishhi, T. 2015, *"Mineral chemistry and alteration characteristics of spinel in serpentinised peridotites from the Northern Central Indian Ridge"*, J. Geol Soc India, v. 86, p. 41-51.
28. Basu Sarbadhikari, A., Marhas, K. K., Sameer and Goswami, J. N. 2016, *"Water in the lunar interior"*, Curr. Sci., v. 110, p. 1536-1539.
29. Chattopadhyay, T., Vadawale, S., Goyal, S. K., Mithun, N. P. S., Patel, A. R., Shukla, R., Ladiya, T. , Shanmugam, M., Patel, V. R. and Ubale, G. P. 2015, *"Development of a Hard X-ray focal plane Compton Polarimeter: A compact polarimetric configuration with Scintillators and Si Photomultipliers"*, Exp Astron, v. 41, p. 197-214.
30. Goswami, T. K., Ray, D., Sarmah, R. K., Goswami, U., Bhattacharyya, P., Majumdar, D., Bezbaruah, D. and Borgohain 2016, *"Fall of a new meteorite at Komargaon, Assam, India"*, Curr. Sci., v. 110, p. 1894-1895.
31. Groopman, E., Zinner, E., Amari, S., Gyngard, F., Hoppe, P., Jadhav, M., Lin, Y., Xu, Y., Marhas, K. and Nittler, L. 2015, *"Inferred initial 26Al/27Al ratios in presolar stardust grains from supernovae are higher than previously estimated"*, ApJ, v809, pp. 1-16.
32. Mahajan, R. R. 2015, *"Lunar meteoriteYamato-983885: Noble gases, nitrogen and cosmic ray exposure history"*, Planet. Space Sci., v. 117, p. 24-34.
33. Mahajan, R. R., Varela M. E. and Joron J. L. 2016, *"Santa Lucia (2008) (L6) Chondrite, a Recent Fall: Composition, Noble Gases, Nitrogen and Cosmic Ray Exposure Age"*, Earth Moon Planets, v. 117, p. 65-76.
34. Mishra, R. K., Marhas, K. K. and Sameer 2016, *"Abundance of 60Fe inferred from nanoSIMS study of QUE 97008 (L3.05) chondrules"*, Earth Planet. Sci. Lett., v. 436, p. 71-81.
35. Mukhopadhay, R., Iyer, S. D., Ray, D., Karissidaiah, S. M. and Drolia, R. K. 2015, *"Morphotectonic and Petrological variations along the southern Central Indian Ridge"*, Indian Ocean. International Journal of Earth Sciences, v. 105, p. 905-920.
36. Pabari, J. P. and Banerjee, D. 2016, *"Levitation of Charged Dust Grains and Its Implications in Lunar Environment"*, Curr. Sci., v. 110, p. 1984-1989

37. Ray, D., Ghosh, S. and Murty, S. V. S. 2015, *"Shock-thermal history of Kavarpura IVA iron: Evidences from micro textures and Ni profiling"*, Planetary and Space Science, v. 117, p. 136-145.
38. Shanmugam, M., Acharya, Y. B., Vadawale, S. V. and Mazumdar, H. S. 2015, *"Radiation effects on Silicon Drift Detector based X-ray spectrometer on-board Chandrayaan-2 Mission"*, JINST, v. 10 , p. 09005.
39. Srivastava, N. and Varatharajan, I. 2016, *"Geomorphology of Lowell crater region on the Moon"*, Icarus, v. 244, p. 44-56.

Space and Atmospheric Sciences

40. Bagiya, M. S., Sridharan, R., Sunda, S., Jose, L., Pant, T. K., and Choudhary, R. 2015, *"Impact of the perturbation zonal velocity variation on the spatio/temporal occurrence pattern of L-band scintillation - a case study"*, J. Geophys. Res. Space Phys., v. 120, p. 5882-5889.
41. Chakrabarty, D., Rout, D., Sekar, R., Narayanan, R., Pant, T. K., Thampi, S. V., Reeves, G. D., Veenadhari, B., and Shiokawa, K. 2015, *"Three different types of electric field disturbances affecting equatorial ionosphere during a long duration prompt penetration event"*, J. Geophys. Res. Space Phys., v. 120 , p. 4993-5008.
42. Chandra, H. 2015, *"VHF scintillations at the Indian low latitudes"*, Asian J. Phys., v. 24 , p. 851-867.
43. Chandra, N., Lal, S., Venkataramani, S., Patra, P. K., and Sheel,V. 2015, *"Temporal variations in* CO_2 *and CO at Ahmedabad in western India"*, Atmos. Chem. Phys. Discuss., v. 15, p. 1-54.
44. Guharay, A., Batista, P. P., and Clemesha, B. R. 2015, *"On the variability of the diurnal tide and coupling with planetary waves in the MLT over Cachoeira Paulista (22.7° S, 45° W)"*, J. Atmos. Sol. Terr. Phys., v. 133, p. 7-17.
45. Guharay, A., Batista, P. P., and Clemesha, B. R. 2015, *"Variability of the quasi-2-day wave and interaction with longer period planetary waves in the MLT at Cachoeira Paulista"*, J. Atmos. Sol. Terr. Phys., v. 130-131 , p. 57-67.
46. Gupta, S. P., and Thampi, S. V. 2015, *"Electrical conductivity of the stratosphere over Hyderabad, India: Results from Balloon borne measurements "*, Ind. J. Radio & Space Phys., v. 44 , p. 132-137.
47. Haider, S. A., Batista, I. S., Abdu, M. A., Muralikrishna, P., Shah, S. Y., and Kuroda, T. 2015, *"Dust storm and electron density in the equatorial D region ionosphere of Mars: Comparison with Earth's ionosphere from rocket measurements in Brazil"*, J. Geophys. Res. Space Physics, v. 120 , p. 8968-8977.
48. Haider, S. A., and Pandya, B. M. 2015, *"Probing of meteor showers at Mars during the encounter of comet C/2013 A1 predictions for the arrival of MAVEN/Mangalyaan"*, Geosci. Lett., v. 2, pp. 1-13.
49. Kumar, P., Shukla, B. P., Sharma, S. K., Kishtawal, C. M., and Pal, P. K. 2015, *"A high resolution simulation of catastrophic rainfall over Uttarakhand, India"*, Natural Hazards, v. 80, p. 1119-1134.
50. Lal, S., Chandra, N., and Venkataramani, S. 2015, *"A study of* CO_2 *and related trace gases using a laser based technique at an urban site in western India"*, Curr. Sci., v. 109 , p. 2111-2116.
51. Mallik C., Lal, S., and Venkataramani, S. 2015, *"Trace gases at a semi-arid urban site in western India: Variability and inter-correlations"*, J. Atmos. Chem., v. 72 , p. 143-164.
52. Mittal, M., Chandra, H., and Sharma, R. 2015, *"Effect of Interplanetary magnetic field on Ionospheric Drift"*, Asian J. Phys., v. 24, p. 869-873.
53. Rajesh, T. A., Vinchhi, J. T., and Bhavsar, M. 2016, *"Auto-start hardware for double conversion UPS"*, J. Ins. Soc. Ind., v. 45, p. 195-197.
54. Ramachandran, S. 2015, *"New Directions: Mineral Dust and Ozone-Heterogeneous Chemistry"*, Atmos. Environ., v. 106, p. 379-370.
55. Ramachandran, S., Kedia, S., and Sheel, V. 2015, *"Spatiotemporal characteristics of aerosols in India: Observations and model simulations"*, Atmos. Environ., v. 116, p. 225-244.
56. Rastogi, R. G., and Chandra, H. 2015, *"Equatorial electrojet in the African sector"*, Ind. J. Radio & Space Phys., v. 44, p. 187-198.
57. Rastogi, R. G., Chandra, H., Das, A. C., Sridharan, R., Reinisch, B. W., Ahmed, K., Fontes, S. L., and Sanchez, J. A. A. 2015, *"A new feature of equatorial electrojet and space weather"*, Asian J. Phys., v. 24, p. 1507-1521.
58. Rastogi, R. G. and Chandra, H. 2015, *"Spread F at Tropical Latitude Stations in India Ahmedabad"*, Ind. J. Radio & Space Phys., v. 44, p. 177-186.
59. Sahu, L. K., and Saxena, P. 2015, *"High time and mass resolved PTR-TOF-MS measurements of VOCs at an urban site of India during winter: role of anthropogenic, biomass burning, biogenic and photochemical sources"*, Atmos. Res., v. 164, p. 84-94.
60. Sahu, L. K., Sheel, V., Pandey, K., Yadav, R., Saxena, P., and Gunthe, S. S. 2015, *"Regional biomass burning trends in India: Analysis of satellite fire data"*, J. Earth Syst. Sci., v. 124, p.1377-1387.
61. Sahu, L. K., Yadav, R., and Pal, D. 2016, *"Source identification of VOCs at an urban site of western India: Effect of marathon events and anthropogenic emissions"*, J. Geophys. Res. Atmos., v. 121, p. 2416-2433.
62. Sarangi, T., Naja, M., Lal, S., Venkataramani, S., Bhardwaj, P., Ojha, N., Kumar, R., and Chandola, H. C. 2016, *"First observations of light non-methane hydrocarbons (C2-C5) over a high altitude site in the central Himalayas"*, Atmos. Environ., v. 125, p. 450-460.
63. Sharma, S., and Chandra, H., 2015, *"Electromagnetic precursor in the ionosphere associated with the Bhuj earthquake of 26 January, 2001"*, Asian J. Phys., v. 24 , pp. 843-850.
64. Sharma, S., Chandra, H., and Beig, G. 2015, *"Long term changes in the ionosphere over Indian low latitudes: Impact of greenhouse gases"*, J. Atmos. Sol. Terr. Phys., v. 128, p. 24-32.

65. Sharma, S., Chandra, H., Beig, G., Kumar, P., and Vaishnav, R. 2015, *"Investigations of Mesospheric Temperature Inversions over Subtropical Location using Lidar and Satellites Measurements"*, J. Atmos. Sol. Terr. Phys., v. 138-139, p. 54-65.
66. Sharma, S., Chandra, H., Lal, S., Acharya, Y. B., Jayaraman, A., Gadhavi, H., Sridharan, S., and Chandra, S. 2015, *"Study of Thermal Structure Differences from Coordinated Lidar Observations over Mt. Abu (24.5°N, 72.7°E) and Gadanki (13.5°N, 79.2°E)"*, Earth, Planets and Space, v. 67, pp. 1-11
67. Sharma, S., Vaishnav, R., Shukla, M. V., Kumar, P., Thapliyal, P. K., Lal, S., and Acharya, Y. B. 2016, *"Evaluation of Cloud Base Height measurement from Ceilometer CL31 and MODIS satellite over Ahmedabad, India: Preliminary results"*, Atmos. Meas. Tech., v. 9, p. 711-719.
68. Shreedevi, P. R., Thampi, S. V., Chakrabarty, D., Choudhary, R. K., Pant, T. K., Bhardwaj, A., Mukherjee, S. 2016, *"On the latitudinal changes in ionospheric electrodynamics and composition based on observations over the 76-77°E meridian from both hemispheres during a geomagnetic storm"*, J. Geophys. Res. Space Phys., v. 121 , p. 1557-1568.
69. Singh, R. P., and Pallamraju, D. 2015, *"On the latitudinal distribution of mesospheric temperatures during sudden stratospheric warming events"*, J. Geophys. Res. Space Phys., v. 120, p. 2926-2939.
70. Sinha, P. R., Gupta, P., Kaskaoutis, D. G., Sahu, L. K., Nagendra, N., Manchanda, R. K., Kumar, Y. B., and Sreenivasan, S. 2015, *"Estimation of particulate matter from satellite and ground-based observations over Hyderabad, India"*, Int. J. Remote Sensing, v. 36, p. 6192-6213.
71. Sridharan, R., Jose, L., Bagiya, M. S., Sunda, S., Chaudhary, R. K., and Pant, T. K. 2015, *"Refinement of the background ionospheric conditions and plausible explanation based on neutral dynamics for the occurrence/non- occurrence of L-band scintillation patches against forecast"*, J. Atmos. Sol. Terr. Phys., v. 133, p. 18-24.
72. Valsan, A. E., Priyamvada, H., Ravikrishna, R., Despres, V. R., Biju, C. V., Sahu, L. K., Kumar, A., Verma, R. S., Philip, L., and Gunthe, S. S. 2015, *"Morphological characteristics of bioaerosols from contrasting locations in southern tropical India-A case study"*, Atmos. Environ., v. 122, p. 321-331.
73. Yadav, S., and Pallamraju, D. 2015, *"On the coupled interactions between ring current intensity and high-latitude ionospheric electron density variations"*, J. Atmos. Sol.- Terr. Phy., v. 125-126, p. 50-58.

Geosciences

74. Agrawal, S., Srivastava, P., Sonam, Meena, N.K., Rai, S.K., Bhushan, R., Misra, D.K. and Gupta, A.K. 2015, *"Stable (δ^{13}C and δ^{15}N) isotopes and magnetic susceptibility record of late Holocene climate change from a lake profile of the northeast Himalaya"*, J. Geol. Soc. India, v. 86, p. 696-705.
75. Banerji, U. S., Pandey, S., Bhushan, R. and Juyal, N., 2015, *"Mid-Holocene climate and land-sea interaction along the southern coast of Saurashtra, western India"*, J. Asian Earth Sci, v. 111, p. 428-439.
76. Bhavya P. S., Kumar, S., Gupta, G. V. M., Sudharma, K. V., Sudheesh, V. and Dhanya, K. R. 2016, *"Carbon isotopic composition of suspended particulate matter and dissolved inorganic carbon in the Cochin estuary during post-monsoon"*, Curr. Sci., 110, p. 1539-1543.
77. Francis, T., Sarin, M. M., and Rengarajan, R., 2016, *"Atmospheric SO_2 oxidation efficiency over a semi-arid region: Seasonal patterns from observations and GEOS-Chem model"*, Atmos. Environ., v. 125, p. 383-395.
78. Godhe, A., Narayanaswamy, C., Klais, R., Moorthy, K. S. V., Ramesh, R., Rai, A. and Reddy, H. R. V., 2015, *"Long-term patterns of net phytoplankton and hydrography in coastal SE Arabian Sea: What can be inferred from genus level data?"*, Estuar. Coast. Shelf Sci., v. 162, p. 69-75.
79. Kaur-Kahlon, G., Kumar, S., Rehnstam-Holm, A., Rai, A., Bhavya, P. S., Edler, L., Singh, A., Andersson, B., Karunasagar, I., Ramesh, R. and Godhe, A. 2016, *"Aquatic Response of a coastal tropical pelagic microbial community to changed salinity and temperature"*, Aquatic Microbial Ecology, 77, p. 37-50.
80. Krishnamoorthy, K., Satheesh, S. K., Sarin, M. M. and Panday, A. K., 2016, *"South Asian aerosols in perspective: Preface to the special issue"*, Atmos. Environ., v. 125, p. 307-311.
81. Laskar, A. H., Ramesh, R., Burman, J., Midhun, M., Yadava, M. G., Jani, R. A. and Gandhi, N., 2015, *"Stable Isotopic Characterization of Nor'westers of Southern Assam, NE India"*, J. Climate Change, v. 1, p. 75-87.
82. Lekshmy, P. R, Midhun, M. and Ramesh, R., 2015, *"Spatial variation of amount effect over peninsular India and Sri Lanka: Role of seasonality"*, Geophys. Res. Lett., v. 42, p. 5500-5507.
83. Löscher, C. R., Fischer, M. A., Neulinger, S. C., Fiedler, B., Philippi, M., Schtte, F., Singh, A., Hauss, H., Karstensen, J., Körtzinger, A., Künzel, S. and Schmitz, R. A., 2015, *"Hidden biosphere in an oxygen-deficient Atlantic open-ocean eddy: future implications of ocean deoxygenation on primary production in the eastern tropical North Atlantic"*, Biogeosciences, v. 12, p. 7467-7482.
84. Managave , S. R., Jani, R. A., Narayana Rao, T., Sunilkumar, K., Satheeshkumar, S. and Ramesh, R., 2015, *"Intra-event isotope and raindrop size data of tropical rain reveal effects concealed by event averaged data"*, Clim. Dyn., v. 47, p. 1-7.
85. Midhun, M. and Ramesh, R., 2016, *"Validation of δ^{18}O as a proxy for past monsoon rain by multi?GCM simulations"*, Clim. Dyn., v. 46, p. 1371-1385.
86. Rastogi, N., Patel, A., Singh, A. and Singh, D., 2015, *"Diurnal variability in secondary organic aerosol formation over the Indo-Gangetic Plain during winter using online measurement of water-soluble organic carbon"*, Aerosol Air Qual. Res., v. 15, p. 2225-2231.
87. Rastogi, N., Singh, A., Sarin, M. M. and Singh, D., 2016, *"Temporal variability of primary and secondary aerosols over northern India: Impact of biomass burning emissions"*, Atmos. Environ., v. 125, p. 396-403.
88. Sarkar, S., Prakasam, M., Banerji, U. S., Bhushan, R., Kumar, P. and Meena, N. K., 2016, *"Rapid sedimentation history of Rewalsar Lake, Lesser Himalaya, India during the last fifty years-Estimated using ^{137}Cs and ^{210}Pb dating techniques: A comparative study with other North-Western Himalayan Lakes"*, Himalayan Geol., v. 37, pp. 1-7.

89. Singh, A., Srivastava, R., Rastogi, N. and Singh, D., 2016, *"Absorbing and Scattering Aerosols over the Source Region of Biomass Burning Emissions: Implications in the Assessment of Optical and Radiative Properties"*, Atmos. Environ., v. 127, p. 61-68.
90. Singh, A., Tiwari, S., Sharma, D., Singh, D., Tiwari, S., Srivastava, A. K., Rastogi, N. and Singh, A. K., 2016, *"Characterization and radiative impact of dust aerosols over northwestern part of India: a case study during a severe dust storm"*, Meteorol Atmos. Phys., v. 128, pp. 1-14.
91. Srinivas, B. and Sarin, M. M., 2015, *"Atmospheric deposition of phosphorus to the North Indian Ocean"*, Curr. Sci., v. 108, p. 1300-1305.
92. Srinivas, B., Rastogi, N., Sarin, M. M., Singh, A. and Singh, D., 2016, *"Mass absorption efficiency of light absorbing organic aerosols from source region of paddy-residue burning emissions in the Indo-Gangetic Plain"*, Atmos. Environ., v.125, p. 360-370.
93. Srinivas, B., Sarin, M. M. and Chinni, V., 2015, *"Atmospheric ^{210}Pb and anthropogenic trace metals in the continental outflow to the Bay of Bengal"*, Atmos. Environ., v. 122, p. 737-747.
94. Sudheer, A. K. and Rengarajan, R., 2015, *"Time-resolved inorganic chemical composition of fine aerosol and associated precursor gases over an urban environment in western India: Gas-aerosol equilibrium characteristics"*, Atmos. Environ., v. 109, p. 217-227.
95. Sudheer, A. K., Rengarajan, R. and Sheel, V. 2015, *"Secondary organic aerosol over an urban environment in a semi-arid region of western India"*, Atmospheric Pollution Research, v. 6, p. 11-20.
96. Tripathy G. R. and Singh, S. K., 2015, *"Re-Os depositional age for black shales from the Kaimur Group, Upper Vindhyan, India"*, Chem. Geol., v. 413, p. 63-72.
97. Unnikrishnan W. C, Praveen B. M, Sudheesh M. and Deshpande R. D. 2015, *"Studies on stable isotopic composition of daily rainfall from Kozhikode, Kerala, India"*, Isotopes in Environmental and Health Studies, v. 52, p. 219-230.
98. Yadava, M. G., Ramesh, R., Narayana, A. C. and Jani, R. A., 2016, *"Stable Oxygen and Hydrogen Isotopes in Drip and Rain Waters at the Belum Cave, Andhra Pradesh, India"*, J. Clim. Change., v. 2, p. 113-122.

Theoretical Physics

99. Adhikari, R., Dasgupta, A., Fong, C. S., Rangarajan, R. 2015, *"Nonthermal CP violation in soft leptogenesis"*, Phys. Rev. D, v. 91, p.096001, pp. 1-14
100. Arun Prasath, V., Godbole, R. M. and Rindani, S. D. 2015, *"Top polarisation measurement and anomalous* Wtb *coupling"*, Eur. Phys. J. C, v. 75, 402 pp.1-18
101. Bambhaniya, G., Dev, P. S. B., Goswami, S. and Mitra. M 2016, *"The Scalar Triplet Contribution to Lepton Flavour Violation and Neutrinoless Double Beta Decay in Left-Right Symmetric Model"*, JHEP, 1604, 046 , p.27
102. Bambhaniya, G., Goswami, S., Khan, S., Konar, P. and Mondal, T., 2015, *"Looking for hints of a reconstructible seesaw model at the Large Hadron Collider"*, Phys.Rev. D, v.91, p.075007, pp.1-12
103. Bambhaniya, G., Khan, S., Konar, P. and Mondal, T. 2015, *"Constraints on a seesaw model leading to quasi-degenerate neutrinos and signatures at the LHC"*, Phys.Rev. D, v. 91, p. 095007, pp. 1-12
104. Basak, T., Mohanty, S. and Tomar, G. 2016, *"Explaining AMS-02 positron excess and muon anomalous magnetic moment in dark left-right gauge model"*, JHEP, v.1603, p.062, pp. 1-16.
105. Bhalla, P., Das, N. and Singh, N. 2016, *"Moment Expansion to the Memory Function for Generalized Drude Scattering rate"*, Physics Letters A, v.380, p.2000-2007
106. Bhalla, P. and Singh, N. 2016, *"Generalized Drude Scattering rate from the memory function formalism: an independent verification of the Sharapov-Carbotte result"*, Eur. Phys. J. B, v.89, p.49
107. Chakravarty, G. and Mohanty, S. 2015, *"Power law Starobinsky model of inflation from no-scale SUGRA"*, Phys.Lett.B, v.746, p.242-247
108. Chattopadhyay, S., Mani, B. K. and Angom, D. 2015, *"Triple excitations in perturbed relativistic coupled-cluster theory and electric dipole polarizability of group-IIB elements"*, Phys. Rev. A, v 91, p. 052504, pp. 1-14.
109. Das, N. and Singh, N. 2016, *"Hot-electron relaxation in metals within the GoetzeWoelfle memory function formalism "*, Int. J. Mod. Phys. B , v.30, pp. 1-11.
110. Das, S., Goswami, G., Prasad, J. and Rangarajan, R. 2015, *"Revisiting a pre-inflationary radiation era and its effect on the CMB power spectrum"*, J. Cosmol Astropart Phys., v. 06, pp. 1-28.
111. Das, S., Goswami, G., Prasad, J. and Rangarajan, R. 2016, *"Constraints on just enough inflation preceded by a thermal era"*, Phys. Rev. D, v. 93, pp. 1-6.
112. Deppisch, F. F., Graf, L., Kulkarni, S., Patra, S., Anusandhan, S. O., Bhubaneswar, U., Rodejohann, W., Sahu, N. and Sarkar, U. 2016, *"Reconciling the 2 TeV excesses at the LHC in a linear seesaw left-right model"*, Phys.Rev. D, v.93, pp. 1-15.
113. Deppisch, F. F., Patra, S., Anusandhan, S. O., Bhubaneswar, U., Sahu, N., Sarkar, U. and Gonzalo, T. E. 2015, *"Double beta decay, lepton flavor violation, and collider signatures of left-right symmetric models with spontaneous D-parity breaking"*, Phys.Rev. D, v. 91, pp. 1-18.
114. Dhuria, M., Hati, C., Rangarajan, R. and Sarkar, U. 2015, *"Falsifying leptogenesis for a TeV scale* $\mathrm{W}_{\mathrm{R}}^{\pm}$ *at the LHC"*, Phys. Rev. D (Rapid Communications), v. 92, pp. 1-6.
115. Dhuria, M., Hati, C., Rangarajan, R. and Sarkar, U. 2015, *"The* $eejj$ *excess signal at the LHC and constraints on leptogenesis"*, J. Cosmol. Astropart. Phys., v.09, pp. 0-16.
116. Dhuria, M., Hati, C., Rangarajan, R. and Sarkar, U. 2015, *"Explaining the CMS eejj and e missing pT jj excess and leptogenesis in superstring inspired E6 models"*, Phys.Rev. D, v. 91, pp. 1-9.
117. Dhuria, M., Hati, C. and Sarkar, U. 2016, *"Moduli induced cogenesis of baryon asymmetry and dark matter"*, Phys.Lett. B, v. 756, p. 376-383.
118. Dhuria, M., Hati, C. and Sarkar, U. 2016, *"Explaining the CMS excesses, baryogenesis and neutrino masses in E6 motivated U(1)N model"*, Phys.Rev. D, v.93, pp. 1-11.

119. Dutta, J., Konar, P., Mondal, S., Mukhopadhyayaa, B. and Rai, S. K. 2016, *“A revisit to a compressed supersymmetric spectrum with 125 GeV Higgs”*, JHEP, v. 1601, pp. 1-28.
120. Garg, I. and Mohanty, S. 2015, *“No scale SUGRA SO(10) derived Starobinsky Model of Inflation”*, Phys.Lett. B, v.751, p. 7-11.
121. Ghosh, M. 2016, *“Reason for T2K to run in dominant neutrino mode for detecting CP violation”*, Phys. Rev. D, v. 93, pp. 1-9.
122. Ghosh, M., Ghoshal, P., Goswami, S., Nath, N. and Raut, S. K. 2016, *“New look at the degeneracies in the neutrino oscillation parameters, and their resolution by T2K, NOνA and ICAL”*, Phys. Rev. D , v. 93, pp. 1-16.
123. Ghosh, M., Goswami, S., and Raut, S. K. 2016, *“Maximizing the DUNE early physics output with current experiments”*, Eur. Phys. J.C , v.76, p. 1-14.
124. Goswami, G. and Mohanty, S. 2015, *“Higgs instability and de Sitter radiation”*, Phys. Lett. B, v.751, p. 113-118.
125. Gupta, G., Rangarajan, R. and Sen, A.A. 2015, *“Thawing quintessence from the inflationary epoch to today”*, Phys. Rev. D, v. 92, pp.1-8.
126. Hati, C., Kumar, G. and Mahajan, N. 2016, *“$\mathrm{B}^- \rightarrow \mathrm{D}^{(*)}\tau\bar{\nu}$ excesses in ALRSM constrained from B, D decays and D^0-$\bar{\mathrm{D}}^0$ mixing”*, JHEP, v.1601, pp. 1-20.
127. Hati, C. and Sarkar, U. 2016, *“Neutrino dark energy and leptogenesis with TeV scale triplets”*, Eur.Phys.J.C, v.76, pp. 1-7.
128. Kadam, G. P. and Mishra, H. 2015, *“Dissipative properties of hot and dense hadronic matter in an excluded-volume hadron resonance gas model”*, Phys. Rev. C, v.92, pp. 1-9.
129. Kadam, G. P. and Mishra, H. 2016, *“Medium modification of hadron masses and the thermodynamics of the hadron resonance gas model”*, Phys. Rev. C, v.93, pp. 1-6.
130. Kaur, J., Singh, S., Arora, B. and Sahoo, B. K. 2015, *“Magic wavelengths in the alkaline-earth-metal ions”*, Phys. Rev. A, v. 92, pp. 1-6.
131. Kaur, K., Arora, B. and Sahoo, B. K. 2015, *“Dispersion coefficients for the interactions of the alkaline-earth metal ions with a graphene layer”*, Phys. Rev. A, v. 92, pp. 1-7.
132. Kumar, A., Bhatt, J. R., Predhiman and K. Kaw 2016, *“On the Chiral imbalance and Weibel Instabilities”*, Phys. Lett. B, v. 757, p. 317-323.
133. Kumar, G. and Mahajan, N. 2016, *“$\mathrm{B} \rightarrow \mathrm{K}^*\ell^+\ell^-$ Zeroes of angular observables as test of standard model”*, Phys. Rev. D, v.93, pp. 1-10.
134. Mendiratta, G., Godbole, R. M. and Rindani, S. D. 2015, *“Looking for bSM physics using top-quark polarization and decay-lepton kinematic asymmetries”*, Phys. Rev. D, v. 92, pp. 1-18.
135. Mondal, T., Dey, U. K. and Konar, P. 2015, *“Implications of unitarity and charge breaking minima in a left-right symmetric model”*, Phys.Rev. D, v. 92, pp. 1-9.
136. Nandy, D. K. and Sahoo, B. K. 2015, *“Forbidden Transition Properties in the Ground State Configurations of Singly Ionized Noble Gas Atoms for Stellar and Interstellar Media”*, MNRAS, v. 450, p. 1012-1016.
137. Nandy, D. K., Singh, S. and Sahoo, B. K. 2015, *“Radiative properties of few F- and Cl-like alkali and alkaline-earth metal ions”*, MNRAS, v. 452, p. 2546-2552.
138. Pandey, A. K. and Bhatt, J. R. 2016, *“Primordial magnetic field and kinetic theory with Berry curvature”*, Phys.Rev. D, v.1503, pp. 1-11.
139. Pathak, H., Sahoo, B. K., Sengupta, T., Das, B.P., Vaval, N., and Pal, S., 2015, *“A Relativistic Equation-of-Motion Coupled-cluster Investigation of the Trends of Single and Double Ionization Potentials in the He and Be Isoelectronic Systems”*, J. Phys. B, v. 48, pp. 1-9.
140. Rindani, S. D., Sharma, P. and Thomas, A. W. 2015, *“Polarization of top quark as a probe of its chromomagnetic and chromoelectric couplings in $t\mathrm{W}$ production at the LHC”*, JHEP, v. 10, 180 pp. 1-24.
141. Roy, A. and Angom, D. 2015, *“Thermal suppression of phase separation in condensate mixtures”*, Phys. Rev. A, v 92, pp. 1-5.
142. Sahoo, B. K. 2016, *“Conforming the measured lifetimes of the $5d\ ^2\mathrm{D}_{3/2;5/2}$ states in Cs with theory”*, Phys. Rev. A, v. 93, pp. 1-10.
143. Sahoo, B. K. 2015, *“Appraising nuclear octupole moment contributions to the hyperfine structures in ^{211}Fr”*, Phys. Rev. A, v. 92, pp. 1-10.
144. Sahoo, B. K., Aoki, T., Das, B. P. and Sakemi,Y. 2016, *“Enhanced spin-dependent parity non-conservation effect in the $7s\ ^2\mathrm{S}_{1/2} \rightarrow 6d\ ^2\mathrm{D}_{5/2}$ transition in Fr: A possibility for unambiguous detection of nuclear anapole moment.”*, Phys. Rev. A, v. 93, pp. 1-6.
145. Sahoo, B. K. and Das, B. P. 2015, *“Theoretical studies of the long lifetimes of the $6d\ ^2\mathrm{D}_{3/2;5/2}$ states in Fr: Implications for parity nonconservation measurements.”*, Phys. Rev. A, v. 92, pp. 1-5.
146. Sahoo, B. K., Nandy, D. K., Das, B. P. and Sakemi, Y. 2015, *“Correlation Trends in the Hyperfine Structure of ^{210,212}Fr”*, Phys. Rev. A, v. 91, pp. 1-9.
147. Sarkar, U. 2016, *“Neutron-Antineutron Oscillations: Theoretical Status and Experimental Prospects”*, Phys. Rep., v.612, p. 1-45.
148. Sarkar, U., Hati, C., Patra, S., Pritimita, P., Deppisch, F, F., Anusandhan, S. O. and Bhubaneswar, U. 2016, *“Implications of the diphoton excess on leftright models and gauge unification”*, Phys.Lett. B, v.757, p. 223-230.
149. Selvaganapathy, J., Das, P.K. and Konar, P. 2015, *“Search for associated production of Higgs with Z boson in the noncommutative Standard Model at linear colliders”*, Int.J.Mod.Phys. A, v.30, pp. 1-20.
150. Singh, Y. and Sahoo, B. K. 2015, *“Relativistic many-body calculations for electric dipole moments in ^{129}Xe, ^{199}Hg, ^{223}Rn, ^{225}Ra and ^{171}Yb atoms”*, J. Atomic, Molecular, Condensate and Nano Physics, v. 2, p. 115-125
151. Singh, Y. and Sahoo, B. K. 2015, *“Electric dipole moment of ^{225}Ra due to P- and T-violating weak interactions”*, Phys. Rev. A, v. 92, pp. 1-4.
152. Suthar, K., Roy, A. and Angom, D. 2015, *“Fluctuation-driven topological transition of binary condensates in optical lattices”*, Phys. Rev. A, v 91, pp. 1-9.

153. Swain, A. K. and Konar, P. 2016, *"Mass reconstruction with M_2 under constraint in semi-invisible production at a hadron collider"*, Phys. Rev. D, v. 93, pp. 1-12.
154. Tomar, G., Mohanty, S. and Pakvasa, S. 2015, *"Lorentz Invariance Violation and IceCube Neutrino Events "*, JHEP, v.1511, pp. 1-16.

Atomic, Molecular and Optical Physics

155. Aadhi, A., Vaity, P., Chithrabhanu, P., Reddy, S. G., Prabhakar, S. and Singh, R. P. 2016, *"Non−coaxial superposition of vector vortex beams"*, Applied Optics, v. 55, p. 1107−1111.
156. Bhattacharjee, D., Jain, V., Chattopadhyay, A., Biswas, R. H. and Singhvi, A. K. 2015, *"Geomorphic evidences and chronology of multiple neotectonic events in a cratonic area Results from the Gavilgarh Fault Zone, central India"*, Tectonophysics, v. 677-678, p. 199-217
157. Bisht, P. S., Nawaz Ali, Shukla, A. D., Negi, S., Sundriyal, Y. P., Yadava, M. G. and Juyal, N. 2015, *"Chronology of late Quaternary glaciation and landform evolution in the upper Dhauliganga valley, (Trans Himalaya), Uttarakhand, India"*, Quaternary Sci Rev, v. 129, p. 147-162.
158. Chaitanya, A. N., Aadhi, A., Jabir, M. V. and Samanta, G. K. 2015, *"High-power, high-repetition-rate, Yb-fiber laser based femtosecond source at 355 nm"*, Opt Lett, v. 40, p. 4269-4272.
159. Chaitanya, A. N., Aadhi, A., Jabir, M. V. and Samanta, G. K. 2015, *"Frequency-doubling characteristics of high- power, ultrafast phase singular optical beams"*, Opt Lett, v. 40, p. 2614-2617.
160. Chithrabhanu, P., Aadhi, A., Reddy, S. G., Prabhakar, S., Samanta, G. K., Paul, G. and Singh, R. P. 2015, *"Three−particle hyper−entanglement teleportation and quantum key distribution"*, Quantum Inf. Process., v. 14, p. 3813−3826.
161. Chithrabhanu, P., Reddy, S. G., Anwar, A., Aadhi, A., Prabhakar, S. and Singh, R. P. 2015, *"Scattering of non−separable states of light"*, Opt Commun, v. 355, p. 301−305.
162. Das, A., Majumdar, L., Sahu, D., Gorai, P., Sivaraman, B. and Chakrabarti, S. K. 2015, *"Methyl acetate and its singly deuterated isotopomers in the interstellar medium"*, ApJ, v. 808, pp. 1-14.
163. Jabir, M. V., Chaitanya, A. N., Aadhi, A. and Samanta, G. K. 2016, *"Generation of "perfect" vortex of variable size and its effect in angular spectrum of the down-converted photons"*, Sci. Rep., v. 6, pp. 1-15.
164. Lancaster, N., Wolfe, S., Thomas, D., Bristow, C., Bubenzer, O.,Burrough, S., Duller, G., Halfen, A., Hesse, P.,Roskin, J.,Singhvi, A., Tsoar, H., Tripaldi, A., Yang, X. and Zarate, M. 2015, *"The INQUA Dunes Atlas chronologic database"*, Quatern. Int., v. 410, p. 3-10.
165. Malik, J. N., Banerjee, C., Khan, A., Johnson, F. C., Shishikura, M., Satake, K. and Singhvi, A.K. 2015, *"Stratigraphic evidence for earthquakes and tsunamis on the west coast ofSouth Andaman Island, India during the past 1000 years"*, Tectonophysics, v. 661, p. 45-65.
166. Morthekai, P., Chauhan, P. R., Jain, M., Shukla, A. D., Rajapara, H. M., Krishnan, K., Sant, D. A., Patnaik, R., Reddy, D. V. and Singhvi, A. K. 2015, *"Thermally re−distributed IRSL (RD−IRSL) A new possibility of dating sediments near B/M boundary"*, Quat Geochronol, v.30, p. 154−160.
167. Narayanan, R., Inomata, K., Gopakumar, G., Sivaraman, B., Zempo, Y. and Hada, M. 2015, *"Theoretical study of the infrared frequencies of crystalline methyl acetate under interstellar medium conditions"*, Spectrochim Acta A, v.153, p. 415-421.
168. Nomoto, S., Aadhi, A., Prabhakar, S., Singh, R. P., Vyas, R. and Singh, S. 2015, *"Polarization properties of the Airy beam"*, Opt Lett, v. 40, p. 4516-4519.
169. Pandey, A., Saha, K., Bapat, B., Kumar, P., Banerjee, S. B. and Subramanian, K. P. 2016, *"Probing high−lying $N_2^{++} and \mathrm{CO}^{++}$ states via energy−selective fragment spectra"*, J. Phys. B, v. 49, p.1-7.
170. Pandey, A., Kumar, P., Banerjee, S.B., Subramanian, K. P. and Bapat, B. 2016, *"Electron−impact dissociative double ionization of N_2 and CO Dependence of transition probability on impact energy"*, Phys. Rev. A, v. 93, pp. 1-6.
171. Prabhakar, S., Reddy, S. G., Aadhi, A., Chithrabhanu, P., Samanta, G. K. and Singh, R. P. 2015, *"Violation of Bell's inequality for phase−singular beams"*, Phys. Rev. A, v. 92, pp. 1-6.
172. Reddy, S. G., Chithrabhanu, P., Prabhakar, S., Anwar, A., Banerji, J., and Singh, R. P. 2015, *"Divergence of optical vortex beams"*, Appl. Optics, v. 54, p. 6690-6693.
173. Reddy, S. G., Chithrabhanu, P., Prabhakar, S., Anwar, A. and Singh, R. P. 2015, *"Recovering the vorticity of a light beam after scattering"*, Appl Phys Lett, v. 107, pp. 1-6.
174. Reddy, S. G., Chithrabhanu, P., Vaity, P., Aadhi, A., Prabhakar, S. and Singh, R. P. 2016, *"Non−diffracting speckles of a perfect vortex beam"*, Journal of Optics, v. 18, pp. 1-7.
175. Reddy, S. G., Prabhakar, S., Chithrabhanu, P., Singh, R. P. and Simon, R. 2016, *"Polarization state transformation using two quarter wave plates application to Mueller polarimetry"*, Appl. Optics, v. 55, p. B14-B19.
176. Roy, P. D. and Singhvi, A. K. 2016, *"Climate variation in the Thar Desert since the Last Glacial Maximum andevaluation of the Indian Monsoon"*, TIP Revista Especializada en Ciencias Qumico−Biolgicas, v. 19(1), p. 32−44.
177. Sharma, S. K., Thomas, J., Pandian, M. S., Rao, P. S., Gartia, R. K. and Singhvi, A. K. 2015, *"Exploring stable thermoluminescence signal in natural Barite (BaSO4) for retrospective dosimetry"*, Appl Radiat Isotopes, v. 105, p. 198-203.
178. Sivaraman, B. 2016, *"Electron Impact Dissociation of Carbon dioxide-Carbon disulphide Ice Analog and its Implications on the Identification of Carbon disulphide on Moon"*, J. Chem. Sci., v.128, p. 159-164.
179. Sivaraman, B., Venkataraman, V., Kalyaan, A., Arora, S. and Ganesh, S. 2015, *"Exposed Amorphous Water ice on Comet 49P / Arend-Rigaux"*, Adv Space Res, v.56, p. 2428-2431.
180. Sundriyal, Y. P., Shukla, A. D., Rana, N., Jayangondaperumal, R., Srivastava, P., Chamyal, L. S., Sati, S. P. and Juyal, N. 2015, *"Terrain response to the extreme rainfall event of June 2013 Evidence from the Alaknanda and Mandakini River Valleys, Garhwal Himalaya, India"*, Episodes, v. 38, p. 179-188.

Library & Information Services

181. Alam, M. N. 2016, *“Scanner for Digitization: An Overview”*, Knowledge Librarian, v. 3, p. 47-56
182. Alam, M. N. 2016, *“Research Trends on Astrometry and Celestial Mechanics in India: A Scientometric Study”*, e-Library Science Research Journal , v. 4, p. 1-15.
183. Pandey, P., 2016, ”GIS research in India from 1991-2014: A Bibliometric Contemplation”, International Research Journal of Library and Information Science, v. 6, p. 144-158.

Publications

Publications in Proceedings of Conference/ Symposia/ Workshops

Astronomy and Astrophysics

1. Baliyan, K. S., Kaur, N., Sameer, Ganesh, S. and Chandra, S., 2015, *“Study of AGNs using Blazar Variability as a tool”*, Recent Trends in the Study of Compact Objects (RETCO-II): Theory and Observation. ASI Conference Series, 2015, Vol. 12, pp 101-104
2. Vadawale, S. V., 2015, *“Understanding galactic black hole binary systems in the era of Astrosat and beyond”*, Proceedings of Recent Trends in the Study of Compact Objects (RETCO-II): Theory and Observation, ASI Conference Series, 2015, Vol. 12, pp 159-165

Planetary Sciences and PLANEX Program

3. Basu, S. A., Babu, E.V.S.S.K., and Vijaya Kumar, T.2016, *“Olivine*$-\mathrm{H}osted$ *Melt*$-\mathrm{I}nclusions$ *in Martian Meteorite Tissint”*, 47^{th} Lunar and Planetary Science Conference. Houston Texas, Abstract#1836
4. Basu, S. A., Mahajan, R. R., Sisodia, M. S., Babu, E.V.S.S.K., Kumar, V. T., Prasad, S. M. and Bhandari, N., 2016, *“Multiple Stages of Early Evolution of Heterogeneous Type*$-7\mathrm{P}iplia$ *Kalan Eucrite”*, 47^{th} Lunar and Planetary Science Conference. Houston Texas, Abstract#1841.
5. Durga Prasad, K., Rai, V. K. and Murty, S. V. S., 2016, *“A Comprehensive 3D Thermal Model for an insight into diurnal and latitude variability of lunar subsurface temperatures”*, 47^{th} Lunar and Planetary Science Conference. Houston Texas, Abstract#1290
6. Ghosh, S. and Ray, D., 2016, *“Oblique impact induced microtextures in ordinary chondrite: Evidences from Shytal, Dacca, Bangladesh”*, 47^{th} Lunar and Planetary Science Conference. Houston Texas, Abstract#1017
7. Mishra, R. K., Simon, J. I., Ross, D. K. and Marhas, K. K., 2016, *“CAIs in Semarkona (LL3.0)”*, 47^{th} Lunar and Planetary Science Conference. Houston Texas, Abstract#2750
8. Misra, S. and Ray, D., 2016, *“Eu anomalies of lunar basalts reflect both source characters and magmatic fractionation”*, 47^{th} Lunar and Planetary Science Conference. Houston Texas, Abstract#1153
9. Misra, S., Ray, D., Andreoli, M. A. G. and Wilson, A. H., 2016, *“Petrochemistry of the deeper section of the impact-melt sheet, Morokweng crater, South Africa: Evidence from a 250 m basal chill zone”*, 47^{th} Lunar and Planetary Science Conference. Houston Texas, Abstract#1293
10. Pabari, J. P., Bhalodi, P. J. and Patel, D. K., 2016, *“Mars Orbit Dust Experiment (MODEX) for future Mars orbiter”*, 47^{th} Lunar and Planetary Science Conference. Houston Texas, Abstract#1419
11. Ray, D., Shukla, A. D. and Chandra, U., 2016, *“Mineralogy, geochemistry and Msbauer spectroscopy of iron concretions from Jurassic formation of Kutch, India: More insights into the depositional history and implications to Martian ‘blueberries’”*, 47^{th} Lunar and Planetary Science Conference. Houston Texas, Abstract#1016
12. Ray, D. Shukla, A.D. and Ghosh, S2016, *“The cumulate and basaltic eucrite: Comparative geochemistry with terrestrial MORB and implications to igneous history”*, 47^{th} Lunar and Planetary Science Conference. Houston Texas, Abstract#1015
13. Sanghani, M. N., Kooten, E. V., Shukla, L. K., Wielandt, D., Bizzarro, M. and Marhas, K. K., 2015, *“O*$-rich$ *presolar grains from Isheyevo lithic clasts”*, 5^{th} NanoSIMS meeting, Manchester

14. Srivastava, N., 2016, *"Lowell crater: A region of prime geological importance on the Moon"*, Geophysical Research Abstracts Vol.18, EGU2016−12570, 2016 EGU General Assembly 2016.

Theoretical Physics

15. Rangarajan, R., 2016, *"Inflation after Planck and BICEP2"*, Proceedings of the XXI DAE-BRNS High Energy Physics Symposium at IIT Guwahati, Springer Proc. Phys., v. 174, p. 453-461.
16. Rangarajan, R., 2016, *"Resonant Gravitino Production in the Early Universe"*, Proceedings of the XXI DAE-BRNS High Energy Physics Symposium at IIT Guwahati,Springer Proc. Phys. v. 174 p. 463-466.
17. Swain, A. K. and Konar, P., 2016, *"Mass Determination and Event Reconstruction at Large Hadron Collider"*, Springer Proc.Phys., v. 174, pp. 1-5.

Atomic, Molecular and Optical Physics

18. Aadhi, A., Chaitanya, A. N., Jabir, M. V., Pathak, M. R., Shaikh, N. U. and Samanta, G. K., 2015, *"Generation and Characterization of High Power and Higher Order Ultrafast Optical Vortices"*, Advanced Solid State Lasers, AM5A. 48 (2015)
19. Aadhi, A., Chaitanya, A. N., Jabir, M. V. and Samanta, G. K., 2015, *"Fiber Laser Based High Power, Ultrafast Source for 355 nm"*, Advanced Solid State Lasers, AM5A. 49 (2015)
20. Aadhi, A., Chaitanya, A. N., Jabir, M. V., Singh, R. P. and Samanta, G. K., 2015, *"Single-frequency continuous-wave tunable ultraviolet sources based on BIBO and PPKTP crystals and their comparative studies"*, International Conference on Optics & Photonics 2015, 96541G-96541G-6
21. Aadhi, A., Vaity, P., Chaitanya, A. N., Jabir, M. V., Singh, R. P. and Samanta, G. K., 2015, *"High-Power, CW, Airy Beam Optical Parametric Oscillator"*, CLEO: 2015 Postdeadline Paper Digest, (Optical Society of America, 2015), paper JTh5A.6. USA
22. Aadhi, A., Chaitanya, A. N., Jabir, M. V., Vaity, P., Singh, R. P. and Samanta G. K., 2015, *"High−Power, Continuous−wave, Source Of Coherent Radiation In 2−D Airy Intensity Distribution"*, Laser Science 2015, October 18−22, San Jose, California, United States, p. LTh1H.3
23. Aadhi, A., Chaitanya, A. N. and Samanta, G. K., 2015, *"All periodically-poled crystals based source of tunable, continuous-wave, single-frequency, ultraviolet radiation"*, CLEO: QELS_Fundamental Science, JTu5A. 26
24. Nomoto, S. M., Aadhi, A., Prahbakar, S., Singh, R. P., Vyas, R. and Singh, S., 2015, *"Polarization of the Airy Beam"*, Laser Science 2015, October 18−22, San Jose, California, United States, p. LTh4I. 2

Library & Information Services

25. Pandey, P. 2015, *'Application of Scientometrics for evaluating research: a case study of six decades of Science at Physical Research Laboratory, Ahmedabad, India"*, IASLIC 30th All India Conference, Gujarat University, Ahmedabad, 28-31 December.

Publications

Books Edited / Review Articles / Other Publications

Books Edited

1. Hood, R. R., Bange, H.W., Beal, L., Beckley, L. E., Burkill, P., Cowie, G.L., DAdamo, N., Ganssen, G., Hendon, H., Hermes, J., Honda, M., McPhaden, M., Roberts, M., Singh, S., Urban, E., Yu, W.2015, *"The Second International Indian Ocean Expedition (IIOE-2): Science Plan"*, SCORpp. 149.
2. Naik, Sachindra, 2015, "Be/X-ray Binary Pulsars", Chapter in a Book - Introduction to Astronomical Data Analysis, Scholars' Press, Deutschland, Germany, pp 1-21.

Review Articles

1. B Sivaraman, N J Mason2015, *"Simulating molecular synthesis on icy mantles"*, Asian Journal of Physics, v.24, 1151-1169

PRL Technical Note

1. Rajesh, T. A., Ramachandran, S., 2016, "Real time data acquisition and computation software package for Aethalometer", PRL Technical Note, PRL-TN-2016-108.

Promotion of Basic Sciences, Official Language and Outreach Activities

Vikram Jayanti Celebration at PRL-12 August, 2015

The 96th birth anniversary of Prof. Vikram A. Sarabhai was celebrated at Physical Research Laboratory (PRL), Ahmedabad on 12^{th} August 2015 by having a "Tree plantation ceremony" followed by a function in which "Shri Hari Om Ashram Prerit Senior Scientist Award for the year 2014 was bestowed on Prof. T. V. Ramakrishnan, DAE Homi Bhabha Chair, Department of Physics, Banaras Hindu University, Varanasi. Prof. Ramakrishnan is given this award for his significant contributions in condensed matter physics especially to the theory of liquid solid transition and of mixed valence systems.

A Tree Plantation Ceremony at PRL, in a photo from left to right: Prof. T. V. Ramakrishnan, Prof. Utpal Sarkar, Prof. Kartikey A. Sarabhai, Shri Revanta Sarabhai, Ms. Mallika Sarabhai and Prof. U. R. Rao.

Shri Hari Om Ashram Prerit Senior Scientist Award for the year 2014 was presented to Prof. T. V. Ramakrishnan by Prof. U. R. Rao. After the award function Prof. T. V. Ramakrishnan delivered an illustrative and elaborate award lecture entitled, "Superconductivity: a Slice of Science that Refuses to Die", covering the important aspects of his research work in the field of Superconductivity, a branch of science especially Physics, which has an everlasting research potential.

In a photo from left to right: Prof.P. Janardhan, Prof. Utpal Sarkar, Prof. T. V. Ramakrishnan, Shri Sanatbhai Patel and Prof. U. R. Rao .

Shri Hari Om Ashram Prerit Senior Scientist Award was instituted in 1998 by the Hari Om Ashram Trust, Nadiad, to commemorate the birth centenary of Pujya Shri Mota, the founder of the Hari Om Ashram, Nadiad. The Award of Rs. 2.0 lac is made to an Indian scientist for

Promotion of Basic Sciences, Official Language and Outreach Activities

outstanding contributions in Science and Technology. An endowment fund, administered by Physical Research Laboratory was created for this purpose by the Hari Om Ashram Trust and the Award is given biennially. The previous recipients of this Award are: Late Dr. A.P.J. Abdul Kalam (first recipient), Dr. R. Chidambaram, Dr. C.N.R. Rao, Dr. R.A. Mashelkar, Dr. M.G.K. Menon, Prof. Man Mohan Sharma, Prof. Yash Pal and Dr. Anil Kakodkar.

Buti Foundation Award 2015

The Buti Foundation Award for the year 2015 was awarded in a function held on 03 November-2015 to mark the celebration of PRL's foundation (11 November). This award was conferred to Dr. Prateek Sharma, Department of Physics, Indian Institute of Science, Bangaluru for his significant contributions in the field of Space and Astrophysical Plasma modelling. This award is given to young scientists below 45 years for innovative and outstanding research work in India in the field of plasma science and technology. The award carries a citation, a silver medal and a cash prize.

PLANEX Programme

With the aim of creating awareness amongst students and research scholars particularly in the Universities and other Laboratories and Academic Institutions and to attract bright talented students to take up research work in the challenging area of Planetary Science and Exploration, the PLANEX programme of ISRO has been organizing periodic workshops and training programmes. Following 'Outreach Activities' were organized by PLANEX group during the year 2015-2016.

Participants of the 16^{th} PLANEX Workshop, 7-10 March 2016.

- Thirteen PLANEX supported projects are presently supported under PLANEX Program.
- PLANEX National facilities have been used by PLANEX PIs, PRL scientists and other visitors.
- Four issues of PLANEX newsletter have been published in the previous year.

RESPOND Programme

The Indian Space Research Organization (ISRO) has evolved a programme through which financial support is provided to academia in India for conducting research and development activities related to Space Science (PRL), Space Technology and Space Application. This programme is called RESPOND. In special cases research and development projects proposed by non-academic R & D laboratories can also be supported through this programme. The aim of RESPOND is to encourage quality research in areas of relevance to the Indian space programme.

During the year 2015-16, under the RESPOND programme, out of a total of 17 proposals, 5 were completed. Four new proposals were approved and around 10 proposals are at different stages of reviewing and recommendation processes. About 15 publications resulted in peer reviewed journals based on these ongoing projects and the results of these proposals form the basis for 2 theses works.

Annual RESPOND (Space Science) review meeting was held on 3-4 March 2016 PRL to monitor the progress of ongoing projects. Reports on 14 projects were presented by investigators (PIs/Co-PIs/research students of PIs) working in different fields in space sciences and hailing from universities spanning from different part of our country. The subjects of the proposals encompass Astronomy and Astrophysics, Physics of the Earth atmosphere/ionosphere, Solar Physics, Space Weather, and the Space Plasma Physics. A general discussion was held on 4 March, 2016 to give opportunity to PIs to express their views on RESPOND and other matters related to research funding. The meeting was concluded on 4 March with the remarks by panel of experts. The comments of the panel of reviewers for improving the projects are consolidated.

Activities on the promotion of Basic Sciences

On 26 June, 2015 a Science Exhibition Centre was initiated at PRL with an objective to create a facility for a common man to quench their quest to know about the research activities being pursued at PRL. This science Exhibition Centre had received a lot of appreciation from PRL colleagues, distinguished guests and outside students and teachers who visited this exhibition. Considering outreach as an important component of PRL, it was planned to develop additional space for science exhibition in the same area. Consequently, on 28 February, 2016 a new hall (1250 sq. feet) for a permanent science exhibition was inaugurated and an Openhouse / Science Exhibition was organized for three days, details of the same are described in the following sections. Besides items displayed in the first exhibition in June, 2015, various other posters, models, live demonstration, exhibits, PRLs ongoing real experiments (Raman Lidar, Trace gases monitoring, iron measurement) etc from various divisions were also displayed in the second exhibition. More than 3000 students, teachers and general public visited and appreciated these exhibitions. The plans to further expand the existing exhibition are underway.

PRL has been organizing popular lectures by eminent scientists open to the public. In this series the following popular lectures were organized during the this year.

- "Amazing Photons ", Prof. Girish S. Agarwal, Noble Foundation Chair and Regents Professor, Department of Physics Oklahoma State University, USA.
- "Climate Change: Role of Aerosols", popular lecture under aegis of Indian Meteorological Society, Ahmedabad, Prof. S. Ramachandran, Professor, Space and Atmospheric Sciences Division, PRL, Ahmedabad.

Science Day Celebration and PRL Scholarship

As has been the practice for several years, a day-long celebration was held at the Physical Research Laboratory, Ahmedabad to mark the

Promotion of Basic Sciences, Official Language and Outreach Activities

National Science Day. The celebrations aim to attract young minds and motivate them to take up science as one of their career options.

Glimpses of various activities during National Science Day Celebration.

National Science Day is also observed to spread the message of the importance of science and its application among the people and to accelerate the pace of development among them. PRL Scholarships from the Aruna Lal Endowment Fund, established by late Prof. Devendra Lal, former Director, were awarded to five students on this occasion. The selection was done on the basis of their performances in the state level screening test, poster competition and oral interview. All the five students are to receive Rs. 10,000/- per year for two consecutive years and for the third year provided the students continue to study in the science stream with high academic record.

In addition to the Aruna Lal scholarship, other prizes were awarded like centre wise top students (13) in the state level screening test held in February 2016 and poster/model competitions (12). Most students were accompanied by their teachers. Teachers and students had close interaction with PRL scientists and the judges of the poster/model competition throughout the day.

Also, to give an impetus to young students about the various scientific research being done at PRL, a small science exhibition was organized. All the students and teacher participants visited the exhibits and interacted with PRL scientists.

A unique panel discussion for teachers and parents on ”Frontiers of basic research and career options” was also organized on this day. An interactive lecture on ”Astronomy” was also delivered.

Open house Science Exhibition

PRL organized an ‘Open house Science Exhibition’ from 28th February to 1st March, 2016 at PRL that coincided with National Science Day celebrations. In this exhibition live experiments, live laboratory measurements, dynamic models, path breaking in-house built equipment, rare specimens of terrestrial and extra-terrestrial material, together with infographics on current research trends were exhibited. The objective of this exhibition was to reach out to students, teachers, researchers and a common man with interesting and exciting exhibits. Around 3000 people including kids and young school/college/university students visited PRL during this event. On this occasion a permanent Outreach Centre was also inaugurated.

Glimpses of Open house science exhibition.

Promotion of Basic Sciences, Official Language and Outreach Activities

Activities on the Promotion of Official Language

- The newly recruited assistants have been trained in-house for Hindi typing.
- PRL was awarded second prize on July 21, 2015 for outstanding implementation of the Official Language.
- Mobile app "Sampark" was launched in July where bilingual telephone directory can be seen.
- Hindi Technical Seminar was conducted on July 30, 2015 in which 14 scientific articles and 4 Official Language papers were presented.
- Participation of PRL Hindi section members in Inter-Center Hindi technical seminar conducted on August 5, 2015 at the Space Applications Centre, Ahmedabad.
- Hindi/English extempore was organized on August 20, 2015 on the occasion of Sadbhavana Diwas.
- A meeting of Space Glossary was arranged in PRL, USO from August 24-28, 2015.
- Hindi Pakhwada celebration from September 14-28, 2015.
- Meeting of PRL Official Language Committee on September 29, 2015.
- Hindi workshop held on September 29, 2015.
- Translation of the PRL Annual Report.
- An Essay Contest on "Corruption-free India" (Hindi/English) was organized to mark Vigilance Awareness Week in PRL on 28 October 2015.
- Translation of question paper for Scientific Assistant Recruitment exam in November 2015.
- In November 2015, Registrar, PRL inspected ADRIN, Secunderabad.
- Translation of PRL - FRSR, Manual.
- In December, 2015 Senior Hindi Officer inspected SDSC-SHAR, Liaison Office, Chennai and Antrix.
- Hindi Annual Inspection of PRL on December 18, 2015.
- Meeting of PRL Official Language Committee on December 31, 2015 in Mount Abu.
- Hindi workshop held on December 31, 2015 in Mount Abu. Participation of PRL members in the meeting of Space Glossary held from 4 to 8 January 2016 in Delhi. On January 12, 2016 an essay competition was organized, in which 8 employees participated.
- On January 12, 2016 a training session for administration employees was organized on the use of Hindi in COWAA.
- On 28-29 January 2016, the Department of Space Rajbhasha Orientation Program was conducted in PRL.
- Translation of National Science Day booklet.
- From the month of March, every day new Hindi words including their meaning and usage are sent through Sampark mobile app.
- Meeting of PRL Official Language Committee on March 14, 2016 in Udaipur.
- Hindi workshop held on March 14, 2016 in Udaipur.
- Shri RS Gupta, Hindi Officer II & OSD delivered lectures in Hindi workshops organized by various organisations like ONGC, IIM, BSNL etc. regarding How to work in Hindi in Computer.

back to contents

Facilities and Services

Computer Centre

Vikram-100 HPC The VIKRAM-100 is a High Performance Computing (HPC) Cluster with 100 teraflops sustained performance. This is a centrally-run service to support scientists/researchers and research scholars at PRL who require high performance computing. This includes workloads with requirements that can't be met by desktop PCs. Currently, Vikram-100 is the 15th fastest supercomputer in India.

Vikram-100 HPC

The 97 computing nodes of the HPC facility offers 2,328 CPU cores, 1,15,200 GPU Cores, 25 TB of RAM and 300 TB of high performance parallel filesystem. The cluster operating system is Red Hat Enterprise Linux 6.5, with job submission handled by IBM Platform Computing. The service supports a wide variety of third-party software including numerical packages, libraries and C and Fortran compilers. More Information about the Vikram-100 HPC is available at `https://www.prl.res.in/hpc`

Qmail to Postfix MTA migration

PRL has been using Free and Open Source Qmail as inbound and outbound mail transferring agent for over 12 years. Though Qmail is highly secure, its support has ended and therefore adding new features has become challenging. Now, Computer Centre has completely phased out Qmail, replacing it with much more advanced FOSS Postfix. CC has also incorporated latest security features like:

DKIM: Prevents spoofing of email by adding a digital signature to outgoing message headers. The Recipient server then retrieve the public key from PRL DNS server to decrypt incoming mail headers and verify that the message really came from PRL domain and has not been changed on transit.

DMARC: E-mail validation system designed to detect email spoofing by providing a mechanism to allow receiving mail server to check that incoming mail from a domain is authorized by that domain's administrators and that the email (including attachments) has not been modified during transport.

SSL Encryption & SPF Record Checking: PRL now supports SSL encrypted email delivery to and acceptance from Internet. SPF Record Checking: PRL now also supports checking SPF records of domains from where mails are received. This helps in ensuring that the mail has arrived from a legit source.

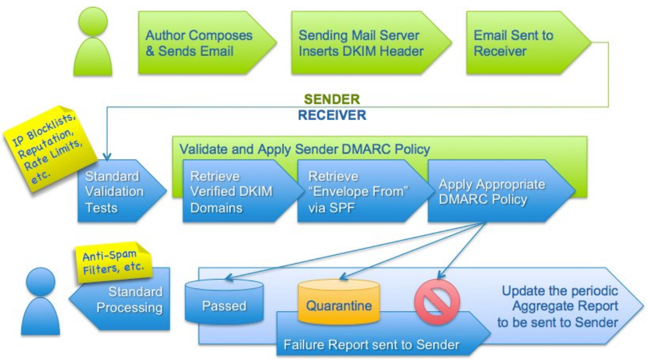

DMARC in Action

Optical Mark Recognition (OMR) based exam evaluation software

Open source software, customized in-house to cater the requirement to conduct OMR based examinations within PRL. The software only scans the OMR based answer sheet. A separate software is also developed to generate the result as per requirements. This software can be used to conduct various OMR base examinations. However, few modifications are required to process answer sheets. The software was successfully used to conduct Junior Research Fellow (JRF) - 2015 examination.

ShareLatex

ShareLatex is an easy to use, online, version controlled, collaborative LaTeX editor for PRL scientific community. In comparison to other LaTeX editors, ShareLaTeX is a server based application which is accessed via a web browser. PRL maintained instance of ShareLaTeX is available at http://sharelatex.lan.prl.res.in. ShareLaTeX is Node.js application served by Nginx reverse proxy written in CoffeeScript with data stored in MongoDB and Redis.

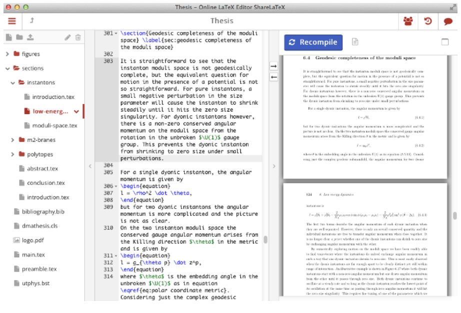

```
\section{Geodesic completeness of the moduli
space} \label{sec:geodesic completeness of
the moduli space}

It is straightforward to see that the
instanton moduli space is not geodesically
complete, but the equivalent question for
motion in the presence of a potential is not
so straightforward. For pure instantons, a
small negative perturbation in the size
parameter will cause the instanton to shrink
steadily until it hits the zero size
singularity. For dyonic instantons however,
there is a non-zero conserved angular
momentum on the moduli space from the
rotation in the unbroken $\U(1)$ gauge
group. This prevents the dyonic instanton
from shrinking to zero size under small
perturbations.

For a single dyonic instanton, the angular
momentum is given by
\begin{equation}
l = \rho^2 \dot \theta,
\end{equation}
but for two dyonic instantons the angular
momentum is more complicated and the picture
is not as clear.
On the two instanton moduli space the
conserved gauge angular momentum arises from
the Killing direction $\theta$ in the metric
and is given by
\begin{equation}
l = g_{\theta p} \dot z^p,
\end{equation}
where $\theta$ is the embedding angle in the
unbroken $\U(1)$ as in equation
\eqref{eq:polar coordinate metric}.
Considering just the complex geodesic
```

ShareLatex Screenshot

Sampark: PRL has Contributory Health Service Scheme (CHSS) to provide various medical facilities to PRL employees, pensioners and their dependents. PRL employees in the need of medical help may use the medical directories to get the details of doctors and facilities in the directory. At present, the medical directory is available in two formats. (1) Online: on PRL website (2) Offline: in the printed format available with each employee. However, these have limitations under various circumstances like unavailability of Internet, emergency medical requirements, etc. To overcome such issues, Sampark, an Android based mobile application is developed. Sampark leverages the benefits of smart phone technology and brings medical and telephone directories to mobile devices. Sampark doesn't require internet connections for its working. In addition, Sampark is also used to notify users about various events/updates happening in PRL.

MailMan

Mailman is free and open-source software for managing electronic mailing lists that supersedes PRL 'allusers' mail. The mailing list can either be a announcement list or discussion list. In contrast to traditional PRL allusers mail, in mailman: Mail is delivered from actual sender, i.e. 'From Address' is preserved. Mailman has archiving functionality through which new users can read old mails. Any user(s) can be designated as moderator(s) who can then forward the message withtout the need for Computer Centre's intervention for the mail forward. Certain addresses whose mail are to beforwared without anyones intervention can be exempted from moderation.

DNSSEC Operational

Computer Centre has configured DNSSEC in PRL's DNS server a while back. However, for DNSSEC to work, PRL's Internet Registrar (Ernet, (res.in)) must also support DNSSEC in their DNS. Computer Centre has pushed Ernet in configuring DNSSEC in their DNS thereby securing not only PRL but also all other domains in res.in (e.g. tifr, ipr, etc).

The Domain Name System Security Extensions (DNSSEC) is a specification used for securing information provided by the Domain Name System (DNS) as used on Internet. It provides DNS clients (resolvers) origin authentication of DNS data, authenticated denial of existence, and data integrity thereby preventing "Man in the Middle" and "DNS Cache Poisoning" attacks. By installing "DNSSEC/TLSA Validator" Add-on for browsers, PRL users can check if a (DNSSEC secured DNS) website (like PRL) is actually what it claims to be.

Website Certificate

Computer Centre has configured Symantec SSL certificate for PRL Website and PRL Mail access web services. Therefore PRL users will no longer be prompted to install self-signed certificate that was used before. This certificate has Extended Validation (Anti-Phishing Green Address bar) and ECC encryption algorithm support.

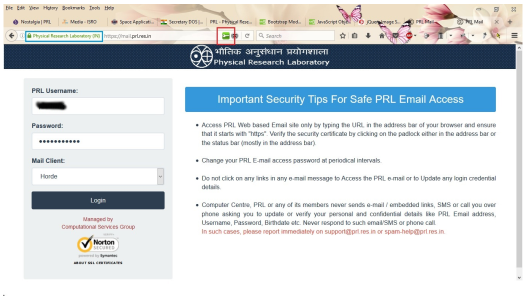

PRL Username: [redacted]

Password: •••••••••••

Mail Client: Horde

Managed by
Computational Services Group

Important Security Tips For Safe PRL Email Access

- Access PRL Web based Email site only by typing the URL in the address bar of your browser and ensure that it starts with "https". Verify the security certificate by clicking on the padlock either in the address bar or the status bar (mostly in the address bar).
- Change your PRL E-mail access password at periodical intervals.
- Do not click on any links in any e-mail message to Access the PRL e-mail or to Update any login credential details.
- Computer Centre, PRL or any of its members never sends e-mail / embedded links, SMS or call you over phone asking you to update or verify your personal and confidential details like PRL Email address, Username, Password, Birthdate etc. Never respond to such email/SMS or phone call. In such cases, please report immediately on support@prl.res.in or spam-help@prl.res.in.

Screenshot highlighting DNSSEC and Website Certificate

Library & Information Services

During 2015-16, two hundred and five (205) scientific and general books, 60 hindi books and 80 CDs/DVDs were added in the Main, Thaltej and USO libraries. Subscription of six journals has been added to the existing library collection of 165 journals. During this period, number of visitors, visiting the library was 2739 and number of documents issued and returned were 1683 and 1721 respectively Twenty five (25) book grant requests were processed to assist the students this year. Number of photocopies made, in house were 33553 and by outside agency were 44678.

PRL Library continues to subscribe to full-text databases like AGU Digital Library, GSA Archive, Nature archive (access from 1987), PROLA, and Science Archive. During 2015-16, SPIE Digital Library and IEEE Digital Library were made accessible as a part of ISRO Consortium. Also three backfiles of Elsevier - General Physics, High Energy Physics & Astronomy and Earth & Planetary Sciences (a total of 226 journals) were added to the library collection. Backfiles access is from Volume 1 issue 1 of the journal till 1994. As no library can be completely self-sufficient, the Library also provides document delivery service through Inter-Library Loan (ILL). The number of ILL requests for articles from other institutes fulfilled by PRL Library was 147 and that of requests of PRL staff fulfilled by other libraries was 159.

The Library homepage acts like a window through which it is possible to access the digital content subscribed by PRL as well as open access content. Primarily, it gives links to 165 online journals out of the 174 journals subscribed by the library.

The PRL institutional repository consisting of journal articles published by the PRL authors from 1994 to present is also linked through the Library homepage. More than 3300 articles by PRL authors are now part of the repository. All the PRL theses from 1952 onwards (383) are now available full text for PRL users. All the Technical Notes since 1977, published by PRL have been digitized (105) and are available full text for PRL users. E-books page has been redesigned so as give access to the collection by subject, alphabetical and publisher wise lists. These collections can be accessed from library homepage (http://www.prl.res.in/ library). The Library has taken up the digitization of the photographs archive. Scanning of the photographs of about 200 albums is completed. Tagging the photographs for retrieval will start soon.

A snapshot of PRL library at main campus.

Workshop

Establishment of Workshop at New building Thaltej campus

The workshop at new building Thaltej, PRL campus is established to meet mechanical requirement of the various ongoing and upcoming scientific programmes regarding the satellite payload prototype development work. The workshop will be useful to manufacture the accurate mechanical components for the various Space related and other scientific project at Thaltej campus. The newly established workshop has the following state—of—the—art machines (Figure 1).

Figure No.1: Newly established Workshop at PRL Thaltej campus with VMC, CNC Turning center, wire cute EDM, conventional lathe machine and other accessories.

CNC Turning centre: A Slant bed turning centre (DX—200) is installed for manufacturing high precision components. This machine will be more useful to produce specific diameters, depths, taper turning, specific generation, facing, parting, grooving, boring, drilling, knurling, reaming, threading, polygonal turning etc. with specified accuracy and tolerances.

Vertical Machining Centre with fourth axis: A vertical machining centre (VMC—640) is a machining centre with its spindle in a vertical orientation. High—end VMCs are high— precision machines often used for tight—tolerance milling. When it comes to mass production requiring higher rapids with multiple drills and taps Vertical Machining Centre VMC 640 brings easy solution. Equipped with directly coupled 10000 rpm spindle and rapid traverse of 40 m/min and 12 Station tool magazine, VMC 640 is a C-Framed rugged machine with moving table for easy access meeting short positioning times with highest degree of precision. Its structure supports rapid axes take— offs 2 with an acceleration of 5m/s.

Wire-Cut Electrical discharge machine: A wire—cut Electrical discharge machine (EDM) (continuously reciprocating using molybdenum and brass wire) is intended for the use of complex profile cutting and thin wall cutting with high aspect ratio on aerospace materials of various high strength steels, Titanium alloys, Super alloys etc. The machine can also be used to cut HSS and Carbide material. This machine shall have 4 axes linear interpolation configured with geometry X, Y, U & V. The machine shall be equipped with state−of−the−art CNC control system, drives and generator.

In addition to these machines a conventional lathe machine, drilling machine and Surface Grinder platform along with accessories has been installed and commissioned successfully.

In order to put the workshop at new building in operation, the renovation of mini old workshop room has been initiated. The installation of horizontal band saw machine, drill machine and shearing machine are under process. The old workshop will be utilised for the job preparation (marking, cutting, etc.), raw material storage (ferrous and non ferrous different sections) and hardware stock (fasteners, machine oils, coolant, cutting tools and assorted accessories, etc.).

Multi-wavelength PRL Radiometer

A multi−wavelength radiometer for study of aerosol columnar properties has been developed at PRL Workshop. It has been designed to accommodate six optical channels (380, 440, 500, 675, 870 and 1020 nm) with a field-of-view of 1.6 degree.

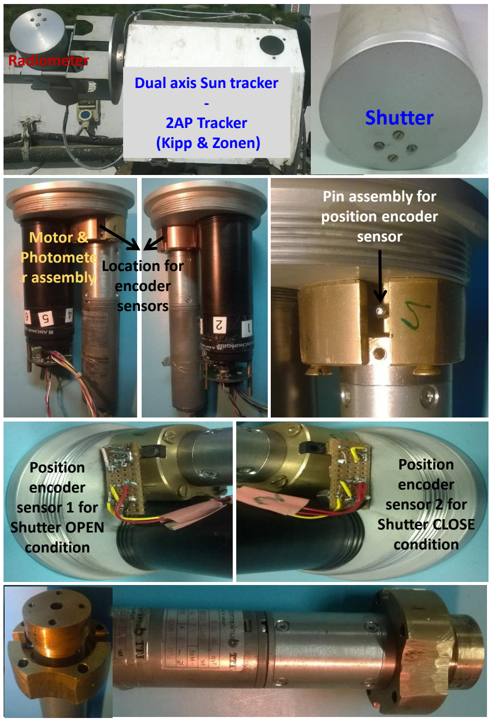

Figure No. 2: Schematic and components of radiometer.

The optical front end subsystem encompasses the optical interference filters (12.5 mm), baffle arrangement (to reduce the field of view), photo detectors board, temperature sensor, quartz window and strip heater. The complete assembly is made of aluminium using vertical milling machine VMC-850 and has been black anodized for dark current reduction. The optical front end subsystem is mounted inside nylon tube of diameter 105 mm and length 350 mm along with analog signal processing board, real time clock and state−of−the−art micro−controller (ATmega 2560) based control electronics. The radiometer dark current measurement prior to each observation is achieved through a micro−controller (Arduino Nano) based shutter mechanism. The entire sealed (water and dust proof) assembly is further housed inside a aluminium cylinder of diameter 125 mm and length 350 mm in order to reduce the maintain the temperature of the radiometer. The radiometer has been mounted on a 2−axis tracker and positioner (2AP−Kipp & Zonen) which is used to point the radiometer at the Sun's movement across the sky (Figure 2). It is working satisfactorily at Aerosol Radiation Monitoring Laboratory, PRL.

Ambient air dryer system

Real-time atmospheric ambient air dryer system has been designed and developed at PRL Workshop (Figure 3). The state−of−the−art system samples the atmospheric air at dry condition (using Silica beads) which is used as heart of the aerosol sampling system. The sample conditioner (dryer) consists of aluminium cylinder (length 6 feet and diameter 6 inch), houses 11 ducts (diameter 10 mm) made up from stainless steel (SS 316) wire mesh, inlet and outlet cone. Silica beads (10 kg) are used to remove the moisture content in the ambient air sample. The inlet and outlet cone carries the temperature and relative humidity sensors in order to monitor the change in the relative humidity. The complete assembly is made of aluminium using vertical milling machine VMC−850 and has been silver hard anodized for moisture resistant. The system has been tested successfully at Aerosol Monitoring Laboratory, PRL.

Figure No. 3: Schematic of dryer system.

Multi-Pixel Photon Counter (MPPC) modules for optical polarimeter

Adjustable hardware for supporting and mounting Multi−Pixel Photon Counter (MPPC) modules for optical polarimeter. The MPPC modules are compact photon counting detectors with built in cooling facilities and are replacing the bulky photo−multiplier tubes with their associated large cooling mechanisms. In the optical polarimeter we use two detectors (one for each beam coming from a Wollaston prism). As the beams coming from the Wollaston are inclined at different angles, a mechanism is needed to orient the detectors appropriately. Such a mechanism was designed and built with adjustable spacing facility to provide method to accurately align the detector with the outgoing optical beam from the Wollaston. The mechanism has been fabricated and two MPPC detectors have been installed in the structure which has been attached to the polarimeter (Figure 4). This has reduced the volume (and hence weight) of the instrument by half. Testing is in progress to verify operational suitability at the Mount Abu IR Observatory.

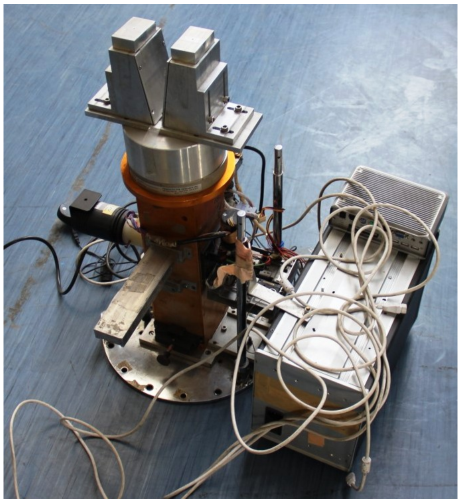

Figure No. 4: Multi-Pixel Photon Counter (MPPC) modules for optical polarimeter.

Adjustable coupler system for IR 50 cm telescope

The 50cm telescope has a fixed focal point with very small margin available in the focusing unit.

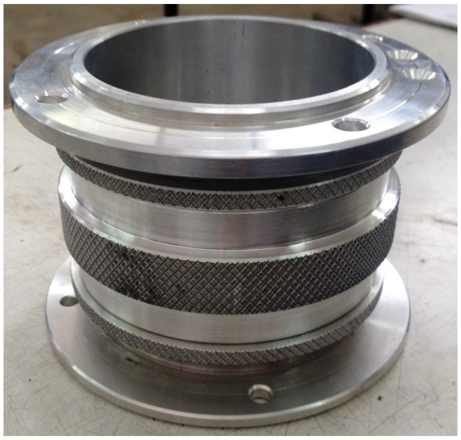

Figure No. 5: Adjustable coupler system for 50 cm telescope.

In order to change instruments with differing focal plane attachment points it was decided to design and build a coupler unit with variable separation but fixed relative orientation of the telescope and instrument. The design uses 3 parts with counter threading in the upper and lower halves. A 'sleeve' with threads going in one direction couple these two halves and by rotating this sleeve in clockwise or counter-clockwise directions the spacing between the telescope and the instrument can be changed coarsely without rotating the instrument. This was made by using aluminium alloy AL−6061 material with fine accuracy and micro− fine pitch threading (Figure 5).

Mount structure for CMAP system

For the ease of operation of instruments at Optical Aeronomy Observatory, Gurushikhar, Mt. Abu; a stand structure was fabricated at PRL workshop. The dimensions of this structure are 1m x 1m with variable length extensions. The frame was made of MS for robustness and platforms of aluminium sheets. Two platforms were provided with both being adjustable to any height as per the requirement of the experiment. The frame and platforms were fabricated at PRL workshop and installed at the observatory under one dome. This involved drilling and fitting of the stand to the ceiling with special screws. Currently, CMAP system is operational at the observatory which is using this stand (Figure 6).

Figure No. 6: Mount structure for CMAP system.

Turn table for the MISE instrument A turn−table was designed and fabricated in PRL workshop for the MISE instrument commissioned at JNTU, Hyderabad. It was made of two thick aluminium sheets with one resting on top of the other with ball bearings in between them. The upper sheet was locked with the bottom sheet with a check nut designed in such a way that it allows free movement of the sheet in azimuth direction. The turn−table was successfully installed and MISE was aligned accordingly to take day glow measurements in both meridional and zonal directions.

Charge Sharing Experiment with CZT Detectors Cadmium Zinc Telluride (CZT) detectors provide high quantum efficiency in hard X−rays, high energy resolution, moderate position sensitivity, room temperature operation and sufficient radiation hardness. In this experiment, we try to map the charge sharing region in the pixels and there from determine the size of cloud radius as a function of energy to verify that the fitted higher cloud radius is not because of fitting artifact; rather it is due to some physical phenomena (24−28 keV fluorescence photons) inside CZT detectors. The experiment set up consists of a CZT detector, radioactive sources, micrometer screw and a lead circular plate with a narrow hole at the centre of it (Figure 7). The source is kept on the top of the lead plate and scanned across the detector pixels with few micrometer step size using the micrometer stage. We developed the mechanical design of (Figure 7). There is a source holder made of Al connected to the micrometer screw through an L shaped Al plate. This precise mechanical assembly was made in PRL workshop. With this assembly we could map the charge sharing region in the CZT detector pixels. We are further working on improving the mechanical design specially to get hole size with diameter of 100m to get better results.

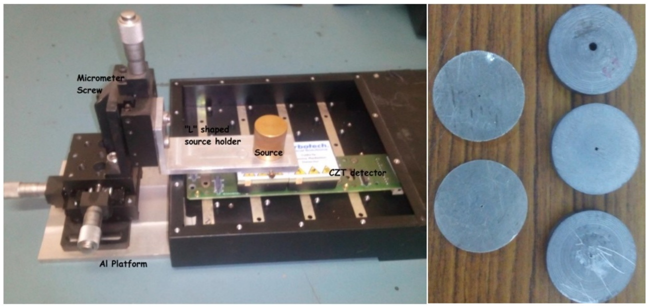

Figure No. 7: Experiment Set up for the CZT detector charge sharing experiment and Lead plates with different hole sizes.

Prototype development of Mars Orbit Dust Experiment (MODEX)

To study origin, abundance, distribution and possible seasonal variation of Martian dust, a Mars Orbit Dust Experiment (MODEX) is proposed for future Mars orbiter. The additional objective is to measure the Interplanetary Dust Particle (IDP) during the cruise phase of orbiter for enhancing understanding of the dynamical evolution.

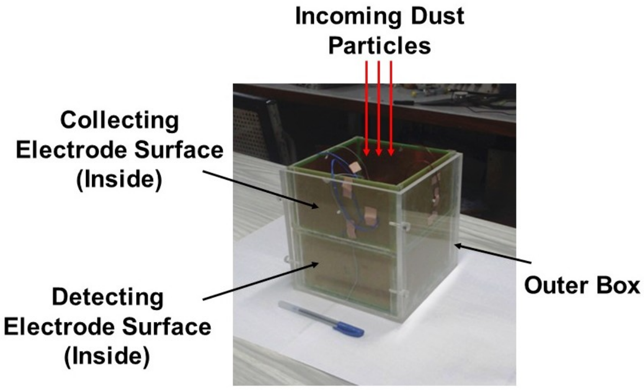

Figure 8: Snapshot of a prototype dust detector with mechanical package.

A prototype design of impact ionization dust detector and its electronics have been initiated at PRL. The preliminary circuit of front end electronics has been designed, implemented and tested successfully. Figure 8 shows a snapshot of the prototype detector, for which a mechanical package (160 mm (L) × 160 mm (W) × 170 mm (H)) has been made from Perspex material in PRL workshop.

Robotic arm based sampler system

An innovative and low cost approach, using a robotic arm, to perform contamination free handling of liquid samples. It consists of a robotic arm with control electronics and has provision of handling multiple samples in a single run. In this approach, a robotic arm reaches to sample bottles as per the user determined sequence and a sampling tube attached to its arm gripper is inserted into the sample bottles for suction.

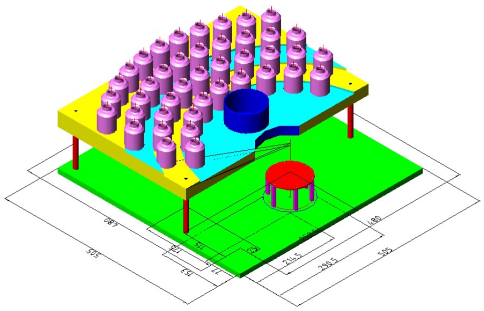

Figure No.9:Robotic arm based auto sampler.

The arm movement calculations are based on inverse kinematics approach. The structure of the Auto Sampler is fabricated from Perspex sheet of size 356 mm x 505mm x 38mm thick Perspex sheet.

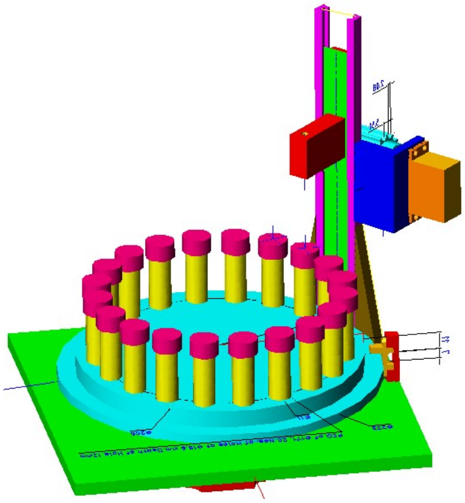

Figure No.10: PILS-Fraction collector.

Also all the parts of the structure are made from non metallic materials for protection against corrosion and contamination because structure is used in chemistry lab. The auto sampler can be integrated with any analytical instrument making it useful for various liquid sampling applications. A state−of−the−art robotic arm based auto sampler has been designed and developed in order to measure dissolved iron in seawater samples (Figure 9), water extract from particle into liquid sampler (PILS−Fraction collector, Figure 10) and fraction collector for trace elements like Strontium, Neodymium, Rubidium etc from chromatography column (CHROMATOGRAPHY— Fraction collector, Figure 11).

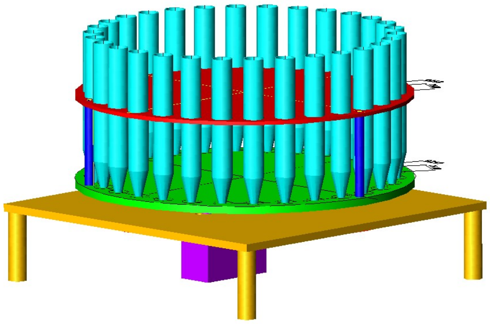

Figure No.11:CHROMATOGRAPHY—Fraction collector

Auto splitter system An auto splitter system (59 mm length x 74 mm width x 76 mm height) has been designed, developed and fabricated at PRL Workshop (Figure 12). It has more than 50 nos. of precise parts in an assembly which has been fabricated from Aluminium material using VMC 850 machine. The auto sampler has been installed and working satisfactorily as per the scientific requirement.

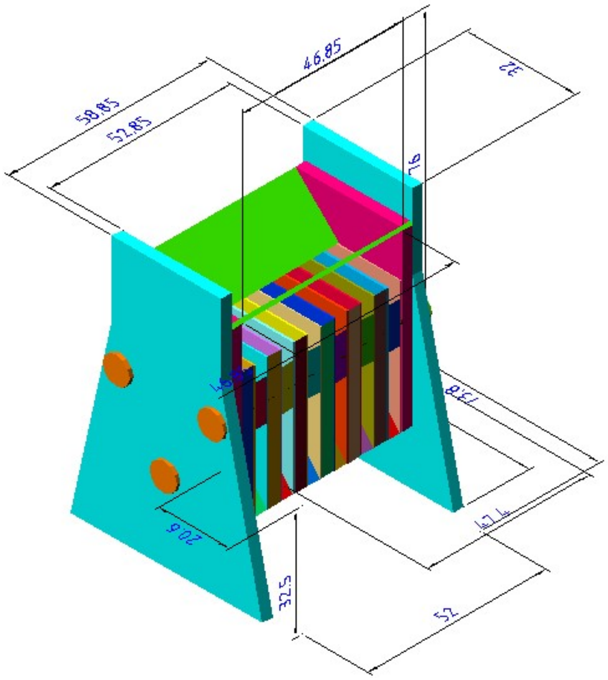

Figure No.12: Auto splitter system

Honorary Fellows

A. Hewish

J. E. Blamont

K. Kasturirangan

M. G. K. Menon

P. J. Crutzen

U. R. Rao

Honorary Faculty

A. Ambastha

A. Singal

A. C. Das

A. K. Singhvi
FNA, FASc, FNASc, FTWAS

A. R. Prasanna

A. S. Joshipura
FNA, FASc, FNASc

B. G. Anand Rao

D. P. Dewangan
FNASc

H. Chandra

H. O. Vats

H. S. S. Sinha

J. Banerji

J. N. Goswami
FNA, FASc, FNASc, FTWAS

M. M. Sarin
FNA, FASc, FNASc

N. Bhandari
FNA, FASc, FNASc, INSA Honorary Scientist

R. G. Rastogi
FNA, FASc, FNASc

R. Sridharan
FASc, FNASc, NASI Senior Scientist

Shyam Lal
FNA, FASc, FNASc

S. K. Gupta
FNASc

S. P. Gupta

S. V. S. Murty
FASc

T. Chandrasekhar

U. C. Joshi

V. K. B. Kota

Y. B. Acharya

Academic Faculty

Name	Designation	Specialization	Academic Qualification
Sarkar U. *FNA, FASc, FNASc*	Director (upto 31.05.2016)	Particle Physics	Ph.D., Calcutta Univ.(1984)
Acharyya K.	Reader	Astrochemistry	Ph.D., University of Calcutta (2008)
Ashok N. M.	Senior Professor	Close Binary Stars, NovaeIR spectroscopy	Ph.D., PRL, Gujarat Univ. (1983)
Baliyan K. S.	Professor	AGNs, Comets, Atomic Physics, Milky Way	Ph.D., Roorkee Univ. (1986)
Banerjee D.	Associate Professor	Thermoluminescence & Planetary Physics	Ph.D., PRL, Gujarat Univ. (1997)
Banerjee D. P. K.	Senior Professor	Novae, Be Stars, Planetary Nebulae, IR and Optical Studies	Ph.D., PRL, Gujarat Univ. (1990)
Banerjee S. B.	Scientist - SE	Experimental Molecular Physics	Ph.D., Saurashtra Univ. (2011)
Basu Sarbadhikari A.	Scientist-SE	Petrology & Geochemistry	Ph.D., IIT, Khargpur (2006)
Bhatt J. R.	Professor	Astrophysics	Ph.D., IPR, M.S. Univ. (1992)
Bhattacharyya R.	Associate Professor	Plasma Physics	Ph.D., Jadavpur Univ. (2006)
Bhushan R.	Scientist-SF	Oceanography and Paleoclimatology	Ph.D., PRL, M.S. Univ. (2009)
Chakrabarty A.	Associate Professor	Extra-solar planets, Star Formation & Instrumentation	Ph.D., PRL, Gujarat Univ. (1999)

Name	Designation	Specialization	Academic Qualification
Chakrabarty D.	Associate Professor	Upper Atmosphere and Geomagnetic storm	Ph.D., PRL, M.L.S Univ.(2008)
Chauhan N.	Scientist-SD	Luminescence Dating and Luminescence Dosimetry	Ph.D. Gujarat University (2012)
Deshpande R. D.	Scientist-SF	Application of Environmental Tracers in Hydrology	Ph.D., PRL, M.S. Univ. (2007)
Dewangan. L. K.	Scientist-SD	Astrophysics	Ph.D., Gujarat Univ. (2011)
Ganesh S.	Scientist-SE	Milky Way, Comets, AGN, Astronomical polarimetry	Ph.D., PRL, Gujarat Univ. (2010))
Goswami S.	Professor	High Energy Physics	Ph.D., Calcutta Univ. (1998)
Haider S. A. *FASc, FNA, FNASc*	Senior Professor	Planetary and Cometary Atmospheres	Ph.D., Banaras Univ. (1984)
Janardhan P.	Senior Professor	Solar Radio Astronomy & Space Weather	Ph.D., PRL, Gujarat Univ. (1991)
Joshi B.	Reader	Solar Physics, Astronomy	Ph.D., ARIES, Kumaun Univ. (2007)
Joshi V.	Scientist-SD	Observational Astronomy	Ph.D, Gujarat Univ. (2013)
Juyal N.	Scientist-SF	Quaternary Geology & Paleoclimate	Ph.D., PRL, M.S. Univ. of Baroda (2004)
Konar P.	Reader	Particle Physics	Ph.D.,HRI, Allahabad Univ. (2005)
Kumar B.	Reader	Solar Physics	Ph.D., PRL, M.L.S Univ. (2007)
Kumar S.	Reader	Aquatic and Terrestrial Biogeochemistry	Ph.D., PRL, M.S. Univ. of Baroda (2004)
Mahajan N.	Associate Professor	Particle Physics	Ph.D., Delhi Univ.(2004)
Marhas K. K.	Associate Professor	Solar System studies	Ph.D., PRL, D.A.V.V Indore (2001)
Mathew S. K.	Associate Professor	Solar Magnetic & Velocity Fields	Ph.D., PRL, Gujarat Univ. (1999)
Mishra H.	Professor	Strong Interaction Physics & Nuclear Astrophysics	Ph.D., IOP, Utkal Univ. (1994)
Mohanty S.	Senior Professor	Astroparticle Physics	Ph.D., Wisconsin Univ. (1989)
Naik S.	Associate Professor	High Energy Astrophysics, X-ray Binaries	Ph.D., TIFR, Bombay Univ. (2003)
Pallamraju D.	Professor	Space Weather and Atmospheric coupling processes	Ph.D., PRL, D.A.V.V Indore (1997)
Rai V.	Associate Professor	Stable Isotope Cosmochemistry	Ph.D., PRL, M.S Univ. of Baroda (2001)
Rajpurohit A. S.	Scientist-SD	Astronomy & Astrophysics	PhD, Observatory de Besancon, Universit de Franche-Comt, France (2013)

Name	**Designation**	**Specialization**	**Academic Qualification**
Ramachandran S.	Professor	Aerosols, Radiation & Chemistry-Climate Interactions	Ph.D., PRL, M.S Univ. of Baroda (1996)
Ramesh R. *FNA, FASc, FNASc, FTWAS*	Outstanding Scientist	Paleoclimatology, Oceanography & Modelling	Ph.D., PRL, Gujarat Univ. (1984)
Rangarajan R.	Professor	Particle Physics & Cosmology	Ph.D., Univ. of California, Santa Barbara (1994)
Rastogi N.	Reader	Atmospheric & Aerosol Chemistry	Ph.D., PRL, M.L.S Univ. (2005)
Ray J. S.	Professor	Isotope Geochemistry	Ph.D., PRL, M.S Univ. of Baroda (1998)
Ray D.	Scientist-SD	Marine Geology & Igneous Petrology	Ph.D., Jadavpur Univ. (2009)
Rengarajan R.	Scientist-SF	Atmospheric aerosols & aqueous geochemistry	Ph.D., PRL, M.L.S Univ. (2004)
Rindani S. D. *FNA, FASc, FNASc*	Senior Professor-H	Particle Physics	Ph.D., IIT, Bombay (1976)
Sahoo B. K.	Associate Professor	Atomic Physics	Ph.D., IIA, Mangalore Univ. (2006)
Sahu L. K.	Associate Professor	Atmospheric Science, Trace gases	Ph.D., PRL, M.L.S.Univ. (2005)
Samanta G. K.	Reader	Laser and Nonlinear optics	Ph.D., Universitat Politecnica de Catalunya Uni., Barcelona (2009)
Sarkar A.	Reader	MHD simulation & Solar Physics	Ph.D, University of Goettingen, Germany (2005)
Sekar R.	Senior Professor	Upper Atmoshperic & Ionospheric Physics	Ph.D., PRL, Gujarat Univ. (1991)
Sharma S. K.	Reader	Middle Atmosphere & Long Term Atmospheric Changes	Ph.D., PRL, Gujarat Univ. (2010)
Sheel V.	Associate Professor	Modelling of Lower Atmosphere	Ph.D., PRL, Gujarat Univ. (1996)
Shukla A. D.	Scientist-SE	Geochemistry & Cosmochemistry	Ph.D., PRL, M.S. Univ. (2012)
Singh A.	Reader	Ocean Biogeochemistry	Ph.D, MLSU Udaipur (2011)
Singh A. D.	Professor	Atomic Physics	Ph.D., IIA, Bangalore Univ. (1998)
Singh N.	Reader	Theoretical condensed matter and Statistical Physics	Ph.D., RRI, Bangaluru (2006)
Singh R. P.	Professor	Laser Physics	Ph.D., J.N.U., New Delhi. (1994)
Singh S. K.	Professor	Isotope Geochemistry	Ph.D., PRL, M.S. Univ. of Baroda (1999)
Singh V.	Scientist-SD	Active Galactic Nuclei and evolution of galaxies	Ph.D., Calicut University (2011)
Sivaraman B.	Reader	Low Temperature Astrochemistry	Ph.D., The Open University, UK (2008)

back to contents

Name	Designation	Specialization	Academic Qualification
Srivastava M.	Scientist - SD	Astronomical Instrumentation	Ph.D., Univ. of Pune (2012)
Srivastava N.	Professor	Solar Physics	Ph.D., PRL, Ravi Shankar Shukla Univ. (1994)
Subramanian K. P.	Professor	Experimental Atomic and Molecular Physics	Ph.D., PRL, Gujarat Univ. (1987)
Vadawale S. V.	Associate Professor	High Energy Astrophysics and X-Ray Spectroscopy	Ph.D., TIFR, Bombay Univ. (2003)
Vijayan S.	Scientist-SD	Planetary Remote Sensing	Ph.D., Anna Univ. Chennai (2013)
Yadava M. G.	Scientist-SF	Palaeoclimate, Radiocarbon dating and stable isotopes	Ph.D., PRL, DAVV, Indore (2003)

Technical Faculty

Name	**Designation**
Adhyaru P. R.	Engineer-SE
Bayanna A. R.	Scientist-SE
Bhavsar K. J.	Scientist-SE
Jani R. A.	Scientist-SE
Mahajan R.R.	Scientist-SE
Nishtha A.	Librarian-SE
Pabari J. P.	Engineer-SE
Panda D. K.	Scientist-SE
Rajesh T. A.	Scientist-SE
Rao D. K.	Scientist-SE
Raval J. R.	Engineer-SE
Shah A. B.	Engineer-SF
Shah R. R.	Engineer-SF
Shanmugam M.	Engineer-SE
Singh R. P.	Scientist-SE
Sudheer A. K.	Scientist-SE
Ubale G. P.	Engineer-SF
Vaghela H. R.	Engineer-SE
Venkataraman V.	Scientist-SE
Venkataramani S.	Scientist-SF
Wairagade S.	Engineer-SE

पी.आर.एल. में गतिविधियां
Events at PRL


पी.आर.एल. में गतिविधियां
Events at PRL

















पी.आर.एल. में गतिविधियां
Events at PRL

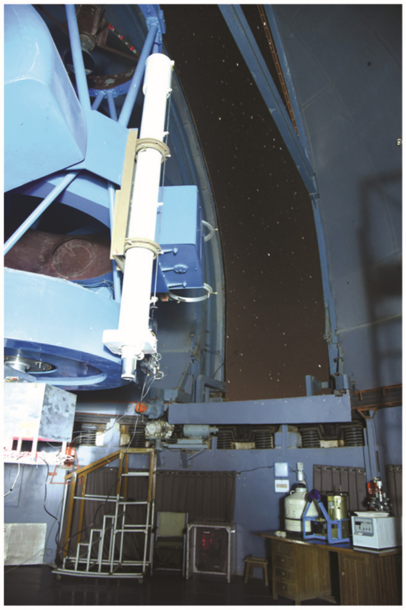

> *"One way to advance our understanding of the growth of institutions is through a wider sharing of knowledge gained from meaningful experience"*
>
> ***- Dr. Vikram A. Sarabhai***